UNIVERSITÀ DEGLI STUDI DI PADOVA

University of Padova

Department of Chemical Sciences

Ph.D. COURSE: Science and Engineering of Materials and Nanostructures

CYCLE: XXXIV

Lead Halide Perovskite Nanomaterials by Laser Ablation in Solution for More Sustainable Perovskite-based Optoelectronics

Coordinator: Ch.mo Prof. Giovanni Mattei

Supervisor: Ch.mo Prof. Moreno Meneghetti

Co-Supervisor: Ch.mo Prof. Gaudenzio Meneghesso

Ph.D. Candidate: Simone Sansoni

Abstract

In the last decade, the lead halide perovskite (LHP) semiconductor materials have drawn enormous attention since their exceptional optoelectronic properties and defect tolerance, finding application in a variety of optoelectronic devices like solar cells, light–emitting diodes, photodetectors, photocatalyst, field–effect transistors, sensors, and lasers. However, the high–temperature, in–vacuum "hot–injection" synthesis widely employed to produce colloidal solutions of LHP nanocrystals (NCs) is challenging to scale up. Room temperature (RT) processes, performed without environmental control and in non–hazardous solvents represent a far more attractive proposal. Thus, the suitability of deposition methods for large–scale processing and, particularly, the identification of suitable green solvents for the synthesis are relevant aspects to consider nowadays. The present doctoral thesis is based on a recent alternative route to produce LHP NCs in ambient conditions and in eco–friendly solvents using, as perovskite precursors, lead halide nanoparticles by laser ablation synthesis in solution (LASiS). Thin films made of the LHP NCs obtained with this methodology were deposited by spray coating – the roll-to-roll compatible deposition technique selected and optimized within this thesis. The relevant feature of the nanomaterials produced with this methodology is the presence of a carbon phase linked to the NCs, which was found to significantly decrease the LHP sensitivity towards moisture – one of the main drawbacks of this class of perovskite materials. This allowed to perform prolonged electric field application and extensive electrical characterizations, not possible for standard solution-processed LHPs, to better investigate the reasons behind the current-voltage hysteresis often observed for this material. Several applications of LHP NCs by LASiS were investigated, from single–junction perovskite solar cells to textured monolithic tandem devices, up to light–emitting devices. Out of these studies, the main limitations and future developments of the technique were delineated, proposing LASiS as a valuable alternative top–down route for the eco–sustainable synthesis of lead halide nanomaterials for optoelectronics.

Acknowledgments

The present doctoral dissertation represents the result of three years of research, none of which would have been brought to completion without the essential collaborations, discussions, and relationships I built throughout. I owe much to all those who shared their time and knowledge with me during my studies, for you have all played a key role at some point. A famous quote summarizes my journey:

"Scientific research, although almost constantly guided by reasoning, is still an adventure"

(Louis de Broglie)

A journey that began with the enrolment in the bachelor's degree in materials science at the University of Padua, that made me discover one of the best university cities in Italy where I have lived during the last eight years. The ever-growing passion for science and research drove me to further increase my academic training undertaking the master's degree, till the Ph.D. course in materials science and engineering. A matured sensitivity towards sustainability and energy transition pushed me to undertake a foreign internship in Saudi Arabia, through which I had the possibility to grow enormously both professionally and personally, but above all to confirm and consolidate the motivations that brought me there. My journey is far from over, and a new chapter of my life is about to begin, still to be written and discovered...

First and foremost, I would like to thank my supervisor, Prof. Moreno Meneghetti for his guidance, mentorship, and advice, but also for giving me freedom of initiative and teaching me to take my own responsibilities. Your support and trust have let me explore my passion to work in the laboratories, present my work at conferences, and establish research collaborations. I truly appreciate it and I thank you for giving me these valuable opportunities to grow.

I would also thank my co-supervisor, Prof. Gaudenzio Meneghesso and Prof. Matteo Meneghini for being the first to introduce me to the field of semiconductor-based devices from an engineering point of view.

Many thanks to all my office mates and my colleagues of the Nanostructure and Optics Laboratory research group who have helped me a lot over the years, as Dr. Lucio Litti, Dr. Ilaria Fortunati, and Dr. Andrea Basagni for being always available for scientific discussions and data interpretation, and

Dr. Valentina Piotto, Dr. Giovanni Ponzana, and Dr. Simona Ricci for the moments of leisure and the coffee breaks spent together.

I express my sincere gratitude to Prof. Stefaan De Wolf and all his research group and collaborators for making my internship at King Abdullah University of Science and Technology such a contaminating and impactful experience. I thank Dr. Michele De Bastiani, Dr. Erkan Aydin, and Dr. Anand S. Subbiah for involving and supporting me, as well as for sharing their wide knowledge in the photovoltaic field.

A great thanks to Dr. Simone Meroni and Dr. David Baynon from the SPECIFIC Innovation and Knowledge Centre for all the brainstorming and meetings made together to carry on our "remote" research collaboration due the pandemic.

During the last year and a half of my Ph.D. I supervised two master's students, Dr. Filippo Anoè and Dr. Alex Zilio, to whom I address my best wishes for their working careers and I sincerely thank for continuously giving me new stimuli, new challenges to face and to solve together, and, above all, a solid shoulder you can count on both inside and outside the laboratory.

A heartfelt thanks goes to my family, to whom I dedicate my thesis as a symbol of all their countless efforts, sacrifices and support that they have given to me in these years and without which my journey would have never been possible.

A last, huge, and sincere thank you goes to my girlfriend Giulia, who gave meaning to my grey days, who supported and encouraged me in the moments of discouragement, and who showed me her love even from thousands of miles away. "Without you, my journey and all my achievements wouldn't have tasted the same."




Padua, the city of three "without":

The nameless saint

(Sant'Antonio)

The cafe without doors

(Pedrocchi cafe)

The lawn without grass

(Prato della Valle)

"Here I leave a piece of my heart…"

Table of Contents

Chapter 1

The Breakthrough of Lead Halide Perovskites

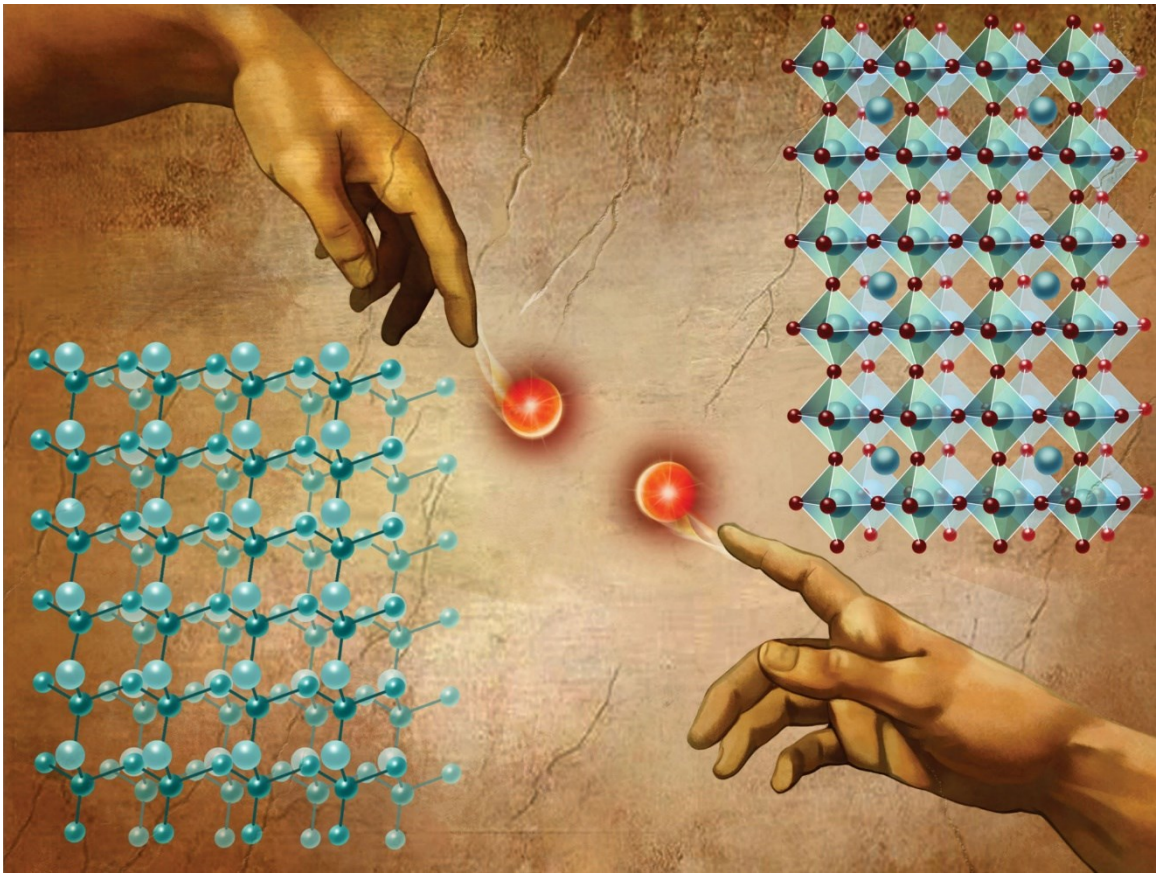

Mater. Horiz., 2020, 7, 2791-2809

1. The Breakthrough of Lead Halide Perovskites

The purpose of this introduction is to provide the reader with a broad overview of the plethora of excellent optical and electronic properties of lead halide perovskites, which have made this class of semiconductor materials so popular and object of study for many types of applications in the last decade. In addition, their low cost, ease of synthesis and processability made lead halide perovskites attractive also outside academia, increasing their commercial appeal, and promoting their implementation into optoelectronic devices.

The intrinsic phase instability, the susceptibility towards environmental factors, the toxicity of some of the precursor materials and the hazardous solvents used for the synthesis and depositions of lead halide perovskite materials still hinder their commercialization. Although some intrinsic issues have still to be solved, many progresses have recently been made to overcome lead halide perovskite weak points, with some companies announcing the imminent market entry of their perovskite-based devices.[1]

1.1 Halide Perovskite Materials

1.1.1. *Crystal Structure*

The term "perovskite" was originally coined for the mineral calcium titanate ($CaTiO_3$), discovered in the Ural Mountains in Russia in 1839 by Gustav Rose and named in honor of Count Lev Perovski.[2] Nowadays, perovskites are not only the most abundant solids on the planet (about 38% of those present of the Earth's crust),[3] but also one of the most chemically diverse families of crystalline materials. Currently, the perovskite library includes about 2000 compounds both natural and synthetic, and more compositions are yet to be discovered.[4] The typical perovskite structure, described by the ABX_3 general chemical formula, consists of a 3D framework of corner-shared BX_6 octahedra and A cations occupying the 12-fold coordination site between 8 such octahedra (Figure 1.1 a).[5] Notably, the structural stability of ABX_3 perovskite can be semi-empirically predicted by the Goldschmidt's tolerance factor (t):[6]

$$t = \frac{r_A + r_X}{\sqrt{2(r_B + r_X)}} \qquad 1.1$$

where r_A and r_B are the ionic radius of the A and B cations respectively, and r_X is the ionic radius of the X anion.

The tolerance factor assesses whether the A site cation can fit within the cavities in the BX_3 framework. t = 1 indicates the case of a perfect fit, corresponding to the ideal cubic perovskite crystal structure. However, perovskites generally do form in the range $0.83 \leq t \leq 1.10$, although their crystal structure may be distorted at the ends of the range due to tilting of the BX_6 octahedra and lowering of the symmetry.

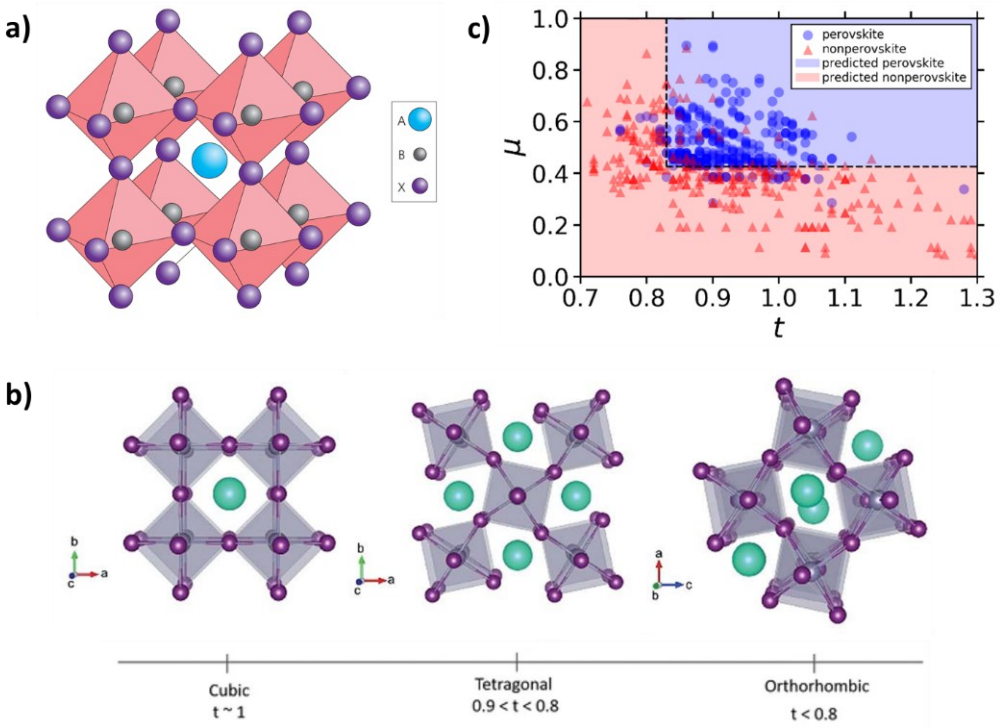

Figure 1.1 a) Archetypal ABX_3 face centered cubic perovskite lattice.[5] b) Schematic depiction of perovskite phases for different tolerance factor values.[6] c) μ–t map showing the stability area of perovskite structures.[8]

t > 1.10 and t < 0.85 indicates that the A site cation is respectively too large or too small; this generally precludes the formation of the perovskite phase, leading to alternative structures (Figure 1.1 b). To assess the fit of the B site cation into the X_6 octahedron, the octahedral factor μ is usually employed, defined as:[7]

$$\mu = \frac{r_B}{r_X} \qquad 1.2$$

For a stable perovskite structure, the condition $0.42 < \mu < 0.90$ must be satisfied. A plot of t against μ can then be constructed and used as a structure map.[8] Such a map assesses the suitability of both the A and B site cations for the perovskite structure (Figure 1.1 c), highlighting the stability region of perovskite crystal structures.

1.1.2 *Chemical Composition*

Perovskite materials can be classified into two main groups according to their X-site anion: oxide perovskites (X = O^{2-}) and halide perovskites (X = Cl^-, Br^-, I^-). Historically, the oxide perovskites (ABO_3) have been the most studied ones due to their diverse physical properties, which have found use in a wide range of technological applications including memory devices, sensors, capacitors, catalysts, electrolytes, refractories, superconductors, etc.[9] However, owing to the large electronegativity difference between oxygen and transition-metal atoms at the B-site, most oxide perovskites exhibit large bandgaps (3–5 eV). On the other hand, the recently discovered remarkable semiconducting properties of halide perovskites (ABX_3), coupled with their inexpensive and facile fabrication, have made them as promising materials for a wide range of optoelectronic applications such as solar cells, light-emitting devices, photocatalysts, photodetectors, field-effect transistors, and lasers.[10–15] In this type of perovskites the A-site cation is either a monovalent organic cation such as methylammonium (MA^+) and formamidinium (FA^+), or an alkali metal cation like Cs^+ and Rb^+. The B-site cation is a divalent transition metal cation, namely Pb^{2+}, Sn^{2+}, and Ge^{2+}, while the X-site anion is a halide ion including Cl^-, Br^- and I^-. Since their composition, halide perovskites are also referred to as hybrid organic-inorganic perovskites (HOIPs), highlighting that their lattice consists of both organic and inorganic A- and B- site cations.

HOIPs	A-Site	B-Site	X-Site	Symmetry	Tolerance factor	Physical properties
Halides	MA and FA	Pb^{2+}, Sn^{2+} and Ge^{2+}	Cl^-, Br^- or I^-	• Orthorhombic • Trigonal • Tetragonal • Cubic	~0.912–1.142	• Semiconductivity • Photovoltaics • Laser physics • Light-emitting diodes • Mechanical properties
	MA	K^+/Bi^{3+} and Tl^+/Bi^{3+} *			~0.906–923‡	
	PIP, $[DABCOH_2]^{2+}$ §	K^+, Cs^+ and Rb^+	Cl^-	• Monoclinic • Orthorhombic • Trigonal	~0.922–1.037	
Formates	Cs^+, K^+, NH_4^+, MA, FA, GUA, EA, DMA, AZE, HIM and HAZ	Mg^{2+}, Mn^{2+}, Fe^{2+}, Co^{2+}, Ni^{2+}, Cu^{2+}, Zn^{2+} and Cd^{2+}	$HCOO^-$	• Monoclinic • Orthorhombic • Trigonal • Tetragonal	~0.784–1.001‖	• Magnetism • Dielectricity • Ferroelectricity • Ferroelasticity • Multiferroicity • Mechanical properties
	TrMA, DMA and EA	Na^+/Cr^{3+}, Na^+/Al^{3+}, Na^+/Fe^{3+} and K^+/Sc^{3+} *	$HCOO^-$	• Triclinic • Trigonal	~0.897–1.040‡	
Azides	MA, DMA, TrMA and TMA	Mn^{2+}, Cd^{2+} and Ca^{2+}	N_3^-	• Triclinic • Monoclinic • Cubic	~0.786–1.023	• Magnetism • Dielectricity • Ferroelasticity
	TMA	Na^+/Cr^{3+}, Na^+/Fe^{3+}, K^+/Fe^{3+} and K^+/Cr^{3+} *			~0.934–1.008‡	
Dicyanamides	BTBA, BTEA, SPh_3^+ and TPrA	Mn^{2+}, Fe^{2+}, Co^{2+} and Ni^{2+}	$[N(CN)_2]^-$	• Orthorhombic • Tetragonal	~1.142–1.166¶	• Magnetism • Dielectricity
Dicyanometallates	PPN	Cd^{2+}	$[Ag(CN)_2]^-$	• Monoclinic • Trigonal • Cubic	~0.998–1.141	Magnetism
		Mn^{2+}, Co^{2+}, Ni^{2+} and Cd^{2+}	$[Au(CN)_2]^-$			
Cyanides	HIM, DMA, MA, TMA, TrMA and GUA	K^+/Fe^{3+} and K^+/Co^{3+} *	CN^-	• Triclinic • Monoclinic • Cubic	~0.840–1.031‡	Dielectricity
Borohydrides	MA	Ca^{2+}	BH_4^- #	• Cubic	~0.980	Hydrogen storage

Figure 1.2 Summary table of the chemical compositions, crystal symmetries and physical properties of hybrid organic-inorganic perovskite materials.[2]

By extending the X-site from a halide to other anions or molecules, such as chalcogenides (S^{2-}, Se^{2-}), nitrides (N^{3-}), azides (N_3^-), formates ($HCOO^-$), cyanides (CN^-), and thiocyanates (SCN^-), other families of HOIPs have been discovered in the last years but their physical properties are still under study (Figure 1.2).[2] A list of abbreviations is reported in an appendix (pp. 242) at the end of the dissertation.

The introduction of additional organic components into the X-site gives another variety of HOIPs derivative, namely metal–organic framework (MOF) perovskites. By introducing ions with different valence and dimension into halide perovskite lattice, many types of crystal structures can be obtained. Similarly to conventional perovskites, HOIPs can be categorized from a structural perspective as: ABX_3 3D perovskites, A_2BX_4 2D perovskite, $A'_mA_{n-1}B_nX_{3n+1}$ quasi-2D (also called Ruddlesden–Popper) perovskite, $A_2BB'X_6$ double perovskites, and A_3BX anti-perovskite subclasses.[16] Many examples of 2D and double hybrid perovskites have been created, while hybrid anti-perovskites are still rare. The abundant variations of organic components and metal salts offer enormous chemical possibilities for creating HOIPs, reason why this class of materials now spans a considerable part of the periodic table. Such a wide compositional variability lead to a plethora of functional properties (magnetic, dielectric, electrical, optical, and charge storage) to study.[17] For the purposes of this discussion, the attention will be now focused on 3D lead halide perovskites ($APbX_3$).

1.1.3 *Optoelectronic Properties*

Lead halide perovskites (LHPs) are semiconductor materials with outstanding optoelectronic properties that can efficiently convert both light-into-electricity and electricity-into-light.[18,19] With respect to the traditional inorganic semiconductors, such as silicon (Si) and gallium arsenide (GaAs), LHPs demonstrate comparable long charge-carrier diffusion lengths (1–100 μm) and low exciton binding energies (5–50 meV) but moderate, yet balanced, electron-hole mobility (10–100 $cm^2 V^{-1} s^{-1}$). The study of the band structure of halide perovskites reveals their direct energy bandgap (E_{GAP}) with strong light absorption (absorption coefficients up to 105 cm^{-1}) and radiative recombination with quantum efficiencies up to near-unity (Figure 1.3 a-b).[20,21] The p–p transitions at band-edge in halide perovskites have higher density of states than the p–s transition in GaAs.[22] Hence, LHPs can absorb the incident light with significantly smaller thickness of an absorber layer than GaAs (0.5 vs 2 μm, respectively).[23] Furthermore, the bandgaps of lead halide perovskites can be tuned over a broad range of visible light spectrum via a compositional engineering approach.[24]

While the A- and B-site cations play significant roles in the stability of the perovskites, their optical and charge carrier properties are controlled by halide ions and perovskite crystal size. For instance, the most intensively investigated methylammonium lead trihalide perovskites ($MAPbX_3$) show absorption edges at around 1.6, 2.0, and 2.8 eV for X = I^-, Br^-, and Cl^- respectively.[19] Intermediate bandgap values can be achieved in the $MAPbBr_xI_{3-x}$ and $MAPbCl_xBr_{3-x}$ mixed-halide phases. The photoluminescence (PL) emission properties exhibit the same trend with respect to composition, ranging from 790 nm in pure iodide $MAPbI_3$ to 390 nm in pure chloride $MAPbCl_3$ phases. This range can be further extended through cation substitution or blending.[25] On the A-site cation, MA^+ mixed with FA^+ and Cs^+ extends the emission wavelength to about 820 nm and has led to the most recent photovoltaic performance breakthroughs.[10,26] By mixing Pb and Sn at the B-site, the halide perovskite emission spectra can be shifted towards the infrared region, down to more than 1000nm.[27] Cs-based full-inorganic perovskites ($CsPbX_3$) are another type of halide perovskites widely investigated for their higher thermal- and in ambient conditions- stability than HOIPs due to the absence of volatile and more reactive organic cations.[28] Colloidal $CsPbX_3$ perovskite quantum dots (QDs), intensively studied for light-emitting diodes (LEDs) application, offer a spectral range spanning 410–700 nm through both halide composition and quantum tuning (Figure 1.3 c). Their narrow PL spectra, coupled with their continuous spectral tunability, enable a pure color distribution covering a wide range on the CIE chromaticity diagram.[29]

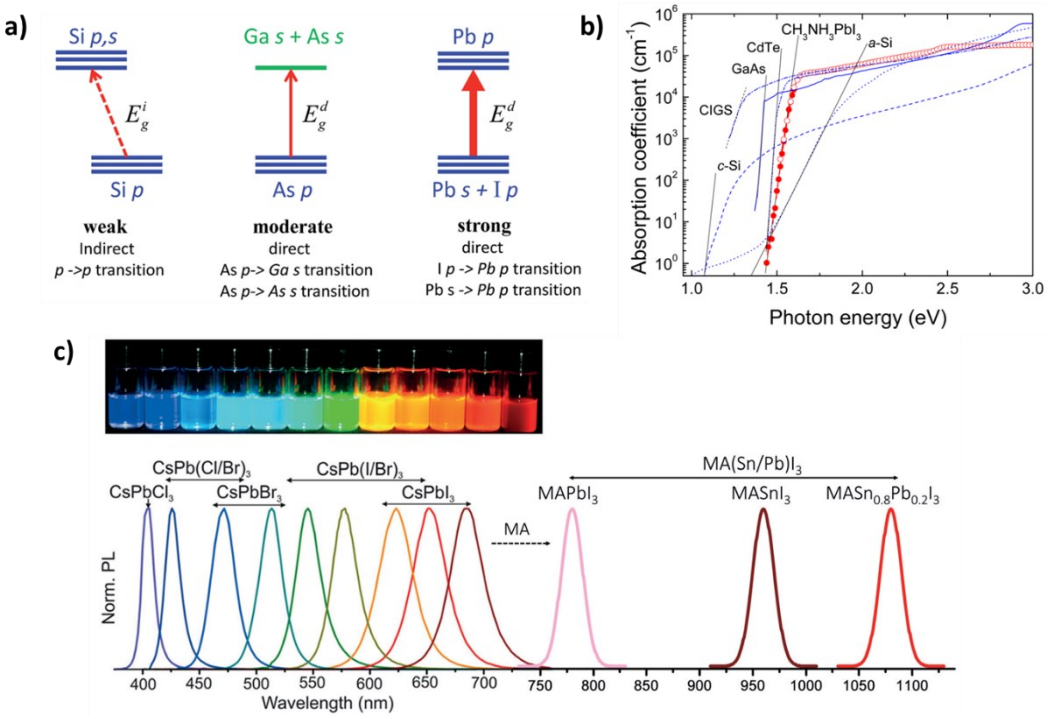

Figure 1.3 a) Schematic optical absorption of Si, GaAs, and lead halide perovskite materials.[23] b) Absorption coefficient of a $MAPbI_3$ perovskite thin film compared with other typical photovoltaic materials.[21] c) Size- and composition-tunable bandgap energies of colloidal $CsPbX_3$ perovskite nanocrystals.[29]

1.1.4 *Defect Tolerance*

One of the key features of lead halide perovskites that make them stand-out from other semiconductors is their superior defect tolerance, which derives from their unique band structure and their ionic lattice.[19] The concentration of different defect types is determined by the enthalpy of their formation and the growth temperature.[30] Despite the overwhelming advantages of LHPs, their "soft" crystal structure and the subsequent low defect formation energies are expected to introduce relatively large concentrations of defects which are detrimental to the performance of optoelectronic devices. However, the defect energy levels in LHPs favor the formation of relatively shallow and even benign states, making LHPs tolerant to imperfections (Figure 1.4 a).[31] In fact, not all defects introduce carrier trapping in a semiconductor; only the ones residing below or above the conduction band and valence band edges (i.e., within the energy gap), respectively. On the contrary, if a defect energy level resides outside the energy gap of the material, the defect state (called shallow trap) is typically considered harmless. This because shallow traps typically only restrict the efficient movement of free charges in a semiconductor through trapping and de-trapping processes, while the deep traps hinder de-trapping and promote the non-radiative recombination pathways (Figure 1.4 b). If traditional inorganic semiconductors (e.g., Si, Ge, III–V materials) normally require high-temperature and high-vacuum processing using ultra-pure precursors to minimize the defects concentration in their crystal lattice, lead halide perovskites benefit from inexpensive wet-chemistry techniques thanks to their good defect tolerance. This, together with the relatively low concentration of active charge recombination sites,[32,33] render very easy their processability allowing LHPs to be solution-processed at relatively low temperatures without affecting their remarkable optoelectronic properties.

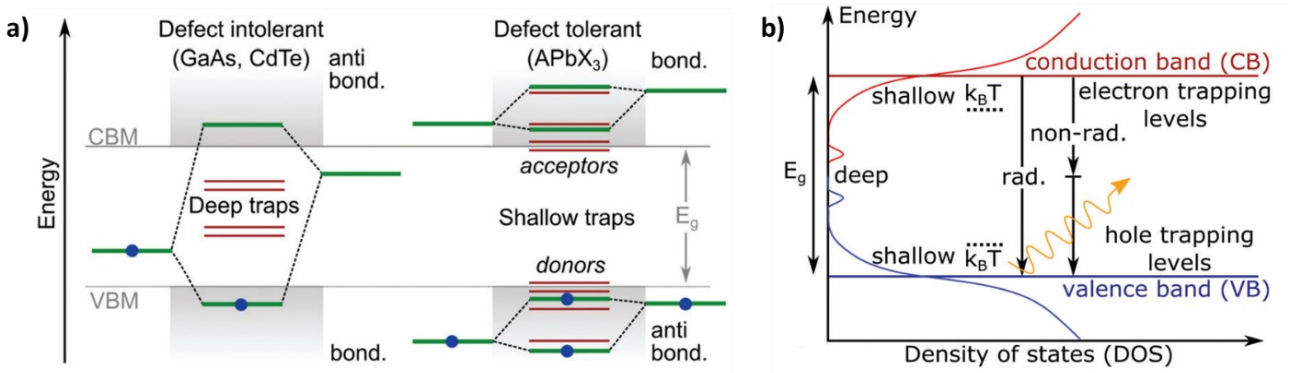

Figure 1.4 a) Comparison of typical trap energies relative to the electronic band structure of traditional defect intolerant semiconductors (i.e., III–V and II–VI varieties) and defect tolerant lead halide perovskite materials. b) Schematic representation of state density in a disordered semiconductor, whereby both radiative (rad.) non-radiative (non-rad.) recombination can occur.[31]

Moreover, LHPs can be synthesized from solution in a broad variety of forms, from nanocrystals to polycrystalline thin films and bulk single crystals, with relative ease thanks to their low formation energies.[34] Importantly, each form of material has its own advantages to be exploited for certain purposes and will be discussed in the next paragraphs.

1.1.5 *Low-Dimensional Lead Halide Perovskites*

Motivated by previously reported nanostructured semiconductor materials, many researchers have recently focused on the synthesis of low-dimensional lead halide perovskite nanostructures and the investigation of their properties and potential applications. Various low-dimensional LHPs including 0D nanostructures such as QDs and nanocrystals (NCs), 1D nanostructures such as nanowires and nanorods, and 2D nanostructures such as nanoplatelets and layered structures have been reported with various synthetic methods and applications (Figure 1.5 a).[35,36] Since low-dimensional LHPs are synthesized in a single-crystalline state, they have higher crystallinity than conventional poly-crystalline halide perovskite thin films by solution processes. Higher crystallinity of lead halide perovskites means fewer ionic defects and grain boundaries. The former allows to reduce hysteresis effects, due to mobile ion species, and to decrease the probability of non-radiative recombination processes.[37,38] The latter provides higher carriers mobility and better perovskite phase stability towards moisture.[39,40] Therefore, the devices in which low-dimensional LHPs are implemented show superior reliability and stability because they do not present the drawbacks affecting poly-crystalline lead halide perovskite thin films. Depending on dimensionality and size, low-dimensional LHPs show significantly different optical properties due to the quantum size effects, which heavily affect the density of states of electronic structure and their applications (Figure 1.5 b).[41,42]

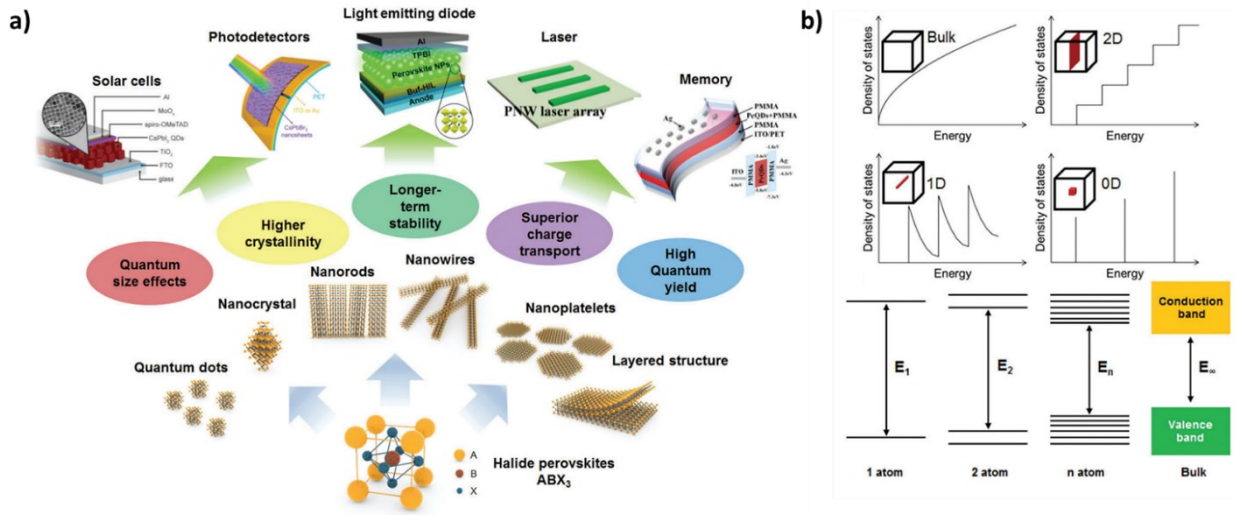

Figure 1.5 a) Schematic of various low-dimensional halide perovskites with related applications. b) Quantum size effects on electronic properties in nanostructured semiconductors.[47]

For instance, the absorption properties of LHPs are directly related to parameters of bond angles, bond lengths and crystal system of the unit cells. Moreover, at the nanoscale the emission wavelength and the charge carrier lifetimes depend on the size of the nanomaterials. Consequently, it is important to correlate the structural factors and the properties of lead halide perovskite for not only interpreting but also for exploring novel optoelectronic properties of lead halide perovskites, further extending the application of these innovative functional materials.[12] For sake of time, in the next paragraphs the discussion will be mainly focused on lead halide perovskite thin films and nanocrystals, how they are synthesized and their application in solar cells and LEDs.

1.2 Synthesis and Processing

Different methods for the synthesis of lead halide perovskites in the form of thin films and nanocrystals with different compositions have been developed. This section aims to summarize them, and to give an overview of the most up-to-date solution processes employed to deposit LHPs as thin films to be implement into optoelectronic devices. The ion exchange post-synthetic treatment will be also introduced as an key tool to tune the chemical composition of LHP nanocrystals, without affecting their size and shape.[43,44]

1.2.1 *Synthesis of Perovskite Nanocrystals*

The facile methods for the synthesis of lead halide perovskite NCs with different dimensions and shapes have aroused huge research interest in recent years. Among all the possible bottom-up and top-down approaches to synthesize LHP nanocrystals,[45] this paragraph will introduce some of the most diffused wet chemistry processes including hot injection, ligand-assisted reprecipitation, ultrasonic-assisted method, and spray synthesis.[46–48]

Hot-Injection

Colloidal synthesis of lead halide perovskite nanocrystals by hot injection method was firstly reported by Protesescu et al.[49] This method takes advantage of the ionic nature of chemical bonding in $CsPbX_3$ compounds and it is the most employed synthetic route to produce LHP nanocrystals. Their crystallization is achieved by reacting lead halides (PbX_2) and Cs-oleate in a high-boiling-point organic solvent such as octadecene at 140 – 200 °C. Long-chain organic ligands such as oleic acid and oleyl amine are employed to confine the crystal size of the resulting nanocrystals (Figure 1.6 a). Most of the crystal growth occurred within the first few seconds after the injection of Cs-oleate into PbX_2 in octadecene owing to the fast nucleation and growth kinetics. The crystal size of the $CsPbX_3$

NCs fabricated by this process depends on the reaction temperature rather than the reaction time. Thus, by tuning the temperature and the ligands introduced in the solution, the size and shape of the LHP nanocrystals can be precisely controlled, respectively.[50] Lead halide perovskite NCs by hot injection exhibit strong and narrow PL emissions, with near-unit quantum yield.[51] However, this method is not suitable for the synthesis of hybrid organic-inorganic perovskite (HOIP) nanocrystals owing to the low stability of organic cations (MAX) at high temperature.

Ligand-Assisted Reprecipitation

The synthesis of HOIP nanocrystals was performed for the first time by Schmidt et al.[52] In this work, $MAPbBr_3$ nanocrystals were obtained at room temperature by employing octyl ammonium bromide and octadecyl ammonium bromide as organic capping ligands. As a result, these halide perovskite nanocrystals showed bright PL emissions with a quantum efficiency (i.e., the ratio between emitted photons and absorbed photons) of 20%. The ligand-assisted reprecipitation method for the fabrication of LHP nanocrystals was further developed by Zhang and co-workers.[53] In their work, lead halide perovskite NCs were simply obtained by vigorously stirring a LHP precursors solution including PbX_2, MAX, N,N-dimethylformamide (DMF), and long-chain organic ligands such as n-octylamine and oleic acid in a poor solvent such as toluene or hexane (Figure 1.6 b). The quantum efficiency of the perovskite nanocrystal prepared by ligand-assisted reprecipitation was reported to be up to 70%. Later, Deng et al. adopted this strategy for the synthesis of all-inorganic $CsPbX_3$ halide perovskite NCs, achieving quantum efficiency values up to >80%.[54] It should be noted that, as for NCs by hot injection method, the LHP nanocrystals morphology can be tuned from nanodots to nanosheets and nanowires by changing the type and concentration of organic ligands.[35,47]

Ultrasonic-Assisted Method

The ultrasonic-assisted methods show potential for large-scale production due to the polar solvent-free fabrication. Song et al. first reported ultrasound-based synthesis of colloidal $APbX_3$ perovskite NCs at room temperature (where A = Cs^+, MA^+, or FA^+; X = I^-, Br^-, or Cl^-).[55] The perovskite precursors solution was prepared by adding halide salts and oleyl amine to toluene; then the reaction vessel was placed in a high-density probe-type ultra-sonicator to produce LHP nanocrystals (Figure 1.6 c).[56] Bals, Urban, Polavarapu and colleagues developed a polar-solvent free synthesis method for $CsPbX_3$ perovskite NCs with high quality, which was based on direct tip sonication of the combination of capping ligands and precursor salts in a non-polar solvent under ambient conditions.[57] Later, Rogach et al. used a top-down approach to synthesize monodisperse $MAPbX_3$ NCs (with X = I^-, or Br^-) with

quantum efficiency up to 70 % and remarkably improved stability. In their work, organic and inorganic perovskite precursors are mixed under ultrasonication with oleic acid and oleyl amine to quickly form bulk $MAPbX_3$. The latter is then broken into perovskite NCs under continuous ultrasonication with the assistance of ligands, acting as coordinating solvents.[58]

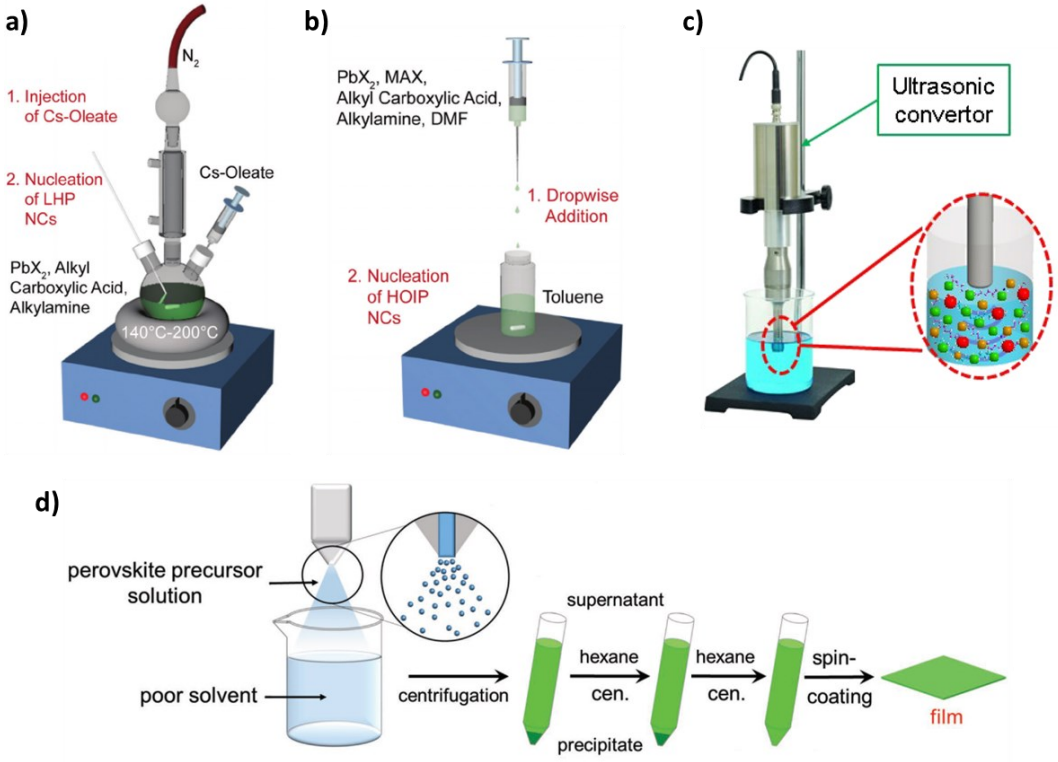

Figure 1.6 Lead Halide Perovskite nanocrystals synthetic methods. Schematic representation of the a) hot injection, b) ligand-assisted reprecipitation,[48] c) ultrasonic-assisted,[56] and d) spray synthesis techniques.[60]

Spray Synthesis

Ogale et al. used an electro-spray method to synthesize $MAPbX_3$ NCs, where a bath of the antisolvent (with or without a capping agent) in a metal-electrode container was used as the substrate.[59] Their method was similar to ligand-assisted reprecipitation but applying a high electric field to the droplets of precursor solution, which broke them into a jet of nanodroplets. These fell into toluene, resulting in rapid perovskite crystallization leading to $MAPbX_3$ NCs. The capping agent, in this case oleyl amine, contributed to the formation of 2D sheet-like layered perovskites by intercalation via host-guest chemistry. Later, Lin in et al. developed a novel spray-synthesis method by combining the traditional synthesis of LHP nanocrystals with the spray pyrolysis principles (Figure 1.6 d).[60] A perovskite precursors solution in DMF, together with oleic acid and oleyl amine organic ligands, was sprayed in toluene and then purified by centrifugation and redispersion in hexane. Importantly, the so-obtained colloidal $MAPbBr_3$ NCs solution showed quantum efficiency close to

100% even in the solid-state neat film. A quantum efficiency of 28 % was obtained once $MAPbBr_3$ NCs film was implemented in an LED device. This approach was recently extended also to other $MAPbX_3$ nanocrystals compositions by ligand-optimized ion-exchange method.[61]

1.2.2 *Ion Exchange Post-Synthetic Treatment*

The ionic and "soft" nature of LHPs lattice, which endows its relatively low formation energy, is beneficial for the post-synthetic management of their chemical compositions.[62] Post-synthetic ion exchanges preserve the overall NCs size and shape, allowing for compositionally tunable materials.[43] Generally, the ion exchange is controlled by two mechanisms: diffusion (outward or inward the crystal lattice) and ion exchange reaction. In this process, the ions present in the environment (solid, liquid or gas phase) diffuse and exchange with the counterpart of parent crystalline compound to form into a novel crystal lattice with completely or partly exchanged ionic components.[63] The common vertex connection of $[BX_6]^{4-}$ octahedron in LHP lattice has larger lattice gap than that of common edges and common planes. Such structural characteristics not only enable perovskite materials to maintain structural stability with a great quantity of lattice defects, but also facilitate the diffusion and migration of ions in perovskite lattice making ion exchange post-synthetic method an effective way to tune LHP nanocrystals composition (Figure 1.7 a).[63] This is why, for instance, the full compositional tuning in lead halide perovskite NCs is more versatile than ion exchange in conventional metal chalcogenide ones, where cation exchange is easier to control than anion exchange.[64] In LHP nanocrystals, the A-site, B-site cations and X anion can be partially or fully exchanged with other similar but foreign ions: Cs^+ with Rb^+, FA^+ or MA^+; Pb^{2+} with Sn^{2+},Cd^{2+}, and Zn^{2+}; Br^- with Cl^-, Br^- with I^-, and vice versa (Figure 1.7 b).[44]

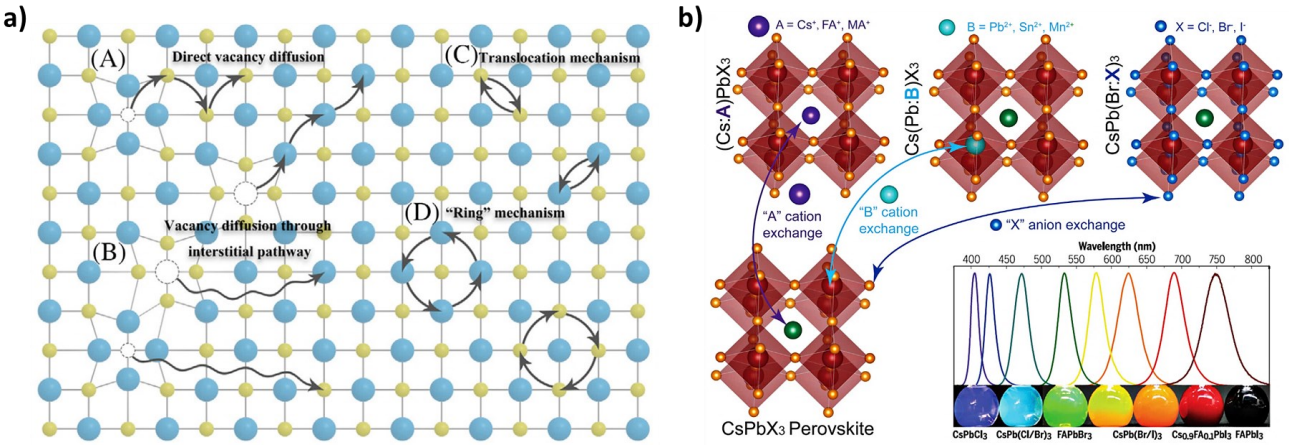

Figure 1.7 a) Schematic diagram of vacancy diffusion in LHP crystal lattice.[63] b) Schematic showing ions exchange of LHP NCs, enabling a bandgap tuning over the whole visible spectrum (as shown in the inset).[44]

Additionally, cation- or anion exchange in LHP nanocrystals can be tuned arbitrarily over the full compositional range, even if some parts of this compositional space may be more difficult to achieve in thin-film counterparts. By manipulating A- or B-site cations via post-synthetic transformations, new halide perovskite NCs which cannot be directly synthesized may be obtained, and their ambient stability can potentially be improved.[65] Moreover, complex compositions in a wider range with simultaneous A- and X-site alloying can be realized in a single post-synthetic step.[66] The simplest post-synthetic alloying of LHP nanocrystals can be achieved either by mixing two different compositions of nanocrystals synthesized individually (e.g., combining $CsPbCl_3$ with $CsPbBr_3$ NCs), or by exposing nanocrystals to salts containing A, B, or X ions (for example by exposing $CsPbCl_3$ to oleyl ammonium bromide).[67,68] Other examples of post-synthetic transformations include photo-induced anion exchange of $CsPbX_3$ nanocrystals in dihalomethane solution.[69]

In comparison with singly charged highly mobile halide ions, the rigid cationic sublattice increases the difficulty of such cation-exchange transformations either in solution or solid state. This is why the post-synthetic A-site alloying has been developed only in the last years.[70] Regarding the B-site cations, there are still no successful reports of full-range B-site exchange in LHP NCs (particularly interesting for the synthesis of Pb-free halide perovskite materials),[71] and it has been suggested that such an exchange is facilitated by X-site vacancy migration.[72]

1.2.3 *Perovskite Thin Films Deposition*

The most decisive factor in determining the performance of perovskite-based devices is the quality of LHPs film. Its properties like morphology, uniformity, crystallinity and phase purity depend upon the processing techniques which have a direct impact on the performance of the devices in which perovskite films are implemented.[73,74]

Single-step deposition

Single-step deposition is the most widely used technique because of the simplicity and low-cost requirement (Figure 1.8 a). In this technique, the precursor solution is generally deposited by spin coating onto a substrate. Here, the organic and inorganic salts are mixed in an aprotic polar solvent with high boiling point and low vapor pressure like DMF, dimethyl sulfoxide (DMSO), γ-Butyrolactone, and N-methyl-2-pyrrolidone, resulting in a precursor solution. Due to strong ionic interaction among halogen anions and metal cations, a uniform and crystalline lead halide perovskite layer can be obtained. The formation of such a good-quality layer is due to the convective

self-assembly and the evaporation of solvent occurred during the spinning.[75] After the precursor solution is spin-coated over the substrate, a thermal annealing is generally performed at 80-150 °C depending on the precursor solution composition. However, simply spin coating never yields uniform and homogeneous layer over large areas. Despite this deposition method requires a very low number of processing steps, making the procedure cheap and easy to execute, it usually forms a non-uniform layer with pinholes due to slow crystallization.

The antisolvents assisted crystallization method was then developed to solve this issue, costituting an efficient yet simple method to prepare high-quality LHP film by manipulating the nucleation and crystal growth process.[76] This method is nowadays the most widely used method to synthesize LHP thin films on the lab scale. The process is analogous to 1-step deposition method, with the additional step of an antisolvent (i.e., a liquid in which the solute is insoluble, such as chlorobenzene or toluene) dripping onto a wet perovskite film to trigger sudden homogeneous nucleation. The perovskite solution around the nucleated crystal seeds is in a dynamic state and continuously transports perovskite solutes for the formation of bigger grains as the solvent evaporates.[77]

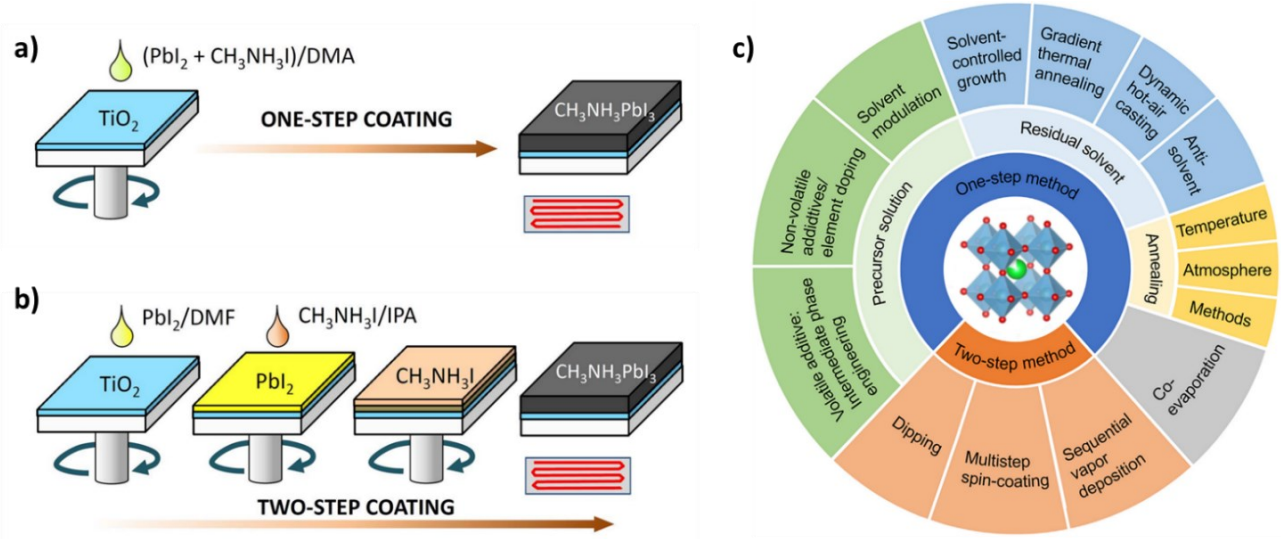

Figure 1.8 Example of a) one-step and b) two-step spin-coating procedures for $MAPbI_3$ perovskite thin film formation.[78] c) Summary of most up-to-date preparation techniques for lead halide perovskite thin films.[80]

2-Step Deposition

The uncontrollable growth of LHP films along with the variable morphology for grown crystals was be also overcome by using a 2-step deposition approach (Figure 1.8 b).[78] In this technique, a first solution of inorganic perovskite precursors (PbX_2) is spin coated on a substrate. Secondly, the inorganic layer is converted to lead halide perovskite thin film upon reaction with a solution

containing the organic precursors (AX). As for the 1-step method, the resulting film is then annealed to complete perovskite crystallization. Although this method produces perovskite films with a better coverage of the substrate as compared to the one-step deposition method, it does have some shortcomings. The main drawback arises from the correlation between surface roughness and grain size. As the grain size increases in LHP thin films by two-step deposition method, the surface roughness also increases. Once implemented in a working device, a rough perovskite film with larger grain size leads to high leakage current and high surface recombination losses, whereas a smooth film with small grain suffers small carrier lifetime and short diffusion length. Therefore, an appropriate composition must be fixed. Moreover, in the case of a non-complete conversion of inorganic perovskite precursors, the residual PbX_2 reduces the light absorption and hinders carrier transport which further degrades the performance of perovskite-based solar cells. To tackle these issues, the solvent engineering technique was applied to LHP precursors solution and a wide range of different deposition techniques than spin coating was investigated (Figure 1.8 c).[79,80]

1.2.4 *Scalable Coating Methods for Large-Area Perovskite Films*

Solution-processed lead halide perovskite materials have shown remarkable achievements for application in optoelectronic devices. One of the important contributions to the great advance involves the establishment of fundamental solution chemistry.[81] The “solvent engineering technique”, including precursor–solvent interaction in solution and dropping anti-solvent onto lead halide perovskite films have been proved as significant keys to control the nucleation and crystal growth of the perovskites. This allows to achieve uniform, crystalline and pinhole-free surface morphology over larger areas, heavily influencing the performance the perovskite-based devices.[79] Also, a combination of environmental conditions, rheology, and drying microfluidics processes can all influence the final material-phase quality and morphology and must be considered and optimized depending on which the solution process involved.[82] The scalability of a deposition processes is important too. The most used solution processes for LHPs thin films deposition compatible with roll-to-roll setups are briefly reported below.[83,84]

Blade-Coating

In the blade-coating deposition method, a blade is used to spread perovskite precursor solution (also called “ink”) on substrates to form wet thin films (Figure 1.9 a). The film thickness is controlled by several factors, including the concentration of the precursor ink, the gap between the blade and substrate, and the speed at which the blade moves across the substrate. This technique can be

adapted for continuous fabrication with roll-to-roll setups, in which the blade is stationary and flexible substrates on a roller are in motion.[85] The ink waste is substantially reduced compared with spin coating, especially in continuous roll-to-roll deposition.

Slot-Die Coating

Slot-die coating is similar to blade coating but uses an ink reservoir with a thin slit to apply perovskite precursors solution over the substrate (Figure 1.9 b). The ink flow can be better controlled in slot-die coating, but this method normally requires larger quantities of ink to fill the ink reservoir and supply pipe and thus is generally less suitable for use in the development of new ink chemistries. However, slot-die coating shows better yield and reproducibility than blade coating when the ink is already fully developed. Thus, it has more potential to be applied in roll-to-roll fabrication in the near future.[86]

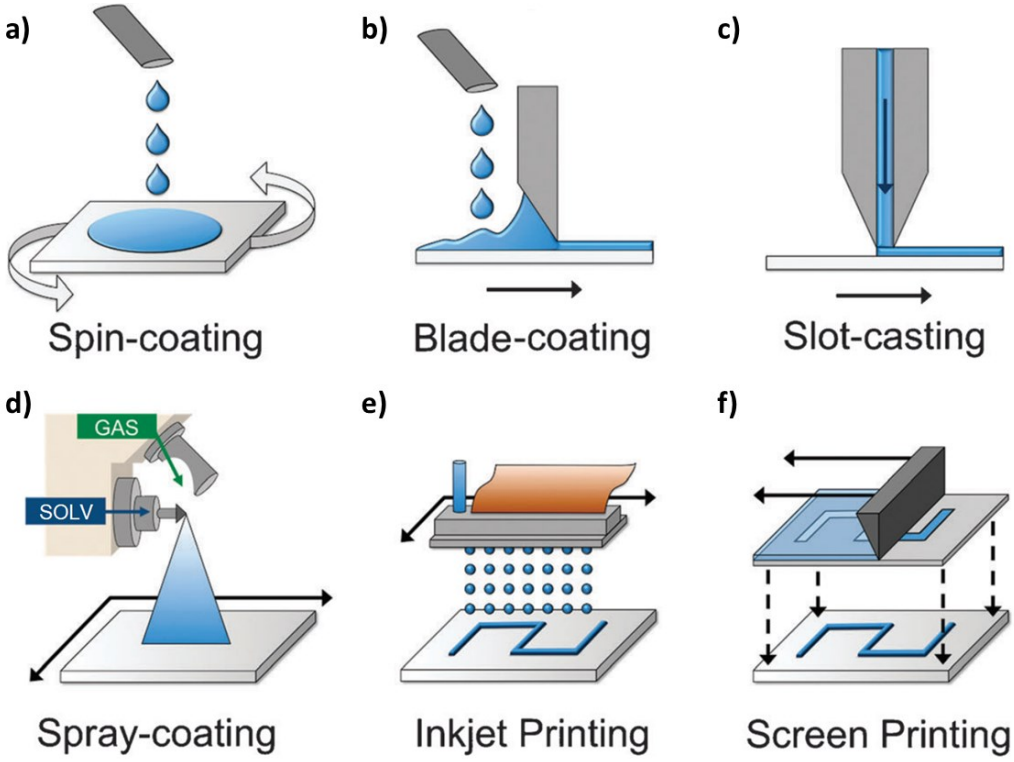

Figure 1.9 Other than traditional spin-coating (a) technique, scalable solution deposition methods for the roll-to-roll fabrication of perovskite-base devices are available, including b) blade coating, c) slot-die coating d), spray coating, e) inkjet printing and f) screen printing.[81]

Spray Coating

In spray coating technique, a nozzle is used to disperse tiny liquid droplets onto substrates (Figure 1.9 c). Spray coating can be further classified according to the method used for generating droplets, such as pneumatic spraying (through fast gas flow), ultrasonic spraying (through ultrasonic

vibration) or electro-spraying (through electrical repulsion). Pneumatic spraying and ultrasonic spraying are commonly used for compact oxide layer deposition in perovskite solar cells. The LHP layer can also be deposited by ultrasonic spraying.[87,88] Droplet size and placement are random in the spraying process, and several droplets need to overlap in a local area to ensure full coverage of the substrate. Furthermore, new droplets can dissolve the already deposited materials, adding to the processing complexity. Keeping the substrate at an elevated temperature during spraying increases the rate of solvent evaporation and suppresses the redissolution of deposited material. The balance between solvent removal and material redissolution can be controlled by carefully tuning the solvent ratio and substrate temperature.

Inkjet Printing

In inkjet printing, nozzles are used to disperse the perovskite precursors ink with a fine control of the droplet size and trajectory (Figure 1.9 d). Miniaturized nozzles and a short distance between the nozzles and substrate enable a very high lateral resolution, as already widely demonstrated in digital printers. This patterning ability is suitable for printing electronics, with several attempts in perovskite solar cells by inkjet printing have already been made.[89] However, whether inkjet printing is suitable for the high-volume, large-area production of perovskite solar modules will mainly depend on the printing speed and the device structure.

Screen Printing

In screen printing, a patterned mesh screen is used to hold and transfer ink to the substrate (Figure 1.9 e). This method has good patterning ability with a lateral resolution, but lower than inkjet printing one. The unwanted area of the mesh screen is blocked by the exposed photo-sensitive polymer emulsion, and the open holes of the mesh hold the viscous ink as a squeegee spreads ink across the screen. The ink is then transferred to the substrate to form the desired pattern. The thickness of the resulting film is determined by the mesh size and thickness of the emulsion layer. Screen printing is usually used to deposit film 1–10 μm thick, and it has been used to fabricate mesoporous scaffolds and carbon back electrodes in perovskite solar cells.[90]

1.3 Perovskite-Based Optoelectronics

Halide perovskites have emerged as a class of most promising and cost-effective semiconductor materials for next generation photoluminescent, electroluminescent and photovoltaic devices. Their exceptional optoelectronic properties (Section 1.1.3) make these materials superior to the

classical semiconductors such as silicon. Most importantly, the simple synthesis of halide perovskites in the form of high-quality thin films, single crystals, nanocrystals, and other low-dimensional materials has attracted both researchers all over the world to develop novel functional perovskite materials with unique properties to exploit for countless purposes.[91] Other than their extensively use in photovoltaics,[92] nowadays halide perovskites are studied for many optoelectronic and electronic applications, including LEDs,[93] photocatalysts,[94] photodetectors,[95] field-effect transistors,[96] lasers,[97] memories,[98] batteries,[99] and sensors.[100] For discussion purposes, next paragraphs will be focused only on perovskite- solar cells and LEDs devices.

1.3.1 *Solar Cells*

Working Principles

In a photovoltaic (PV) process the first step is light absorption by a semiconductor material, which produces a splitting of the electrons (e^-) and holes (h^+) at quasi-Fermi levels. The difference between these two levels is the maximum free energy available, which can be used to produce work only after the second photovoltaic step, the charge separation.[101] It is required to contact each quasi-Fermi level independently by charge-selective contacts, namely electron- and hole- transporting material (ETM and HTM, respectively). Consequently, the photovoltage limit depends on the selective contacts and how its selectivity is obtained.[102] Typically, in a solar cell an intrinsic light-absorbing semiconductor is contacted by a couple of doped layers: p and n, respectively (Figure 1.10 a). In dark conditions with no applied bias the Fermi level equilibrates along the complete device. As the p-doped (i.e., HTM) and n-doped (i.e., ETM) layers present higher and lower work functions (W_F), respectively, the equilibration produces a built-in potential.[103] Due to the intrinsic nature of the light-absorbing layer sandwiched between HTM and ETM, their bands are inclined along its complete thickness with an electrical field acting in the intrinsic region. Consequently, the contact selectivity is basically produced by the electrical field that pushes electrons and holes to n-doped and p-doped contacts, respectively.[101] Here, the drift current plays a determinant role in charge separation and collection. The inclination of the band is affected by the applied bias and the light photocarrier generation. Under illumination at open circuit, the Fermi levels splitting produces flat band conditions where the electrical field is removed and consequently the collection driving force cancelled, annulling the photocurrent (Figure 1.10 b). In this case, the open-circuit voltage (V_{OC}) is limited by the W_F of the contacts.[103] This model has been used to explain the V_{OC} in amorphous Si solar cells and originally in organic solar cells.[101]

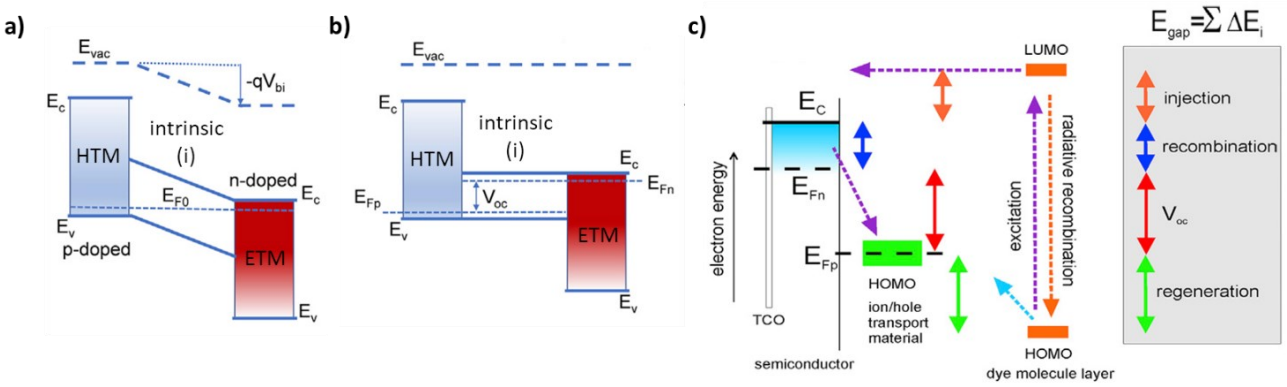

Figure 1.10 Energy band diagram at open circuit conditions for a p-i-n solar cell under a) dark condition and c) illumination. c) Energy diagram of organic- and perovskite solar cells.[101]

Nevertheless, the presence of an electric field is not the only way to obtain contact selectivity. It can also be attained by a preferential kinetic exchange at one selective contact of carriers of one kind while the other kind is blocked. For instance, in dye-sensitized solar cells (DSSCs) the light is absorbed by a dye molecule layer and e^- are selectively injected into the conduction band of a semiconductor while h^+ are blocked due to the band alignment (Figure 1.10 c). In the same way, the h^+ are injected into an HTM. In this case, the V_{OC} is limited by the difference of quasi-Fermi levels at the electron- and hole-selective contacts. Here, the difference in W_F is absorbed in thin interfacial layers, such as the transparent conduction oxide interface in the case of DSSCs.

Si solar cells have a similar selectivity mechanism where the band bending produced by the p-n junction is limited to a very narrow interfacial layer, significantly thin in comparison with the whole absorber thickness.[102] In the early days of DSSCs there was an intense debate about the photovoltage-determining mechanism in these kinds of cells. Between the two models presented (Figure 1.10 b-c) it was demonstrated that is the one attributing contact selectivity to the kinetic exchange of photogenerated carriers (e^-, h^+) that rules sensitized devices.[104] Regarding the more recent perovskite solar cells, despite they were derived from DSSCs (Figure 1.11)[105] it is not straight-forward to determine the working mechanisms. Up-to-date PSCs employ a planar architecture, in which LHP photoactive layer is sandwiched between charge-transport materials (CTMs, i.e., ETM and HTM).[75] A list of abbreviations is reported in an appendix (pp. 242) at the end of the dissertation. Several published works vary the work function of the contacts in PSCs with a broad dispersion of results.[106] Contacts influence the perovskite light-absorbing layer itself, hampering a fair comparison among PSCs prepared with different techniques and on different contacts.[101] In this sense, it is difficult to decouple the effect of the contact and the effect of the change of morphology.

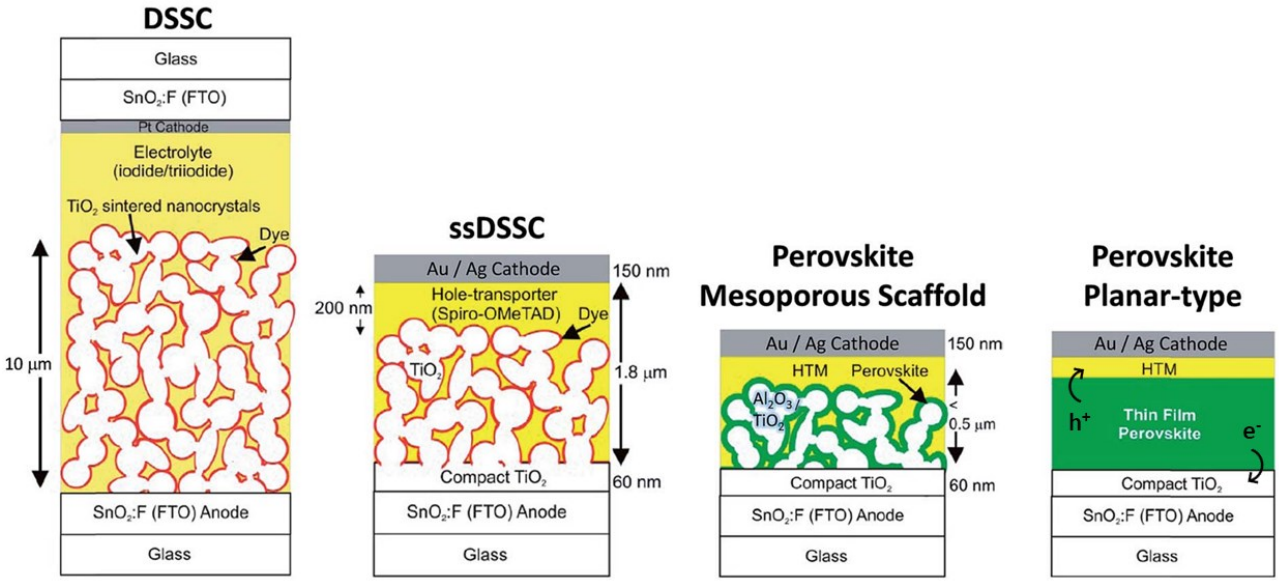

Figure 1.11 Structural evolution of PSC technology (dimensions not in scale). Starting from the electrolyte-based mesoscopic and solid state (ss) DSSC, where the electrolyte is replaced with an organic p-type hole conductor, PSCs evolved from sensitized solar cell by implementing: (i) nanodot perovskite, (ii) mesoporous scaffold with a thin and continuous layer of perovskite, (iii) perovskite capping layer of perovskite, and (iv) finally a perovskite thin film is sandwiched between charge-transport layers (the most up-to-date planar architecture).[105]

Moreover, the deposition of the contact onto the absorber could also influence the upper part of the perovskite layer; and those changes, even in a very thin region of the perovskite interface, can produce significant effects.[107] Ravishankar et al. demonstrated that the V_{OC} of PSC was not affected despite the use of CTMs with huge difference in W_F, highlighting a minor role of the built-in electrical field.[108]

In contrast, V_{OC} is generated by the Fermi level splitting at the perovskite layer, where each selective contact follows the quasi-Fermi level of respective carrier in the perovskite layer. This has important consequences in the working principles of PSCs as quasi-Fermi level splitting, and consequently the V_{OC} are controlled by light absorption and carrier recombination (Figure 1.10 c). If electrical fields are not playing a major role, mostly flat bands should be expected in the perovskite layer with transport dominated by diffusion. If the selective contact follows the LHP Fermi level and is influenced by the perovskite layer, they should not be treated as a mere series of connected systems but as parallel interrelated layers, to consider in future PSCs models. Despite the working principles that determine the photovoltage of perovskite solar cells are not as clear as those defining their photocurrent, the photovoltage is one of the most fascinating properties of PSCs due to the high open-circuit voltage (V_{OC}) obtained with this material if compared to other PV technologies.[101,109]

Figures of Merit

The efficiency of a solar cell to convert light-into-current, called photo-conversion efficiency (PCE), can be determined by the product of three photovoltaic parameters: short-circuit current (I_{SC}), open-circuit voltage (V_{OC}), and fill factor (FF).[110,111] This corresponds to the ratio between electrical power produced by a solar cell (P_{OUT}) and incident power of sunlight (P_{IN}):

$$\mathrm{PCE} = \frac{P_{OUT}}{P_{IN}} = \mathrm{FF}\,\frac{V_{OC} I_{SC}}{P_{IN}} \qquad 1.3$$

The FF is a key parameter to evaluate the performance of a solar cell simply by looking at its current-voltage (I-V) curve (Figure 1.12 a).[112] It is defined as:[111]

$$\mathrm{FF} = \frac{V_{MP} I_{MP}}{V_{OC} I_{SC}} \qquad 1.4$$

where V_{MP} and I_{MP} are the current and voltage at maximum power point, respectively. This ratio corresponds to the deviation from ideality of a solar cell, comparing its actual power with the power it would produce with no series resistance (R_{SERIES}) and infinite shunt resistance (R_{SHUNT}).[113] Ideally, the FF should be as close as possible to 1. The optimization of the PV performance requires the maximization not only of FF, but also J_{SC} and V_{OC} parameters. Although these three values are interrelated, each one is mostly influenced by different physical properties and processes determining the final values.[101] For instance, in a device the maximum photocurrent is limited by light absorbing material's E_{GAP}, but non-optimum charge collection and loss mechanisms can reduce it (Figure 1.12 b).[114]

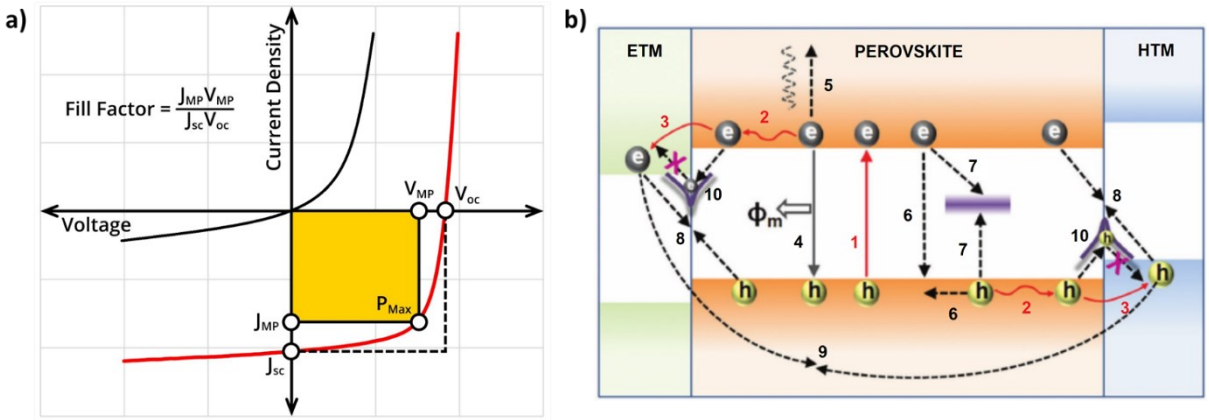

Figure 1.12 a) Typical J-V curve of a solar cell in dark (black line) and under light (red line) conditions. FF is geometrically defined as the ratio between the highlighted and the hatched areas, respectively. P_{MAX} represents the maximum power output of the solar cell.[112] b) Typical charge transfer and recombination processes in a perovskite solar cell: 1) photoexcitation and free carriers (e^-,h^+) generation; 2) charge diffusion; 3) injection of photogenerated e^- into CTLs; 4) radiative decay leading to PL (φ_m: quantum yield for emission); 5) auger recombination; 6) bi-molecular recombination; 7) trap-assisted nonradiative mono-molecular recombination; 8) back charge transfer at CTL/LHP interface; 9) non-radiative charge recombination at ETM/HTM interface; 10) surface recombination.[114]

As a result, establishing the working principles of each photovoltaic parameter helps not only to understand the device but to further improve its performance.[115] While single-junction PSC efficiencies skyrocketed from 3.8% in 2009 to over 25% in 2020,[116] this is still well below the thermodynamic limit of about 31% for $MAPbI_3$ perovskite material or the Shockley–Queisser limit (≈ 33%).[31] Evidently, there is still room for improvement and a large portion of this possibility resides in the negative influence of traps. Following the approaches adopted for DSSCs, it appears to be two separate trends for the types of scientific breakthroughs which have been driving up the PCE of perovskite-based solar cells (Figure 1.13). Between 2013 and 2016, solvent engineering and refining grain formation, together with compositional tuning for suitable bandgaps and stability, facilitated massive gains in device performance.[117,118] The large technological advances made during this early development were realized via improved materials processing, to harness the intrinsic potential of LHPs within photovoltaics.[27]

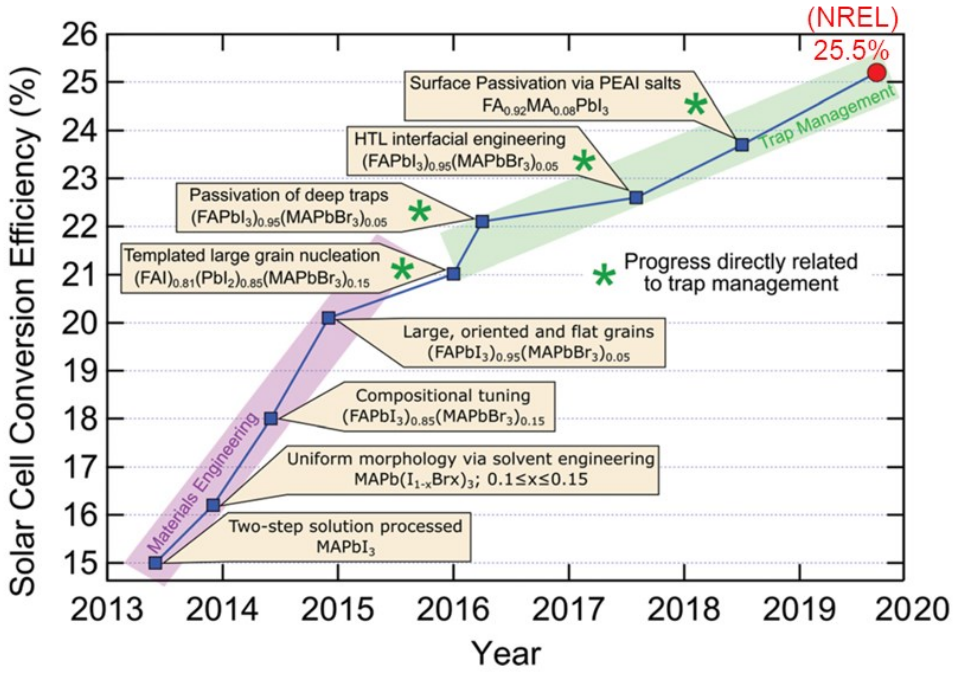

Figure 1.13 Overview of recent progress in single-junction perovskite solar cell efficiency, identifying the key technological advances.[31] The red circle indicates the current efficiency record (25.5%) confirmed by the National Renewable Energy Laboratory (NREL).[26]

More recently, since 2016, researchers have had to shift their focus toward trap management, in the interest of harnessing the remaining potential efficiency contained in LHP solar cells. For this, reducing the trap populations (both intrinsic and extrinsic), and their negative influence on devices, has seen a steady, albeit slower, rise in efficiencies.[119] A lack of precise control over the crystallization process will introduce some unwanted defects. By using a template to control crystal growth, larger grain size and oriented microstructure can be obtained with an efficiency of 21%.[118]

Interstitial and antisite defects in LHP may be responsible for non-radiative recombination. Through the introduction of additional iodide ions into the organic cation solution, the efficiency record was advanced decreasing deep traps (interstitial and antisite defects) in the bulk and achieving an efficiency over 22%.[119] In 2017, the record was further updated to 22.6% using fluorene-terminated materials as hole transport layer, passivating interfacial traps.[120] As surface defects often result in deep mid-gap traps for charge carriers,[31] surface trap passivation strategies allowed further improvements with an efficiency of 23.3% in 2018.[92,121] As of now, the new efficiency record of 25.5% was recently confirmed by National Renewable Energy Laboratory (NREL).[26]

Multi-Junction Solar Cells

In the past decade the Si photovoltaic module manufacturing costs have continued to diminish so extensively that nowadays the cost of a module amounts to less than half the overall PV installation cost. Therefore, increasing the overall power output of a PV module per unit area represents the best way to continue to drive down the overall cost of installed PV generated electricity.[122] Multi-junction (tandem) solar cells show great potential of breaking the Shockley−Queisser theoretical efficiency limit of 33.7% for single-junction solar cell, which becomes ∼46% for two-junctions solar cells.[123] In a tandem solar cell, single-junction solar cells are stacked on one another, typically with a top wide band gap solar cell absorbing high-energy photons and a bottom narrow band gap solar cell absorbing low-energy photons. This allows a broader region of wavelength absorption (Figure 1.14 a), which mitigates the hot carrier thermalization loss and achieves higher PCE than single-junction solar cells.[124]

Crystalline Si solar cells suits very well the role of low bandgap bottom cell due to their suitable bandgap of 1.1 eV, high V_{OC} of up to 750 mV, low cost, and high efficiency.[125] On the other hand, finding its ideal wide-bandgap partner is more difficult. III–V solar cells have been proposed for their high efficiency and tunable bandgap, and tandem cells together with Si have recently demonstrated efficiencies > 32%.[126] However, the high manufacturing costs of III–V solar cells hinder their large-scale deployment. A possible answer in terms of high efficiency and low cost came with the emergence of perovskite solar cells.[127] LHP solar cells present several advantages that make them highly interesting for their use as a top cell in silicon-based tandem solar cells, already reaching a PCE above 29%.[26,128] Their exceptional optoelectronic properties are well suited for tandem applications, including a high absorption coefficient, low sub-bandgap absorption, and a steep absorption edge.[21]

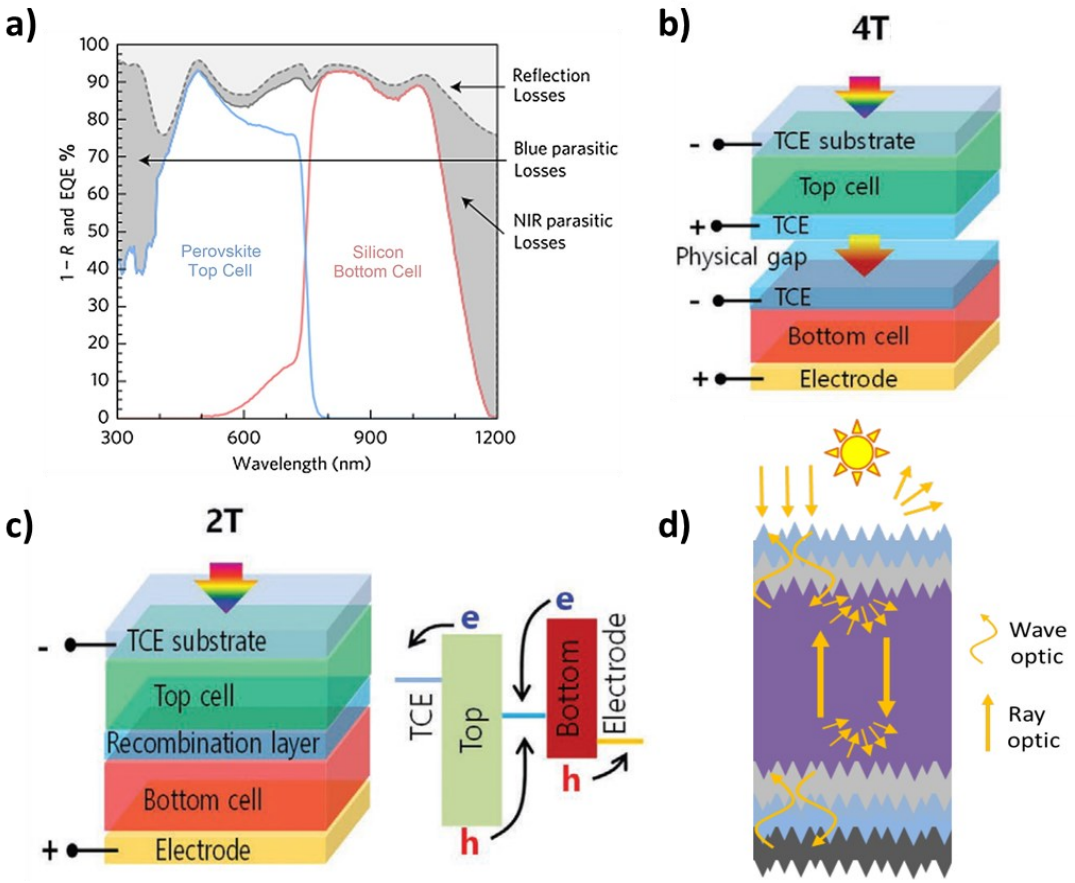

Figure 1.14 a) Quantum efficiency and reflection spectra of perovskite-silicon tandem solar cell with parasitic absorptions and reflection losses highlighted. The blue curve refers to the contribute of perovskite top cell, the red curve refers to the one of Si bottom cell.[200] b) Four-terminal (4T), c) two-terminal (2T),[141] and d) textured tandem architecture employed to reduce optical losses in the device.[149]

Moreover, perovskite solar cells offer bandgap tunability throughout a wide spectral range,[24] high V_{OC},[129] high defect tolerance, long charge carrier diffusion lengths,[130] and photon recycling.[131] Importantly, PSCs combine excellent optoelectronic properties and high efficiencies with the potential for low-cost processing and Earth-abundant constituent elements.[132,133] Reported fabrication protocols for PSCs include a variety of deposition techniques [134,135] based on solution processes, such as spin coating,[136] blade-coating,[137] or slot-die coating,[138] as well as vacuum-based methods, such as thermal evaporation,[139] or chemical vapor deposition.[140]

A perovskite-silicon tandem solar cell can be made in several configurations,[141] each of them having specific advantages and disadvantages. The simplest tandem device architecture from a process development point of view is the mechanically stacked four-terminal tandem (Figure 1.14 b). The two subcells are fabricated independently, stacked on top of each other and contacted individually (in series). This has the advantage of process simplicity and lower sensitivity towards spectral variations, but at the same time optimum transparency of the contacts in different spectral

ranges.[125] During operation the two subcells work independently, reducing the constraints on the choice of the top cell bandgap.[142] However, using four terminals implies also doubling all the power electronics, which increase the overall cost. As a possible solution to this problem, monolithic tandem modules have been proposed, using only two-terminals and arranging the cells in submodules connected in parallel (Figure 1.14 c).[141] Their high efficiency potential results from a gain in photocurrent due to reduced parasitic absorption due to contacts (they do not require the two intermediate transparent conductive oxide electrodes, needed in the four-terminal design).

Despite this advantage, the two-terminal approach has more constraints with respect to the device processing. Moreover, as the V_{OC} varies logarithmically with light intensity, a voltage-matched connection can be more resilient toward spectral variations compared to a current-matched one.[125] Practically, the perovskite and silicon subcells need to be electronically coupled, where the interfacial structure should guarantee efficient charge recombination of majority carriers (collected from each subcell) in the so-called recombination layer, without inducing minority-carrier recombination.[143] Other tandem concepts were demonstrated, such as three-terminal,[144] spectral splitting systems,[145] reflective tandems,[146] and the more advanced bifacial tandems.[147] Despite the way the subcells are connected together, textured architectures has been recently investigated to further increase the PCE of tandem devices.[148] Since the high number of layers stacked on top of each, reflection losses are non-negligible in tandem solar cells (Figure 1.14 a). As a result, additional antireflection coatings are usually applied on top of multi-junction devices. However, because this involves additional processes, a technique that allows to void such steps is required. Textured surfaces allow to avoid the use of antireflection materials, both limiting the reflection losses and enhancing light-trapping in tandem solar cells (Figure 1.14 d).[149] These effects are the more evident as the degree of texturing employed (e.g., one-side, double-side, or fully textured architecture).[150]

1.3.2 *Light-Emitting Diodes*

Working Principles

In simplest p-n junction LED device, light is emitted when e^- and h^+ that flow as majority carriers are injected across the junction and recombine at or near the junction causing radiative recombination to take place.[111] This is a diffusion-driven process near the junction as opposed to the drift mechanism that underlies solar cell operation.[18] LED efficiency is limited by two main factors namely: (i) non-radiative recombination, in which electron-hole pairs recombine but do not generate a photon; (ii) limited optical outcoupling, in which not all the generated photons leave the

device. Since radiative recombination processes are favored in direct-gap semiconductors, such materials are generally chosen for most practical LEDs. Compared with early-stage incandescent and fluorescent lamps, LEDs have gained commercial acceptance because of their high luminous efficiency, low energy consumption, and long operational life. The discovery of the electroluminescence phenomenon in the early 20th century, based on a silicon carbide - metal Schottky junction, can be considered a precedent of LEDs.[151] Then, LEDs based on homogenous p–n junctions (also referred to as homojunctions) were processed and developed rapidly (Figure 1.15 a, b).[111] In homojunction LEDs, by applying a forward bias the energy barrier between p-type and n-type semiconductors is reduced. Then, e^- and h^+ are respectively injected from the n- and p-type semiconductors, which induces radiative recombination accompanied by the release of photons. The homojunction structure is an early-stage LED structure, which suffers from photon reabsorption loss caused by the same bandgap of p- and n-type semiconductors.[151] LEDs based on heterogeneous p–n junction (also referred to as a heterojunction) formed by two semiconductors with different bandgaps were later developed (Figure 1.15 a, c). The heterojunction structure is suitable for avoiding reabsorption of photons.

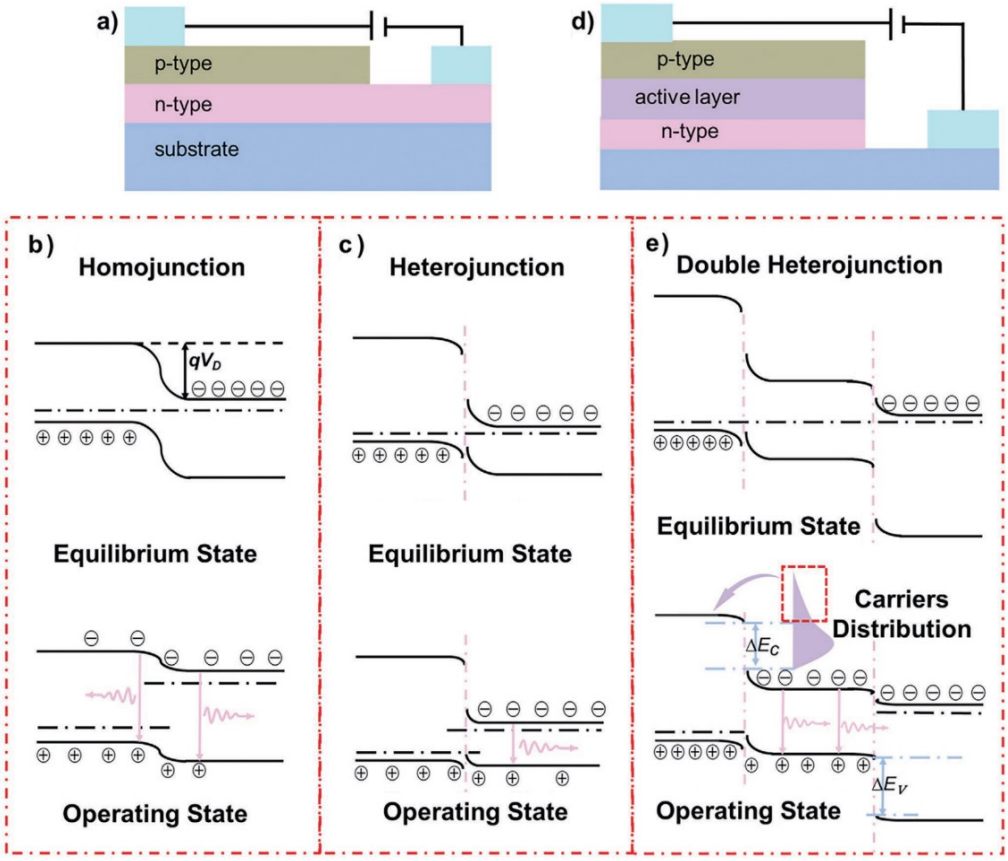

Figure 1.15 Basic structure and working principle of LEDs. a) Device structure of p–n junction LEDs, including the energy level diagrams of b) homojunction and c) heterojunction LEDs at equilibrium and operating states. d) Device structure of double heterojunction LED, with the corresponding e) energy level diagrams at equilibrium and operating states.[151]

In such LEDs, a wide bandgap semiconductor is used as the charge injection source, and the narrow-bandgap semiconductor serves as light emission source. In this configuration, e^- and h^+ have different energy barriers through the junction. The light emission in heterojunction LEDs only occurs in the narrow-bandgap semiconductor at a suitable operating voltage. Owing to the low energy of photons emitted by the narrow-bandgap semiconductor, this will not cause absorption in the wide bandgap semiconductor.[151]

Therefore, using a wide-bandgap semiconductor as the light exit window can effectively reduce the photon reabsorption loss in LEDs. However, both heterojunction and homojunction LEDs suffer from insufficient utilization of injected carriers. Since the diffusion length of the carrier is greater than the thickness of the active layer, some injected carriers pass directly through the active layer and reach the electrode surface without recombination, which results in loss of efficiency in the form of leakage current.[151] Thus, carriers are expected to be confined within the active layer to improve the utilization rate of injected carriers. This idea inspired the emergence of double heterojunction LEDs (Figure 1.15 d, e) with a sandwich structure, where wide bandgap p- and n-type semiconductors serve as the HTM and ETM, respectively, and the narrow-bandgap semiconductor serves as the active layer. During the operation, e^- and h^+ are injected into the active layer from the ETM and HTM, respectively. Then, photons are emitted through the radiative recombination of electron–hole pairs.[151] Therefore, the double heterojunction structure can improve the utilization of injected carriers, reason why all state-of- the-art LEDs, including LHP ones, are based on this device architecture.[152,153]

Figures of Merit

In light emission application, external quantum efficiency (EQE) serves as the key figure of merit under consideration that requires maximization. EQE depends on several parameters, that can be expressed as follow:[154]

$$EQE = f_{balance} \times f_{e-h} \times \eta_{radiative} \times f_{out-coupling} \quad 1.5$$

where $f_{balance}$ is the probability of balanced charge injection, f_{e-h} is the probability of forming correlated electron–hole pair or exciton from each pair of injected carriers, $\eta_{radiative}$ is the probability of radiative recombination for each electron–hole pair, and $f_{out-coupling}$ is the photon escaping probability. $\eta_{radiative}$ is usually known as photoluminescence quantum yield (PLQY) and can be expressed as the ratio of the radiative to the total recombination rates:

$$PLQY = \frac{nk_2}{k_1 + nk_2 + n^2k_3} \quad 1.6$$

where n refers to the carrier density, while k_1, k_2 and k_3 are the coefficients of the first-order monomolecular recombination, second-order bimolecular recombination, and third-order Auger recombination respectively.[155] Approaches to ensure high PLQY of emitting materials such as complete control of film morphology,[156] chemical composition of the emitter,[157] as well as suitable interface engineering aimed at defect reduction at interfaces and grain boundaries [158] led to almost-unity PLQY in lead halide perovskites.[159] Thus, maximizing both f_{balance} and $f_{\text{e–h}}$ via device engineering is essential to further enhance EQE of perovskite LEDs. In general, the choice of electron- or hole-injection layers are adopted from the well-studied solution-processed organic LEDs (OLEDs) or conventional QDs-based LEDs. Indeed, with internal quantum efficiency (IQE, defined as product of f_{balance}, $f_{\text{e–h}}$ and $\eta_{\text{radiative}}$) almost reaching its limits, efficient light out-coupling management strategies will play a major role in the future to amplify EQE of LEDS. Strategies to enhance $f_{\text{out-coupling}}$ include modifications to the design of materials and interfaces from optics point of view.[155]

Perovskite LEDs

In addition to their remarkable PV performance LHPs also possess excellent luminescence performance. Despite perovskite LEDs have adopted similar emitter and device configuration as OLEDs, they highlighted the advantage of photon recycling due to the small Stokes shift for perovskite emitters as compared to organic ones (Figure 1.16 a).[160] Such process can be exploited to boost the $f_{\text{out-coupling}}$ and overall device performances, with many strategies that have already been employed.[155] In addition, organic emitters generally possess high exciton binding energies that severely limits the PLQY due to the non- emissive nature of spin-triplet excitons.[161] Accumulation of triplet excitons at high carrier densities leads to optical losses within the system.[162] On the contrary, such limitations do not exist in lead halide perovskites due to reduced excitonic interactions. In addition, owing to smaller emission linewidths and facile bandgap tuneability, LHPs materials seem to provide a clear advantage in devices over OLEDs becoming promising candidates for applications in high-performance light-emitting diodes.[151] With the advent of colloidal lead halide perovskite QDs in 2015 [163] with very high PLQY and higher exciton bounding energies than perovskite bulk counterparts,[164] colored perovskite LEDs based were achieved in the same year.[64,165] At present, EQEs of 21.3%, 21.63%, and 12.3% were achieved for red, green, and blue QDs-perovskite LEDs, respectively.[166–168] Thanks to their narrowband emission, wide color gamut (Figure 1.16 b), near-unity PLQY, and cost-effective solution processability QDs-perovskite LEDs have recently attracted

considerable interest for their potential applications in high-definition displays (Figure 1.16 c-d). However, QDs present high surface energy and defect density owing to the large surface–volume ratio, which reduces the optical performance and stability of the NCs. Recently, some strategies, such as ligand exchange, doping, core-shell structures, and self-assembly have been proposed to improve luminescence performance and stability of NC-perovskite LEDs.[151,169]

1.4 Challenges and Future Perspectives

Despite lead halide perovskites have emerged as prospective materials for high-efficiency, and inexpensive next generation optoelectronics in the last years, their poor stability in ambient conditions and under electric field still hinders their applications.[28,170] Moreover, the toxicity of lead contained in LHP films and suitable ways to achieve sustainable large-area production need to be considered before commercialization.[171] Recently, many technological improvements have been made to improve both stability and scalability of the perovskite-based devices,[172] including interfacial modification, charge transport layers engineering, strategies on avoiding lead contamination, and compositional and solution engineering approaches for large-scale production.[173] The next paragraphs will elucidate the main strategies and countermeasures that have been adopted to counter the drawbacks of LHP materials in the last years.

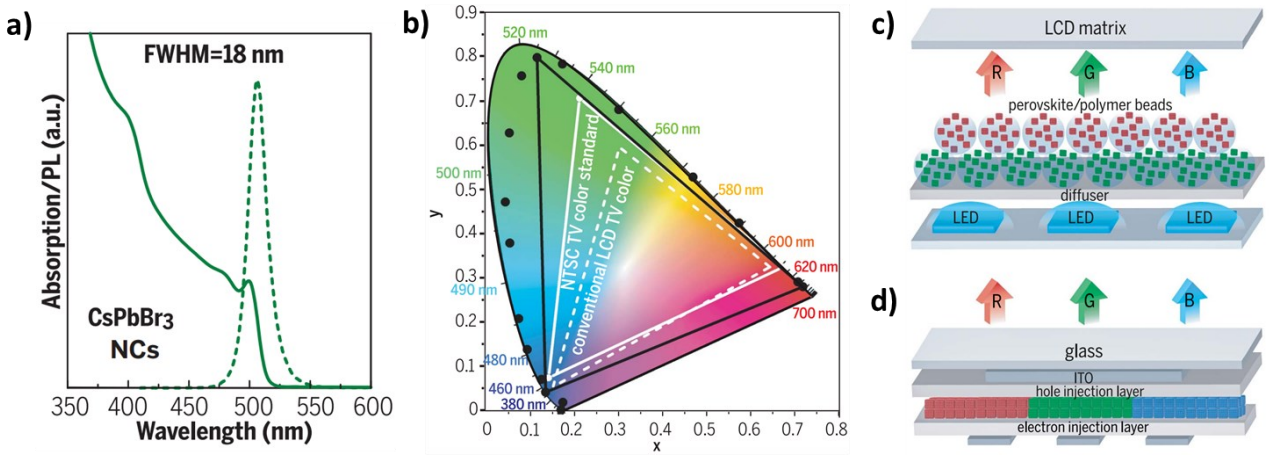

Figure 1.16 Absorption and PL spectra of 8-nm colloidal $CsPbBr_3$ NCs, exhibiting quantum-size effects and highlighting very small Stokes shift. b) PL spectra of $CsPbX_3$ NCs plotted on CIE chromaticity coordinates (black points) compared with common colour standards (LCD television - dashed white line, and NTSC television - solid white line), reaching 140% of the NTSC colour standard. c) Operation principle of a QD LCD display, showing blue emission from standard InGaN LEDs transmitted by the diffuser into a polymer film containing LHP NCs, undergoing partial conversion into green and red PL. d) Schematic of a three-color LED pixel with LHP NCs as the emissive layer. LEDs have fewer layers in their device architecture than LCDs and can therefore afford thinner devices and make more efficient use of the light.[93]

1.4.1 *Long Term Stability*

Despite lead halide perovskites have been proposed as next-generation semiconductors, their stability remains a challenge. Inorganic LHPs has emerged as an alternative to hybrid organic-inorganic ones, due to their higher intrinsic and thermal stability.[28] However, inorganic lead halide perovskites undergo degradation too, affecting device performance significantly.[28,174] Therefore, there is an urgent need to gain insights into the chemical stability and instability in both hybrid and inorganic LHPs, which will help in developing high-performance perovskite optoelectronic devices sufficiently durable for real-world applications.[175] There are four different key factors influencing the stability of lead halide perovskites: (i) environmental moisture, (ii) photoinduced degradation, (iii) thermal stability, and (iv) electric field effects.[170,176] It is useful to underline how degradation mechanisms in a perovskite-based device also involve other components (e.g., charge transport layers, contacts) and not only the photoactive perovskite layer itself.[177]

Tolerance to Humidity

Moisture induces reversible and/or irreversible degradation of HOIPS films in which water molecules easily penetrate the perovskite structure and form intermediate hydrate phases.[178] This because water forms strong hydrogen bonds with organic A-site cations,[179] weakening its bond with the PbI_6 octahedra and allowing a faster deprotonation of the organic cation. Such mechanism makes external stressors such as heat and electric field to be more effective at degrading the LHP phase.[180] Furthermore, water molecules protonate iodides creating volatile hydroiodic acid (HI) and generating yellow-colored lead iodide as a decomposition product (Figure 1.17 a).[181] Several approaches to enhance moisture stability of LHP materials have been developed, including compositional tuning and modification of the device stack.[170] For the former, lattice strain induced by halide substitution,[182] minimization of the organic cation volatilization by mixing A-site cations,[183] and the incorporation of hydrophobic 2D lead halide perovskites into 3D ones [184] to passivate grain boundaries [185] and/or modifying the top surface [186] proved to be valuable strategies to minimize moisture-induced LHPs degradation. Regarding the stack modification of the perovskite-based device, thin oxide buffer layers deposited onto perovskite surface,[187] hydrophobic materials employed as charge transport materials,[188] mesoporous structures,[189] encapsulation techniques,[190] and the use of micrometer-thick carbon top electrodes [191] have shown to ensure an impressive enhancement in device stability in ambient conditions (from a few days up to years) and under prolonged thermal stress.[192]

Stability under Illumination

Since light exposure can accelerates photooxidation and moisture-induced degradation of LHPs (Figure 1.17 c-e),[170,174,176] the influence of light on LHP optoelectronics should be considered in the absence of any other environmental factors. Many reports showed the high stability of encapsulated perovskite solar cells working for hundreds of hours under light exposure.[193,194] On the contrary, without encapsulation significant changes occur in LHP films during illumination, including halides segregation, ions migration, and compositional degradation.[195–197] Recently, a photodecomposition reaction mechanism for lead halide perovskites has been proposed, in which X^- halide anions in the perovskite lattice are oxidized by photogenerated h^+ resulting in coupled formation of X neutral halogen interstitials and halide vacancies.[195] This process can provoke irreversible decomposition to metallic lead, neutral halogens (X), and AI species if the generated X species are removed via sublimation or reactions at the perovskite interface with other materials.[198,199] Though not yet fully explored for all compositions and device architectures, there is likely to be a correlation between the phenomenon of light-induced halide vacancy creation and the light-induced ionic migration and segregation.[175] Charge-transport materials also play a role, by hindering or further enhancing light-induced cation segregation in LHP layers.[200,201] Despite all these parameters to take into account, promising results have already been obtained, with many research groups demonstrating over 1000 hours of operation under illumination with negligible drops in the performance of perovskite-based devices.[198,202]

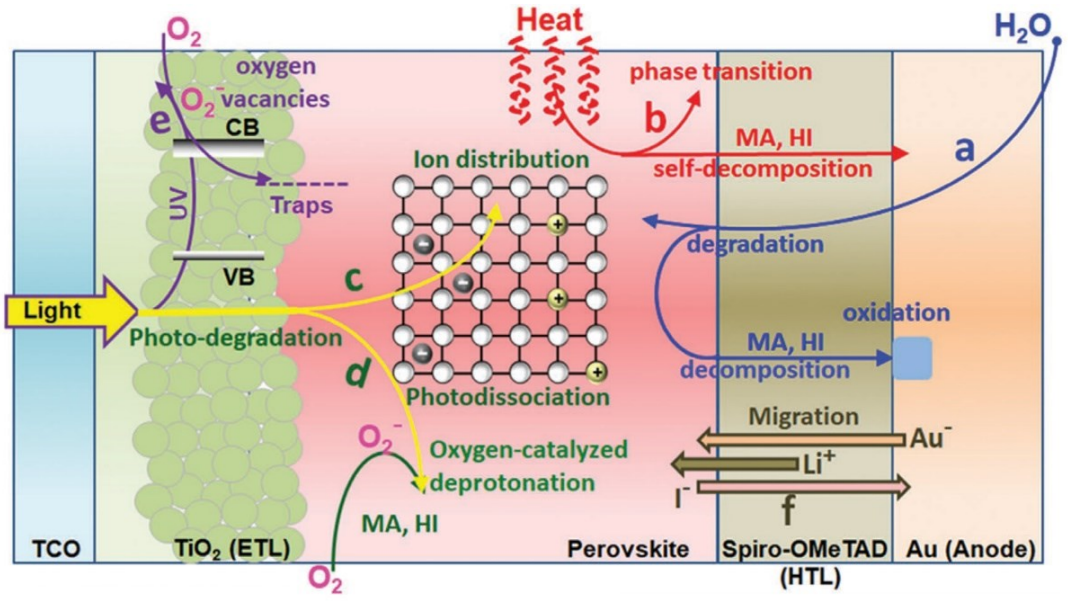

Figure 1.17 Schematics illustrating representative degradation pathways induced by moisture, heat, and light in perovskite solar cells. a) hydration of $MAPbI_3$ perovskite and its decomposition in MA and HI; b) perovskite phase transition due to thermal stress; c) Photoactivated mechanisms for halide and cation vacancy migration; d) Dissociation mechanism of MA^+ due to the capture of a photogenerated electron; e) Oxygen-induced formation of deep trap states at mesoporous electron transport layer surface/interface under UV rays; f) Au^- and I^- ionic diffusion across the device.[92]

Such impressive photostability has been obtained by opportunely selecting the charge-transport- and contact layers,[195] as well as by adopting 2D-3D perovskite structures to suppress ion diffusion and vacancy migration.[202]

Thermal Stability

Understanding how the LHPs stability scales with temperature is important for four main reasons: (i) an annealing step is usually required to form perovskite thin films and contacts, (ii) module encapsulation processes typically exceed 140 °C for a certain period of time, (iii) solar cells can reach > 60 °C in hot climates,[203] and (iv) testing at high temperature accelerates chemical reactions and degradation processes that may occur on the time scale of years in the field.[175] LHPs thermal stability depends on its composition and dimensionality, as well as on the device architecture in which the material is implemented.[175,204] While structural stability over the operational temperature range of −15 to 65 °C is a prerequisite for LHPS thermal stability,[205] resistance towards thermally activated chemical decomposition and reactions must also be achieved for stable perovskite-based devices. In fact, lead halide perovskites with a high structural stability (i.e., *t* close to 1, Section 1.1.1) such as $MAPbI_3$, may have poor thermal stability reverting to a non-photoactive phase, segregating into several phases or generating reactive species (Figure 1.17 b).[206,207] This motivated researchers to stabilize alternative composition of LHPs via A-site,[70,208] B-site (less diffused),[209] and/or X-site mixing strategies.[210] The extremely broad range of potential perovskite compounds presents new research opportunities in exploration and refinement of perovskite phases, especially in verifying the thermodynamic stability of many mixed-cation and mixed-anion compounds.[211,212] Under a device point of view, additional layers can improve thermal stability of the LHP layer itself, but requires to take into account the possibility of mobile ions (mainly I^- and Br^-) diffusion into the contact layers.[213] Organic HTMs are prone to thermal instability, especially when additives are used to improve their conductivity. This has motivated the use of either more stable oxide contact layers [194,214] or alternative dopant-free organic transport layers.[215] Moreover, metal contacts are notoriously susceptible to halides,[216] creating stability problems due to metal or halides diffusion at elevated temperatures and under light. These issues have been drastically reduced in “hole-conductor free” architectures made by infiltrating porous layers of carbon, ZrO_2, and TiO_2 with LHP precursor ink, which has been shown remarkable stabilities (more than 10000 hours under standard conditions).[186,217] This topic will be further addressed in Chapter 4.

Bias Effects

Although there are few works focused on the study of electric-field effects on the stability and performance of LHP optoelectronics,[218,219] the perovskite response under bias is an important aspect to investigate since it can simulate and reproduce the working conditions of a device. Applying an electric field to halide perovskite materials significantly impacts their carrier separation, changes direction of the photoinduced currents and generates switchable photovoltaic effect.[220,221] Considering the archetypal case of $MAPbI_3$ perovskite, applying a bias leads to the orientation of MA molecules and thus the diffusion of ions in $MAPbI_3$ lattice.[222] Then, anions and cations accumulate on different side of halide perovskites, and the internal electric field generated by the diffused ions affects photocarrier separation (Figure 1.18 a-b). This process is like the phenomenon induced by the light-induced electric field.[223] Whereas, if symmetrical electrode is applied, the internal electric field controls directly the direction of photo-generated current, which is the origin of the exchangeable photovoltaic effect (Figure 1.18 c-d). Such charge redistribution and moving ions under bias in LHPs not only undermine their stability,[180] but also brings with it the difficulty in achieving reliable evaluations of device performances due to the occurrence of I–V hysteresis.[224]

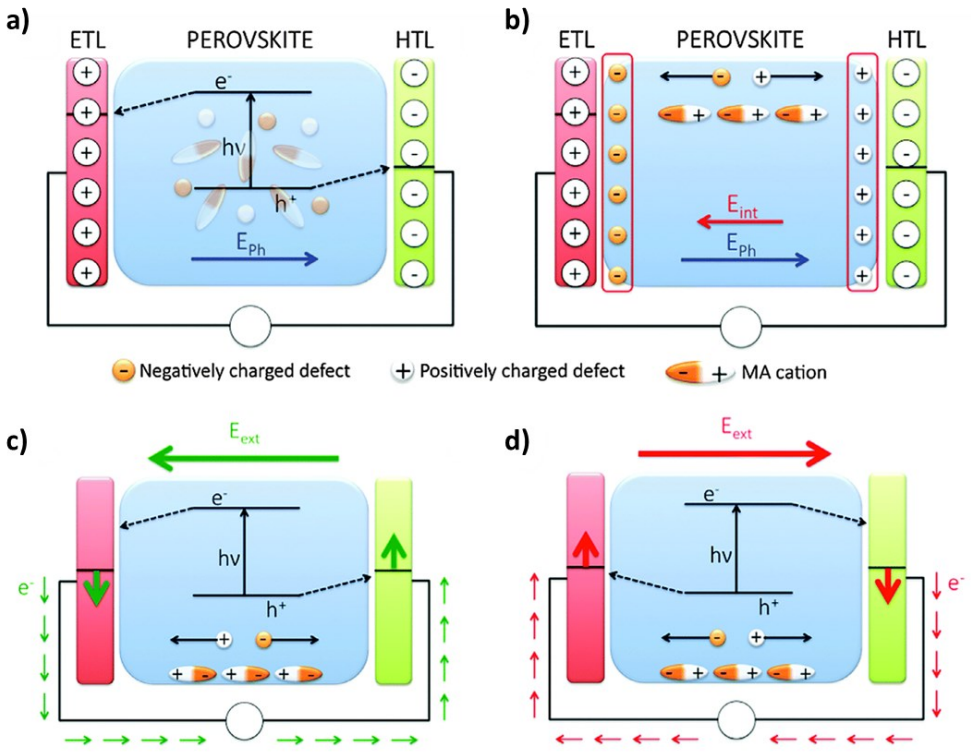

Figure 1.18 Sketch of defect migration and their impact on the operational mechanism of a perovskite solar cell. a) Charge carriers' separation driven by the photogenerated potential (E_{Ph}), along with the even distribution of point defects and random orientation of MA cations. b) Point defects migration and the reorientation of MA cations in response to the photogenerated field (E_{Ph}), together with the developed of an internal electric field (E_{int}). c,d) Switchable current as a function of the applied external field (E_{ext}).[222]

Among the different mechanisms that can dominate it, nowadays I-V hysteresis in LHPs (thus their sensitivity towards electric-field) can be reduced and even eliminated via various strategies including stabilizing the perovskite lattice through compositional engineering,[225] improvement in morphology,[226] reducing traps, and optimizing the charge transport process.[224] This lead to LHP optoelectronic devices with long-term stability, as well as to more reliable and unified procedures and protocols to test perovskite solar cells.[227,228]

Lead Toxicity

In recent years, significant efforts have been spent to develop lead-free halide perovskites and perovskite derivative absorber materials to both improve the sustainability and the bandgap tunability of this promising next generation semiconductors.[22,229] However, optoelectronics based on these materials showed significantly inferior performances as compared to their LHP counterparts so far.[230] Generally, there are two categories for Pb replacement using either homovalent elements such as Sn and Ge, or heterovalent elements such as Bi and Sb. The heterovalent replacement category can be further divided into two subcategories, namely ion-splitting and ordered vacancy (Figure 1.19).[22] While homovalent replacements lead to perovskite phase instability, the heterovalent Pb replacements lead to degraded electronic properties mainly due to the reduction on electronic dimensionality. Consequently, not all the superior optoelectronic properties of lead halide perovskites are maintained in the lead-free counterpart. These are the reasons that reside in the inferior photovoltaic performances of Pb-free PSCs reported in the literature as compared to those implementing LHPs.[22]

Sn(II) is the most obvious candidate for Pb replacement because both possess lone-pair s orbitals.[231,232] Such replacement shows both desirable and unwanted effects. Compared to $MAPbI_3$, the absorption spectrum of $MASnI_3$ shows a reduced bandgap and higher absorption coefficients in the visible light region, making it more suitable for both efficient single-junction and tandem solar cell applications.[233,234] However, the high-energy-lying Sn $5s^2$ states make the Sn-I bonds easy to break, forming high-density Sn vacancies and causing the easy oxidation of Sn (II) to Sn (IV). Therefore, tin halide perovskites are extremely unstable to air and moisture.[235] To overcome the Sn oxidation issue, different strategies have been investigated such as the addition of SnF_2 to SnI_2 to the precursor solutions,[236] the replacement of $MASnI_3$ with $FASnI_3$ to improved film morphology and electrical properties,[237] and the reduction in dimensionality of the Sn perovskite phase.[238]

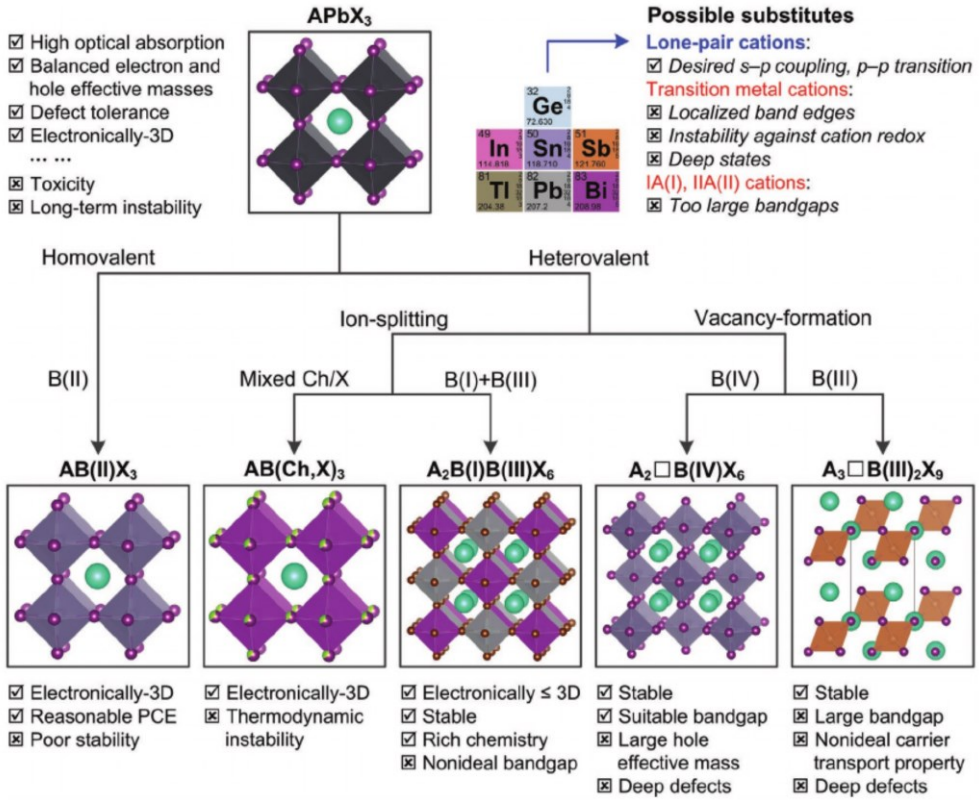

Figure 1.19 Schematic illustration of the approaches and consequences of potential Pb replacement.[22]

Thanks to a suppressed Sn oxidation processes, as well as a slower crystallization rate to produce pinhole-free and highly oriented tin perovskite layer, tin PSCs have emerged as a promising candidate for eco-friendly PV technology in the past few years. Despite their efficiency has increased rapidly from about 6% in 2014 to more than 13% in 2020,[233] they are still far from the > 25% PCE of lead counterpart. Other strategies to replace Pb with Ge or by heterovalent replacements have been recently investigated and applied to PSCs, but still with poor results. PCE around 7% was reached in the case of homovalent Pb replacement with Ge,[239] while only a few % were obtained with heterovalent substitutions.[22,230] Beyond perovskite solar cells, lead-free halide perovskites have been proposed as valuable alternatives for optoelectronic applications, such as photodetectors, photocatalysts, and FETs.[240–242] Apart from device performance, the major hurdle in lead-containing devices is in case of their failure, in which Pb could be dispersed into the soil and enter in the food chain. Since there is a zero tolerance on lead in the human organism, this health hazard is a critical obstacle for commercialization.[243] It was recently shown how Pb contained in LHPs is more dangerous than other sources of lead contamination already present in the ground as it is ten times more bioavailable,[244] pointing out the necessity for a systematic screening of the environmental impact of different perovskite compositions to drive the application of these materials towards a sustainable market.

Interestingly, different strategies to recycle [245] and/or capture [246] lead in failed devices such in-situ metal immobilization have been recently investigated to get efficient lead immobilization and non-leaching LHP optoelectronics (Figure 1.20). Water-induced lead precipitate formation reagents,[246] steric hindrance,[247] ion-exchange materials, and high surface-area adsorbents [248] have been proposed to be incorporated in LHP solar panels.

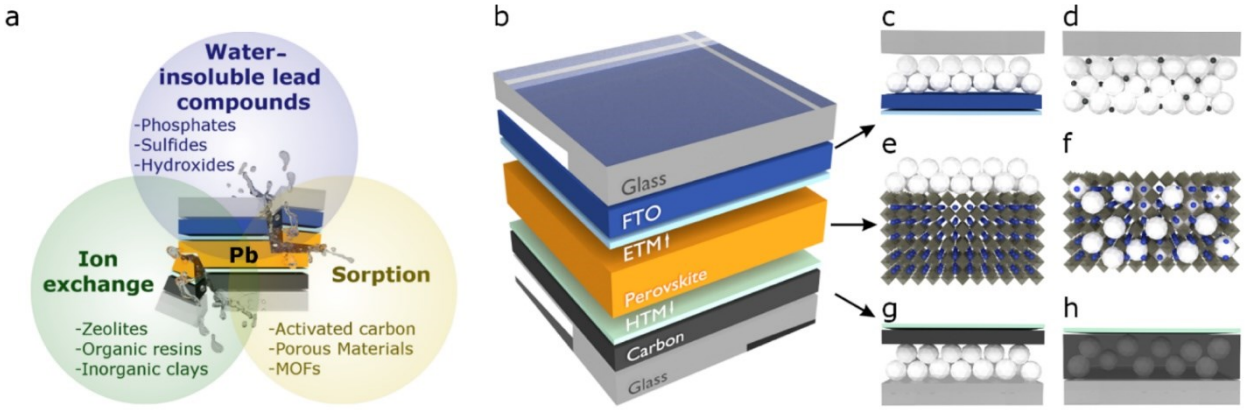

Figure 1.20 Sketch of strategies for Pb capturing in failed PV devices. a) In-situ metal immobilization strategy for lead perovskite-based optoelectronics. b) Typical architecture of a carbon-stacked PSC in which the in-situ metal immobilization materials could be implemented in various configurations: c,d) into the transparent electrodes; e,f) into the photoactive layer; g,h) the non-transparent conductive electrodes.[246]

1.4.2 *Safety and Sustainability*

Other than Pb toxicity, the lack of a robust, green processing technology for high-throughput production of efficient LHP optoelectronics (especially PSCs) on a large scale is still one of the major obstacles in their application and commercialization. For this reason, achieving scalable and sustainable fabrication of next generation perovskite-based devices is now at the top of the agenda for both academia and industry.[249,250] Such a goal is very difficult to handle since it involves all the steps required from materials synthesis to the device fabrication.[251] It is necessary both to develop greener synthesis and fabrication methods,[252,253] as well as to verify and to control their impact on LHP film uniformity, defects and impurities, charge transport and recombination, and the device performance and stability.[254] Moreover, the choice of solvent to use for LHP synthesis and processing is limited since lead halide precursors are scarcely soluble or insoluble in most solvents, and only non-polar or low-polarity solvents can be used as effective antisolvents during the antisolvents assisted crystallization method (Section 1.2.3). In fact, the most efficient solvents for preparing uniform LHP thin films such as polar, aprotic DMF, DMSO, and N-methyl-2-pyrrolidone are highly toxic and carcinogenic substances.

Although DMSO is less dangerous to handle, the high surface tension of LHP precursors-DMSO solutions results in wrinkled perovskite films, which deteriorate the device performance.[255] γ-Butyrolactone, another good candidate for the preparation of perovskite precursors solution, is a regulated chemical in many countries and its industry usage is restricted due its psychotropic effects. Also, the most used antisolvents, such as toluene and chlorobenzene are highly toxic and volatile, which are not suitable for large-scale fabrication and need to be replaced. For the selection of environmentally friendly solvents and antisolvents for fabricating high-quality LHP films three main aspects need to be carefully considered: the formation of a stable, homogeneous and high concentrated precursors solution, an uniform coating of the substrate, and the facile transformation to pinhole-free perovskite layers.[254,256] Solvent properties like the dielectric constant, dipole moment, atomic charge, volume, and mass influence the solubility of lead halides perovskite precursors. The Hansen solubility parameters mode,[257] based on dispersion, intermolecular dipole interactions, and hydrogen bonding between a solute and a solvent molecule, has been used to predict the dissolving ability of a solvent toward PbX_2 powders.[251] Moreover, to help chemists with the selection of sustainable solvents to use for their experiments, many pharmaceutical companies and institutions have brought out broad-ranging, data-rich solvent selection guides.[258,259] Several solvent parameters were carefully evaluated for the safety, health, and environmental (SHE) hazards, such as flammability, explosibility, flash point, boiling point, biodegradability, carcinogenicity, mutagenicity, and reprotoxicity.

Following this direction, much effort has been devoted to developing greener fabrication routes of LHP thin films in the last years, such as the preparation of environmentally friendly perovskite precursors solutions via solvent engineering,[260] and the use of green antisolvents like anisole, methoxybenzene and ethyl acetate.[261,262] Furthermore, the development of a novel molten salt approach opens up a new, versatile perovskite thin film processing concept that obviates the necessity of using toxic antisolvents or solvents commonly used in the fabrication of LHP inks.[263,264] Molten salts are characterized by high conductivity, wide electrochemical window, non-volatility, non-flammability, and excellent chemical and thermal stabilities.[265] Remarkably, they also exhibit flowability, which enables the uniform spreading of the perovskite precursors solution on the substrate to form dense LHP layers. Very recently, an environmentally friendly RT molten salt, methylammonium acetate, was used to prepare high-quality perovskites in ambient atmosphere.[266] Methylammonium acetate is a green ionic liquid with high viscosity and negligible vapor pressure. The strong hydrogen bond interactions between methylammonium acetate molten salt forms and

LHP precursors lead to much more stable solutions than those obtained in DMF/DMSO. Additionally, the methylammonium acetate precursors solution contains a high concentration of uniformly distributed micelles, which favored a homogeneous crystallization of the lad halide perovskites. Subsequently, dense, pinhole-free perovskite layers were prepared by a simple one-step method with good reproducibility without the use of any antisolvent even at relative humidity over 80%. Thus, molten salt approach overcomes the limitations of traditional solvents. More importantly, the new fabrication routes are compatible with the scalable solution processing methods such as spray coating, inkjet printing, and slot die coating, which can effectively reduce the manufacturing cost of LHP devices. Different strategies to produce ETMs and HTMs in more-sustainable ways have been developed too, aimed to implement less-toxic, halogen-free, and dopant-free solvents.[253,267,268]

Regarding low-dimensional LHPs such as NCs and QDs, recent developments in greener and RT synthesis and purification protocols have been proposed, closely evaluating the suitability of particular techniques for industry (Figure 1.21).[252] Polar solvent-free RT methods have been developed, yielding to LHP NCs of comparable quality to high-temperature approaches.[269] The initial weakly binding carboxylic acid/amine ligands have been replaced by strongly binding ligands such as quaternary ammonium halides, multidentate carboxylic-, phosphonic-, and sulfonic acids, and zwitterionic ligands such as long-chain soy lecithin.[252,270] Highly branched “entropic” ligands could substantially enhance colloidal stability of perovskite NCs,[271] so that highly concentrated dispersions of such NCs can be reliably stored/transported for long time. Moreover, given the current lack of Pb-free halide perovskite NCs with comparable properties of Pb-containing ones, researchers are getting more and more careful to ensure that all the other chemicals utilized to synthesize, purify, disperse and to deposit the LHP NCs are as safe and sustainable as possible. Cyrene represents an appealing alternative to DMF in the case of polar solvent route, while Limonene and p-Cymene represent attractive candidates to substitute toluene, the most common non-polar reaction media used both as reaction solvent and dispersing agents for LHP NCs. Regarding the purification step of nanocrystals, toxic Diglyme could be effectively replaced by Octanone and Isopropyl acetate.[252]

All the achievements listed above have considerable practical relevance for the development of high-quality LHP materials by greener fabrication methods for optoelectronics. However, several challenges still need to be overcome. First, the replacement of toxic solvents by greener ones is limited to specific perovskite compositions, and further research is required to ensure the universal application of green solvents for preparing perovskite inks.

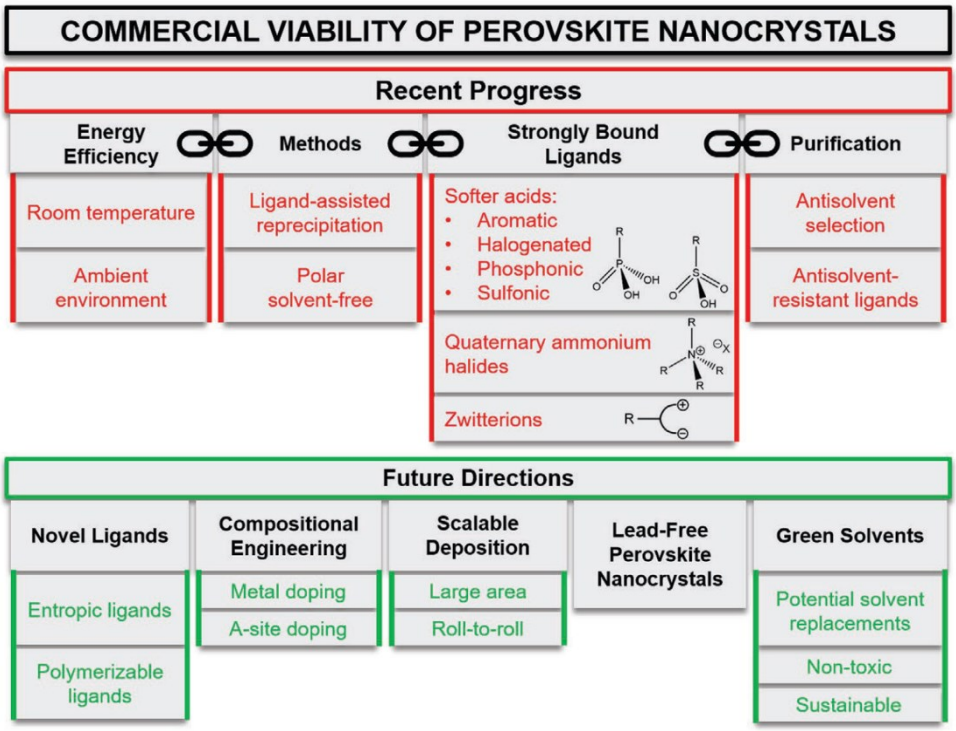

Figure 1.21 Outline summarizing the recent progress (red) and future directions (green) toward commercially viable lead halide perovskite nanocrystals.[252]

For instance, despite 2D Ruddlesden-Popper and Cs-doped/alloyed LHPs are outstanding candidates for many applications due to their very good stability (Section 1.4.1), further research is required to dissolve these perovskites using suitable green solvents and/or molten salts and to deposit them by coating or printing techniques compatible with roll-to-roll large-scale manufacturing processes.[254] Moreover, the crystallization thermodynamics of LHPs need to be in depth investigated to obtain large-scale high-quality thin films by sustainable processes.[251,254] Second, since devices are expected to have a long working life (for instance $\geq$ 25 years for solar panels), reliability assessment is crucial for LHP devices by these new methods.[272,273] The large grain size of the perovskites thin films prepared using greener antisolvents (such as ethyl acetate and methoxybenzene)[274,275] can reduce the amount grain boundaries, thereby preventing the penetration of oxygen and water into the perovskite phase.[276,277] In addition, molten salt-processed perovskites exhibit high stability, which can be attributed to the presence of fewer defects at the grain boundaries and surface passivation.[266] However, the comprehensive effects of external stressors such as light, temperature, humidity, and interfacial reaction between the functional layers on the stability of PSCs need to be systematically investigated (Section 1.4.1). Since 2D or 2D/3D mixed LHPs are much more stable than 3D counterparts,[184,278] such materials prepared by novel molten salt approach may provide robust perovskite-based devices due to improving in grain boundaries.

References

(1) Perovskite companies: the comprehensive list - Perovskite-Info https://www.perovskite-info.com/companies.

(2) Li, W.; Wang, Z.; Deschler, F.; Gao, S.; Friend, R. H.; Cheetham, A. K. Chemically Diverse and Multifunctional Hybrid Organic-Inorganic Perovskites. *Nat. Rev. Mater.* **2017**, *2* (3). https://doi.org/10.1038/natrevmats.2016.99.

(3) Sharp, B. T.; Percy, W. Bridgmanite - Named at Last. *Science (80-.).* **2014**, *346* (6213), 1057–1058.

(4) Filip, M. R.; Giustino, F. The Geometric Blueprint of Perovskites. *PNAS* **2018**, *115* (21), 5397–5402. https://doi.org/10.1073/pnas.1719179115.

(5) Tilley, R. J. D. *The ABX3 Perovskite Structure*; John Wiley & Sons, Ltd, 2016. https://doi.org/10.1002/9781118935651.CH1.

(6) Travis, W.; Glover, E. N. K.; Bronstein, H.; Scanlon, D. O.; Palgrave, R. G. On the Application of the Tolerance Factor to Inorganic and Hybrid Halide Perovskites: A Revised System. *Chem. Sci.* **2016**, *7*, 4548–4556. https://doi.org/10.1039/c5sc04845a.

(7) Li, C.; Lu, X.; Ding, W.; Feng, L.; Gao, Y.; Guo, Z. Formability of ABX3 (X = F, Cl, Br, I) Halide Perovskites. *Acta Crystallogr. Sect. B* **2008**, *64* (6), 702–707. https://doi.org/10.1107/S0108768108032734.

(8) Bartel, C. J.; Sutton, C.; Goldsmith, B. R.; Ouyang, R.; Musgrave, C. B.; Ghiringhelli, L. M.; Scheffler, M. New Tolerance Factor to Predict the Stability of Perovskite Oxides and Halides. *Sci. Adv.* **2019**, *5* (eaav0693).

(9) Hwang, J.; Rao, R. R.; Giordano, L.; Katayama, Y.; Yu, Y.; Shao-Horn, Y. Perovskites in Catalysis and Electrocatalysis. *Science (80-.).* **2017**, *358*, 751–756.

(10) Kim, J. Y.; Lee, J. W.; Jung, H. S.; Shin, H.; Park, N. G. High-Efficiency Perovskite Solar Cells. *Chem. Rev.* **2020**, *120*, 7867–7918. https://doi.org/10.1021/acs.chemrev.0c00107.

(11) Zhang, K.; Zhu, N.; Zhang, M.; Wang, L.; Xing, J. Opportunities and Challenges in Perovskite LED Commercialization. *J. Mater. Chem. C* **2021**, *9* (11), 3795–3799. https://doi.org/10.1039/d1tc00232e.

(12) Pan, S.; Li, J.; Wen, Z.; Lu, R.; Zhang, Q.; Jin, H.; Zhang, L.; Chen, Y.; Wang, S. Halide Perovskite Materials for Photo (Electro) Chemical Applications: Dimensionality, Heterojunction, and Performance. *Adv. Energy Mater.* **2021**, No. 2004002, 1–38. https://doi.org/10.1002/aenm.202004002.

(13) Miao, J.; Zhang, F. Recent Progress on Highly Sensitive Perovskite Photodetectors. *J. Mater. Chem. C* **2019**, *7* (7), 1741–1791. https://doi.org/10.1039/C8TC06089D.

(14) Paulus, F.; Tyznik, C.; Jurchescu, O. D.; Vaynzof, Y. Switched-On: Progress, Challenges, and Opportunities in Metal Halide Perovskite Transistors. *Adv. Funct. Mater.* **2021**, No. 2101029. https://doi.org/10.1002/adfm.202101029.

(15) Lei, L.; Dong, Q.; Gundogdu, K.; So, F. Metal Halide Perovskites for Laser Applications. *Adv. Funct. Mater.* **2021**, *31* (16). https://doi.org/10.1002/ADFM.202010144.

(16) Shi, E.; Gao, Y.; Finkenauer, B. P.; Akriti, A.; Coffey, A. H.; Dou, L. Two-Dimensional Halide Perovskite Nanomaterials and Heterostructures. *Chem. Soc. Rev.* **2018**, *47* (16), 6046–6072. https://doi.org/10.1039/c7cs00886d.

(17) Saparov, B.; Mitzi, D. B. Organic-Inorganic Perovskites: Structural Versatility for Functional Materials Design. *Chemical Reviews*. 2016, pp 4558–4596. https://doi.org/10.1021/acs.chemrev.5b00715.

(18) Kim, H. B.; Yoon, Y. J.; Jeong, J.; Heo, J.; Jang, H.; Seo, J. H.; Walker, B.; Kim, J. Y. Peroptronic Devices: Perovskite-Based Light-Emitting Solar Cells. *Energy Environ. Sci.* **2017**, *10* (9), 1950–1957. https://doi.org/10.1039/c7ee01666b.

(19) Huang, H.; Bodnarchuk, M. I.; Kershaw, S. V.; Kovalenko, M. V.; Rogach, A. L. Lead Halide Perovskite Nanocrystals in the Research Spotlight: Stability and Defect Tolerance. *ACS Energy Lett.* **2017**, *2* (9), 2071–2083. https://doi.org/10.1021/acsenergylett.7b00547.

(20) Manser, J. S.; Christians, J. A.; Kamat, P. V. Intriguing Optoelectronic Properties of Metal Halide Perovskites. *Chem. Rev.* **2016**, *116* (21), 12956–13008.

https://doi.org/10.1021/acs.chemrev.6b00136.
(21) De Wolf, S.; Holovsky, J.; Moon, S.-J.; Lö, P.; Niesen, B.; Ledinsky, M.; Haug, F.-J.; Yum, J.-H.; Ballif, C. Organometallic Halide Perovskites: Sharp Optical Absorption Edge and Its Relation to Photovoltaic Performance. *J. Phys. Chem. Lett.* **2014**, *5*, 1035–1039. https://doi.org/10.1021/jz500279b.
(22) Xiao, Z.; Song, Z.; Yan, Y. From Lead Halide Perovskites to Lead-Free Metal Halide Perovskites and Perovskite Derivatives. *Adv. Mater.* **2019**, *31* (47), 1–22. https://doi.org/10.1002/adma.201803792.
(23) Wan-Jian Yin, S.; Wei, S.-H.; Yin, W.-J.; Ji-Hui Yang, A.; Kang, J.; Yan, Y. Halide Perovskite Materials for Solar Cells: A Theoretical Review. *J. Mater. Chem. A* **2015**, *3*, 8926–8942. https://doi.org/10.1039/c4ta05033a.
(24) Unger, E. L.; Kegelmann, L.; Suchan, K.; Sörell, D.; Korte, L.; Albrecht, S. Roadmap and Roadblocks for the Band Gap Tunability of Metal Halide Perovskites. *J. Mater. Chem. A* **2017**, *5* (23), 11401–11409. https://doi.org/10.1039/c7ta00404d.
(25) Sutherland, B. R.; Sargent, E. H. Perovskite Photonic Sources. *Nat. Photonics* **2016**, *10* (5), 295–302. https://doi.org/10.1038/nphoton.2016.62.
(26) NREL Best Research-Cell Efficiency Chart https://www.nrel.gov/pv/assets/pdfs/best-research-cell-efficiencies.20200104.pdf.
(27) Saliba, M.; Correa-Baena, J.-P.; Grätzel, M.; Hagfeldt, A.; Abate, A. Perovskite Solar Cells: From the Atomic Level to Film Quality and Device Performance. *Angew. Chemie Int. Ed.* **2018**, *57* (10), 2554–2569. https://doi.org/10.1002/anie.201703226.
(28) Zhou, Y.; Zhao, Y. Chemical Stability and Instability of Inorganic Halide Perovskites. *Energy Environ. Sci.* **2019**, *12* (5), 1495–1511. https://doi.org/10.1039/c8ee03559h.
(29) Protesescu, L.; Yakunin, S.; Bodnarchuk, M. I.; Krieg, F.; Caputo, R.; Hendon, C. H.; Yang, R. X.; Walsh, A.; Kovalenko, M. V. Nanocrystals of Cesium Lead Halide Perovskites (CsPbX3, X = Cl, Br, and I): Novel Optoelectronic Materials Showing Bright Emission with Wide Color Gamut. *Nano Lett.* **2015**, *15* (6), 3692–3696. https://doi.org/10.1021/nl5048779.
(30) Vinichenko, D.; Sensoy, M. G.; Friend, C. M.; Kaxiras, E. Accurate Formation Energies of Charged Defects in Solids: A Systematic Approach. *Phys. Rev. B* **2017**, *95* (23). https://doi.org/10.1103/PhysRevB.95.235310.
(31) Jin, H.; Debroye, E.; Keshavarz, M.; Scheblykin, I. G.; Roeffaers, M. B. J.; Hofkens, J.; Steele, J. A. It's a Trap! On the Nature of Localised States and Charge Trapping in Lead Halide Perovskites. *Mater. Horizons* **2020**, *7* (2), 397–410. https://doi.org/10.1039/c9mh00500e.
(32) Yu, Y.; Zhang, F.; Yu, H. Self-Healing Perovskite Solar Cells. *Sol. Energy* **2020**, *209* (September), 408–414. https://doi.org/10.1016/j.solener.2020.09.018.
(33) Guo, Y.; Yin, X.; Liu, D.; Liu, J.; Zhang, C.; Xie, H.; Yang, Y.; Que, W. Photoinduced Self-Healing of Halide Segregation in Mixed-Halide Perovskites. *ACS Energy Lett.* **2021**, 2502–2511. https://doi.org/10.1021/acsenergylett.1c01040.
(34) Zhang, W.; Eperon, G. E.; Snaith, H. J. Metal Halide Perovskites for Energy Applications. *Nat. Energy* **2016**, No. May. https://doi.org/10.1038/NENERGY.2016.48.
(35) Chen, K.; Schünemann, S.; Song, S.; Tüysüz, H. Structural Effects on Optoelectronic Properties of Halide Perovskites. *Chem. Soc. Rev.* **2018**, *47* (18), 7045–7077. https://doi.org/10.1039/c8cs00212f.
(36) Wang, K.; Xing, G.; Song, Q.; Xiao, S. Micro- and Nanostructured Lead Halide Perovskites: From Materials to Integrations and Devices. *Adv. Mater.* **2020**, 2000306. https://doi.org/10.1002/adma.202000306.
(37) Weber, S. A. L.; Hermes, I. M.; Turren-Cruz, S. H.; Gort, C.; Bergmann, V. W.; Gilson, L.; Hagfeldt, A.; Graetzel, M.; Tress, W.; Berger, R. How the Formation of Interfacial Charge Causes Hysteresis in Perovskite Solar Cells. *Energy Environ. Sci.* **2018**, *11* (9), 2404–2413. https://doi.org/10.1039/c8ee01447g.
(38) Dequilettes, D. W.; Frohna, K.; Emin, D.; Kirchartz, T.; Bulovic, V.; Ginger, D. S.; Stranks, S. D. Charge-Carrier Recombination in Halide Perovskites. *Chem. Rev.* **2019**, *119* (20), 11007–11019. https://doi.org/10.1021/acs.chemrev.9b00169.
(39) Castro-Méndez, A. F.; Hidalgo, J.; Correa-Baena, J. P. The Role of Grain Boundaries in Perovskite Solar Cells. *Adv. Energy Mater.* **2019**, *9* (38), 1901489–1901498. https://doi.org/10.1002/aenm.201901489.

(40) Wang, Q.; Chen, B.; Liu, Y.; Deng, Y.; Bai, Y.; Dong, Q.; Huang, J. Scaling Behavior of Moisture-Induced Grain Degradation in Polycrystalline Hybrid Perovskite Thin Films. *Energy Environ. Sci* **2017**, *10*, 516–522. https://doi.org/10.1039/c6ee02941h.

(41) Mino, L.; Agostini, G.; Borfecchia, E.; Gianolio, D.; Piovano, A.; Gallo, E.; Lamberti, C. Low-Dimensional Systems Investigated by x-Ray Absorption Spectroscopy: A Selection of 2D, 1D and 0D Cases. *J. Phys. D. Appl. Phys.* **2013**, *46* (42). https://doi.org/10.1088/0022-3727/46/42/423001.

(42) Pelayo García De Arquer, F.; Talapin, D. V; Klimov, V. I.; Arakawa, Y.; Bayer, M.; Sargent, E. H. Semiconductor Quantum Dots: Technological Progress and Future Challenges. *Science (80-.).* **2021**, *373*, 640–655. https://doi.org/10.1126/science.aaz8541.

(43) Nedelcu, G.; Protesescu, L.; Yakunin, S.; Bodnarchuk, M. I.; Grotevent, M. J.; Kovalenko, M. V. Fast Anion-Exchange in Highly Luminescent Nanocrystals of Cesium Lead Halide Perovskites (CsPbX3, X = Cl, Br, I). *Nano Lett.* **2015**, *15* (8), 5635–5640. https://doi.org/10.1021/acs.nanolett.5b02404.

(44) Yuan, J.; Hazarika, A.; Zhao, Q.; Ling, X.; Moot, T.; Ma, W.; Luther, J. M. Metal Halide Perovskites in Quantum Dot Solar Cells: Progress and Prospects. *Joule* **2020**, *4*, 1–26. https://doi.org/10.1016/j.joule.2020.04.006.

(45) Shamsi, J.; Urban, A. S.; Imran, M.; De Trizio, L.; Manna, L. Metal Halide Perovskite Nanocrystals: Synthesis, Post-Synthesis Modifications, and Their Optical Properties. *Chem. Rev.* **2019**, *119* (5), 3296–3348. https://doi.org/10.1021/acs.chemrev.8b00644.

(46) Wang, S.; Yousefi Amin, A. A.; Wu, L.; Cao, M.; Zhang, Q.; Ameri, T. Perovskite Nanocrystals: Synthesis, Stability, and Optoelectronic Applications. *Small Struct.* **2021**, *2* (3), 2000124. https://doi.org/10.1002/sstr.202000124.

(47) Hong, K.; Le, Q. Van; Kim, S. Y.; Jang, H. W. Low-Dimensional Halide Perovskites: Review and Issues. *J. Mater. Chem. C* **2018**, *6* (9), 2189–2209. https://doi.org/10.1039/c7tc05658c.

(48) Hills-Kimball, K.; Yang, H.; Cai, T.; Wang, J.; Chen, O. Recent Advances in Ligand Design and Engineering in Lead Halide Perovskite Nanocrystals. *Adv. Sci.* **2021**, *8*, 2100214–2100258. https://doi.org/10.1002/advs.202100214.

(49) Protesescu, L.; Yakunin, S.; Bodnarchuk, M. I.; Krieg, F.; Caputo, R.; Hendon, C. H.; Yang, R. X.; Walsh, A.; Kovalenko, M. V. Nanocrystals of Cesium Lead Halide Perovskites (CsPbX3): Novel Optoelectronic Materials Showing Bright Emission with Wide Color Gamut. *Nano Lett.* **2015**, *15*, 3692–3696. https://doi.org/10.1021/nl5048779.

(50) Pan, A.; He, B.; Fan, X.; Liu, Z.; Urban, J. J.; Alivisatos, A. P.; He, L.; Liu, Y. Insight into the Ligand-Mediated Synthesis of Colloidal CsPbBr3 Perovskite Nanocrystals: The Role of Organic Acid, Base, and Cesium Precursors. *ACS Nano* **2016**, *10* (8), 7943–7954. https://doi.org/10.1021/acsnano.6b03863.

(51) Gualdrón-Reyes, A. F.; Masi, S.; Mora-Seró, I. Progress in Halide-Perovskite Nanocrystals with near-Unity Photoluminescence Quantum Yield. *Trends Chem.* **2021**, *3* (6), 499–511. https://doi.org/10.1016/J.TRECHM.2021.03.005.

(52) Schmidt, L. C.; Pertegás, A.; Gonzalez-carrero, S.; Malinkiewicz, O.; Agouram, S.; Espallargas, G. M.; Bolink, H. J.; Galian, R. E.; Pérez-prieto, J.; González-carrero, S. Non-Template Synthesis of CH3NH3PbBr3 Perovskite Nanoparticles Non-Template Synthesis of CH 3 NH 3 PbBr 3 Perovskite Nanoparticles. *J. Am. Chem. Soc.* **2014**, *136*, 850−853.

(53) Zhang, F.; Zhong, H.; Chen, C.; Wu, X. G.; Hu, X.; Huang, H.; Han, J.; Zou, B.; Dong, Y. Brightly Luminescent and Color-Tunable Colloidal CH3NH3PbX3 (X = Br, I, Cl) Quantum Dots: Potential Alternatives for Display Technology. *ACS Nano* **2015**, *9* (4), 4533–4542. https://doi.org/10.1021/acsnano.5b01154.

(54) Sun, S.; Yuan, D.; Xu, Y.; Wang, A.; Deng, Z. Ligand-Mediated Synthesis of Shape-Controlled Cesium Lead Halide Perovskite Nanocrystals via Reprecipitation Process at Room Temperature. *ACS Nano* **2016**, *10* (3), 3648–3657. https://doi.org/10.1021/acsnano.5b08193.

(55) Jang, D. M.; Kim, D. H.; Park, K.; Park, J.; Lee, J. W.; Song, J. K. Ultrasound Synthesis of Lead Halide Perovskite Nanocrystals. *J. Mater. Chem. C* **2016**, *4* (45), 10625–10629. https://doi.org/10.1039/c6tc04213a.

(56) Rao, L.; Ding, X.; Du, X.; Liang, G.; Tang, Y.; Tang, K.; Zhang, J. Z. Ultrasonication-Assisted Synthesis of CsPbBr3 and Cs4PbBr6 Perovskite Nanocrystals and Their Reversible Transformation. *Beilstein J.*

Nanotechnol **2019**, *10*, 666–676. https://doi.org/10.3762/bjnano.10.66.

(57) Tong, Y.; Bladt, E.; Aygüler, M. F.; Manzi, A.; Milowska, K. Z.; Hintermayr, V. A.; Docampo, P.; Bals, S.; Urban, A. S.; Polavarapu, L.; et al. Highly Luminescent Cesium Lead Halide Perovskite Nanocrystals with Tunable Composition and Thickness by Ultrasonication. *Angew. Chemie - Int. Ed.* **2016**, *55* (44), 13887–13892. https://doi.org/10.1002/anie.201605909.

(58) Huang, H.; Xue, Q.; Chen, B.; Xiong, Y.; Schneider, J.; Zhi, C.; Zhong, H.; Rogach, A. L. Top-Down Fabrication of Stable Methylammonium Lead Halide Perovskite Nanocrystals by Employing a Mixture of Ligands as Coordinating Solvents. *Angewandte Chemie - International Edition*. 2017, pp 9571–9576. https://doi.org/10.1002/anie.201705595.

(59) Naphade, R.; Nagane, S.; Shanker, G. S.; Fernandes, R.; Kothari, D.; Zhou, Y.; Padture, N. P.; Ogale, S. Hybrid Perovskite Quantum Nanostructures Synthesized by Electrospray Antisolvent-Solvent Extraction and Intercalation. *ACS Appl. Mater. Interfaces* **2016**, *8* (1), 854–861. https://doi.org/10.1021/acsami.5b10208.

(60) Dai, S.; Hsu, B.; Chen, C.; Lee, C.; Liu, H.; Wang, H.; Huang, Y.; Wu, T.; Manikandan, A. Perovskite Quantum Dots with Near Unity Solution and Neat-Film Photoluminescent Quantum Yield by Novel Spray Synthesis. *Adv. Mater.* **2018**, *30*, 1–8. https://doi.org/10.1002/adma.201705532.

(61) Dai, S. W.; Lai, Y. L.; Yang, L.; Chuang, Y. T.; Tan, G. H.; Shen, S. W.; Huang, Y. S.; Lo, Y. C.; Yeh, T. H.; Wu, C. I.; et al. Organic Lead Halide Nanocrystals Providing an Ultra-Wide Color Gamut with Almost-Unity Photoluminescence Quantum Yield. *ACS Appl. Mater. Interfaces* **2021**. https://doi.org/10.1021/acsami.1c05961.

(62) Wang, Z.; Shi, Z.; Li, T.; Chen, Y.; Huang, W. Stability of Perovskite Solar Cells: A Prospective on the Substitution of the A Cation and X Anion. *Angew. Chemie - Int. Ed.* **2017**, *56* (5), 1190–1212. https://doi.org/10.1002/anie.201603694.

(63) Jiang, H.; Cui, S.; Chen, Y.; Zhong, H. Ion Exchange for Halide Perovskite: From Nanocrystal to Bulk Materials. *Nano Sel.* **2021**, No. February, 1–21. https://doi.org/10.1002/nano.202100084.

(64) Song, J.; Li, J.; Li, X.; Xu, L.; Dong, Y.; Zeng, H. Quantum Dot Light-Emitting Diodes Based on Inorganic Perovskite Cesium Lead Halides (CsPbX3). *Adv. Mater.* **2015**, *27* (44), 7162–7167. https://doi.org/10.1002/adma.201502567.

(65) Hazarika, A.; Zhao, Q.; Gaulding, E. A.; Christians, J. A.; Dou, B.; Marshall, A. R.; Moot, T.; Berry, J. J.; Johnson, J. C.; Luther, J. M. Perovskite Quantum Dot Photovoltaic Materials beyond the Reach of Thin Films: Full-Range Tuning of A-Site Cation Composition. *ACS Nano* **2018**, *12*. https://doi.org/10.1021/acsnano.8b05555.

(66) Suri, M.; Hazarika, A.; Larson, B. W.; Zhao, Q.; Vallés-Pelarda, M.; Siegler, T. D.; Abney, M. K.; Ferguson, A. J.; Korgel, B. A.; Luther, J. M. Enhanced Open-Circuit Voltage of Wide-Bandgap Perovskite Photovoltaics by Using Alloyed (FA1- XCsx)Pb(I1- XBrx)3 Quantum Dots. *ACS Energy Lett.* **2019**, *4* (8), 1954–1960. https://doi.org/10.1021/acsenergylett.9b01030.

(67) Gonzaíez-Pedro, V.; Veldhuis, S. A.; Begum, R.; Josébañ, M.; Uls, J.; Bruno, A.; Mathews, N.; Mhaisalkar, S.; Ngel Maquieira, A.´. Recovery of Shallow Charge-Trapping Defects in CsPbX3 Nanocrystals through Specific Binding and Encapsulation with Amino- Functionalized Silanes. *ACS Energy Lett.* **2018**, *3* (6), 1409–1414. https://doi.org/10.1021/acsenergylett.8b00498.

(68) Akkerman, Q. A.; Valerio D'innocenzo, †; Accornero, S.; Scarpellini, A.; Petrozza, A.; Prato, M.; Manna, L. Tuning the Optical Properties of Cesium Lead Halide Perovskite Nanocrystals by Anion Exchange Reactions. *JACS* **2015**. https://doi.org/10.1021/jacs.5b05602.

(69) Parobek, D.; Dong, Y.; Qiao, T.; Rossi, D.; Son, D. H. Photoinduced Anion Exchange in Cesium Lead Halide Perovskite Nanocrystals. *JACS* **2017**, *139*, 4358–4361. https://doi.org/10.1021/jacs.7b01480.

(70) Li, Z.; Yang, M.; Park, J. S.; Wei, S. H.; Berry, J. J.; Zhu, K. Stabilizing Perovskite Structures by Tuning Tolerance Factor: Formation of Formamidinium and Cesium Lead Iodide Solid-State Alloys. *Chem. Mater.* **2016**, *28* (1), 284–292. https://doi.org/10.1021/acs.chemmater.5b04107.

(71) Eperon, G. E.; Ginger, D. S. B-Site Metal Cation Exchange in Halide Perovskites. *ACS Energy Lett.* **2017**, *2* (5), 1190–1196. https://doi.org/10.1021/acsenergylett.7b00290.

(72) Van Der Stam, W.; Geuchies, J. J.; Altantzis, T.; Van Den Bos, K. H. W.; Meeldijk, J. D.; Aert, S. Van; Bals, S.; Vanmaekelbergh, D.; De Mello Donega, C. Highly Emissive Divalent-Ion-Doped Colloidal CsPb1−xMxBr3 Perovskite Nanocrystals through Cation Exchange. *JACS* **2017**, *139* (11), 4087–4097.

https://doi.org/10.1021/jacs.6b13079.
(73) Soto-Montero, T.; Soltanpoor, W.; Morales-Masis, M. Pressing Challenges of Halide Perovskite Thin Film Growth. *APL Mater.* **2020**, *8* (11). https://doi.org/10.1063/5.0027573.
(74) Chouhan, L.; Ghimire, S.; Subrahmanyam, C.; Miyasaka, T.; Biju, V. Synthesis, Optoelectronic Properties and Applications of Halide Perovskites. *Chem. Soc. Rev.* **2020**, *49* (10), 2869–2885. https://doi.org/10.1039/c9cs00848a.
(75) Roy, P.; Kumar Sinha, N.; Tiwari, S.; Khare, A. A Review on Perovskite Solar Cells: Evolution of Architecture, Fabrication Techniques, Commercialization Issues and Status. *Sol. Energy* **2020**, *198* (January), 665–688. https://doi.org/10.1016/j.solener.2020.01.080.
(76) Zheng, X.; Chen, B.; Wu, C.; Priya, S. Room Temperature Fabrication of CH3NH3PbBr3 by Anti-Solvent Assisted Crystallization Approach for Perovskite Solar Cells with Fast Response and Small J-V Hysteresis. *Nano Energy* **2015**, *17*, 269–278. https://doi.org/10.1016/j.nanoen.2015.08.023.
(77) Bodenschatz, E.; Pesch, W.; Ahlers, G. Recent Developments in Rayleigh-Bénard Convection. *Annu. Rev. Fluid Mech* **2000**, *32*, 709–778.
(78) Im, J.-H.; Kim, H.-S.; Park, N.-G. Morphology-Photovoltaic Property Correlation in Perovskite Solar Cells: One-Step versus Two-Step Deposition of CH3NH3PbI3. *APL Mater.* **2014**, *2* (81510). https://doi.org/10.1063/1.4891275.
(79) Jung, M.; Ji, S.; Kim, G. Perovskite Precursor Solution Chemistry : From Fundamentals to Photovoltaic Applications. *Chem. Soc. Rev.* **2019**. https://doi.org/10.1039/c8cs00656c.
(80) Park, N. G.; Zhu, K. Scalable Fabrication and Coating Methods for Perovskite Solar Cells and Solar Modules. *Nat. Rev. Mater.* **2020**, *5* (5), 333–350. https://doi.org/10.1038/s41578-019-0176-2.
(81) Pasquarelli, R. M.; Ginley, D. S.; O'hayre, R. Solution Processing of Transparent Conductors: From Flask to Film. *Chem. Soc. Rev.* **2011**, *40*, 5406–5441. https://doi.org/10.1039/c1cs15065k.
(82) Swartwout, R.; Hoerantner, M. T.; Bulović, V. Scalable Deposition Methods for Large-Area Production of Perovskite Thin Films. *Energy Environ. Mater.* **2019**, *2* (2), 119–145. https://doi.org/10.1002/EEM2.12043.
(83) Li, Z.; Klein, T. R.; Kim, D. H.; Yang, M.; Berry, J. J.; Van Hest, M. F. A. M.; Zhu, K. Scalable Fabrication of Perovskite Solar Cells. *Nat. Rev. Mater.* **2018**, *3*, 1–20. https://doi.org/10.1038/natrevmats.2018.17.
(84) Lai, Y.; Lin, Z.; Saki, Z.; Byranvand, M. M.; Taghavinia, N.; Kedia, M.; Saliba, M. Solution-Processed Perovskite Thin-Films: The Journey from Lab-to Large-Scale Solar Cells. *Energy Environ. Sci* **2021**. https://doi.org/10.1039/D1EE02018H.
(85) Wu, R.; Wang, C.; Jiang, M.; Liu, C.; Liu, D.; Li, S.; Kong, Q.; He, W.; Zhan, C.; Zhang, F.; et al. Progress in Blade-Coating Method for Perovskite Solar Cells toward Commercialization. *Renew. Sustain. Energy* **2021**, *13* (012701). https://doi.org/10.1063/5.0037307.
(86) Patidar, R.; Burkitt, D.; Hooper, K.; Richards, D.; Watson, T. Slot-Die Coating of Perovskite Solar Cells: An Overview. *Mater. Today Commun.* **2020**, *22* (September 2019), 100808. https://doi.org/10.1016/j.mtcomm.2019.100808.
(87) Bishop, J. E.; Routledge, T. J.; Lidzey, D. G. Advances in Spray-Cast Perovskite Solar Cells. *J. Phys. Chem. Lett.* **2018**, *9* (8), 1977–1984. https://doi.org/10.1021/acs.jpclett.8b00311.
(88) Bishop, J. E. Development and Optimisation of Efficient Spray-Coated Perovskite Solar Cells, 2019.
(89) Mathies, F.; List-Kratochvil, E. J. W.; Unger, E. L. Advances in Inkjet-Printed Metal Halide Perovskite Photovoltaic and Optoelectronic Devices. *Energy Technol.* **2019**, *8* (1900991). https://doi.org/10.1002/ente.201900991.
(90) Meroni, S. M. P.; Hooper, K. E. A.; Dunlop, T.; Baker, J. A.; Worsley, D.; Charbonneau, C.; Watson, T. M. Scribing Method for Carbon Perovskite Solar Modules. *Energies* **2020**, *13*, 1589–1604. https://doi.org/10.3390/en13071589.
(91) Kim, H.; Han, J. S.; Choi, J.; Kim, S. Y.; Jang, H. W. Halide Perovskites for Applications beyond Photovoltaics. *Small Methods* **2018**, *2* (3), 1700310. https://doi.org/10.1002/smtd.201700310.
(92) Rajagopal, A.; Yao, K.; Jen, A. K.-Y. Toward Perovskite Solar Cell Commercialization: A Perspective and Research Roadmap Based on Interfacial Engineering. *Adv. Mater.* **2018**, *30* (32), 1800455. https://doi.org/10.1002/adma.201800455.
(93) Kovalenko, M. V.; Protesescu, L.; Bodnarchuk, M. I. Properties and Potential Optoelectronic

Applications of Lead Halide Perovskite Nanocrystals. *Science (80-.).* **2017**, *358* (6364), 745–750. https://doi.org/10.1126/science.aam7093.

(94) Zhao, Y.; Wang, C.; Hu, X.; Fan, J. Recent Progress in CsPbX3 Perovskite Nanocrystals for Enhanced Stability and Photocatalytic Applications. *ChemNanoMat* **2021**. https://doi.org/10.1002/cnma.202100094.

(95) Deng, J.; Li, J.; Yang, Z.; Wang, M. All-Inorganic Lead Halide Perovskites: A Promising Choice for Photovoltaics and Detectors. *J. Mater. Chem. C* **2019**, *7* (40), 12415–12440. https://doi.org/10.1039/c9tc04164h.

(96) Senanayak, S. P.; Abdi-Jalebi, M.; Kamboj, V. S.; Carey, R.; Shivanna, R.; Tian, T.; Schweicher, G.; Wang, J.; Giesbrecht, N.; Nuzzo, D. Di; et al. A General Approach for Hysteresis-Free, Operationally Stable Metal Halide Perovskite Field-Effect Transistors. *Science (80-.).* **2020**, *6* (15).

(97) Hu, Z.; Liu, Z.; Zhan, Z.; Shi, T.; Du, J.; Tang, X.; Leng, Y. Advances in Metal Halide Perovskite Lasers: Synthetic Strategies, Morphology Control, and Lasing Emission. *Adv. Photonics* **2021**, *3* (03), 1–23. https://doi.org/10.1117/1.ap.3.3.034002.

(98) Jung, J. H.; Kim, S. H.; Park, Y.; Lee, D.; Lee, J. S. Metal-Halide Perovskite Design for Next-Generation Memories: First-Principles Screening and Experimental Verification. *Adv. Sci.* **2020**, *7* (16), 1–8. https://doi.org/10.1002/advs.202001367.

(99) Kostopoulou, A.; Vernardou, D.; Makri, D.; Brintakis, K.; Savva, K.; Stratakis, E. Highly Stable Metal Halide Perovskite Microcube Anodes for Lithium-Air Batteries. *J. Power Sources Adv.* **2020**, *3* (June), 100015. https://doi.org/10.1016/j.powera.2020.100015.

(100) Huang, Y.; Feng, Y.; Li, F.; Lin, F.; Wang, Y.; Chen, X.; Xie, R. Sensing Studies and Applications Based on Metal Halide Perovskite Materials: Current Advances and Future Perspectives. *Trends Anal. Chem.* **2021**, *134* (116127). https://doi.org/10.1016/j.trac.2020.116127.

(101) Mora-Seró, I. How Do Perovskite Solar Cells Work? *Joule* **2018**, *2* (4), 585–587. https://doi.org/10.1016/j.joule.2018.03.020.

(102) Kirchartz, T.; Bisquert, J.; Mora-Sero, I.; Garcia-Belmonte, G. Classification of Solar Cells According to Mechanisms of Charge Separation and Charge Collection. *Phys. Chem. Chem. Phys.* **2015**, *17* (6), 4007–4014. https://doi.org/10.1039/c4cp05174b.

(103) Bisquert, J. *The Physics of Solar Cells - Perovskites, Organics, and Photovoltaic Fundamentals*; 2017. https://doi.org/10.1063/1.326636.

(104) Pichot, F.; Gregg, B. A. The Photovoltage-Determining Mechanism in Dye-Sensitized Solar Cells. *J. Phys. Chem. B* **2000**, *104* (1), 6–10. https://doi.org/10.1021/jp993035y.

(105) Snaith, H. J. Perovskites: The Emergence of a New Era for Low-Cost, High-Efficiency Solar Cells. *J. Phys. Chem. Lett.* **2013**, *4*, 3623−3630. https://doi.org/10.1021/jz4020162.

(106) Pan, H.; Shao, H.; Zhang, X. L.; Shen, Y.; Wang, M. Interface Engineering for High-Efficiency Perovskite Solar Cells. *J. Appl. Phys.* **2021**, *129* (13), 130904–130913. https://doi.org/10.1063/5.0038073.

(107) Will, J.; Hou, Y.; Scheiner, S.; Pinkert, U.; Hermes, I. M.; Weber, S. A. L.; Hirsch, A.; Halik, M.; Brabec, C.; Unruh, T. Evidence of Tailoring the Interfacial Chemical Composition in Normal Structure Hybrid Organohalide Perovskites by a Self-Assembled Monolayer. *ACS Appl. Mater. Interfaces* **2018**, *10*, 5511–5518. https://doi.org/10.1021/acsami.7b15904.

(108) Ravishankar, S.; Gharibzadeh, S.; Roldán-Carmona, C.; Grancini, G.; Lee, Y.; Ralaiarisoa, M.; Asiri, A. M.; Koch, N.; Bisquert, J.; Nazeeruddin, M. K. Influence of Charge Transport Layers on Open-Circuit Voltage and Hysteresis in Perovskite Solar Cells. *Joule* **2018**, *2* (4), 788–798. https://doi.org/10.1016/j.joule.2018.02.013.

(109) Nayak, P. K.; Mahesh, S.; Snaith, H. J.; Cahen, D. Photovoltaic Solar Cell Technologies: Analysing the State of the Art. *Nat. Rev. Mater.* **2019**, *4* (4), 269–285. https://doi.org/10.1038/s41578-019-0097-0.

(110) Qiu, F.; Chu, J.; Liu, Z.; Xiang, J.; Yang, J.; Wang, C. Insight into the Origins of Figures of Merit and Design Strategies for Organic/Inorganic Lead-Halide Perovskite Solar Cells. *Sol. RRL* **2020**, *4*, 2000452–2000480. https://doi.org/10.1002/SOLR.202000452.

(111) Kitai, A. *Principles of Solar Cells, Principles of Solar Cells, LEDs and Related Devices - The Role of the PN Junction*, 2nd Editio.; Wiley, Ed.; 2019.

(112) Solar Cells: A Guide to Theory and Measurement - Ossila https://www.ossila.com/pages/solar-cells-

theory.
(113) Paranthaman, M. P.; Wong-Ng, W.; Bhattacharya, R. N. *Semiconductor Materials for Solar Photovoltaic Cells*; Springer, Ed.; 2016. https://doi.org/10.1007/978-3-319-20331-7.
(114) Chen, C.; Song, H.; Chen, C. Photon Management to Reduce Energy Loss in Perovskite Solar Cells. *Chem. Soc. Rev.* **2021**. https://doi.org/10.1039/d0cs01488e.
(115) Li, D.; Song, L.; Chen, Y.; Huang, W. Modeling Thin Film Solar Cells: From Organic to Perovskite. *Adv. Sci.* **2019**, *1901397*. https://doi.org/10.1002/advs.201901397.
(116) Commercialization, C. Strategies for High-Performance Large-Area Perovskite Solar Cells toward Commercialization. *Crystals* **2021**, *11* (295). https://doi.org/doi.org/10.3390/cryst11030295.
(117) Jeon, N. J.; Noh, H.; Yang, W. S.; Kim, Y. C.; Ryu, S.; Seo, J.; Seok, S. Il. Compositional Engineering of Perovskite Materials for High-Performance Solar Cells. *Nature* **2014**, *517*, 476–480. https://doi.org/10.1038/nature14133.
(118) Bi, D.; Yi, C.; Luo, J.; Décoppet, J.-D.; Zhang, F.; Zakeeruddin, S. M.; Li, X.; Hagfeldt, A.; Grätzel, M. Polymer-Templated Nucleation and Crystal Growth of Perovskite Films for Solar Cells with Efficiency Greater than 21%. *Nat. Energy* **2016**, *1*. https://doi.org/10.1038/NENERGY.2016.142.
(119) Yang, W. S.; Park, B.-W.; Jung, E. H.; Jeon, N. J.; Kim, Y. C.; Lee, D. U.; Shin, S. S.; Seo, J.; Kim, E. K.; Noh, J. H.; et al. Iodide Management in Formamidinium-Lead-Halide-Based Perovskite Layers for Efficient Solar Cells. *Science (80-.).* **2017**, *356* (6345), 1376–1379.
(120) Jeon, N. J.; Na, H.; Jung, E. H.; Yang, T. Y.; Lee, Y. G.; Kim, G.; Shin, H. W.; Il Seok, S.; Lee, J.; Seo, J. A Fluorene-Terminated Hole-Transporting Material for Highly Efficient and Stable Perovskite Solar Cells. *Nat. Energy* **2018**, *3* (8), 682–689. https://doi.org/10.1038/s41560-018-0200-6.
(121) Ye, J.; Byranvand, M. M.; Martínez, C. O.; Hoye, R. L. Z.; Saliba, M.; Polavarapu, L. Defect Passivation in Lead-Halide Perovskite Nanocrystals and Thin Films: Toward Efficient LEDs and Solar Cells. *Angew. Chemie - Int. Ed.* **2021**, *60*, 2–27. https://doi.org/10.1002/anie.202102360.
(122) Song, Z.; McElvany, C. L.; Phillips, A. B.; Celik, I.; Krantz, P. W.; Watthage, S. C.; Liyanage, G. K.; Apul, D.; Heben, M. J. A Technoeconomic Analysis of Perovskite Solar Module Manufacturing with Low-Cost Materials and Techniques. *Energy Environ. Sci.* **2017**, *10* (6), 1297–1305. https://doi.org/10.1039/C7EE00757D.
(123) Li, H.; Zhang, W. Perovskite Tandem Solar Cells: From Fundamentals to Commercial Deployment. *Chem. Rev.* **2020**, *120* (18), 9835–9950. https://doi.org/10.1021/acs.chemrev.9b00780.
(124) Jäger, K.; Sutter, J.; Hammerschmidt, M.; Schneider, P. I.; Becker, C. Prospects of Light Management in Perovskite/Silicon Tandem Solar Cells. *Nanophotonics* **2021**, *1599*. https://doi.org/10.1515/nanoph-2020-0674.
(125) Werner, J.; Niesen, B.; Ballif, C. Perovskite/Silicon Tandem Solar Cells: Marriage of Convenience or True Love Story? – An Overview. *Adv. Mater. Interfaces* **2018**, *5* (1), 1700731–1700749. https://doi.org/10.1002/admi.201700731.
(126) Essig, S.; Allebé, C.; Remo, T.; Geisz, J. F.; Steiner, M. A.; Horowitz, K.; Barraud, L.; Ward, J. S.; Schnabel, M.; Descoeudres, A.; et al. Raising the One-Sun Conversion Eeciency of III-V/Si Solar Cells to 32.8% for Two Junctions and 35.9% for Three Junctions. *Nano Energy* **2017**, *10* (710). https://doi.org/10.1038/nenergy.2017.144.
(127) Correa-Baena, J.-P.; Abate, A.; Saliba, M.; Tress, W.; Jacobsson, T. J.; Grätzel, M.; Hagfeldt, A. The Rapid Evolution of Highly Efficient Perovskite Solar Cells. *Energy Environ. Sci.* **2017**, *10* (3), 710–727. https://doi.org/10.1039/C6EE03397K.
(128) Al-Ashouri, A.; Köhnen, E.; Li, B.; Magomedov, A.; Hempel, H.; Caprioglio, P.; Márquez, J. A.; Belen, A.; Vilches, M.; Kasparavicius, E.; et al. Monolithic Perovskite/Silicon Tandem Solar Cell with >29% Efficiency by Enhanced Hole Extraction. *Science (80-.).* **2020**, *370*, 1300–1309.
(129) Tress, W. Perovskite Solar Cells on the Way to Their Radiative Efficiency Limit – Insights Into a Success Story of High Open-Circuit Voltage and Low Recombination. *Adv. Energy Mater.* **2017**, *7* (14), 1602358–1602375. https://doi.org/10.1002/AENM.201602358.
(130) Stranks, S. D.; Eperon, G. E.; Grancini, G.; Menelaou, C.; Alcocer, M. J. P.; Leijtens, T.; Herz, L. M.; Petrozza, A.; Snaith, H. J. Electron-Hole Diffusion Lengths Exceeding 1 Micrometer in an Organometal Trihalide Perovskite Absorber. *Science (80-.).* **2013**, *342*.
(131) Pazos-Outón, L. M.; Szumilo, M.; Lamboll, R.; Richter, J. M.; Crespo-Quesada, M.; Abdi-Jalebi, M.;

Beeson, H. J.; Vrućinić, M.; Alsari, M.; Snaith, H. J.; et al. Photon Recycling in Lead Iodide Perovskite Solar Cells. *Science (80-.).* **2016**, *351* (6280), 1430–1433. https://doi.org/10.1126/science.aaf1168.

(132) Monteiro Lunardi, M.; Wing Yi Ho-Baillie, A.; Alvarez-Gaitan, J. P.; Moore, S.; Corkish, R. A Life Cycle Assessment of Perovskite/Silicon Tandem Solar Cells. *Prog. Photovoltaics Res. Appl.* **2017**, *25* (8), 679–695. https://doi.org/10.1002/PIP.2877.

(133) Sarialtin, H.; Geyer, R.; Zafer, C. Life Cycle Assessment of Hole Transport Free Planar-Mesoscopic Perovskite Solar Cells. *J. Renew. Sustain. Energy* **2020**, *12*, 23502. https://doi.org/10.1063/1.5129784.

(134) Vaynzof, Y. The Future of Perovskite Photovoltaics - Thermal Evaporation or Solution Processing? *Adv. Energy Mater.* **2020**, *10* (48). https://doi.org/10.1002/aenm.202003073.

(135) Kim, C. U.; Jung, E. D.; Noh, Y. W.; Seo, S. K.; Choi, Y.; Park, H.; Song, M. H.; Choi, K. J. Strategy for Large-scale Monolithic Perovskite /Silicon Tandem Solar Cell: A Review of Recent Progress. *EcoMat* **2021**, No. December 2020, 1–19. https://doi.org/10.1002/eom2.12084.

(136) Hou, Y.; Aydin, E.; Bastiani, M. De; Xiao, C.; Isikgor, F. H.; Xue, D.; Baek, S.; Huang, Z.; Wei, M.; Dong, Y.; et al. Efficient Tandem Solar Cells with Solution-Processed Perovskite on Textured Crystalline Silicon. *Science (80-.).* **2020**, *367* (6482), 1135–1140.

(137) Chen, B.; Yu, Z. J.; Manzoor, S.; Holman, Z. C.; Chen, B.; Yu, Z. J.; Manzoor, S.; Wang, S.; Weigand, W.; Yu, Z. Blade-Coated Perovskites on Textured Silicon for 26 % -Efficient Monolithic Perovskite/Silicon Tandem Solar Cells. *Joule* **2020**, *4*, 1–15. https://doi.org/10.1016/j.joule.2020.01.008.

(138) Subbiah, A. S.; Isikgor, F. H.; Howells, C. T.; De Bastiani, M.; Liu, J.; Aydin, E.; Furlan, F.; Allen, T. G.; Xu, F.; Zhumagali, S.; et al. High-Performance Perovskite Single-Junction and Textured Perovskite/Silicon Tandem Solar Cells via Slot-Die-Coating. *ACS Energy Lett.* **2020**, *5* (9), 3034–3040. https://doi.org/10.1021/acsenergylett.0c01297.

(139) Ávila, J.; Momblona, C.; Boix, P. P.; Sessolo, M.; Bolink, H. J. Vapor-Deposited Perovskites: The Route to High-Performance Solar Cell Production? *Joule* **2017**, *1* (3), 431–442. https://doi.org/10.1016/j.joule.2017.07.014.

(140) Luo, P.; Zhou, S.; Xia, W.; Cheng, J.; Xu, C.; Lu, Y. Chemical Vapor Deposition of Perovskites for Photovoltaic Application. *Adv. Mater. Interfaces* **2017**, *4* (8). https://doi.org/10.1002/ADMI.201600970.

(141) Yeom, K. M.; Kim, S. U.; Woo, M. Y.; Noh, J. H.; Im, S. H. Recent Progress in Metal Halide Perovskite-Based Tandem Solar Cells. *Adv. Mater.* **2020**, *32* (51). https://doi.org/10.1002/adma.202002228.

(142) Almansouri, I.; Ho-Baillie, A.; Bremner, S. P.; Green, M. A. Supercharging Silicon Solar Cell Performance by Means of Multijunction Concept. *IEEE J. Photovoltaics* **2015**, *5* (3), 968–976. https://doi.org/10.1109/JPHOTOV.2015.2395140.

(143) De Bastiani, M.; Subbiah, A. S.; Aydin, E.; Isikgor, F. H.; Allen, T. G.; De Wolf, S. Recombination Junctions for Efficient Monolithic Perovskite-Based Tandem Solar Cells: Physical Principles, Properties, Processing and Prospects. *Mater. Horizons* **2020**, *7* (11), 2791–2809. https://doi.org/10.1039/d0mh00990c.

(144) Tockhorn, P.; Wagner, P.; Kegelmann, L.; Stang, J. C.; Mews, M.; Albrecht, S.; Korte, L. Three-Terminal Perovskite/Silicon Tandem Solar Cells with Top and Interdigitated Rear Contacts. *ACS Appl. Energy Mater.* **2020**, *3* (2), 1381–1392. https://doi.org/10.1021/acsaem.9b01800.

(145) Sheng, R.; Ho-Baillie, A. W. Y.; Huang, S.; Keevers, M.; Hao, X.; Jiang, L.; Cheng, Y.-B.; Green, M. A. Four-Terminal Tandem Solar Cells Using CH3NH3PbBr3 by Spectrum Splitting. *J. Phys. Chem. Lett* **2015**, *6*, 3931–3934. https://doi.org/10.1021/acs.jpclett.5b01608.

(146) Li, Y.; Hu, H.; Chen, B.; Salim, T.; Zhang, J.; Ding, J.; Yuan, N.; Lam, Y. M. Reflective Perovskite Solar Cells for Efficient Tandem Applications. *J. Mater. Chem. C* **2016**, *5* (1), 134–139. https://doi.org/10.1039/C6TC04510C.

(147) Bastiani, M. De; Mirabelli, A. J.; Hou, Y.; Gota, F.; Aydin, E.; Allen, T. G.; Troughton, J.; Subbiah, A. S.; Isikgor, F. H.; Liu, J.; et al. Efficient Bifacial Monolithic Perovskite/Silicon Tandem Solar Cells via Bandgap Engineering. *Nat. Energy* **2021**, *6*, 167–175. https://doi.org/10.1038/s41560-020-00756-8.

(148) Sahli, F.; Werner, J.; Kamino, B. A.; Bräuninger, M.; Monnard, R.; Paviet-Salomon, B.; Barraud, L.; Ding, L.; Diaz Leon, J. J.; Sacchetto, D.; et al. Fully Textured Monolithic Perovskite/Silicon Tandem Solar Cells with 25.2% Power Conversion Efficiency. *Nat. Mater.* **2018**, *17* (9), 820–826.

https://doi.org/10.1038/s41563-018-0115-4.
(149) Lee, S.; Bae, S.; Hwang, J.; Lee, W.; Lee, S.; Hyun, J. Y.; Cho, K.; Kim, S.; Heinz, F. D.; Choi, S. Bin; et al. Perovskites Fabricated on Textured Silicon Surfaces for Tandem Solar Cells. *Nat. Commun. Chem.* **2020**, No. 2020, 1–11. https://doi.org/10.1038/s42004-020-0283-4.
(150) Jošt, M.; Köhnen, E.; Morales-Vilches, A. B.; Lipovšek, B.; Jäger, K.; Macco, B.; Al-Ashouri, A.; Krč, J.; Korte, L.; Rech, B.; et al. Textured Interfaces in Monolithic Perovskite/Silicon Tandem Solar Cells: Advanced Light Management for Improved Efficiency and Energy Yield. *Energy Environ. Sci.* **2018**, *11* (12), 3511–3523. https://doi.org/10.1039/c8ee02469c.
(151) Liu, A.; Bi, C.; Guo, R.; Zhang, M.; Qu, X.; Tian, J. Electroluminescence Principle and Performance Improvement of Metal Halide Perovskite Light-Emitting Diodes. *Adv. Opt. Mater.* **2021**, No. 2002167. https://doi.org/10.1002/ADOM.202002167.
(152) Tan, Z.-K.; Moghaddam, R. S.; Lai, M. L.; Docampo, P.; Higler, R.; Deschler, F.; Price, M.; Sadhanala, A.; Pazos, L. M.; Credgington, D.; et al. Bright Light-Emitting Diodes Based on Organometal Halide Perovskite. *Nat. Nanotechnol.* **2014**, *9*, 687–692. https://doi.org/10.1038/NNANO.2014.149.
(153) Lin, K.; Xing, J.; Quan, L. N.; de Arquer, F. P. G.; Gong, X.; Lu, J.; Xie, L.; Zhao, W.; Zhang, D.; Yan, C.; et al. Perovskite Light-Emitting Diodes with External Quantum Efficiency Exceeding 20 per Cent. *Nature* **2018**, *562* (7726), 245–248. https://doi.org/10.1038/s41586-018-0575-3.
(154) Zhang, Q.; Zhang, D.; Fu, Y.; Poddar, S.; Shu, L.; Mo, X.; Fan, Z. Light Out-Coupling Management in Perovskite LEDs—What Can We Learn from the Past? *Adv. Funct. Mater.* **2020**, *2002570*, 1–22. https://doi.org/10.1002/adfm.202002570.
(155) Kar, S.; Jamaludin, N. F.; Yantara, N.; Mhaisalkar, S. G.; Leong, W. L. *Recent Advancements and Perspectives on Light Management and High Performance in Perovskite Light-Emitting Diodes*; 2021; Vol. 10. https://doi.org/10.1515/nanoph-2021-0033.
(156) Kumar Tailor, N.; Abdi-Jalebi, M.; Gupta, V.; Hu, H.; Dar, M. I.; Li, G.; Satapathi, S. Recent Progress in Morphology Optimization in Perovskite Solar Cell. *J. Mater. Chem. A* **2020**, *8*, 21356–21386. https://doi.org/10.1039/d0ta00143k.
(157) Jung, S.; Kim, J. H.; Choi, J. W.; Kang, J.-W.; Jin, S.-H.; Kang, Y.; Song, M. Enhancement of Photoluminescence Quantum Yield and Stability in CsPbBr3 Perovskite Quantum Dots by Trivalent Doping. *Nanomaterials* **2020**, *10* (710). https://doi.org/10.3390/NANO10040710.
(158) Zheng, X.; Hou, Y.; Sun, H.-T.; Mohammed, O. F.; Sargent, E. H.; Bakr, O. M. Reducing Defects in Halide Perovskite Nanocrystals for Light- Emitting Applications. *J. Phys. Chem. Lett* **2019**, *10*, 2629−2640. https://doi.org/10.1021/acs.jpclett.9b00689.
(159) Ahmed, G. H.; Yin, J.; Bakr, O. M.; Mohammed, O. F. Near-Unity Photoluminescence Quantum Yield in Inorganic Perovskite Nanocrystals by Metal-Ion Doping. *J. Chem. Phys.* **2020**, *152* (20902). https://doi.org/10.1063/1.5131807.
(160) Stranks, S. D.; Hoye, R. L. Z.; Di, D.; Friend, R. H.; Deschler, F. The Physics of Light Emission in Halide Perovskite Devices. *Adv. Mater.* **2019**, *31* (1803336). https://doi.org/10.1002/ADMA.201803336.
(161) Lehnhardt, M.; Riedl, T.; Weimann, T.; Kowalsky, W. Impact of Triplet Absorption and Triplet-Singlet Annihilation on the Dynamics of Optically Pumped Organic Solid-State Lasers. *Phys. Rev. B* **2010**, *81* (16), 165206. https://doi.org/10.1103/PhysRevB.81.165206.
(162) Baldo, M. A.; Holmes, R. J.; Forrest, S. R. Prospects for Electrically Pumped Organic Lasers. *Phys. Rev. B* **2002**, *66* (3), 035321. https://doi.org/10.1103/PhysRevB.66.035321.
(163) Zheng, K.; Zhu, Q.; Abdellah, M.; Messing, M. E.; Zhang, W.; Generalov, A.; Niu, Y.; Ribaud, L.; Canton, S. E.; Pullerits, N. Exciton Binding Energy and the Nature of Emissive States in Organometal Halide Perovskites. *J. Phys. Chem. Lett* **2015**, *6* (15), 2969–2975. https://doi.org/10.1021/acs.jpclett.5b01252.
(164) Ruben Ahumada-Lazo, Rinku Saran, Oliver Woolland, Yunpeng Jia, M.-E. K.; Antonios Kanaras, D. B. and R. J. C. Exciton Effects in Perovskite Nanocrystals. *J. Phys. Photonics* **2021**.
(165) Huang, H.; Zhao, F.; Liu, L.; Zhang, F.; Wu, X. G.; Shi, L.; Zou, B.; Pei, Q.; Zhong, H. Emulsion Synthesis of Size-Tunable CH3NH3PbBr3 Quantum Dots: An Alternative Route toward Efficient Light-Emitting Diodes. *ACS Appl. Mater. Interfaces* **2015**, *7* (51), 28128–28133. https://doi.org/10.1021/acsami.5b10373.
(166) Chiba, T.; Hayashi, Y.; Ebe, H.; Hoshi, K.; Sato, J.; Sato, S.; Pu, Y. J.; Ohisa, S.; Kido, J. Anion-Exchange

Red Perovskite Quantum Dots with Ammonium Iodine Salts for Highly Efficient Light-Emitting Devices. *Nat. Photonics* **2018**, *12* (11), 681–687. https://doi.org/10.1038/s41566-018-0260-y.

(167) Phys, A.; Wu, W.; Liang, T.; Wu, H.; Fan, B.; Zhang, Y.; Fan, J. Green – White Color Switchable Light-Emitting Devices Based on Laterally Fused Cesium Lead Bromide Perovskite Nanowires. *Appl. Phys. Lett* **2021**, *119* (033505). https://doi.org/10.1063/5.0057903.

(168) Dong, Y.; Wang, Y. K.; Yuan, F.; Johnston, A.; Liu, Y.; Ma, D.; Choi, M. J.; Chen, B.; Chekini, M.; Baek, S. W.; et al. Bipolar-Shell Resurfacing for Blue LEDs Based on Strongly Confined Perovskite Quantum Dots. *Nat. Nanotechnol.* **2020**, *15* (8), 668–674. https://doi.org/10.1038/s41565-020-0714-5.

(169) Ren, Z.; Wang, K.; Sun, X. W.; Choy, W. C. H. Strategies Toward Efficient Blue Perovskite Light-Emitting Diodes. *Adv. Funct. Mater.* **2021**, *2100516*, 1–22. https://doi.org/10.1002/adfm.202100516.

(170) Boyd, C. C.; Cheacharoen, R.; Leijtens, T.; Mcgehee, M. D. Understanding Degradation Mechanisms and Improving Stability of Perovskite Photovoltaics. *Chem. Rev.* **2018**, *119*, 3418−3451. https://doi.org/10.1021/acs.chemrev.8b00336.

(171) Peidong Su, Yu Liu, Junke Zhang, Cong Chen, Bo Yang, C. Z. & X. Z. Pb-Based Perovskite Solar Cells and the Underlying Pollution behind Clean Energy: Dynamic Leaching of Toxic Substances from Discarded Perovskite Solar Cells. *J. Phys. Chem. Lett.* **2020**, *11*, 2812–2817. https://doi.org/10.1021/acs.jpclett.0c00503.

(172) Rhee, S.; An, K.; Kang, K. T. Recent Advances and Challenges in Halide Perovskite Crystals in Optoelectronic Devices from Solar Cells to Other Applications. *Crystals* **2021**, *11* (1), 1–28. https://doi.org/10.3390/cryst11010039.

(173) Shalan, A. E. Challenges and Approaches Towards Upscaling Assembly of Hybrid Perovskite Solar Cells. *Mater. Adv.* **2020**, *1*, 292–309. https://doi.org/10.1039/d0ma00128g.

(174) Shangguan, Z.; Zheng, X.; Zhang, J.; Lin, W.; Guo, W.; Li, C.; Wu, T.; Lin, Y.; Chen, Z. The Stability of Metal Halide Perovskite Nanocrystals—a Key Issue for the Application on Quantum-Dot-Based Micro Light-Emitting Diodes Display. *Nanomaterials* **2020**, *10* (7), 1–33. https://doi.org/10.3390/nano10071375.

(175) Boyd, C. C.; Cheacharoen, R.; Leijtens, T.; McGehee, M. D. Understanding Degradation Mechanisms and Improving Stability of Perovskite Photovoltaics. *Chem. Rev.* **2019**, *119* (5), 3418–3451. https://doi.org/10.1021/acs.chemrev.8b00336.

(176) Liu, W. W.; Wu, T. H.; Liu, M. C.; Niu, W. J.; Chueh, Y. L. Recent Challenges in Perovskite Solar Cells Toward Enhanced Stability, Less Toxicity, and Large-Area Mass Production. *Adv. Mater. Interfaces* **2019**, *6* (1801758). https://doi.org/10.1002/admi.201801758.

(177) Chen, J.; Park, N. G. Materials and Methods for Interface Engineering toward Stable and Efficient Perovskite Solar Cells. *ACS Energy Lett.* **2020**, *5* (8), 2742–2786. https://doi.org/10.1021/acsenergylett.0c01240.

(178) Huang, J.; Tan, S.; Lund, P. D.; Zhou, H. Impact of H2O on Organic-Inorganic Hybrid Perovskite Solar Cells. *Energy Environ. Sci.* **2017**, *10*, 2284–2311. https://doi.org/10.1039/c7ee01674c.

(179) Christians, J. A.; Herrera, P. A. M.; Kamat, P. V. Transformation of the Excited State and Photovoltaic Efficiency of CH3NH3PbI3 Perovskite upon Controlled Exposure to Humidified Air. *JACS* **2015**, *137*, 1530−1538. https://doi.org/10.1021/ja511132a.

(180) Leijtens, T.; Hoke, E. T.; Grancini, G.; Slotcavage, D. J.; Eperon, G. E.; Ball, J. M.; De Bastiani, M.; Bowring, A. R.; Martino, N.; Wojciechowski, K.; et al. Mapping Electric Field-Induced Switchable Poling and Structural Degradation in Hybrid Lead Halide Perovskite Thin Films. *Adv. Energy Mater.* **2015**, *5* (1500962). https://doi.org/10.1002/AENM.201500962.

(181) Frost, J. M.; Butler, K. T.; Brivio, F.; Hendon, C. H.; Van Schilfgaarde, M.; Walsh, A. Atomistic Origins of High-Performance in Hybrid Halide Perovskite Solar Cells. *Nano Lett.* **2014**, *14*, 2584−2590. https://doi.org/10.1021/nl500390f.

(182) El-Mellouhi, F.; Marzouk, A.; Bentria, E. T.; Rashkeev, S. N.; Kais, S.; Alharbi, F. H. Hydrogen Bonding and Stability of Hybrid Organic–Inorganic Perovskites. *ChemSusChem* **2016**, *9* (18), 2648–2655. https://doi.org/10.1002/CSSC.201600864.

(183) Yi, C.; Luo, J.; Meloni, S.; Boziki, A.; Ashari-Astani, N.; Grä, C.; Zakeeruddin, S. M.; Rö, U.; Grä, M. Entropic Stabilization of Mixed A-Cation ABX3 Metal Halide Perovskites for High Performance

Perovskite Solar Cells. *Energy Environ. Sci.* **2016**, *9*, 656–662. https://doi.org/10.1039/c5ee03255e.
(184) Na Quan, L.; Yuan, M.; Comin, R.; Voznyy, O.; Beauregard, E. M.; Hoogland, S.; Buin, A.; Kirmani, A. R.; Zhao, K.; Amassian, A.; et al. Ligand-Stabilized Reduced-Dimensionality Perovskites. *J. Am. Chem. Soc* **2016**, *138*, 2649−2655. https://doi.org/10.1021/jacs.5b11740.
(185) Yun, J. S.; Kim, J.; Young, T.; Patterson, R. J.; Kim, D.; Seidel, J.; Lim, S.; Green, M. A.; Huang, S.; Ho-Baillie, A. Humidity-Induced Degradation via Grain Boundaries of HC(NH2)2PbI3 Planar Perovskite Solar Cells. *Adv. Funct. Mater.* **2018**, *28* (1705363). https://doi.org/10.1002/ADFM.201705363.
(186) ARoldán-Carmona, C.; Zimmermann, I.; Mosconi, E.; Lee, X.; Martineau, D.; Narbey, S.; Oswald, F.; De Angelis, F.; Graetzel, M.; Nazeeruddin, M. K. One-Year Stable Perovskite Solar Cells by 2D/3D Interface Engineering. *Nat. Commun.* **2017**, *8*, 15684–15693. https://doi.org/10.1038/ncomms15684.
(187) Koushik, D.; Verhees, W. J. H.; Kuang, Y.; Veenstra, S.; Zhang, D.; Verheijen, M. A.; Creatore, M.; Schropp, R. E. I. High-Efficiency Humidity-Stable Planar Perovskite Solar Cells Based on Atomic Layer Architecture. *Energy Environ. Sci.* **2017**, *10*, 91–100. https://doi.org/10.1039/c6ee02687g.
(188) Furkan H. Isikgor, Anand S. Subbiah, Mathan K. Eswaran, Calvyn T. Howells, Aslihan Babayigit, Michele De Bastiani, Emre Yengel, Jiang Liu, Francesco Furlan, George T. Harrison, Shynggys Zhumagali, Jafar I. Khan, Frédéric Laquai, T. D. A.; Iain McCulloch, Udo Schwingenschlögl, S. D. W. Scaling-up Perovskite Solar Cells on Hydrophobic Surfaces. *Nano Energy* **2021**, *80* (105526). https://doi.org/10.1016/j.nanoen.2020.105633.
(189) Hu, Y.; Si, S.; Mei, A.; Rong, Y.; Liu, H.; Li, X.; Han, H. Stable Large-Area (10x10 Cm2) Printable Mesoscopic Perovskite Module Exceeding 10% Efficiency. *Sol. RRL* **2017**, *1* (2), 1600019–1600025. https://doi.org/10.1002/solr.201600019.
(190) Aranda, C. A.; Caliò, L.; Salado, M. Toward Commercialization of Stable Devices: An Overview on Encapsulation of Hybrid Organic-Inorganic Perovskite Solar Cells. *Crystals* **2021**, *11* (5), 1–16. https://doi.org/10.3390/cryst11050519.
(191) Bogachuk, D.; Zouhair, S.; Wojciechowski, K.; Yang, B.; Babu, V.; Wagner, L.; Xu, B.; Lim, J.; Mastroianni, S.; Pettersson, H.; et al. Low-Temperature Carbon-Based Electrodes in Perovskite Solar Cells. *Energy Environ. Sci* **2020**, *13*, 3880–3916. https://doi.org/10.1039/d0ee02175j.
(192) Zhou, C.; Tarasov, A. B.; Goodilin, E. A.; Chen, P.; Wang, H.; Chen, Q. Recent Strategies to Improve Moisture Stability in Metal Halide Perovskites Materials and Devices. *J. Energy Chem.* **2022**, *65*, 219–235. https://doi.org/10.1016/j.jechem.2021.05.035.
(193) Wang, Z.; Lin, Q.; Wenger, B.; Greyson Christoforo, M.; Lin, Y.-H.; Klug, M. T.; Johnston, M. B.; Herz, L. M.; Snaith, H. J. High Irradiance Performance of Metal Halide Perovskites for Concentrator Photovoltaics. *Nat. Energy* **2018**, *3*, 855–861. https://doi.org/10.1038/s41560-018-0220-2.
(194) Seo, S.; Jeong, S.; Bae, C.; Park, N. G.; Shin, H. Perovskite Solar Cells with Inorganic Electron- and Hole-Transport Layers Exhibiting Long-Term (≈500 h) Stability at 85 °C under Continuous 1 Sun Illumination in Ambient Air. *Adv. Mater.* **2018**, *30* (1801010). https://doi.org/10.1002/ADMA.201801010.
(195) Yeong Kim, G.; Senocrate, A.; Yang, T.-Y.; Gregori, G.; Grätzel, M.; Maier, J. Large Tunable Photoeffect on Ion Conduction in Halide Perovskites and Implications for Photodecomposition. *Nat. Mater.* **2018**, *17*, 445–449. https://doi.org/10.1038/s41563-018-0038-0.
(196) Hoke, E. T.; Slotcavage, D. J.; Dohner, E. R.; Bowring, A. R.; Karunadasa, H. I.; McGehee, M. D. Reversible Photo-Induced Trap Formation in Mixed-Halide Hybrid Perovskites for Photovoltaics (SI). *Chem. Sci.* **2015**, *6* (1), 613–617. https://doi.org/10.1039/c4sc03141e.
(197) Wei, J.; Wang, Q.; Huo, J.; Gao, F.; Gan, Z.; Zhao, Q.; Li, H. Mechanisms and Suppression of Photoinduced Degradation in Perovskite Solar Cells. *Adv. Energy Mater.* **2021**, *11* (2002326). https://doi.org/10.1002/AENM.202002326.
(198) Tang, X.; Brandl, M.; May, B.; Levchuk, I.; Hou, Y.; Richter, M.; Chen, H.; Chen, S.; Kahmann, S.; Osvet, A.; et al. Photoinduced Degradation of Methylammonium Lead Triiodide Perovskite Semiconductors. *J. Mater. Chem. A* **2016**, *4* (41), 15896–15903. https://doi.org/10.1039/C6TA06497C.
(199) Cappel, U. B.; Svanström, S.; Lanzilotto, V.; Johansson, F. O. L.; Aitola, K.; Philippe, B.; Giangrisostomi, E.; Ovsyannikov, R.; Leitner, T.; Fö, A.; et al. Partially Reversible Photoinduced Chemical Changes in a

Mixed-Ion Perovskite Material for Solar Cells. *ACS Appl. Mater. Interfaces* **2017**, *9*, 34970–34978. https://doi.org/10.1021/acsami.7b10643.

(200) Bush, K. A.; Palmstrom, A. F.; Yu, Z. J.; Boccard, M.; Cheacharoen, R.; Mailoa, J. P.; McMeekin, D. P.; Z Hoye, R. L.; Bailie, C. D.; Leijtens, T.; et al. 23.6-Efficient Monolithic Perovskite/Silicon Tandem Solar Cells with Improved Stability. *Nat. Energy* **2017**, *2* (17009). https://doi.org/10.1038/nenergy.2017.9.

(201) Yang, J.; Siempelkamp, B. D.; Mosconi, E.; De Angelis, F.; Kelly, T. L. Origin of the Thermal Instability in CH3NH3PbI3 Thin Films Deposited on ZnO. *Chem. Mater.* **2015**, *27*, 4229−4236. https://doi.org/10.1021/acs.chemmater.5b01598.

(202) Tsai, H.; Nie, W.; Blancon, J.-C.; Stoumpos, C. C.; Asadpour, R.; Harutyunyan, B.; Neukirch, A. J.; Verduzco, R.; Crochet, J. J.; Tretiak, S.; et al. High-Efficiency Two-Dimensional Ruddlesden-Popper Perovskite Solar Cells. *Nature* **2016**, *536*, 312–316. https://doi.org/10.1038/nature18306.

(203) Wang, Y.; Zhang, T.; Kan, M.; Li, Y.; Wang, T.; Zhao, Y. Efficient α-CsPbI3 Photovoltaics with Surface Terminated Organic Cations. *Joule* **2018**, *2* (10), 2065–2075. https://doi.org/10.1016/j.joule.2018.06.013.

(204) Zhang, C. Reviewing and Understanding the Stability Mechanism of Halide Perovskite Solar Cells. *InfoMat* **2020**, *2* (6), 1034–1056. https://doi.org/10.1002/inf2.12104.

(205) Koehl, M.; Heck, M.; Wiesmeier, S.; Wirth, J. Modeling of the Nominal Operating Cell Temperature Based on Outdoor Weathering. *Sol. Energy Mater. Sol. Cells* **2011**, *95* (7), 1638–1646. https://doi.org/10.1016/j.solmat.2011.01.020.

(206) Williams, A. E.; Holliman, P. J.; Carnie, M. J.; Davies, M. L.; Worsley, D. A.; Watson, T. M. Perovskite Processing for Photovoltaics: A Spectro-Thermal Evaluation. *J. Mater. Chem. A* **2014**, *2*, 19338–19346. https://doi.org/10.1039/c4ta04725g.

(207) Juarez-Perez, E. J.; Hawash, Z.; Raga, S. R.; Ono, L. K.; Qi, P. Y.; Qi, Y. Thermal Degradation of CH3NH3PbI3 Perovskite into NH3 and CH3I Gases Observed by Coupled Thermogravimetry-Mass Spectrometry Analysis. *Energy Environ. Sci.* **2016**, *9*, 3406--3410. https://doi.org/10.1039/c6ee02016j.

(208) Eperon, G. E.; Stranks, S. D.; Menelaou, C.; Johnston, M. B.; Herz, L. M.; Snaith, H. J. Formamidinium Lead Trihalide: A Broadly Tunable Perovskite for Efficient Planar Heterojunction Solar Cells. *Energy Environ. Sci.* **2014**, *7*, 982–988. https://doi.org/10.1039/c3ee43822h.

(209) Liu, M.; Pasanen, H.; Ali-Löytty, H.; Hiltunen, A.; Lahtonen, K.; Qudsia, S.; Smått, J. H.; Valden, M.; Tkachenko, N. V.; Vivo, P. B-Site Co-Alloying with Germanium Improves the Efficiency and Stability of All-Inorganic Tin-Based Perovskite Nanocrystal Solar Cells. *Angew. Chemie - Int. Ed.* **2020**, *59* (49), 22117–22125. https://doi.org/10.1002/ANIE.202008724.

(210) Jacobsson, T. J.; Correa-Baena, J.-P.; Pazoki, M.; Saliba, M.; Schenk, K.; Grä, M.; Hagfeldt, A. Exploration of the Compositional Space for Mixed Lead Halogen Perovskites for High Efficiency Solar Cells. *Energy Environ. Mater.* **2016**, *9*, 1706–1724. https://doi.org/10.1039/c6ee00030d.

(211) Na Quan, L.; Yuan, M.; Comin, R.; Voznyy, O.; Beauregard, E. M.; Hoogland, S.; Buin, A.; Kirmani, A. R.; Zhao, K.; Amassian, A.; et al. Ligand-Stabilized Reduced-Dimensionality Perovskites. *JACS* **2016**, *138*, 2649−2655. https://doi.org/10.1021/jacs.5b11740.

(212) Ono, L. K.; Juarez-Perez, E. J.; Qi, Y. Progress on Perovskite Materials and Solar Cells with Mixed Cations and Halide Anions. *ACS Appl. Mater. Interfaces* **2017**, *9*, 30197−30246. https://doi.org/10.1021/acsami.7b06001.

(213) Divitini, G.; Cacovich, S.; Matteocci, F.; Cinà, L.; Carlo, A. Di; Ducati, C. In Situ Observation of Heat-Induced Degradation of Perovskite Solar Cells. *Nat. Energy* **2016**, *1*. https://doi.org/10.1038/NENERGY.2015.12.

(214) Hoffmann, L.; Brinkmann, K. O.; Malerczyk, J.; Rogalla, D.; Becker, T.; Theirich, D.; Shutsko, I.; Gö, P.; Riedl, T. Spatial Atmospheric Pressure Atomic Layer Deposition of Tin Oxide as an Impermeable Electron Extraction Layer for Perovskite Solar Cells with Enhanced Thermal Stability. *ACS Appl. Mater. Interfaces* **2018**, *10*, 6006−6013. https://doi.org/10.1021/acsami.7b17701.

(215) Zhou, W.; Wen, Z.; Gao, P. Less Is More: Dopant-Free Hole Transporting Materials for High-Efficiency Perovskite Solar Cells. *Adv. Energy Mater.* **2018**, *8* (1702512). https://doi.org/10.1002/AENM.201702512.

(216) Earnshaw, N. N. G. A. *Chemistry of the Elements - 2nd Edition*; Butterworth-Heinemann: Oxford,

1997.
(217) Mei, A.; Li, X.; Liu, L.; Ku, Z.; Liu, T.; Rong, Y.; Xu, M.; Hu, M.; Chen, J.; Yang, Y.; et al. A Hole-Conductor-Free, Fully Printable Mesoscopic Perovskite Solar Cell with High Stability. *Science (80-.).* **2014**, *345* (6194), 295–298. https://doi.org/10.1126/science.1254763.
(218) Bae, S.; Kim, S.; Lee, S.-W.; Cho, K. J.; Park, S.; Lee, S.; Kang, Y.; Lee, H.-S.; Kim, D. Electric-Field-Induced Degradation of Methylammonium Lead Iodide Perovskite Solar Cells. *J. Phys. Chem. Lett.* **2016**, *7*, 3091−3096. https://doi.org/10.1021/acs.jpclett.6b01176.
(219) Anoop, K. M.; Khenkin, M. V.; Di Giacomo, F.; Galagan, Y.; Rahmany, S.; Etgar, L.; Katz, E. A.; Visoly-Fisher, I. Bias-Dependent Stability of Perovskite Solar Cells Studied Using Natural and Concentrated Sunlight. *Sol. RRL* **2020**, *4* (1900335). https://doi.org/10.1002/SOLR.201900335.
(220) Kang, D.-H.; Park, N.-G. On the Current-Voltage Hysteresis in Perovskite Solar Cells: Dependence on Perovskite Composition and Methods to Remove Hysteresis. *Adv. Mater.* **2019**, 1805214. https://doi.org/10.1002/adma.201805214.
(221) Xiao, Z.; Yuan, Y.; Shao, Y.; Wang, Q.; Dong, Q.; Bi, C.; Sharma, P.; Gruverman, A.; Huang, J. Giant Switchable Photovoltaic Effect in Organometal Trihalide Perovskite Devices. *Nat. Mater.* **2015**, *14*. https://doi.org/10.1038/NMAT4150.
(222) Azpiroz, J. M.; Mosconi, E.; Bisquert, J.; De Angelis, F. Defect Migration in Methylammonium Lead Iodide and Its Role in Perovskite Solar Cell Operation. *Energy Environ. Mater.* **2015**, *8*, 2118–2127. https://doi.org/10.1039/c5ee01265a.
(223) Luchkin, S. Y.; Akbulatov, A. F.; Frolova, L. A.; Griffin, M. P.; Dolocan, A.; Gearba, R.; Bout, D. A. Vanden; Troshin, P. A.; Stevenson, K. J. Reversible and Irreversible Electric Field Induced Morphological and Interfacial Transformations of Hybrid Lead Iodide Perovskites. *ACS Appl. Mater. Interfaces* **2017**, *9*, 33478−33483. https://doi.org/10.1021/acsami.7b01960.
(224) Liu, P.; Wang, W.; Liu, S.; Yang, H.; Shao, Z. Fundamental Understanding of Photocurrent Hysteresis in Perovskite Solar Cells. *Adv. Energy Mater.* **2019**, *9* (13), 1803017. https://doi.org/10.1002/aenm.201803017.
(225) Xia, G.; Huang, B.; Zhang, Y.; Zhao, X.; Wang, C.; Jia, C.; Zhao, J.; Chen, W.; Li, J. Nanoscale Insights into Photovoltaic Hysteresis in Triple-Cation Mixed-Halide Perovskite : Resolving the Role of Polarization and Ionic Migration. *Adv. Mater.* **2019**, *1902870*, 1–9. https://doi.org/10.1002/adma.201902870.
(226) L Weber, S. A.; Ilka Hermes, ab M.; Turren-Cruz, S.-H.; Gort, C.; Bergmann, V. W.; Gilson, L.; Hagfeldt, A.; Graetzel, M.; Tress, W.; diger Berger, R. How the Formation of Interfacial Charge Causes Hysteresis in Perovskite Solar Cells. *Energy Environ. Sci* **2018**, *11*, 2404. https://doi.org/10.1039/c8ee01447g.
(227) Khenkin, M. V.; Katz, E. A.; Abate, A.; Bardizza, G.; Berry, J. J.; Brabec, C.; Brunetti, F.; Bulović, V.; Burlingame, Q.; Di Carlo, A.; et al. Consensus Statement for Stability Assessment and Reporting for Perovskite Photovoltaics Based on ISOS Procedures. *Nat. Energy* **2020**, *5* (1), 35–49. https://doi.org/10.1038/s41560-019-0529-5.
(228) Hu, Y.; Chu, Y.; Wang, Q.; Zhang, Z.; Ming, Y.; Mei, A.; Rong, Y.; Han, H. Standardizing Perovskite Solar Modules beyond Cells. *Joule* **2019**, *3* (9), 2076–2085. https://doi.org/10.1016/j.joule.2019.08.015.
(229) Miyasaka, T.; Kulkarni, A.; Kim, G. M.; Öz, S.; Jena, A. K. Perovskite Solar Cells: Can We Go Organic-Free, Lead-Free, and Dopant-Free? *Adv. Energy Mater.* **2020**, *10* (13), 1–20. https://doi.org/10.1002/aenm.201902500.
(230) Pecunia, Vincenzo; Occhipinti, Luigi G.; Chakraborty, Abhisek; Pan, Yiting; Peng, Y. Lead-Free Halide Perovskite Photovoltaics: Challenges, Open Questions and Opportunities. *APL Mater.* **2020**, *100901* (September). https://doi.org/10.1063/5.0022271.
(231) Umari, P.; Mosconi, E.; De Angelis, F. Relativistic GW Calculations on CH3NH3PbI3 and CH3NH3SnI3 Perovskites for Solar Cell Applications. *Sci. Rep.* **2014**, *4*, 4467–4474. https://doi.org/10.1038/srep04467.
(232) Huang, L. Y.; Lambrecht, W. R. L. Electronic Band Structure, Phonons, and Exciton Binding Energies of Halide Perovskites CsSnCl3, CsSnBr3, and CsSnI3. *Phys. Rev. B - Condens. Matter Mater. Phys.* **2013**, *88* (16), 1–12. https://doi.org/10.1103/PhysRevB.88.165203.

(233) Wu, T.; Liu, X.; Luo, X.; Lin, X.; Cui, D.; Wang, Y.; Segawa, H.; Zhang, Y.; Han, L. Lead-Free Tin Perovskite Solar Cells. *Joule* **2021**, *5*, 863–886. https://doi.org/10.1016/j.joule.2021.03.001.
(234) Gu, S.; Lin, R.; Han, Q.; Gao, Y.; Tan, H.; Zhu, J. Tin and Mixed Lead–Tin Halide Perovskite Solar Cells: Progress and Their Application in Tandem Solar Cells. *Adv. Mater.* **2020**, *1907392*, 1–16. https://doi.org/10.1002/adma.201907392.
(235) Leijtens, T.; Prasanna, R.; Gold-Parker, A.; Toney, M. F.; Mcgehee, M. D. Mechanism of Tin Oxidation and Stabilization by Lead Substitution in Tin Halide Perovskites. *ACS Energy Lett.* **2017**, *2*, 2159−2165. https://doi.org/10.1021/acsenergylett.7b00636.
(236) Hartmann, C.; Gupta, S.; Bendikov, T.; Kozina, X.; Kunze, T.; Feíix, R.; Hodes, G.; Wilks, R. G.; Cahen, D.; Bä, M. Impact of SnF2 Addition on the Chemical and Electronic Surface Structure of CsSnBr3. *ACS Appl. Mater. Interfaces* **2020**, *12*, 12353–12361. https://doi.org/10.1021/acsami.9b22967.
(237) Zhao, Z.; Gu, F.; Li, Y.; Sun, W.; Ye, S.; Rao, H.; Liu, Z.; Bian, Z.; Huang, C. Mixed-Organic-Cation Tin Iodide for Lead-Free Perovskite Solar Cells with an Efficiency of 8.12%. *Adv. Sci.* **2017**, *4* (11). https://doi.org/10.1002/ADVS.201700204.
(238) Shao, S.; Liu, J.; Portale, G.; Fang, H. H.; Blake, G. R.; ten Brink, G. H.; Koster, L. J. A.; Loi, M. A. Highly Reproducible Sn-Based Hybrid Perovskite Solar Cells with 9% Efficiency. *Adv. Energy Mater.* **2018**, *8* (4). https://doi.org/10.1002/AENM.201702019.
(239) Chen, M.; Ju, M. G.; Garces, H. F.; Carl, A. D.; Ono, L. K.; Hawash, Z.; Zhang, Y.; Shen, T.; Qi, Y.; Grimm, R. L.; et al. Highly Stable and Efficient All-Inorganic Lead-Free Perovskite Solar Cells with Native-Oxide Passivation. *Nat. Commun.* **2019**, *10* (1), 1–8. https://doi.org/10.1038/s41467-018-07951-y.
(240) Abdullah, I.; Macdonald, J. E.; Lin, Y.; Anthopoulos, T. D. Lead-Free Halide Perovskites, beyond Solar Cells and LEDs. *J. Phys. Energy* **2021**, *3* (032014). https://doi.org/10.1088/2515-7655/ac01bf.
(241) Gao, Y.; Pan, Y.; Zhou, F.; Niu, G.; Yan, C. Lead-Free Halide Perovskites: A Review of the Structure-Property Relationship and Applications in Light Emitting Devices and Radiation Detectors. *J. Mater. Chem. A* **2021**, *9* (20), 11931–11943. https://doi.org/10.1039/d1ta01737c.
(242) Li, J.; Duan, J.; Yang, X.; Duan, Y.; Yang, P.; Tang, Q. Review on Recent Progress of Lead-Free Halide Perovskites in Optoelectronic Applications. *Nano Energy* **2021**, *80* (105526). https://doi.org/10.1016/j.nanoen.2020.105526.
(243) Babayigit, A.; Ethirajan, A.; Muller, M.; Conings, B. Toxicity of Organometal Halide Perovskite Solar Cells. *Nat. Mater.* **2016**, *15*, 247–251. https://doi.org/10.1038/nmat4572.
(244) Li, J.; Cao, H.-L.; Jiao, W.-B.; Wang, Q.; Wei, M.; Cantone, I.; Lü, J.; Abate, A. Biological Impact of Lead from Halide Perovskites Reveals the Risk of Introducing a Safe Threshold. *Nat. Commun.* **2020**, *11* (310). https://doi.org/10.1038/s41467-019-13910-y.
(245) Kim, B. J.; Kim, D. H.; Kwon, S. L.; Park, S. Y.; Li, Z.; Zhu, K.; Jung, H. S. Selective Dissolution of Halide Perovskites as a Step towards Recycling Solar Cells. *Nat. Commun.* **2016**, *7* (May), 1–9. https://doi.org/10.1038/ncomms11735.
(246) Horváth, E.; Kollár, M.; Andrič, P.; Rossi, L.; Mettan, X.; Forró, L. Fighting Health Hazards in Lead Halide Perovskite Optoelectronic Devices with Transparent Phosphate Salts. *ACS Appl. Mater. Interfaces* **2021**, *13*, 33995−34002. https://doi.org/10.1021/acsami.0c21137.
(247) Miao, Y.; Chen, Y.; Chen, H.; Wang, X.; Zhao, Y. Using Steric Hindrance to Manipulate and Stabilize Metal Halide Perovskites for Optoelectronics. *Chem. Sci.* **2021**, *12* (21), 7231–7247. https://doi.org/10.1039/d1sc01171e.
(248) Krishnan, U. Factors Affecting the Stability of Perovskite Solar Cells: A Comprehensive Review. *J. Photonics Energy* **2019**, *9* (02), 1. https://doi.org/10.1117/1.jpe.9.021001.
(249) Park, N. G. Green Solvent for Perovskite Solar Cell Production. *Nat. Sustain.* **2021**, *4* (3), 192–193. https://doi.org/10.1038/s41893-020-00647-6.
(250) Pecunia, V.; Occhipinti, L. G.; Hoye, R. L. Z. Emerging Indoor Photovoltaic Technologies for Sustainable Internet of Things. *Adv. Energy Mater.* **2021**. https://doi.org/10.1002/aenm.202100698.
(251) Hoang, M. T.; Ünlü, F.; Martens, W.; Bell, J.; Mathur, S.; Wang, H. Towards the Environmentally Friendly Solution Processing of Metal Halide Perovskite Technology. *Green Chem.* **2021**. https://doi.org/10.1039/d1gc01756j.
(252) Brown, A. A. M.; Damodaran, B.; Jiang, L.; Tey, J. N.; Pu, S. H.; Mathews, N.; Mhaisalkar, S. G. Lead

Halide Perovskite Nanocrystals : Room Temperature Syntheses toward Commercial Viability. *Adv. Energy Mater.* **2020**, *2001349*, 1–19. https://doi.org/10.1002/aenm.202001349.

(253) Cui, Y.; Wang, S.; Ding, L.; Hao, F. Green–Solvent–Processable Perovskite Solar Cells. *Adv. Energy Sustain. Res.* **2021**, *2* (2000047). https://doi.org/10.1002/aesr.202000047.

(254) Zhang, M.; Xin, D.; Zheng, X.; Chen, Q.; Zhang, W. H. Toward Greener Solution Processing of Perovskite Solar Cells. *ACS Sustain. Chem. Eng.* **2020**, *8* (35), 13126–13138. https://doi.org/10.1021/acssuschemeng.0c04289.

(255) Bush, K. A.; Rolston, N.; Gold-Parker, A.; Manzoor, S.; Hausele, J.; Yu, Z. J.; Raiford, J. A.; Cheacharoen, R.; Holman, Z. C.; Toney, M. F.; et al. Controlling Thin-Film Stress and Wrinkling during Perovskite Film Formation. *ACS Energy Lett.* **2018**, *3*, 1225−1232 Controlling. https://doi.org/10.1021/acsenergylett.8b00544.

(256) Taylor, A. D.; Sun, Q.; Goetz, K. P.; An, Q.; Schramm, T.; Hofstetter, Y.; Litterst, M.; Paulus, F.; Vaynzof, Y. A General Approach to High Efficiency Perovskite Solar Cells by Any Antisolvent. *Nat. Commun.* **2021**, 1–11. https://doi.org/10.1038/s41467-021-22049-8.

(257) Hansen, C. M. *Hansen Solubility Parameters - A User's Handbook, Second Edition*; 2007.

(258) Prat, D.; Wells, A.; Hayler, J.; Sneddon, H.; McElroy, C. R.; Abou-Shehada, S.; Dunn, P. J. CHEM21 Selection Guide of Classical- and Less Classical-Solvents. *Green Chem.* **2016**, *18* (1), 288–296. https://doi.org/10.1039/c5gc01008j.

(259) Clarke, C. J.; Tu, W. C.; Levers, O.; Bröhl, A.; Hallett, J. P. Green and Sustainable Solvents in Chemical Processes. *Chem. Rev.* **2018**, *118* (2), 747–800. https://doi.org/10.1021/acs.chemrev.7b00571.

(260) Doolin, A. J.; Charles, R. G.; De Castro, C. S. P.; Rodriguez, R. G.; Péan, E. V.; Patidar, R.; Dunlop, T.; Charbonneau, C.; Watson, T.; Davies, M. L. Sustainable Solvent Selection for the Manufacture of MAPbI3 Perovskite Solar Cells. *Green Chem.* **2021**. https://doi.org/10.1039/D1GC00079A.

(261) Wang, L.; Wang, X.; Deng, L.-L.; Leng, S.; Guo, X.; Tan, C.-H.; H Choy, W. C.; Chen, C.-C. The Mechanism of Universal Green Antisolvents for Intermediate Phase Controlled High-Efficiency Formamidinium-Based Perovskite Solar Cells. *Mater. Horiz.* **2020**, *7*, 934–942. https://doi.org/10.1039/c9mh01679a.

(262) Yun, Y.; Wang, F.; Huang, H.; Fang, Y.; Liu, S.; Huang, W.; Cheng, Z.; Liu, Y.; Cao, Y.; Gao, M.; et al. A Nontoxic Bifunctional (Anti)Solvent as Digestive-Ripening Agent for High-Performance Perovskite Solar Cells. *Adv. Mater.* **2020**, *32* (1907123). https://doi.org/10.1002/ADMA.201907123.

(263) Chen, H.; Ye, F.; Tang, W.; He, J.; Yin, M.; Wang, Y.; Xie, F.; Bi, E.; Yang, X.; Grätzel, M.; et al. A Solvent-and Vacuum-Free Route to Large-Area Perovskite Films for Efficient Solar Modules. *Nature* **2017**, *550* (7674), 92–95. https://doi.org/10.1038/nature23877.

(264) Zhou, Z.; Wang, Z.; Zhou, Y.; Pang, S.; Wang, D.; Xu, H.; Liu, Z.; Padture, N. P.; Cui, G. Methylamine-Gas-Induced Defect-Healing Behavior of CH3NH3PbI3 Thin Films for Perovskite Solar Cells. *Angew. Chemie - Int. Ed.* **2015**, *54* (33), 9705–9709. https://doi.org/10.1002/anie.201504379.

(265) Papageorgiou, N.; Athanassov, Y.; Armand, M.; Bonho$_{\chi}$te, P.; Pettersson, H.; Azam, A.; Grätzel, M. The Performance and Stability of Ambient Temperature Molten Salts for Solar Cell Applications. *J. Electrochem. Soc.* **1996**, *143* (10), 3099–3108. https://doi.org/10.1149/1.1837171.

(266) Chao, L.; Xia, Y.; Li, B.; Xing, G.; Chen, Y.; Huang, W. Room-Temperature Molten Salt for Facile Fabrication of Efficient and Stable Perovskite Solar Cells in Ambient Air. *Chem* **2019**, *5* (4), 995–1006. https://doi.org/10.1016/j.chempr.2019.02.025.

(267) Lee, J.; Malekshahi Byranvand, M.; Kang, G.; Son, S. Y.; Song, S.; Kim, G. W.; Park, T. Green-Solvent-Processable, Dopant-Free Hole-Transporting Materials for Robust and Efficient Perovskite Solar Cells. *JACS* **2017**, *139* (35), 12175–12181. https://doi.org/10.1021/jacs.7b04949.

(268) Wang, M.; Fu, Q.; Yan, L.; Huang, J.; Ma, Q.; Humayun, M.; Pi, W.; Chen, X.; Zheng, Z.; Luo, W. Systematic Optimization of Perovskite Solar Cells via Green Solvent Systems. *Chem. Eng. J.* **2020**, *387* (123966). https://doi.org/10.1016/j.cej.2019.123966.

(269) Song, J.; Li, J.; Xu, L.; Li, J.; Zhang, F.; Han, B.; Shan, Q.; Zeng, H. Room-Temperature Triple-Ligand Surface Engineering Synergistically Boosts Ink Stability, Recombination Dynamics, and Charge Injection toward EQE-11.6% Perovskite QLEDs. *Adv. Mater.* **2018**, *30* (30). https://doi.org/10.1002/ADMA.201800764.

(270) Krieg, F.; Ong, Q. K.; Burian, M.; Rainò, G.; Naumenko, D.; Süess, A.; Grotevent, M. J.; Krumeich, F.;

Maryna, I.; Shorubalko, I.; et al. Stable Ultraconcentrated and Ultradilute Colloids of CsPbX3 (X = Cl, Br) Nanocrystals Using Natural Lecithin as a Capping Ligand (SI). *J. Am. Chem. Soc.* **2020**, *141* (50).

(271) Yang, Y.; Qin, H.; Jiang, M.; Lin, L.; Fu, T.; Dai, X.; Zhang, Z.; Niu, Y.; Cao, H.; Jin, Y.; et al. Entropic Ligands for Nanocrystals: From Unexpected Solution Properties to Outstanding Processability. *Nano Lett.* **2016**. https://doi.org/10.1021/acs.nanolett.6b00737.

(272) Goetz, K. P.; Taylor, A. D.; Hofstetter, Y. J.; Vaynzof, Y. Sustainability in Perovskite Solar Cells. *ACS Appl. Mater. Interfaces* **2020**. https://doi.org/10.1021/acsami.0c17269.

(273) Gholipour, S.; Saliba, M. From Exceptional Properties to Stability Challenges of Perovskite Solar Cells. *Small* **2018**, *14* (46). https://doi.org/10.1002/SMLL.201802385.

(274) Fei, C.; Li, B.; Zhang, R.; Fu, H.; Tian, J.; Cao, G. Highly Efficient and Stable Perovskite Solar Cells Based on Monolithically Grained CH3NH3PbI3 Film. *Adv. Energy Mater.* **2017**, *7* (9). https://doi.org/10.1002/AENM.201602017.

(275) Wang, Z.; Lou, J.; Zheng, X.; Zhang, W.-H.; Qin, Y. Solution Processed Nb2O5 Electrodes for High Efficient Ultraviolet Light Stable Planar Perovskite Solar Cells. *ACS Sustain. Chem. Eng.* **2019**, *7*, 7421–7429. https://doi.org/10.1021/acssuschemeng.9b00991.

(276) Berhe, T. A.; Su, W.-N.; Chen, C.-H.; Pan, C.-J.; Cheng, J.-H.; Chen, H.-M.; Tsai, M.-C.; Chen, L.-Y.; Dubale, A. A.; Hwang, B.-J. Organometal Halide Perovskite Solar Cells: Degradation and Stability. *Energy Environ. Sci* **2016**, *9*, 323–356. https://doi.org/10.1039/c5ee02733k.

(277) Shao, Y.; Fang, Y.; Li, T.; Wang, Q.; Dong, Q.; Deng, Y.; Yuan, Y.; Wei, H.; Wang, M.; Gruverman, A.; et al. Grain Boundary Dominated Ion Migration in Polycrystalline Organic-Inorganic Halide Perovskite Films. *Energy Environ. Sci.* **2016**, *9*, 1752–1759. https://doi.org/10.1039/c6ee00413j.

(278) Wang, Z.; Lin, Q.; Chmiel, F. P.; Sakai, N.; Herz, L. M.; Snaith, H. J. Efficient Ambient-Air-Stable Solar Cells with 2D–3D Heterostructured Butylammonium-Caesium- Formamidinium Lead Halide Perovskites. *Nat. Energy* **2017**, *2*. https://doi.org/10.1038/nenergy.2017.135.

Chapter 2

Nanomaterials by Laser Ablation in Liquid

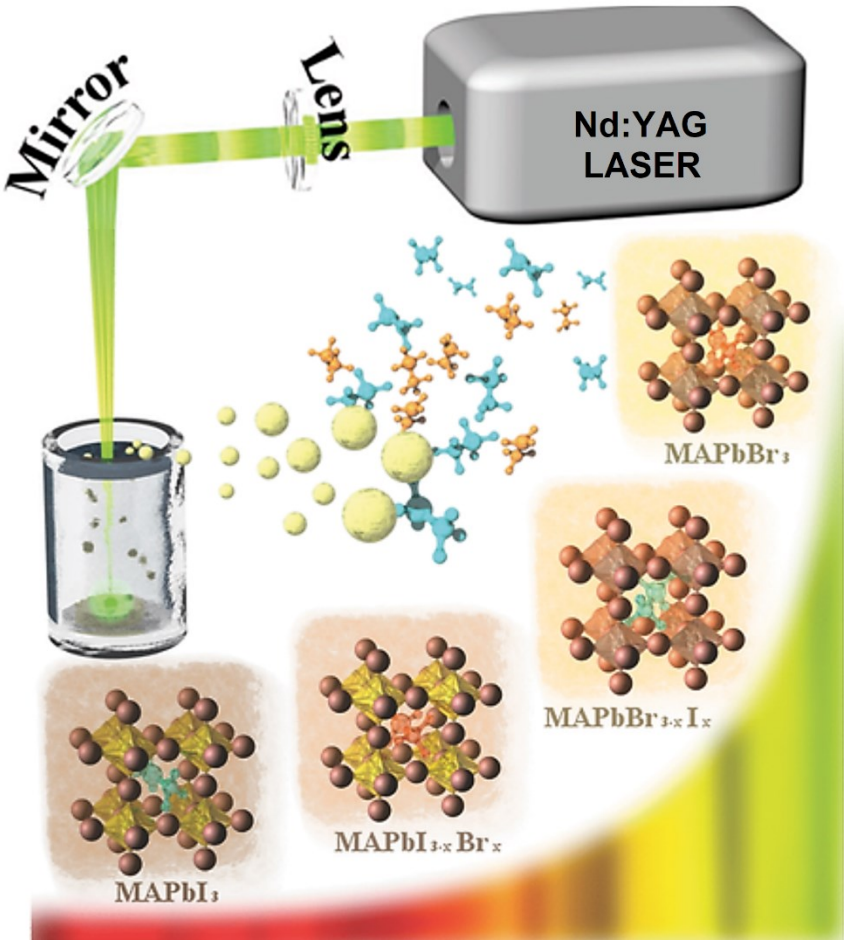

Adv. Energy Mater. 2017, 7, 1601703

2. Nanomaterials by Laser Ablation under Liquids

The intrinsic properties of nanoparticles (NPs), even combined with other materials, disclose several applications where one can achieve miniaturization (e.g., of electronic equipment), weight reduction (e.g., an increased material efficiency) and/or improved functionalities of materials (e.g., higher durability, conductivity, thermal stability, solubility, reduced friction, selective molecular detection).[1,2] Bottom-up and top-down procedures are the two approaches used for the synthesis of nanomaterials.[3] The former methods, typically chemical, include a self-assembling process that leads to the formation of nanostructures.[4] Instead, top-down approaches use macroscopic starting structures that are externally controlled by the processing down to nanostructures.[5] Nanomaterials produced by laser–matter interaction usually follows the second approach and make them a hot research topic in material science, with applications ranging from quantum computers to cures for cancer.[6–8]

Many studies, focused on the laser interaction with hard, soft, and smart materials, also look to the understanding of the fundamental mechanisms involved in laser processing.[9] Such laser techniques for the production of nanomaterials also enable the processing of materials for energy applications.[10–12] The characteristic of nanoparticles obtained by laser ablation in liquid/solution is their purity since they do not need stabilizing molecules or polymers because particles are charged and coulomb interaction among them makes stable their solutions. Nowadays, the interest towards the pure and electrostatically stabilized nanocolloids is well recognized.[8,13–15] Laser synthesis of colloids, powered by robust, high-power lasers, appears to be a key enabling process that is chemically clean and sustainable (since it usually operates in water or in organic liquids under ambient conditions),[8,15] and appealing for industrial manufacturing of functional nanomaterials.

Laser ablation of solid targets under a liquid medium (LAL, laser ablation under liquid) for usual syntheses and sometimes also LASiS (laser ablation synthesis in solution) when a controlled liquid phase composition is specified can be realized to fabricate nanostructures with various compositions (such as metals, alloys, semiconductors, oxides, hydroxides, carbides, and polymers) and morphologies (such as nanoparticles, nanocubes, nanorods, and nanocomposites).[8,16] At the same time, it does not require the use of toxic, hazardous, or pyrophoric chemical precursors nor long reaction times, high temperatures, or multi-step chemical synthetic procedures for nanomaterial synthesis. Thus, LAL is an eco-friendly and laboratory safe method. Moreover, laser

post-irradiation of suspended nanomaterials can be applied to further modify their size, shape, and composition.[17,18] Recently, LAL has been developed to prepare nanomaterials with special morphologies, microstructures, and phases, and to achieve one-step formation of various functionalized nanostructures in the pursuit of novel properties and applications. The method can be applied with an almost unlimited combination of target materials and solutions, leading to the direct synthesis of NPs in a medium of choice.

The generation of NPs with LAL brings some challenging aspects, such as the fabrication of NPs with a specific size and shape, the reduction of polydispersity and the increase of productivity.[18] Despite some unsolved problems, several strategies have been proposed to overcome them. For example, the initial low productivity of LAL has been remedied, reaching NPs production rates of several grams per hour.[19] In addition to LAL, Laser Melting in Liquids (LML), Laser Fragmentation in Liquids (LFL), and Pulsed Laser photoreduction/oxidation in Liquids (LPL) offer alternative routes to obtain colloids with controlled nanoparticles size.[8] A list of abbreviations is reported in an appendix (pp. 242) at the end of the dissertation.

Together with the development of new strategies to increase NPs productivity, future efforts will be directed to further improve the surface properties of the NPs, since each application requires a different surface/interface chemistry. The nanomaterials used in the present thesis were produced by LASiS and, in this chapter, an overview of the fundamentals of pulsed laser ablation in solutions will be presente.[20,21] The high complexity and multiple time-scale transient physics and chemistry typical of the laser ablation synthesis under a solvent will be remarked,[22–24] providing some hints on promising applications of NPs by laser ablation in liquid.

2.1 The Technique

2.1.1 *Basic Concepts of Laser Ablation under liquid*

From the invention of the first laser in 1960 by Maiamn on,[25] lasers have been widely used in a range of science and technological fields, among which the laser-assisted fabrication of functional nanomaterials is one of the significant application. The ablation of the target material upon laser irradiation is a very complex process. The incident laser pulse penetrates the surface of the material within a certain penetration depth, depending on the laser wavelength and the refraction index of the target material and is typically in the range of 10^1 nm. The strong electrical field generated by the laser pulse is sufficient to quickly remove electrons from the bulk of the penetrated volume

(e.g., within 10 ps for a ns laser pulse).[26] The free electrons oscillate within the electromagnetic field and can collide with the atoms of the bulk material, thus transferring some energy to the lattice. The irradiated surface is then heated up and vaporized.[26] At a sufficient high laser flux, the material is typically converted to plasma containing various energetic species including atoms, molecules, electrons, ions, clusters, particulates, and molten globules at high temperature, pressure and density. Subsequently, the large pressure difference between the initial plasma seed produced by the laser beam and the liquid environment causes a rapid expansion of a plasma plume, which cools down, following a nearly adiabatic and transonic process.[27]

The laser-target interaction can be designed in different environments to fabricate various nanomaterials. While first nanomaterials by laser ablation date back to 1965, when thin films were produced in vacuum chambers by pulsed laser deposition (PLD),[28] laser ablation in liquid technique was firstly investigated only in the '90s.[29] Since then, LAL has been developed into an important method to prepare metal, semiconductor, and even polymer NPs.[18] LAL technique is somewhat different from other laser ablation approaches operating in vacuum or gaseous environments because the liquid medium both provides some effective controlling parameters for fabrication and greatly affects the morphology and microstructure of the products. Indeed, interesting shape and size modifications of NPs prepared by laser post irradiation have been observed.[18] The amazing prospects emerging from the interaction of matter with light have inspired numerous research groups to focus their work on the laser generation and modification of NPs in liquid and on the properties and applications of nanomaterials produced by LAL.[16]

2.1.2 *Nanoparticles Formation Mechanism*

Laser ablation under liquid to produce nanostructures is based on the ejection of material by a laser pulse irradiating a solid target immersed in liquid. The laser-matter interaction and the consequent ablation are strongly dependent on the irradiance and the duration of the pulse, on the liquid, on the sample geometry and morphology as well as on the focusing condition. [18,22,30] For a general viewpoint of the complexity of the sequence of processes involved in NPs generation by ns-pulsed laser ablation under a liquid one can consider the following time sequence: (i) laser ablation and plasma induction, (ii) energy exchange from plasma to the liquid and (iii) consequent generation of the cavitation bubble and release of particles from the bubble to the solvent (Figure 2.1).

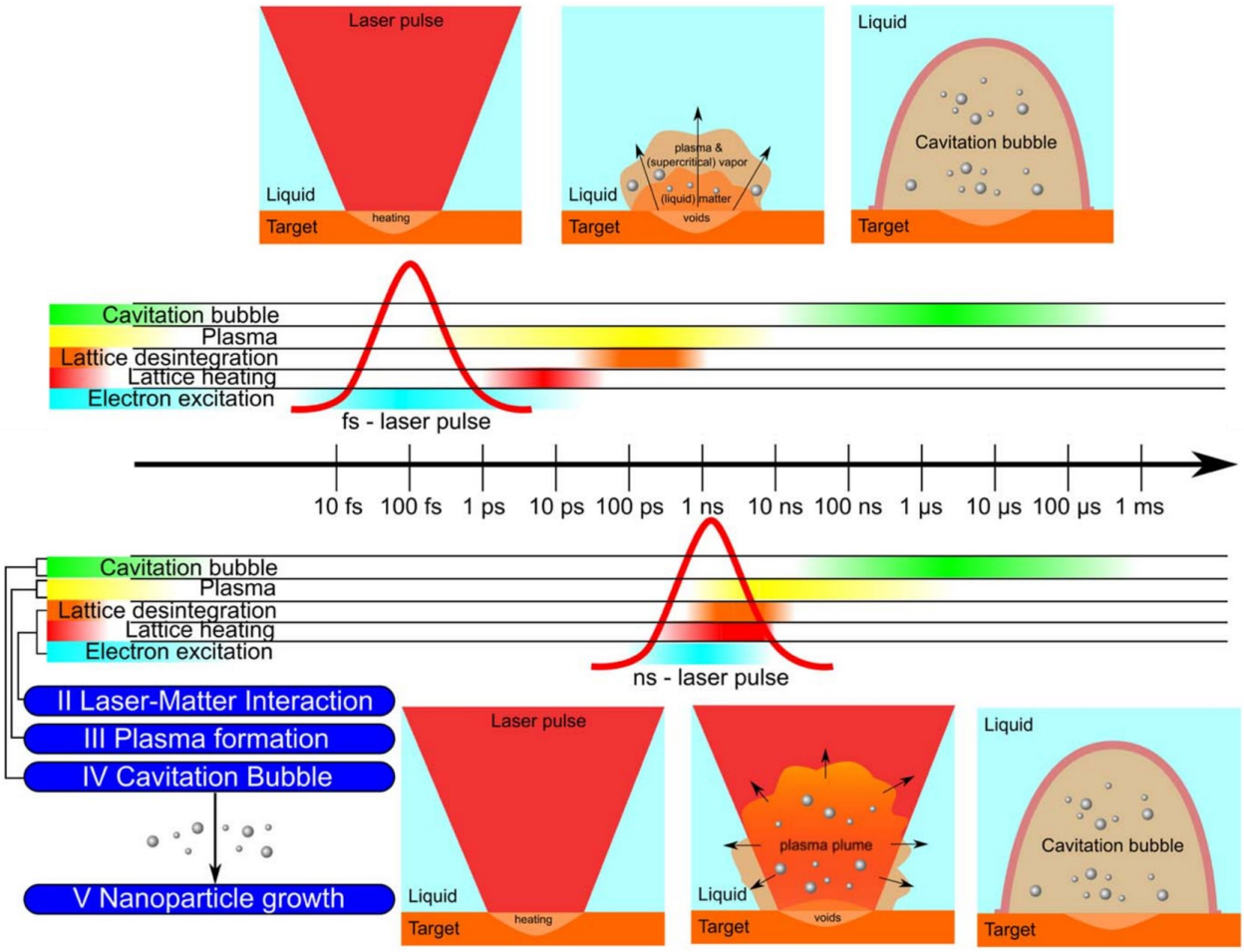

Figure 2.1 Schematics of the laser ablation in liquid process at different timescales. The time frames give an insight into the different characteristic times of the main physical process in laser ablation in liquid-phase for fs- and ns-laser pulses: (i) energy transfer from the laser-excited electron gas to the lattice (10^0 ps), (ii) phase transition of the target (> 10^2 ps), (iii) plasma lifetime (10^0 µs), and (iv) bubble lifetime (10^2 ms).[22]

Laser-Matter Interaction

With respect to laser ablation in vacuum or gaseous environment,[23] only a portion of the laser pulse reaches directly the target surface, while most of its energy is spent in electron heating by inverse bremsstrahlung.[16] Differently to what can be observed in a gas medium, as a consequence of the water incompressibility, the ablated material is strongly confined and reaches high density. This effect decreases the penetration of the laser through the plasma during the initial stage of expansion, inducing the propagation of gradient of temperature in the plasma. Optical, electrical and morphological properties of the target affect the initial interaction of the material with the laser pulse, and, for example, a metallic target needs lower ablation irradiance with respect to a semiconductor one. If an irradiance well above the breakdown threshold is used the LAL can be assumed congruent, and similar plasma behavior can be observed. The mechanisms concerning the evolution of the ejected material after laser ablation are strongly correlated to the duration of the laser pulse.

Ideally, with a laser pulse duration < 10^1 fs (Figure 2.1 a), the effect of the interaction of the laser pulse with the ejected material can be neglected and the evolution of the ablated material can be investigated with atomistic models.[31] On the contrary, when the laser pulse is long and interacts with the ablated material, as in the case of ns-pulses (Figure 2.1 b), further ionization and electron heating can be expected and the role of plasma becomes dominant. In these cases kinetics models coupled with fluid dynamics are required for a full description of the phenomenon.[32]

The Plasma Phase

The plasma phase plays an important role, in particular for ns-pulses. Laser Induced Plasma (LIP) in liquid can be temporally and spatially investigated by Optical Emission Spectroscopy, which allows to estimate plasma parameters,[33–35] such as density and temperature, as well as to observe the features of plasma dynamics (Figure 2.2). From OES measurements it was observed that in the core of the plasma there is a decrease in temperature. [36,37] As a matter of fact, the high pressure of the plasma under liquid confinement condition allows the condensation of the materials at higher temperatures than those in standard condition. This observation indicates that NPs can be formed in the bulk of the plasma and not only at its borders where the plasma quickly cools because of the rapid exchange of energy with the surrounding liquid.[38] Interaction between plasma and liquid phases may result in the appearance of unusual phases since products quickly quench from very high temperatures.[39–41] Considering that the material at plasma borders condensates in particle and that this region is out of equilibrium, particles with various sizes and shapes can be formed.

On the contrary, particles formed in the bulk of the plasma, where thermodynamic equilibrium between growth and evaporation is present, are characterized by a spherical shape with a narrow size distribution. The growth mechanism of nanoparticles in the plasma phase during ns-pulsed LAL has been investigated with theoretical models, in which the competition between thermodynamic condensation and electrostatic growth has been investigated.[36] The results suggested that as soon as small clusters are formed, they attract electrons in the ps timescale, because of the high-density gradient at the initial stage of laser ablation. Consequently, the particles become negatively charged and attract positive ions present in the plasma. Electron charging and ion attraction allow the particles to grow until the growth rate is balanced by the evaporation process due to the high plasma temperature (4000÷6000 K).[16,24] In this scenario, the equilibrium between electrostatic growth and evaporation determines the nanoparticles dimensions and induces their typical spherical shape observed in the LAL process. It has been recently shown that the charging effect of the plasma is

involved also in the subsequent steps of LAL process.[42,43] In fact, when particles exit the plasma, they still show an excess of electrons. This charge (in the order of a few nC for the entire NPs produced per laser pulse), allows the repulsion between the particles and preserves the NPs from massive aggregation.

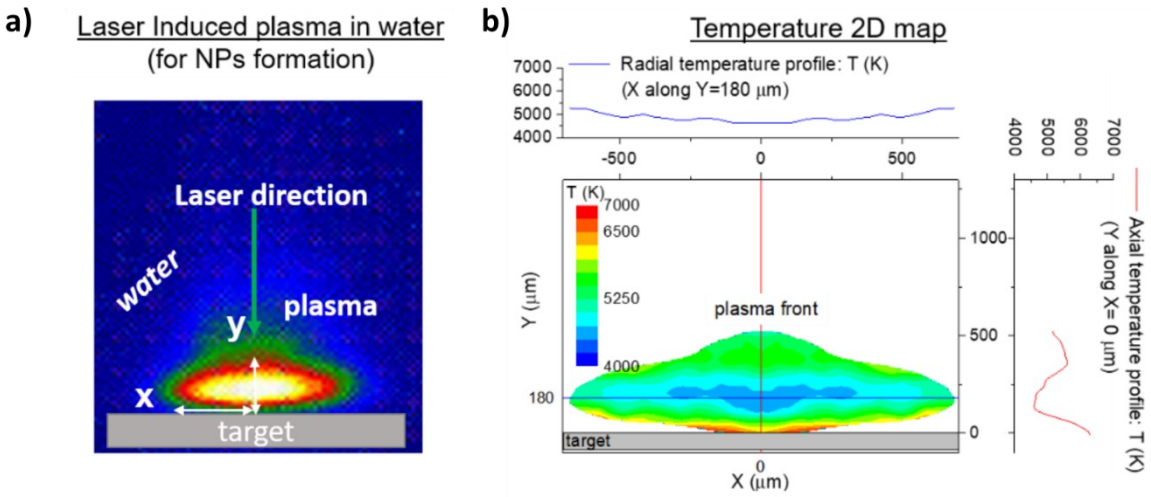

Figure 2.2 a) Image of a laser-induced plasma on a metallic target immersed in water acquired with ICCD camera (E_{laser} = 270 mJ, laser crater size = 1 ± 0.2 mm, λ_{laser} = 532 nm, pulse duration = 6 ns, f_{laser} = 10 Hz, delay time = 40 ns). b) 2D temperature map of plasma temperature calculated with data processing.[34]

The Cavitation Bubble

The fast transfer of energy from the plasma to the surrounding water induces the formation of a thin layer of vapor around the plasma border with high temperature and high pressure. To reach the equilibrium with the liquid, the vapor expands, producing a cavitation bubble (Figure 2.3).[44,45] The bubble quickly expands (10^1 μs) until it reaches the equilibrium with the surrounding liquid. Due to the fast expansion, the liquid at the border of the cavitation is compressed and when the pressure of the bubble reaches its minimum, at the maximum of the expansion (10^2 μs), the bubble is compressed, and its shrinking stage begins. During this stage, the bubble increases its pressure again and impacts the target, eventually pushing back the material to the target surface (Figure 2.3 a-f). There are several models and simulations describing the evolution of a laser-induced bubbles that, although not considering the interaction of laser-induced plasma with the vapor inside the bubble, they provide acceptable qualitative description of the cavitation bubble evolution.[46,47] As a result of the charging effect on the NPs produced in the plasma phase, the nanoparticles clouds expand as well due to the electrostatic repulsion. If the NPs store enough charge immediately after the plasma stage, the induced electrostatic pressure can be higher than the pressure at the liquid/vapor boundary. Consequently, NPs exit the cavitation bubble and enter the solution.

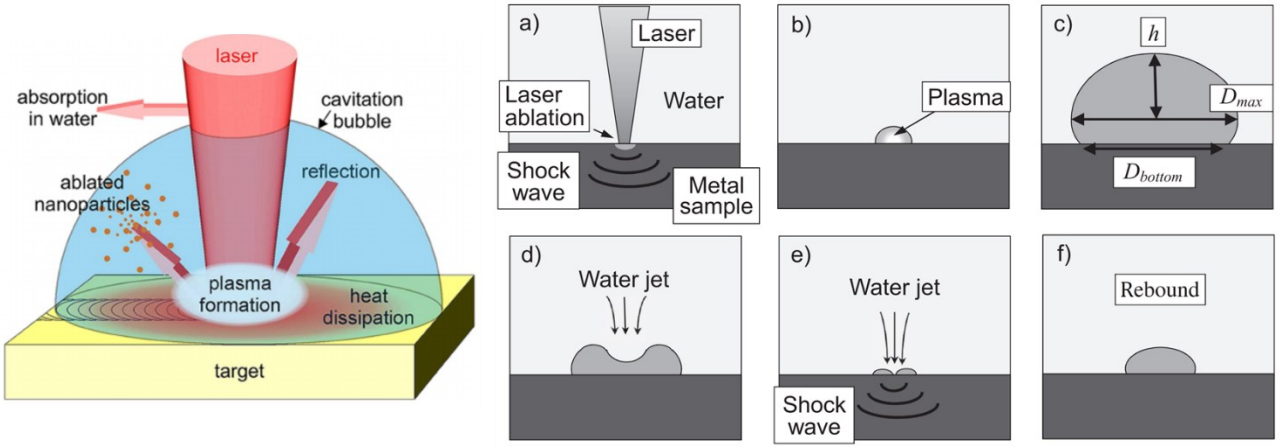

Figure 2.3 (left) Schematic illustration of the energy loss mechanisms of the laser beam during ns-pulsed laser ablation in liquid while leaving a trace on the moving target.[44] (right) Schematic diagrams of cavitation bubble dynamics during laser ablation of a metal target under water at: a) laser irradiation, b) bubble generation, c) maximum size, d) shrinking, e) collapse, and (f) rebound.[45]

This phenomenon has been recently investigated in detail in and it has been found that the two main streams of NPs ejection occurs (i) immediately after the beginning of the expansion phase and (ii) between the collapsing stage and the bubble rebound (Figure 2.3 f).[42] Spherical small NPs (10÷20 nm) are not the only one produced. In terms of mass, the fraction of material converted in this kind of nanoparticles is a minor component. Big NPs (10^2 nm) can be the result of aggregation of smaller spherical NPs during the collapse stage of the cavitation bubble and the NPs that are not ejected can remain trapped in the bubble and are compressed (because of the high pressure of the collapse stage), rearranging in aggregates. Finally, as an intrinsic result of the laser ablation, debris of several hundred of nm (10^2÷10^3 nm) can be found at the bottom of the ablation cell.

2.1.3 *Control of Size Distribution*

Under laser ablation in liquid, particles in the suspension can transform into smaller sized particles of same or different shape, phase, and composition.[48–50] Two mechanisms were proposed for the resizing/reshaping of the nanostructures and/or their surface modification using laser irradiation in liquid media.[18] The former is the so-called laser-induced photothermal melting/evaporation mechanism, in which the laser induces melting and/or vaporization of particles into atoms or molecules,[8] which then rearrange into smaller nanostructures with the same/different shapes and crystal structures depending on the experimental conditions.[51–53] In these situations, the melting/vaporization of metal NPs suspended in liquid media provides an efficient pathway for the synthesis of alloy NPs. In fact, the irradiation of a mixture of two or more colloids of elemental NPs can melt or vaporize them, thus making the formation of their alloys possible upon condensation.

The other mechanism is the laser-induced coulombic explosion, which involves ejection of photoelectrons or thermal electrons from the surfaces of the target nanostructures, leaving positive charges behind on the surface.[8] The induced surface charges develop electrostatic repulsion between different parts of the primary particles, thus causing the consequent fragmentation of a single particle into several smaller ones.[48,54,55] The experimental conditions to switch between the two mechanisms are quite different (Figure 2.4).[8] The melting-evaporation mechanism requires a high laser irradiance, which can make the temperature of the particle suspension higher than its boiling point. The laser-induced coulombic explosion mechanism requires a matching of the laser wavelength with the work function of the target material to eject photoelectrons.[16] Fragmentation with laser photon energy less than the work function can be induced by picosecond or femtosecond laser pulses, in which laser intensity can be high enough to allow multiphoton ionization. Recent theoretical investigations suggested that coulomb explosion is dominating for fs laser irradiation, while thermal evaporation occurs for ns laser one, even at small excitation wavelength (e.g, 355 nm).[49,56]

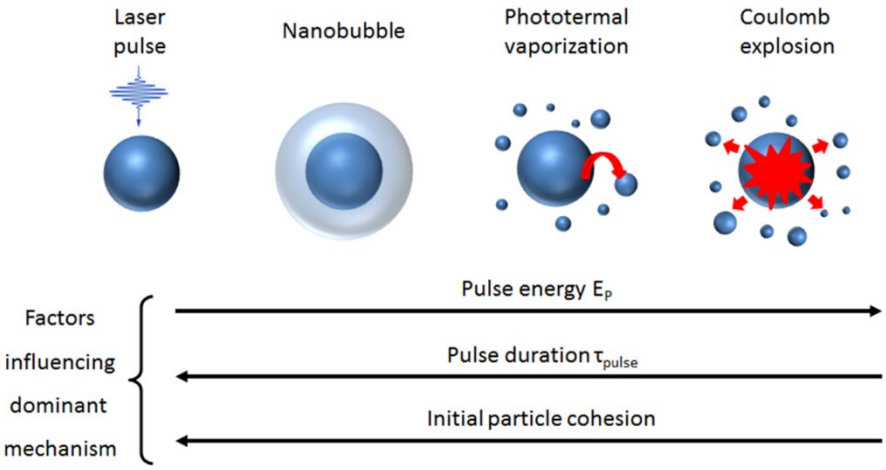

Figure 2.4 Schematic illustration of size-reduction and fragmentation mechanisms of NPs in a colloidal solution.[8]

Other processes to functionalize and control size and/or morphology of NPs produced by laser ablation were investigated, such as the application of external electromagnetic fields,[57,58] the addition of electrolyte solutions,[59] surfactants,[60,61] polymers,[62,63] and/or biomolecules[64] to the liquid in which the ablation occurs. In the next chapters synthesis of NPs by laser ablation only in pure liquids and these alternative routes are beyond the scope of this discussion. However, even if nanoparticles by LAL are referred as ligand/surfactant-free, one should recall that a surface chemistry is possible with, for example, oxidations or surface interactions with the solvent molecules.[8] Such a surface chemistry can be important since it influences, for example, the stability of the colloidal solution, which, for many applications, is an important property of the produced

solutions.[65,66] At present, a definite protocol, to realize performance-oriented colloidal synthesis, and related processing to prepare more isochronous surface modification of metal and semiconductor NPs is still not defined. The latter is an urgent request of modern manufacturing based on laser ablation to make possible in-situ engineering, thereby opening the way for the fabrication of functionalized nanostructures.

2.1.4 *Reactive/Non-Reactive Laser Ablation in Liquid*

Laser ablation in liquid can be divided into two main methodologies: non-reactive and reactive LAL.[18] The former implies that there is no reaction between the ablated species and the surrounding liquid medium, and thus the formed nanostructures have the same composition as the applied targets. This is the most basic configuration for LAL process and has been extensively exploited.[59,67] Silver, gold, and platinum metals have low reactivity so that the laser ablation of these metals in most liquids is very likely to generate their corresponding elemental NPs.[63] The LAL of more reactive metal targets (such as Zn, Cd, Cu, Ti, Al, Mg, Pb, and Fe) usually generates compound NPs through the reaction of a created plasma with the liquid. However, if the generation rate of the plasma species is high and the time for their clustering into particles is small, then the reaction between the species inside the plasma dominates over the reaction between the plasma species and liquid medium at the plasma/liquid interface. Under such conditions, active metal particles[68] or active metal core/metal compound shell particles[69] are produced by non-reactive LAL.

On the other hand, reactive LAL implies reactions between the ablated species and the liquid medium, and thus the formed nanostructures have a different composition from that of the targets. Obviously, this greatly expands the product composition spanning oxide, hydroxide, carbide, sulfide, nitride, and composite nanostructures that can be smartly designed via the reaction between selected targets and liquid media. Laser induced plasma from a target material can heat the surrounding liquid medium turning it to plasma state, and the two plasmas can react intensely to form metal compound nanostructures. The LAL of active metals in water or alcohols produces their hydroxides as the primary product.[70,71] These hydroxide seeds then either become dehydrated into oxide by losing water through hydrothermal reaction processes,[72] or become clustered to form hydroxide NPs.[73] Moreover, the simultaneous flow of oxygen in the close vicinity of a laser-produced plasma plume can modify the final products by increasing the oxygen content in the NPs, oxide/hydroxide ratio in nanocomposites, and the NPs crystallinity, while decreasing the NPs

dimension and sharpening their size distribution.[73,74] It is worth to report that, irrespective of the liquid media used, smaller NPs were shown to incorporate higher concentration of impurities.[75]

Besides metal and metal compound NPs, LAL approach has also been applied to fabricate nanostructures with more complex structures.[18] The technique showed potential as a relatively simple, versatile, and promising technique for the synthesis of diverse nanostructures with different chemistries and morphologies, hollow and core/shell NPs,[76,77] heterostructures,[78] 1D nanowires,[79] 2D layered nanocomposites,[80] and the nanoarchitectures derived from them.[81]

2.1.5 *Relevant Applications*

Many applications have been developed starting from nanoparticles obtained by LAL; those relevant to the present thesis are reported in the following paragraph.

Semiconductor NPs for Luminescence Applications

Laser ablation in liquid has been widely applied for the fabrication of luminescent semiconductor NPs, which have attracted much attention due to their broad range of interesting applications.[8,50,82,83] Because of the possibility of non-equilibrium thermodynamic situations present in the LAL process (transient plasma process with high temperatures and pressures, ultrafast chemical reactions, high-rate thermal quenching), high-density defects, uncommon micro-structures, and metastable phases have been often reported for LAL-generated NPs.[84] That is why semiconductor NPs, such as ZnO, Si, SiC, and W_2C, prepared by this technique have been reported to exhibit unique photoluminescence properties that are different from those observed from NPs by conventional methods.[85–87] The strong violet photoluminescence peaks (425 nm) of Zn/ZnO core/shell NPs prepared by LAL is an example.[88] Indeed, while the most typical emission of ZnO appears as a green band (520-550 nm), the ZnO emission in the violet-blue spectral range is very rare and indicates the existence of unusual defect states due to unique features of LAL as synthetic method. The violet-blue light emission demonstrated by the LAL-generated Zn/ZnO NPs and the possibility to tune their emission properties within a large spectral range by changing laser ablation parameters make such materials very beneficial for applications in light emitters, display devices, and biological labelling.[8,16,18] Alternatively, LAL can be used to fabricate doped and complex highly luminescent oxide NPs (such as sesquioxydes, oxysulfides, silicates, and tantalates)[87,89] due to the strong ablating ability of laser beam, very useful for applications such as biolabeling or anticounterfeit marking.[90] Importantly, hybrid inorganic/organic LED made of Si QDs by LAL has

shown outstanding performance, with current and optical power densities about 300 times those of such devices reported previously.[91] More recently, laser ablation in liquid was applied to lead halide perovskite materials for LED and solar cell applications, [92–95] confirming the technique as a viable and sustainable top-down approach to produce NCs of these promising and innovative class of semiconductors. More details will be provided in Chapter 6.

Other Applications

Bioconjugated NPs have attracted increasingly more attention as convenient and relevant analytical tools for biological and medical applications. If certain surfactants, polymers, or biomolecules are added into the liquid medium, both during (in-situ) or after (as post-treatment) laser ablation in liquid, the conjugation onto NPs surface can be easily realized.[63,64] In this way, many applications can be explored by attaching different molecules/species to the naked surface of NPs such as cell targeting,[96] for sensing and diagnosis,[97] for drug monitoring,[98] and also for photothermal therapy.[99] In addition, theragnostic nanosystems can be obtained by multiple functionalization approaches.[16] Thanks to its high selectivity and sensitivity, surface enhanced Raman scattering has rapidly grown as a powerful tool to detect chemical and biomolecule traces for the environmental pollution monitoring.[100,101] In this context, because of their purer surfaces, noble metal NPs prepared by LAL were demonstrated to perform better as components of surface enhanced Raman scattering active substrate when compared with their chemically obtained counterparts, also showing a good reproducibility.[52,102]

In addition to the above-mentioned applications, various LAL-generated nanostructures can also be used in photocatalysis,[103] reduction of heavy metal ions,[104] gas sensing and ferromagnetic response.[105,106] One of typical problems faced in catalytic applications of transition metal NPs is their instability towards aggregation and formation of larger particles, which changes the catalytic properties or even can lead to inactive materials. Very importantly, higher colloidal stability of transition metal NPs by LAL can solve the issues of nanoparticles aggregation.[107] Moreover, since all materials suitable for fluorescent, photoconductive, or energy harvesting applications, as well as those used in batteries[108] or as bone implants,[109] can be converted into their NPs via the laser ablation of their pellets or via the laser-induced melting and fragmentation of liquid suspended powders, LAL technique has the potential to prepare nanomaterials for a very wide range of applications (Figure 2.5).[16]

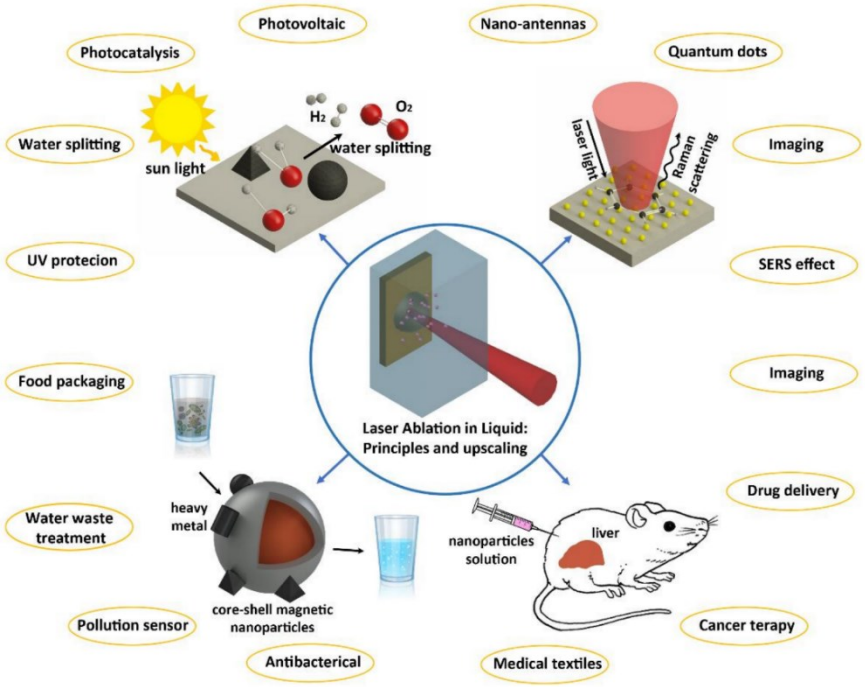

Figure 2.5 Schematic of fundamentals and up-scaling applications of NPs produced by laser ablation in liquid.[16]

2.2 Scaling/Control Factors for Laser Ablation under Liquids

Applications usually need enough colloidal solutions and the parameters for the productivity of these solutions need to be well understood. LAL process parameters are adjustable and related to the laser (ablation time, laser irradiance, and repetition rate), the optical setup (in particular the laser focusing), the ablation chamber (where the liquid over the solid and/or the total volume are relevant parameters to evaluate), the fluid flow elements (if present), and the liquid environment (density, surface tension and viscosity).[16,110,111] The concentration of suspended NPs and the dynamics of cavitation bubble generated by the laser pulse are also other important parameters to take into account.[18] Since the relatively low product yield is one of the main disadvantages associated with LAL, NPs productivity need to be optimized. The latter is defined as the volume of product achieved in a defined irradiation time (considering energy efficiency, additional reference values like the laser power become relevant as well). The only, obvious solution for scaling up LAL-based synthesis is to optimize the synthesis to get enhanced output. In literature, ablation rate is frequently used for productivity comparisons and corresponds to the loss of target volume achieved in a defined irradiation time. A process is defined with the input parameters and characterized by an output, namely the NPs and their colloidal solutions. In Figure 2.6 is reported a scheme for recalling the relevant parameters to take into account in a LAL process.[16] Some of them will be elucidated in the following sections.

2.1.1 *Laser Wavelength*

The laser wavelength essentially influences the ablation rate.[112,113] All studies agree, independently from the ablated material, that the chosen liquid and the used laser pulse duration led to higher ablation yields by using IR laser light compared to UV or Vis. Such difference in productivity is most likely caused by NP-induced shielding due to Rayleigh scattering,[114] which indeed depends on laser wavelength. The NPs absorption cross-section is strictly correlated to wavelength too. For instance, NPs of nearly all metals have higher absorption cross-section at UV or Vis wavelengths compared to IR one.[115] The above wavelength dependences are strongly indicated by the smaller NP diameters observed at shorter applied wavelengths,[113,116] which may be the result of fragmentation induced by subsequent laser pulses during LAL.

By comparing the concentration of NPs produced by LAL at different process times for IR and Vis wavelengths and three different metals it was shown how the respective ablation yield was similar for both wavelengths at short process times, while it increased differently with time or NPs concentration, although less strongly at short wavelengths.[117] These results clearly demonstrate the shielding effect of the colloidal NPs. Moreover, the individual light absorption properties of bulk materials influence the number of absorbed photons of different wavelengths and provide optimums for high ablation rates. However, the optical properties of an irradiated surface significantly depend on its temperature,[118] roughness,[119,120] and oxidation state/degree,[121] which change differently during LAL and strongly depend on the ablated material. This limits the a priori choice of the most productive wavelength for LAL according to the standard light absorption spectrum of the material to be ablated.

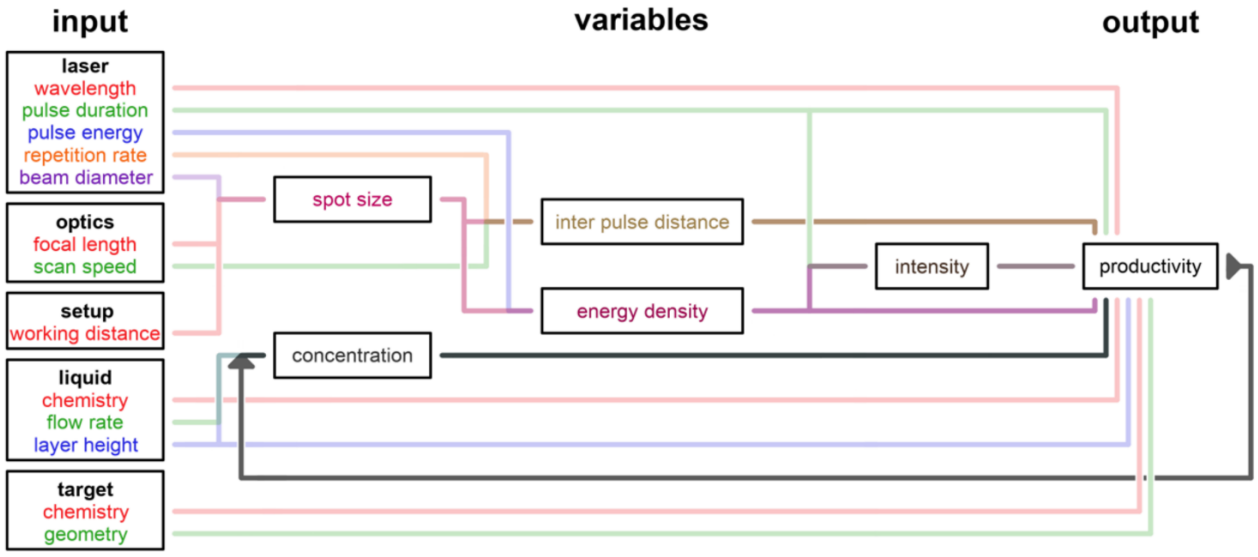

Figure 2.6 Graph highlighting the dependence of process parameters relevant to LAL up-scaling.[16]

For example, it may be concluded that higher ablation rates for metals generally occur at UV laser wavelengths due to their inter-band absorption.[16] However, the productivity at Vis and IR wavelengths can be comparable. This can be understood considering the strong dependence of the ablation on the laser pulse duration (Figure 2.7 a) and on high colloidal concentrations with higher absorbance and/or scattering at short wavelengths (Figure 2.7 b). The two conditions lead to a small dependence of the productivity on the laser wavelength. It should be also noticed that, for semiconducting and dielectric materials, the initial ablation rate in absence of a light-extinction colloid can be higher at red and near IR wavelengths under specific conditions due to differences in the ablation mechanism compared to metals.[122,123]

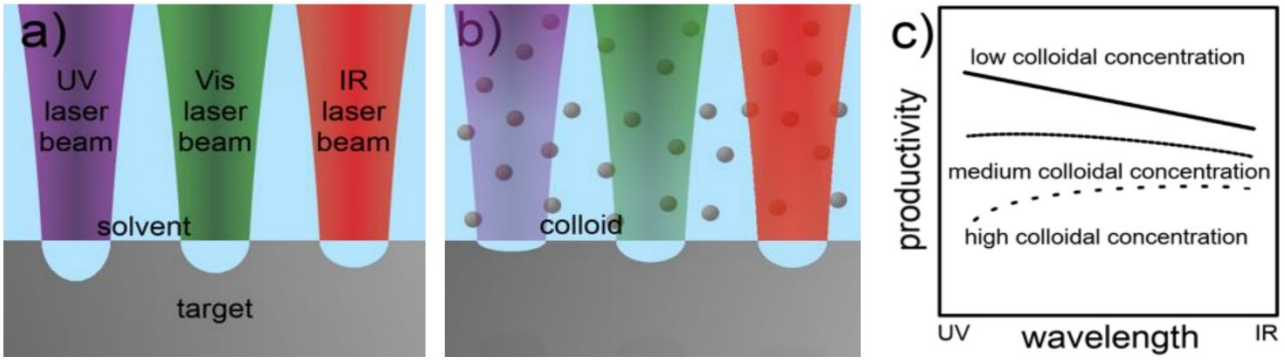

Figure 2.7 Schematic of the laser ablation of metals in liquids at different wavelengths a) in absence and b) in presence of colloidal particles (equal fluences were assumed for all cases). C) Diagram demonstrating the effect of an increasing colloidal concentration on the NPs productivity in LAL at different wavelengths (linear scales for both axes).[111]

2.1.2 *Laser Fluence*

The laser fluence or energy density describes the pulse energy penetrating the area of the effective laser spot on the surface of the ablation target. A variation of the laser fluence may be realized by either varying the pulse energy,[124,125] or the spot area via the working distance (Figure 2.8 a,b).[116,126] Different results by both procedures can occur due to variations of the beam propagation within the liquid phase. Furthermore, the distribution of the laser energy density in the spot of a Gaussian beam changes. The ablation yield in liquid, as well as in a gaseous environment, follows a logarithmic growth when increasing the laser fluence of fs-,[127] ps-,[128] and ns-pulses (Figure 2.8 c).[129] The onset of the saturation occurs at lower laser fluences for shorter laser pulse durations,[127] which may be due to higher laser intensities and the related optical breakdown of the liquid. The lowered thermal impact on the material, and therefore stronger independence of laser penetration depths and fluence at shorter laser pulse length, may also play a role here. In addition, the type of the ablated material influences the onset of the saturation in the ablation rate by different laser fluence

thresholds and penetration depths.[129,130] The conventional definition of productivity in LAL (volume ablation per time) can also be related to the applied laser energy. This extended definition allows an assessment of the energy efficiency, which seems reasonable from an economic and ecological point of view. Both theoretically and experimentally studies demonstrated that a maximum energy efficiency of pulsed laser ablation is reached at an optimum fluence, which depends on the material-specific threshold fluence of laser ablation.[131,132]-

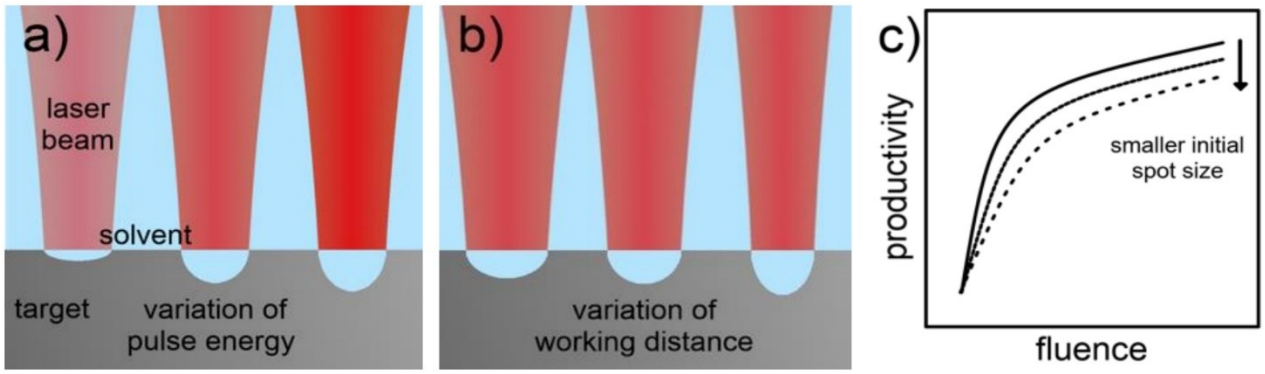

Figure 2.8 Illustration of laser ablation of metals in liquids at different fluences varied by a) the pulse energy and b) the working distance. c) Diagram demonstrating how the fluence variation caused by different spot sizes (assuming a Gaussian beam profile) affects the NP productivity in the high-fluence regime. Axes scale linearly.[111]

2.1.3 *Laser Pulse Duration*

The mechanism of laser ablation crucially depends on the pulse duration (Figure 2.9). The influence of moderate fluences on the ablation rate of metals in gaseous atmosphere can be well described by the two-temperature model for femtosecond and picosecond pulses,[133] and by a simple evaporation model at longer durations.[132] Extensions and refinements of the two-temperature model even allow accurate predictions of the ablation rate in the femtosecond-pulsed laser ablation of dielectrics.[134] Exchanging the gaseous ambient by a liquid causes a more intense cooling of the ablation target and of the LIP, which may affect the ablation process but should neither change the principal ablation mechanism nor invalidate the describing models. In principle, if a wide-range variation of the pulse duration would be possible (keeping the pulse energy constant), a more effective use of the energy of single laser pulses should occur at shorter pulse durations due to the reduced heat loss. However, the optical breakdown of the liquid in front of the ablation target, as well as non-linear optical effects such as the optical Kerr leading to filamentation limits the applicable fluence stronger at shorter laser pulses due to their higher intensities.[16] Interestingly, it was observed a decreasing ablation rate at an increasing pulse duration during the ns-pulsed laser ablation of copper in water (Figure 2.9 c),[135] although this effect did not occur during laser ablation in air.

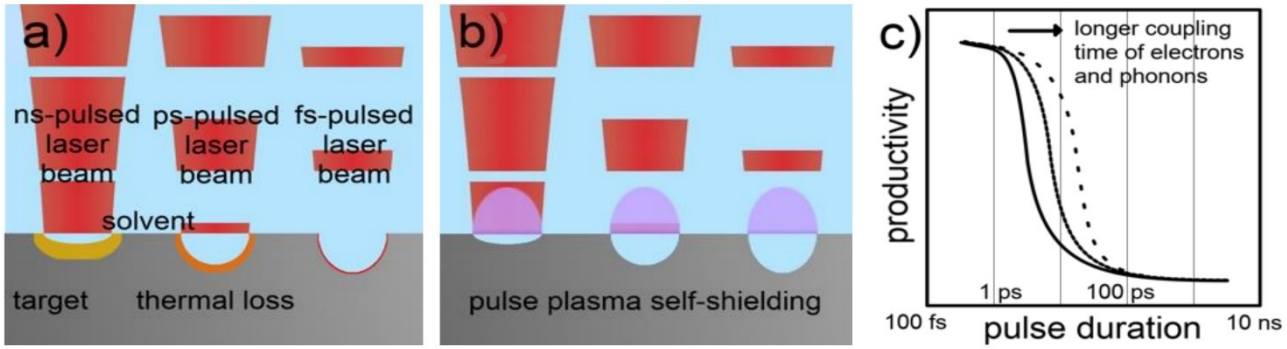

Figure 2.9 Illustration of the laser ablation of metals in liquids at different pulse durations neglecting non-linear effects. a) Thermal losses and b) self-shielding by plasma of pulses of different duration regimes. c) Diagram showing how the coupling constant of electrons and phonons affects the NPs productivity in LAL, depending on the laser pulse duration (y-axis scales linearly). A change in coupling constant was assumed to have no influence on other material properties.[111]

This finding confirms the origin of a negative impact of an increasing pulse duration on the ablation rate in the presence of the liquid environment. In another study, the absolute and power-specific productivity of laser ablation of gold in water was compared for different laser systems,[136] applying LAL in a liquid flow and with sufficient laser scanning to limit shielding effects. The results showed that even though the absolute productivity was the lowest for the low-power laser system, power-specific productivity was much higher compared to the other systems. Noticeably, while ablation rate was found to decrease by increasing the pulse duration in the fs time regime,[137,138] the threshold fluence for ablation rate becomes constant in the ns timescale.[139] Moreover, ablation rates become independent from the optical penetration depths using ns-pulses due to the more thermal ablation mechanism.[140] The thermal nature of the laser ablation intensifies at even longer pulse durations. Heat losses get more dominant, and the ablation rate is consequently reduced in these conditions.[141] In addition, the lifetime of the laser-induced plasma and the pulse duration act on a comparable time scale for laser pulses longer than 10÷100 ns, which intensifies a self-induced plasma shielding of single laser pulses. In conclusion, an optimum in the pulse duration for achieving a maximized ablation rate in LAL exists. It is probably located in the order of picoseconds.[124] As the productivity limitation at lower pulse durations stems from the optical breakdown of the liquid, the optimum of the pulse duration strongly depends on the laser intensity, wavelength, and the liquid.

2.1.4 *Laser Intensity*

Since there is a tight connection between laser intensity, laser fluence and pulse duration, a differentiation between each contribution is difficult. The optical breakdown of the liquid environment, which may significantly reduce the ablation rate, is usually related to the laser intensity. Additionally, self-focusing of the laser beam may be induced by the optical Kerr effect and

consequently increase the laser intensity. This may promote filamentation of the laser beam or an optical breakdown of the liquid. However, the intensity thresholds needed for the optical breakdown and the filament formation in liquid are comparable for fs-pulsed laser radiation.[142] For ps-pulses, the intensity threshold for filamentation is generally much higher than for the optical breakdown and becomes comparable only at low focusing angles.[143]

Due to higher electron densities, plasmas induced by ns-laser pulses more effectively shield later irradiation than plasmas induced by ps- or fs-pulses (Figure 2.10 a).[144] The intensity threshold for the optical breakdown of the liquid environment further depends on the chemical nature and the purity of the liquid (Figure 2.10 b). In the case of linear hydrocarbons, it was found a decrease in the breakdown threshold for an increasing chain length or molecular weight using IR, ns-pulses.[145] This is probably due to the increasing absorption cross-section of the hydrocarbons. The threshold intensities for the optical breakdown of different hydrocarbon aromatics at IR, nanosecond pulses are in the range of 25-50 kJ/cm^2.[16,146] Regarding impurities, it was demonstrated how particulate impurities in water and different alcohols act as seeds for the plasma formation in the laser-induced optical breakdown of the liquids.[147] In addition, the presence of soluble species also significantly reduces the intensity threshold of a liquid for its breakdown.[148,149] It must be assumed that NPs act as solutes or impurities in this context. In summary, the optical breakdown of the liquid environment in absence of an ablation target must be excluded for the applied laser parameters in LAL. Thereby it needs to be considered that colloidal particles and dissolved species reduce the breakdown threshold. Therefore, it should always be checked if an optical breakdown of the liquid occurs during LAL.

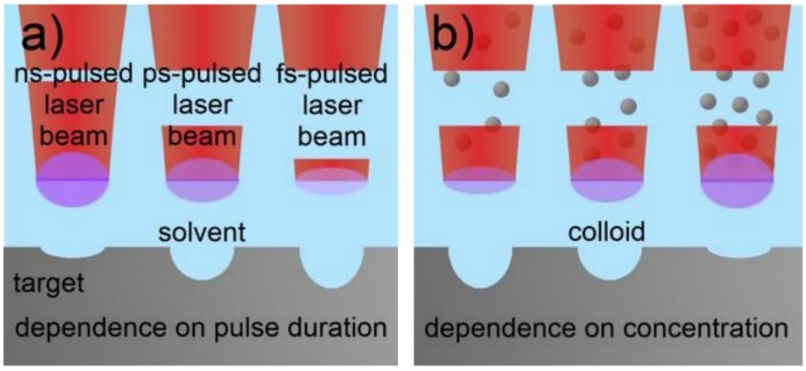

Figure 2.10 Illustration of the optical breakdown of the liquid during the laser ablation of metals in liquids at different intensities, neglecting non-linear effects. Dependence of the occurrence of the optical breakdown on the a) laser pulse duration and b) on the colloid concentration.[111]

2.1.5 *Spatial Inter-Pulse Distance*

The interaction of laser pulses with laser-induced plasma, bubble and particle species limits the NPs production in LAL. Whereas the shielding of a laser pulse by the self-induced plasma can only be reduced by using shorter pulse lengths, shielding effects induced by previous laser pulses can be reduced procedurally. The strategy is to spatially separate successive laser pulses by adjusting the interplay of the laser spot size, the scanning speed (moving target) and the pulse repetition rate to avoid shielding caused by the previous pulse (Figure 2.11).[125–127,150,151] Regarding ns-pulsed IR laser ablation in liquid, it was found that LAL productivity can be increased by reducing the spatial overlap of successive laser pulses by increasing the scanning speed.[125] The maximum productivity is reached at a specific inter-pulse distance achieving a full pulse separation, while a linear decrease in productivity was observed at higher distances. The thermal heating of the ablation target also influences the optimal inter-pulse distance.[16]

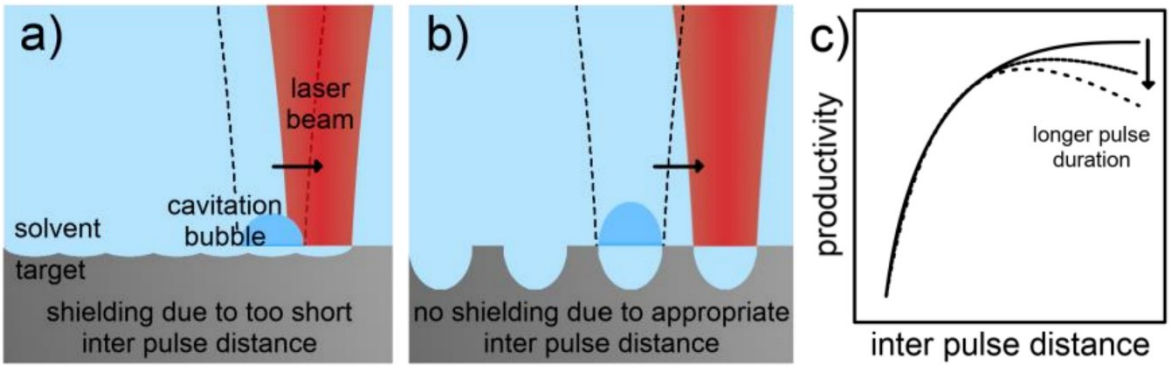

Figure 2.11 illustration of a) a too short and b) an optimum inter-pulse distance during laser ablation of metals in liquids. c) Diagram showing the relative effects of different laser pulse durations on the dependence of the productivity on the inter-pulse distance (both axes scale linearly).[111]

2.1.6 *Liquid Environment*

The relative motion,[152] layer height,[124,153] and physicochemical nature[113,154] of the liquid environment influence the productivity in LAL (Figure 2.12). A flowing liquid homogenizes the LAL products compared to a static fluid environment.[137,138] Despite the productivity of LAL can be optimized by varying the flow velocity of the liquid,[19] a dilution of the colloid must be accepted in parallel if LAL is applied continuously. The increase in productivity is probably caused by a faster transport of shielding species away from the ablation zone and an overall reduction of the concentration of shielding species. Consequently, the improvement of the productivity must saturate at a specific flow rate. Interestingly, the height of the liquid layer on top of the ablation target also has an impact on the productivity.[124,155]

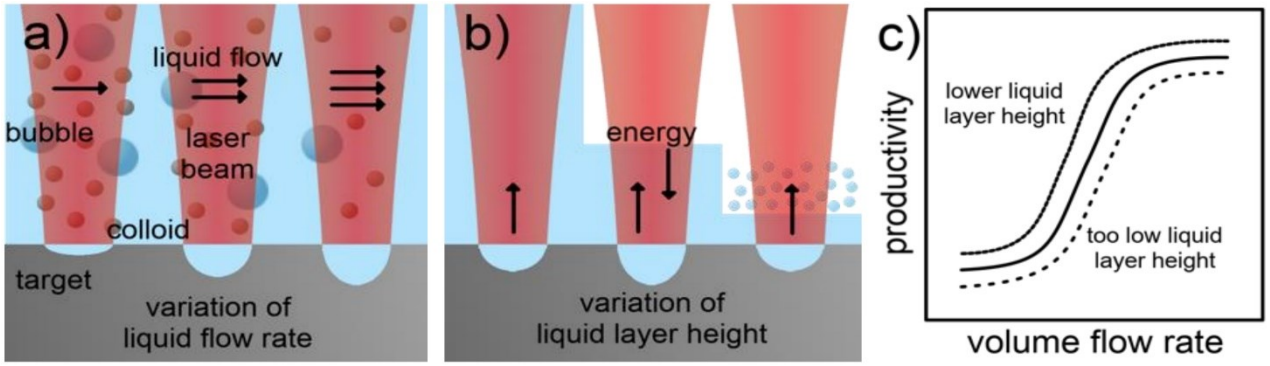

Figure 2.12 Illustration of the effect of a) the liquid flow rate and b) the liquid layer height on the productivity in the laser ablation of metals in liquids. c) Diagram showing the relative effects of different liquid layer heights on the dependence of the productivity on the volume flow rate (both axes scale linearly). Continuous lines show the effect of lower liquid layer height on the productivity, while dashed line shows the effect of a too low liquid layer height compared to the solid line, respectively.[111]

Confinement effects are assumed to be a reason for the generally higher productivity at lower liquid layer heights (e.g., shock waves generated in the ablation process could be reflected to the target from the liquid/air interface). In addition, the experimental implementation must also be considered. Especially for long ablation times and batch setups, the exponential absorption of the laser radiation by the nanoparticle colloid, described by the Beer–Lambert law, will be much stronger at high liquid levels. The compensation of the change in beam propagation induced by the refraction at the air/liquid interface is also important when changing the liquid layer height.[131] The productivity-limiting effect of explosive vaporization of the liquid at a critical minimum of the liquid layer height must also be considered.[156] The impact of the physicochemical nature of the liquid on the LAL yield is more complex. By comparing the ablation rate in the ns-pulsed, IR laser ablation of metals in different solvents at similar laser fluences, similar ablation rates were found in some solvents such as alcohols and acetone, while very different in others such as ethylene glycol and n-hexane.[157,158] The fundamental reasons for those differences in productivity remain unclear.

However, the reduced productivity could be correlated to intensified shielding of the laser beam by persistent bubbles.[153] The size and dwell time of cavitation bubbles depend on the viscosity of the liquid. Consequently, a higher viscosity promotes shielding and reduces the ablation rate. However, some low-viscous liquid (e.g., ethyl acetate) does not follow trend. Other factors such as the vapor pressure or the specific heat of vaporization should be considered to make the shielding by persistent bubbles more predictive.[16] In addition, no significant difference was found in the ablation-effective spot diameter and the amount of reflected laser energy. However, the plasma radiation in different liquids qualitatively mirrored the productivity. To summarize, the productivity of LAL can be improved by applying a liquid flow, by choosing a low liquid level, and by performing

LAL in water. In specific cases, water undesirably alters the properties of the NPs, for instance, by oxidation. Low-viscous organic solvents like ethanol or acetone represent the best alternatives in such a case.

2.1.7 *Target Geometry*

There are three dimensions to vary on the geometry of a bulk ablation target. By reducing single dimensions of a bulk to sizes comparable to the laser spot, the available target geometries include foils, wires, and particles. Many authors investigated the impact of the dimensional reduction of the ablation target on the productivity. A decrease in the productivity was observed when ablating metal foils with thicknesses < 0.1 mm immersed in aqueous solution,[159] finding debris of the metal in the so-obtained colloids (Figure 2.13 a). LAL of wires led to ablation rates higher by a factor of 15 if compared to the bulk target.[160] A confinement of heat in the wire and differing cavitation bubble dynamics were named to cause the improved productivity (Figure 2.13 b).[155]

In conclusion, a higher productivity of laser ablation in liquid can be accessed when ablating macroscopic metal targets compared to thin foils (Figure 2.13 c). However, the highest LAL productivity in ns-pulsed metal ablation should be achievable with wires due to heat confinement. An optimal wire diameter exists, probably in dependence on laser parameters. Heat confinement in the ablation target plays a minor role in ultrashort-pulsed laser ablation of metals, making wire ablation less advantageous in such conditions.

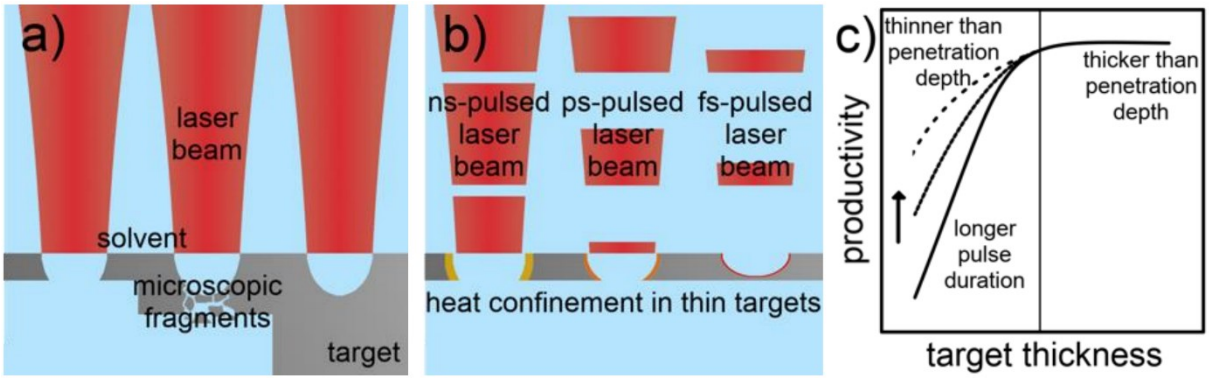

Figure 2.13 Illustration of a) the effect of target thickness in the laser ablation of metals in liquids and b) the influence of laser pulse duration on the heat confinement in thin targets. c) Diagram demonstrating the relative effects of different laser pulse duration on the dependence of the productivity on the ablation target thickness (both axes scale linearly) The arrow and thinner line indicate the effect of longer pulse duration on productivity, while the vertical solid line in the center marks the penetration depths of the laser pulse into the target material.[111]

2.1.8 *Other Relevant Parameters*

The amount of productivity-effective process parameters and variables in laser ablation in liquid is extensive and hard to cover due to the variety and the existing cross-dependencies between the parameters and variables. In addition, the relevant literature does not provide the data required for a productivity evaluation in a full-range parameter variation, not even for a single laser system. Furthermore, important studies on the impact of the pulse duration on the productivity investigated only one material and one liquid environment, in which neither scanning of the laser beam nor a liquid flow were applied.[128] Other important aspects to consider are the limitations given by the equipment and the desired product. In the specific cases in which oxidation states or NPs size distributions are required, laser ablation probably needs to be performed at specific laser parameters and in a particular liquid. However, there is an optimum set of laser parameters of a specific laser system for each combination of ablation material and liquid environment. Ideally, this set is experimentally evaluated in each case productivity plays a major role.

References

(1) Ealias, A. M.; Saravanakumar, M. P. A Review on the Classification, Characterisation, Synthesis of Nanoparticles and Their Application. *IOP Conf. Ser. Mater. Sci. Eng.* **2017**, *263* (3), 0–15. https://doi.org/10.1088/1757-899X/263/3/032019.

(2) Neri, G.; Fazio, E.; Mineo, P. G.; Scala, A.; Piperno, A. SERS Sensing Properties of New Graphene/Gold Nanocomposite. *Nanomaterials* **2019**, *9* (9), 1–13. https://doi.org/10.3390/nano9091236.

(3) Wolfsteller, A.; Geyer, N.; Nguyen-Duc, T. K.; Das Kanungo, P.; Zakharov, N. D.; Reiche, M.; Erfurth, W.; Blumtritt, H.; Kalem, S.; Werner, P.; et al. Comparison of the Top-down and Bottom-up Approach to Fabricate Nanowire-Based Silicon/Germanium Heterostructures. *Thin Solid Films* **2010**, *518* (9), 2555–2561. https://doi.org/10.1016/j.tsf.2009.08.021.

(4) Bera, D.; Qian, L.; Tseng, T. K.; Holloway, P. H. Quantum Dots and Their Multimodal Applications: A Review. *Materials (Basel).* **2010**, *3* (4), 2260–2345. https://doi.org/10.3390/ma3042260.

(5) Benjamin Damilano, Pierre-Marie Coulon, Stéphane Vézian, Virginie Brändli, Jean-Yves Duboz, J. M. and P. A. S. Top-down Fabrication of GaN Nano-Laser Arrays by Displacement Talbot Lithography and Selective Area Sublimation. *Appl. Phys. Express* **2019**, *12*, 045007–045012. https://doi.org/10.7567/1882-0786/ab0d32.

(6) Kuzmin, P. G.; Shafeev, G. A.; Bukin, V. V.; Garnov, S. V.; Farcau, C.; Carles, R.; Warot-Fontrose, B.; Guieu, V.; Viau, G. Silicon Nanoparticles Produced by Femtosecond Laser Ablation in Ethanol: Size Control, Structural Characterization, and Optical Properties. *J. Phys. Chem. C* **2010**, *114* (36), 15266–15273. https://doi.org/10.1021/JP102174Y.

(7) Szefler, B. Nanotechnology, from Quantum Mechanical Calculations up to Drug Delivery. *Int. J. Nanomedicine* **2018**, *13*, 6143–6176. https://doi.org/10.2147/IJN.S172907.

(8) Zhang, D.; Gökce, B.; Barcikowski, S. Laser Synthesis and Processing of Colloids: Fundamentals and Applications. *Chem. Rev.* **2017**, *117* (5), 3990–4103. https://doi.org/10.1021/acs.chemrev.6b00468.

(9) Malinauskas, M.; Žukauskas, A.; Hasegawa, S.; Hayasaki, Y.; Mizeikis, V.; Buividas, R.; Juodkazis, S. Ultrafast Laser Processing of Materials: From Science to Industry. *Sci. Appl.* **2016**, *5*, e16133–e16146. https://doi.org/10.1038/lsa.2016.133.

(10) Petridis, C.; Savva, K.; Kymakis, E.; Stratakis, E. Laser Generated Nanoparticles Based Photovoltaics. *J. Colloid Interface Sci.* **2017**, *489*, 28–37. https://doi.org/10.1016/j.jcis.2016.09.065.

(11) Zang, X.; Jian, C.; Zhu, T.; Fan, Z.; Wang, W.; Wei, M.; Li, B.; Diaz, M. F.; Ashby, P.; Lu, Z.; et al. Laser-Sculptured Ultrathin Transition Metal Carbide Layers for Energy Storage and Energy Harvesting Applications. *Nat. Commun.* **2019**, *10*. https://doi.org/10.1038/s41467-019-10999-z.

(12) Xie, B.; Wang, Y.; Lai, W.; Lin, W.; Lin, Z.; Zhang, Z.; Zou, P.; Xu, Y.; Zhou, S.; Yang, C.; et al. Laser-Processed Graphene Based Micro-Supercapacitors for Ultrathin, Rollable, Compact and Designable Energy Storage Components. *Nano Energy* **2016**, *26*, 276–285. https://doi.org/10.1016/j.nanoen.2016.04.045.

(13) Tsuji, T.; Yahata, T.; Yasutomo, M.; Igawa, K.; Tsuji, M.; Ishikawa, Y.; Koshizaki, N. Preparation and Investigation of the Formation Mechanism of Submicron-Sized Spherical Particles of Gold Using Laser Ablation and Laser Irradiation in Liquids. *Phys. Chem. Chem. Phys.* **2013**, *15* (9), 3099–3107. https://doi.org/10.1039/C2CP44159D.

(14) Pyatenko, A.; Wang, H.; Koshizaki, N.; Tsuji, T. Mechanism of Pulse Laser Interaction with Colloidal Nanoparticles. *Laser Photon. Rev.* **2013**, *7* (4), 596–604. https://doi.org/10.1002/LPOR.201300013.

(15) Kucherik, A. O.; Ryabchikov, Y. V.; Kutrovskaya, S. V.; Al-Kattan, A.; Arakelyan, S. M.; Itina, T. E.; Kabashin, A. V. Cavitation-Free Continuous-Wave Laser Ablation from a Solid Target to Synthesize Low-Size-Dispersed Gold Nanoparticles. *ChemPhysChem* **2017**, *18* (9), 1185–1191. https://doi.org/10.1002/CPHC.201601419.

(16) Fazio, E.; Gökce, B.; De Giacomo, A.; Meneghetti, M.; Compagnini, G.; Tommasini, M.; Waag, F.; Lucotti, A.; Zanchi, C. G.; Ossi, P. M.; et al. Nanoparticles Engineering by Pulsed Laser Ablation in Liquids: Concepts and Applications. *Nanomaterials* **2020**, *10* (11), 1–50. https://doi.org/10.3390/nano10112317.

(17) Gonzaíez-Rubio, G.; Liz-Marza, L. M. Reshaping, Fragmentation, and Assembly of Gold Nanoparticles Assisted by Pulse Lasers. *Acc. Chem. Res.* **2016**, *49*, 678−686. https://doi.org/10.1021/acs.accounts.6b00041.
(18) Zeng, H.; Du, X. W.; Singh, S. C.; Kulinich, S. A.; Yang, S.; He, J.; Cai, W. Nanomaterials via Laser Ablation/Irradiation in Liquid: A Review. *Adv. Funct. Mater.* **2012**, *22* (7), 1333–1353. https://doi.org/10.1002/adfm.201102295.
(19) Streubel, R.; Bendt, G.; Gökce, B. Pilot-Scale Synthesis of Metal Nanoparticles by High-Speed Pulsed Laser Ablation in Liquids. *Nanotechnology* **2016**, *27*, 205602. https://doi.org/10.1088/0957-4484/27/20/205602.
(20) Lam, J.; Lombard, J.; Dujardin, C.; Ledoux, G.; Merabia, S.; Amans, D. Dynamical Study of Bubble Expansion Following Laser Ablation in Liquids. *Appl. Phys. Lett* **2016**, *108*, 074104–074108. https://doi.org/10.1063/1.4942389.
(21) Itina, T. E. On Nanoparticle Formation by Laser Ablation in Liquids. *J. Phys. Chem. C* **2011**, *115*, 5044–5048. https://doi.org/10.1021/jp1090944.
(22) Huang, H.; Zhigilei, L. V; Kanitz, A.; Kalus, M.-R.; Gurevich, E. L.; Ostendorf, A.; Barcikowski, S.; Amans, D. Review on Experimental and Theoretical Investigations of the Early Stage, Femtoseconds to Microseconds Processes during Laser Ablation in Liquid-Phase for the Synthesis of Colloidal Nanoparticles. *Plasma Sources Sci. Technol.* **2019**, *28*, 103001–103034. https://doi.org/10.1088/1361-6595/ab3dbe.
(23) Schwenke, A.; Wagener, P.; Nolte, S.; Barcikowski, S.; Nolte, S.; Barcikowski, S. Influence of Processing Time on Nanoparticle Generation during Picosecond-Pulsed Fundamental and Second Harmonic Laser Ablation of Metals in Tetrahydrofuran. *Appl Phys A* **2011**, *104*, 77–82. https://doi.org/10.1007/s00339-011-6398-9.
(24) Kim, M.; Osone, S.; Kim, T.; Higashi, H.; Seto, T. Synthesis of Nanoparticles by Laser Ablation: A Review. *KONA Powder Part. J.* **2017**, *2017* (34), 80–90. https://doi.org/10.14356/kona.2017009.
(25) MAIMAN, T. H. Stimulated Optical Radiation in Ruby. *Nature* **1960**, *187*, 493–494.
(26) Hashida, M.; Mishima, H.; Tokita, S.; Sakabe, S. Non-Thermal Ablation of Expanded Polytetrafluoroethylene with an Intense Femtosecond-Pulse Laser. *Opt. Express* **2009**, *17*, 13116–13121.
(27) Chakraborty, S.; Sakata, H.; Yokoyama, E.; Wakaki, M.; Chakravorty, D. Laser-Induced Forward Transfer Technique for Maskless Patterning of Amorphous V2O5 Thin Film. *Appl. Surf. Sci.* **2007**, *254* (2), 638–643. https://doi.org/10.1016/j.apsusc.2007.06.066.
(28) Turner, A. F.; Smith, H. M. Vacuum Deposited Thin Films Using a Ruby Laser. *Appl. Opt.* **1965**, *4* (1), 147–148. https://doi.org/10.1364/AO.4.000147.
(29) Neddersen, J.; Chumanov, G.; Cotton, T. M. Laser Ablation of Metals: A New Method for Preparing SERS Active Colloids. *Appl. Spectrosc.* **1993**, *47* (12), 1959–1964. https://doi.org/10.1366/0003702934066460.
(30) Amendola, V.; Meneghetti, M. Laser Ablation Synthesis in Solution and Size Manipulation of Noble Metal Nanoparticles. *Phys. Chem. Chem. Phys.* **2009**, *11* (20), 3805–3821. https://doi.org/10.1039/b900654k.
(31) Shih, C.-Y.; Streubel, R.; Heberle, J.; Letzel, A.; Shugaev, M. V; Wu, C.; Schmidt, M.; Gökce, B.; Barcikowski, S.; Zhigilei, L. V. Two Mechanisms of Nanoparticle Generation in Picosecond Laser Ablation in Liquids: The Origin of the Bimodal Size Distribution. *Nanoscale* **2018**, *10*, 6900–6910. https://doi.org/10.1039/c7nr08614h.
(32) Giacomo, A. De; Casavola, A. R.; Colonna, G.; Capitelli, M.; Pascale, O. De. Experimental and Theoretical Investigation of Laser-Induced Plasma of a Titanium Target. *Appl. Opt. Vol. 42, Issue 30, pp. 5963-5970* **2003**, *42* (30), 5963–5970. https://doi.org/10.1364/AO.42.005963.
(33) Chemin, A. A.; Lam, J.; Etan Laurens, G.; Trichard, F.; Motto-Ros, V.; Ledoux, G.; Itězslavıtˇıtězslav Jar´y, V. ´; Jar´y, J.; Laguta, V.; Nikl, M.; et al. Doping Nanoparticles Using Pulsed Laser Ablation in a Liquid Containing the Doping Agent. *Nanoscale Adv.* **2019**, *1*, 3963–3972. https://doi.org/10.1039/c9na00223e.
(34) Gökce, B.; Streubel, R.; Barcikowski, S. Continuous Multigram Nanoparticle Synthesis by High-Power, High-Repetition-Rate Ultrafast Laser Ablation in Liquids. *Opt. Lett.* **2016**, *41* (7), 1486–1489.

https://doi.org/10.1364/OL.41.001486.
(35) Wagener, P.; Barcikowski, S. Laser Fragmentation of Organic Microparticles into Colloidal Nanoparticles in a Free Liquid Jet. *Appl Phys A* **2010**, *101*, 435–439. https://doi.org/10.1007/s00339-010-5814-x.
(36) Dell, M.; De Giacomo, A.; Kohsakowski, S.; -, al; Hermann -, J.; Taccogna, F.; Dell, M.; Rutigliano, M.; Valenza, G.; De Giacomo, A. On the Growth Mechanism of Nanoparticles in Plasma during Pulsed Laser Ablation in Liquids. *Plasma Sources Sci. Technol* **2017**, *26*, 045002–045011. https://doi.org/10.1088/1361-6595/aa595b.
(37) Gornushkin, I. B.; Dell'Aglio, M.; Motto-Ros, V.; Pelascini, F.; De Giacomo, A. Investigation on the Material in the Plasma Phase by High Temporally and Spectrally Resolved Emission Imaging during Pulsed Laser Ablation (PLAL) in Liquid for NPs Production and Consequent Considerations on NPs Formation. *Plasma Sources Sci. Technol.* **2019**, *28* (8), 085017. https://doi.org/10.1088/1361-6595/AB369B.
(38) Zeng, H.; Zhi, C.; Zhang, Z.; Wei, X.; Wang, X.; Guo, W.; Bando, Y.; Golberg, D. "White Graphenes": Boron Nitride Nanoribbons via Boron Nitride Nanotube Unwrapping. *Nano Lett.* **2010**, *10*, 5049–5055. https://doi.org/10.1021/nl103251m.
(39) Liu, P.; Cao, Y. L.; Wang, C. X.; Chen, X. Y.; Yang, G. W. Micro-and Nanocubes of Carbon with C 8-like and Blue Luminescence. *Nano Lett.* **2008**, *8* (8), 2570–2575. https://doi.org/10.1021/nl801392v.
(40) Hu, S.; Sun, J.; Du, X.; Tian, F.; Jiang, L. The Formation of Multiply Twinning Structure and Photoluminescence of Well-Dispersed Nanodiamonds Produced by Pulsed-Laser Irradiation. *Diam. Relat. Mater.* **2008**, *17* (2), 142–146. https://doi.org/10.1016/j.diamond.2007.11.009.
(41) Hu, S.; Zhang, J.; Yang, J.; Liu, J.; Cao, S. Theoretical Analysis of the Formation of Face-Centered Cubic Si Nanocrystals by Magnetron Sputtering. *Appl. Phys. Lett* **2011**, *99*, 151901. https://doi.org/10.1063/1.3651485.
(42) Dell'Aglio, M.; De Giacomo, A.; Dell'Aglio, M.; De Giacomo, A. Plasma Charging Effect on the Nanoparticles Releasing from the Cavitation Bubble to the Solution during Nanosecond Pulsed Laser Ablation in Liquid. *ApSS* **2020**, *515*, 146031. https://doi.org/10.1016/J.APSUSC.2020.146031.
(43) Lauterborn, W.; Vogel, A. *A. Shock Wave Emission by Laser Generated Bubbles - Bubble Dynamics and Shock Waves*; Delale, C. F., Ed.; Springer, 2013. https://doi.org/10.1007/978-3-642-34297-4_1.
(44) Reich, S.; Letzel, A.; Gökce, B.; Menzel, A.; Barcikowski, S.; Plech, A. Incubation Effect of Pre-Irradiation on Bubble Formation and Ablation in Laser Ablation in Liquids. *ChemPhysChem* **2019**, *20* (8), 1036–1043. https://doi.org/10.1002/CPHC.201900075.
(45) Takata, T.; Enoki, M.; Chivavibul, P.; Matsui, A.; Kobayashi, Y. Effect of Confinement Layer on Laser Ablation and Cavitation Bubble during Laser Shock Peening. *Mater. Trans.* **2016**, *57* (10), 1776–1783. https://doi.org/10.2320/matertrans.M2016150.
(46) Brenner, M. P.; Hilgenfeldt, S.; Lohse, D. Single-Bubble Sonoluminescence. *Rev. Mod. Phys.* **2002**, *74* (2), 425. https://doi.org/10.1103/RevModPhys.74.425.
(47) Casavola, A.; De Giacomo, A.; Dell'Aglio, M.; Taccogna, F.; Colonna, G.; De Pascale, O.; Longo, S. Experimental Investigation and Modelling of Double Pulse Laser Induced Plasma Spectroscopy under Water. *Spectrochim. Acta - Part B At. Spectrosc.* **2005**, *60* (7–8), 975–985. https://doi.org/10.1016/j.sab.2005.05.034.
(48) Giusti, A.; Giorgetti, E.; Laza, S.; Marsili, P.; Giammanco, F.; Pontecorvo, B. Multiphoton Fragmentation of PAMAM G5-Capped Gold Nanoparticles Induced by Picosecond Laser Irradiation at 532 Nm. *J. Phys. Chem. C* **2007**, *111*, 14984–14991. https://doi.org/10.1021/jp072611k.
(49) Werner, D.; Hashimoto, S. Improved Working Model for Interpreting the Excitation Wavelength-and Fluence-Dependent Response in Pulsed Laser-Induced Size Reduction of Aqueous Gold Nanoparticles. *J. Phys. Chem. C* **2011**, *115*, 5063–5072. https://doi.org/10.1021/jp109255g.
(50) Zeng, H.; Yang, S.; Cai, W. Reshaping Formation and Luminescence Evolution of ZnO Quantum Dots by Laser-Induced Fragmentation in Liquid. *J. Phys. Chem. C* **2011**, *115*, 5038–5043. https://doi.org/10.1021/jp109010c.
(51) Mafuné, F.; Kohno, J.-Y.; Takeda, Y.; Kondow, T. Formation of Gold Nanonetworks and Small Gold Nanoparticles by Irradiation of Intense Pulsed Laser onto Gold Nanoparticles. *J. Phys. Chem. B* **2003**, *107*, 2589–12596. https://doi.org/10.1021/jp030173l.

(52) Mafuné, F.; Kohno, J.-Y.; Takeda, Y.; Kondow, T. Formation of Stable Platinum Nanoparticles by Laser Ablation in Water. *J. Phys. Chem. B* **2003**, No. 107, 4218–4223. https://doi.org/10.1021/jp021580k.
(53) Singh, S. C.; Mishra, S. K.; Srivastava, R. K.; Gopal, R. Optical Properties of Selenium Quantum Dots Produced with Laser Irradiation of Water Suspended Se Nanoparticles. *J. Phys. Chem. C* **2010**, *114*, 17374–17384. https://doi.org/10.1021/jp105037w.
(54) Yamada, K.; Tokumoto, Y.; Nagata, T.; Mafuné, F. Mechanism of Laser-Induced Size-Reduction of Gold Nanoparticles as Studied by Nanosecond Transient Absorption Spectroscopy. *J. Phys. Chem. B* **2006**, *110*, 11751–11756. https://doi.org/10.1021/jp061020b.
(55) Muto, H.; Miyajima, K.; Mafuné, F. Mechanism of Laser-Induced Size Reduction of Gold Nanoparticles As Studied by Single and Double Laser Pulse Excitation. *J. Phys. Chem. C* **2008**, *112*, 5810–5815. https://doi.org/10.1021/jp711353m.
(56) Pyatenko, A.; Yamaguchi, M.; Suzuki, M. Mechanisms of Size Reduction of Colloidal Silver and Gold Nanoparticles Irradiated by Nd:YAG Laser. *J. Phys. Chem. C* **2009**, *113*, 9078–9085. https://doi.org/10.1021/jp808300q.
(57) Liu, P.; Wang, C. X.; Chen, X. Y.; Yang, G. W. Controllable Fabrication and Cathodoluminescence Performance of High-Index Facets GeO2 Micro-and Nanocubes and Spindles upon Electrical-Field-Assisted Laser Ablation in Liquid. *J. Phys. Chem. C* **2008**, *112*, 13450–13456. https://doi.org/10.1021/jp802529r.
(58) Liu, P.; Cao, Y. L.; Chen, X. Y.; Yang, G. W. Trapping High-Pressure Nanophase of Ge upon Laser Ablation in Liquid. *Cryst. Growth Cryst. Des.* **2009**, *9* (3), 1390–1393. https://doi.org/10.1021/cg800633j.
(59) Skov, K. S.; Blanka, ^; Ckov, V.; Turpin, P.-Y.; Thorel, A.; Proch, M. Laser Ablation of Silver in Aqueous Solutions of Organic Species: Probing Ag Nanoparticle-Adsorbate Systems Evolution by Surface-Enhanced Raman and Surface Plasmon Extinction Spectra. *J. Phys. Chem. C* **2011**, *115*, 5404–5412. https://doi.org/10.1021/jp110907d.
(60) Cristoforetti, G.; Pitzalis, E.; Spiniello, R.; Ishak, R.; Muniz-Miranda, M. Production of Palladium Nanoparticles by Pulsed Laser Ablation in Water and Their Characterization. *J. Phys. Chem. C* **2011**, *115*, 5073–5083. https://doi.org/10.1021/jp109281q.
(61) Muniz-Miranda, M.; Gellini, C.; Giorgetti, E. Surface-Enhanced Raman Scattering from Copper Nanoparticles Obtained by Laser Ablation. *J. Phys. Chem. C* **2011**, *115*, 5021–5027. https://doi.org/10.1021/jp1086027.
(62) Petersen, S.; Barcikowski, S. In Situ Bioconjugation: Single Step Approach to Tailored Nanoparticle-Bioconjugates by Ultrashort Pulsed Laser Ablation. *Adv. Funct. Mater.* **2009**, *19* (8), 1167–1172. https://doi.org/10.1002/ADFM.200801526.
(63) Petersen, S.; Barchanski, A.; Taylor, U.; Klein, S.; Rath, D.; Barcikowski, S.; Laser, ‡ ‡; Hannover, Z. Penetratin-Conjugated Gold Nanoparticles-Design of Cell-Penetrating Nanomarkers by Femtosecond Laser Ablation. *J. Phys. Chem. C* **2011**, *115*, 5152–5159. https://doi.org/10.1021/jp1093614.
(64) Zeng, H.; Cui, J.; Cao, B.; Gibson, U.; Bando, Y.; Golberg, D. Electrochemical Deposition of ZnO Nanowire Arrays: Organization, Doping, and Properties. *Sci. Adv. Mater.* **2010**, *2* (3), 336–358. https://doi.org/10.1166/SAM.2010.1096.
(65) Fischer, M.; Hormes, J.; Marzun, G.; Wagener, P.; Hagemann, U.; Barcikowski, S. In Situ Investigations of Laser-Generated Ligand-Free Platinum Nanoparticles by X-Ray Absorption Spectroscopy: How Does the Immediate Environment Influence the Particle Surface? *Langmuir* **2016**, *32*, 8793−8802. https://doi.org/10.1021/acs.langmuir.6b00685.
(66) Simã, T.; Chevallier, P.; Lagueux, J.; Cô, M.-F.; Rehbock, C.; Barcikowski, S.; Fortin, M.-A.; Guay, D. Laser-Synthesized Ligand-Free Au Nanoparticles for Contrast Agent Applications in Computed Tomography and Magnetic Resonance Imaging. *J. Mater. Chem. B* **2016**, *4*, 6413–6427. https://doi.org/10.1039/c6tb01162d.
(67) Yang, S.; Cai, W.; Liu, G.; Zeng, H. From Nanoparticles to Nanoplates: Preferential Oriented Connection of Ag Colloids during Electrophoretic Deposition. *J. Phys. Chem. C* **2009**, *113*, 7692–7696. https://doi.org/10.1021/jp901961h.
(68) Singh, S. C.; Gopal, R. Zinc Nanoparticles in Solution by Laser Ablation Technique. *Bull. Mater. Sci* **2007**, *30* (3), 291–293.

(69) Singh, S. C.; Swarnkar, R. K.; Gopal, R. Zn/ZnO Core/Shell Nanoparticles Synthesized by Laser Ablation in Aque-Ous Environment: Optical and Structural Characterizations. *Bull. Mater. Sci* **2010**, *33* (1), 21–26.
(70) C. Singh, S.; Gopal, R. Drop Shaped Zinc Oxide Quantum Dots and Their Self-Assembly into Dendritic Nanostructures: Liquid Assisted Pulsed Laser Ablation and Characterizations. *Appl. Surf. Sci.* **2012**, *258*, 2211–2218.
(71) Huang, C.-N.; Bow, J.-S.; Zheng, Y.; Chen, S.-Y.; New, •; Ho, J.; Shen, P. Nonstoichiometric Titanium Oxides via Pulsed Laser Ablation in Water. *Nanoscale Res. Lett.* **2010**, *5*, 972–985. https://doi.org/10.1007/s11671-010-9591-4.
(72) Zhang, X.; Zeng, H.; Cai, W. Laser Power Effect on Morphology and Photoluminescence of ZnO Nanostructures by Laser Ablation in Water. *Mater. Lett.* **2009**, *63*, 191–193.
(73) Singh, S. C. Effect of Oxygen Injection on the Size and Compositional Evolution of ZnO/Zn(OH) 2 Nanocomposite Synthesized by Pulsed Laser Ablation in Distilled Water. *J. Nanoparticle Res.* **2011**, *13*, 4143–4152. https://doi.org/10.1007/s11051-011-0359-2.
(74) Singh, S. C.; Gopal, R. Laser Irradiance and Wavelength-Dependent Compositional Evolution of Inorganic ZnO and ZnOOH/Organic SDS Nanocomposite Material. *J. Phys. Chem. C* **2008**, *112*, 2812–2819. https://doi.org/10.1021/jp0753676.
(75) Golightly, J. S.; Castleman, A. W. Analysis of Titanium Nanoparticles Created by Laser Irradiation under Liquid Environments. *J. Phys. Chem. B* **2006**, *110*, 19979–19984. https://doi.org/10.1021/jp062123x.
(76) Jim enez, E.; Abderrafi, K.; Abargues, R.; Vald es, J. L.; Martı, J. P. Laser-Ablation-Induced Synthesis of SiO 2-Capped Noble Metal Nanoparticles in a Single Step. *Langmuir* **2010**, *26* (10), 7458–7463. https://doi.org/10.1021/la904179x.
(77) Amendola, V.; Amans, D.; Ishikawa, Y.; Koshizaki, N.; Scirè, S.; Compagnini, G.; Reichenberger, S.; Barcikowski, S. Room-Temperature Laser Synthesis in Liquid of Oxide, Metal-Oxide Core-Shells, and Doped Oxide Nanoparticles. *Chem. - A Eur. J.* **2020**, *26* (42), 9206–9242. https://doi.org/10.1002/CHEM.202000686.
(78) Bajaj, G.; Soni, R. K. Synthesis of Composite Gold/Tin-Oxide Nanoparticles by Nano-Soldering. *J. Nanoparticle Res.* **2010**, *12*, 2597–2603. https://doi.org/10.1007/s11051-009-9836-2.
(79) Mollah, S. Laser Synthesis of Iron Oxide Nanowires. *Asian J. Chem.* **2009**, *21*, 10–12.
(80) He, C.; Sasaki, T.; Zhou, Y.; Shimizu, Y.; Masuda, M.; Koshizaki, N. Surfactant-Assisted Preparation of Novel Layered Silver Bromide-Based Inorganic/Organic Nanosheets by Pulsed Laser Ablation in Aqueous Media. *Adv. Funct. Mater.* **2007**, *17* (17), 3554–3561. https://doi.org/10.1002/ADFM.200700081.
(81) Lin, X. Z.; Liu, P.; Yu, J. M.; Yang, G. W. Synthesis of CuO Nanocrystals and Sequential Assembly of Nanostructures with Shape-Dependent Optical Absorption upon Laser Ablation in Liquid. *J. Phys. Chem. C* **2009**, *113*, 17543–17547. https://doi.org/10.1021/jp907237q.
(82) Yang, S.; Zeng, H.; Zhao, H.; Zhang, H.; Cai, W. Luminescent Hollow Carbon Shells and Fullerene-like Carbon Spheres Produced by Laser Ablation with Toluene. *J. Mater. Chem.* **2011**, *21*, 4432–4436. https://doi.org/10.1039/c0jm03475d.
(83) Chang, M.; Cao, X.; Zeng, H. Electrodeposition Growth of Vertical ZnO Nanorod/Polyaniline Heterostructured Films and Their Optical Properties. *J. Phys. Chem. C* **2009**, *113*, 15544–15547. https://doi.org/10.1021/jp903881d.
(84) Zeng, H.; Duan, G.; Li, Y.; Yang, S.; Xu, X.; Cai, W. Blue Luminescence of ZnO Nanoparticles Based on Non-Equilibrium Processes: Defect Origins and Emission Controls. *Adv. Funct. Mater.* **2010**, *20* (4), 561–572. https://doi.org/10.1002/ADFM.200901884.
(85) Zeng, H.; Cai, W.; Li, Y.; Hu, J.; Liu, P. Composition/Structural Evolution and Optical Properties of ZnO/Zn Nanoparticles by Laser Ablation in Liquid Media. *J. Phys. Chem. B* **2005**, *109*, 18260–18266. https://doi.org/10.1021/jp052258n.
(86) Zeng, H.; Li, Z.; Cai, W.; Cao, B.; Liu, P.; Yang, S. Microstructure Control of Zn/ZnO Core/Shell Nanoparticles and Their Temperature-Dependent Blue Emissions. *J. Phys. Chem. B* **2007**, *111*, 14311–14317. https://doi.org/10.1021/jp0770413.
(87) Yang, S.; Cai, W.; Zeng, H.; Li, Z. Polycrystalline Si Nanoparticles and Their Strong Aging Enhancement

of Blue Photoluminescence. *J. Appl. Phys.* **2008**, *104*, 023516–023520. https://doi.org/10.1063/1.2957053.

(88) Zeng, H.; Cai, W.; Hu, J.; Duan, G.; Liu, P.; Li, Y. Violet Photoluminescence from Shell Layer of Zn/ ZnO Core-Shell Nanoparticles Induced by Laser Ablation. *Appl. Phys. Lett.* **2006**, *88*, 171910–171912. https://doi.org/10.1063/1.2196051.

(89) Yang, S.; Cai, W.; Zhang, H.; Xu, X.; Zeng, H. Size and Structure Control of Si Nanoparticles by Laser Ablation in Different Liquid Media and Further Centrifugation Classification. *J. Phys. Chem. C* **2009**, *113*, 19091–19095. https://doi.org/10.1021/jp907285f.

(90) Kumar Gupta, B.; Haranath, D.; Saini, S. Facile and Rapid Synthesis of Highly Luminescent Nanoparticles via Pulsed Laser Ablation in Liquid. *Nanotechnology* **2009**, *20*, 445605–445612. https://doi.org/10.1088/0957-4484/20/44/445605.

(91) Xin, Y.; Nishio, K.; Saitow, K.-I. White-Blue Electroluminescence from a Si Quantum Dot Hybrid Light-Emitting Diode. *Appl. Phys. Lett.* **2015**, *106*, 201102–201106. https://doi.org/10.1063/1.4921415.

(92) Amendola, V.; Fortunati, I.; Marega, C.; Abdelhady, A. L.; Saidaminov, M. I.; Bakr, O. M. High-Purity Hybrid Organolead Halide Perovskite Nanoparticles Obtained by Pulsed-Laser Irradiation in Liquid. *ChemPhysChem* **2017**, *18* (9), 1047–1054. https://doi.org/10.1002/cphc.201600863.

(93) Lamberti, F.; Litti, L.; De Bastiani, M.; Sorrentino, R.; Gandini, M.; Meneghetti, M.; Petrozza, A. High-Quality, Ligands-Free, Mixed-Halide Perovskite Nanocrystals Inks for Optoelectronic Applications. *Advanced Energy Materials*. 2017. https://doi.org/10.1002/aenm.201601703.

(94) Rosa-Pardo, I.; Rando-Brotons, M.; Pocoví-Martínez, S.; Galian, R. E.; Pérez Prieto, J. Laser Ablation of Hybrid Perovskite Bulks into Nanoparticles: Adamantylammonium Halides as Ligands and Halide Sources. *ChemNanoMat* **2019**, *5* (3), 328–333. https://doi.org/10.1002/cnma.201800621.

(95) Sansoni, S.; De Bastiani, M.; Aydin, E.; Ugur, E.; Isikgor, F. H.; Al-Zahrani, A.; Lamberti, F.; Laquai, F.; Meneghetti, M.; De Wolf, S. Eco-Friendly Spray Deposition of Perovskite Films on Macroscale Textured Surfaces. *Adv. Mater. Technol.* **2020**, *5* (2). https://doi.org/10.1002/admt.201901009.

(96) Bertorelle, F.; Pinto, M.; Zappon, R.; Pilot, R.; Litti, L.; Fiameni, S.; Conti, G.; Gobbo, M.; Toffoli, G.; Colombatti, M.; et al. Safe Core-Satellite Magneto-Plasmonic Nanostructures for Efficient Targeting and Photothermal Treatment of Tumor Cells. *Nanoscale* **2018**, *10*, 976–984. https://doi.org/10.1039/c7nr07844g.

(97) Tedesco, A. Del; Piotto, V.; Sponchia, G.; Hossain, K.; Litti, L.; Peddis, D.; Scarso, A.; Meneghetti, M.; Benedetti, A.; Riello, P. Zirconia-Based Magnetoplasmonic Nanocomposites: A New Nanotool for Magnetic-Guided Separations with SERS Identification. *ACS Appl. Nano Mater.* **2020**, *3*, 1232−1241. https://doi.org/10.1021/acsanm.9b01982.

(98) Lucio Litti, Andrea Ramundo, Francesca Biscaglia, Giuseppe Toffoli, Marina Gobbo, M. M. A Surface Enhanced Raman Scattering Based Colloid Nanosensor for Developing Therapeutic Drug Monitoring. *J. Colloid Interface Sci.* **2019**, *533*, 621–626.

(99) Litti, L.; Rivato, N.; Fracasso, G.; Bontempi, P.; Nicolato, E.; Marzola, P.; Venzo, A.; Colombatti, M.; Gobbo, M.; Meneghetti, M. A SERRS/MRI Multimodal Contrast Agent Based on Naked Au Nanoparticles Functionalized with a Gd(III) Loaded PEG Polymer for Tumor Imaging and Localized Hyperthermia. *Nanoscale* **2018**, *10*, 1272–1278. https://doi.org/10.1039/c7nr07398d.

(100) Sharma, B.; Frontiera, R. R.; Henry, A. I.; Ringe, E.; Van Duyne, R. P. SERS: Materials, Applications, and the Future. *Mater. Today* **2012**, *15* (1–2), 16–25. https://doi.org/10.1016/S1369-7021(12)70017-2.

(101) Pilot, R.; Signorini, R.; Durante, C.; Orian, L.; Bhamidipati, M.; Fabris, L. A Review on Surface-Enhanced Raman Scattering. *Biosensors* **2019**, *9* (2). https://doi.org/10.3390/bios9020057.

(102) Procházka, M.; Mojzeš, P.; Stěpánek, J.; Vlčková, B.; Turpin, P.-Y. Probing Applications of Laser-Ablated Ag Colloids in SERS Spectroscopy: Improvement of Ablation Procedure and SERS Spectral Testing. *Anal. Chem.* **1987**, *69*, 5103–5108.

(103) Zeng, H.; Cai, W.; Liu, P.; Xu, X.; Zhou, H.; Klingshirn, C.; Kalt, H. ZnO-Based Hollow Nanoparticles by Selective Etching: Elimination and Reconstruction of Metal Semiconductor Interface, Improvement of Blue Emission and Photocatalysis. *ACS Nano* **2008**, *2* (8), 1661–1670. https://doi.org/10.1021/nn800353q.

(104) Yang, S.; Cai, W.; Liu, G.; Zeng, H.; Liu, P. Optical Study of Redox Behavior of Silicon Nanoparticles

Induced by Laser Ablation in Liquid. *J. Phys. Chem. C* **2009**, *113*, 6480–6484. https://doi.org/10.1021/jp810787d.

(105) Niu, K. Y.; Yang, J.; Kulinich, S. A.; Sun, J.; Du, X. W. Hollow Nanoparticles of Metal Oxides and Sulfides: Fast Preparation via Laser Ablation in Liquid. *Langmuir* **2010**, *26* (22), 16652–16657. https://doi.org/10.1021/la1033146.

(106) Niu, K. Y.; Yang, J.; Kulinich, S. A.; Sun, J.; Li, H.; Du, X. W. Morphology Control of Nanostructures via Surface Reaction of Metal Nanodroplets. *JACS* **2010**, *132*, 9814–9819. https://doi.org/10.1021/ja102967a.

(107) Gelesky, M. A.; Umpierre, A. P.; Machado, G.; Correia, R. R. B.; Magno, W. C.; Morais, J.; Ebeling, G.; Dupont, J. Laser-Induced Fragmentation of Transition Metal Nanoparticles in Ionic Liquids. *JACS* **2005**, *127*, 4588–4589. https://doi.org/10.1021/ja042711t.

(108) Takeshi Tsuji, Yuuichi Tatsuyama, Masaharu Tsuji, Kenta Ishida, Shigeto Okada, J. Y. Preparation of LiMn2O4 Nanoparticles for Li Ion Secondary Batteriesby Laser Ablation in Water. *Mater. Lett.* **2007**, *61*, 2062–2065.

(109) Musaev, O. R.; Dusevich, V.; Wieliczka, D. M.; Wrobel, J. M.; Kruger, M. B. Nanoparticle Fabrication of Hydroxyapatite by Laser Ablation in Water. *J. Appl. Phys.* **2008**, *104*, 084316–084320. https://doi.org/10.1063/1.3000666.

(110) Semaltianos, N. G. Nanoparticles by Laser Ablation. *Crit. Rev. Solid State Mater. Sci.* **2010**, *35* (2), 105–124. https://doi.org/10.1080/10408431003788233.

(111) Waag, F. Laser Synthesis of Metallic and Oxidic Transition Metal , Multi-Element Nanoparticles for Catalytic Applications, 2019. https://doi.org/10.17185/duepublico/71120.

(112) Kyu Kim, M.; Higotani, T.; Takao, T.; -, A.; Tsuji, M.; Tanoue, T.; Tanaka, A.; Hamagami, T.; Tsuji, T.; Iryo, K.; et al. Preparation of Metal Colloids by a Laser Ablation Technique in Solution: Influence of Laser Wavelength on the Efficiencies of Colloid Formation. *Jpn. J. Appl. Phys.* **2000**, *39* (10A), 981–983.

(113) Kim, Jinil Kim, D. Amaranatha Reddy, R. M. K. The Influence of Laser Wavelength and Fluence on Palladium Nanoparticles Produced by Pulsed Laser Ablation in Deionized Water. *Solid State Sci.* **2014**, *37*, 96–102.

(114) Strutt, H. J. W. On the Scattering of Light by Small Particles. *Lond. Edinb. Dublin Philos. Mag. J. Sci* **2009**, *41* (275), 447–454. https://doi.org/10.1080/14786447108640507.

(115) Creighton, J. A.; Eadon, D. G. Ultraviolet–Visible Absorption Spectra of the Colloidal Metallic Elements. *J. Chem. Soc. Faraday Trans.* **1991**, *87* (24), 3881–3891. https://doi.org/10.1039/FT9918703881.

(116) Intartaglia, R.; Bagga, K.; Brandi, F.; Walters, R.; Bourianoff, G.; Atwater, H.; Belomoin, G.; Therrien, J.; Smith, A.; Rao, S.; et al. Study on the Productivity of Silicon Nanoparticles by Picosecond Laser Ablation in Water: Towards Gram per Hour Yield. *Opt. Express* **2014**, *422*, 3117–3127. https://doi.org/10.1002/adhm.201300157.

(117) Schwenke, A.; Wagener, P.; Nolte, S.; Barcikowski, S.; Nolte, S.; Barcikowski, S. Influence of Processing Time on Nanoparticle Generation during Picosecond-Pulsed Fundamental and Second Harmonic Laser Ablation of Metals in Tetrahydrofuran. *Appl. Phys. A* **2011**, *104*, 77–82. https://doi.org/10.1007/s00339-011-6398-9.

(118) Chan, P. W.; Chan, Y. W.; Ng, H. S. Reflectivity of Metals at High Temperatures Heated by Pulsed Laser. *Phys. Lett. A* **1977**, *61* (3), 151–153. https://doi.org/10.1016/0375-9601(77)90275-4.

(119) Xie, J.; Kar, A. Laser Welding of Thin Sheet Steel with Surface Oxidation. *Weld. J.* **1999**, *78*, 343–348.

(120) Ai, H.-V.; Beaglehole, D.; Hunderi, O. Study of the Interaction of Light with Rough Metal Surfaces. I. Experiment. *Phys. Rev. B* **1970**, *2*, 309–321.

(121) Patel, R. S.; Brewster, M. Q. Effect of Oxidation and Plume Formation on Low Power Nd-Yag Laser Metal Interaction. *J. Heat Transf.* **1990**, *112*, 170–177.

(122) Sikora, A.; Grojo,) D; Sentis, M. Wavelength Scaling of Silicon Laser Ablation in Picosecond Regime. *J. Appl. Phys.* **2017**, *112*, 045702–045711. https://doi.org/10.1063/1.4994307.

(123) Nedialkov, N. N.; Atanasov, P. A.; Sawczak, M.; Sliwinski, G. Ablation of Ceramics with Ultraviolet, Visible, and Infrared Nanosecond Laser Pulses. *XIV Int. Symp. Gas Flow, Chem. Lasers, High-Power Lasers* **2003**, *5120*, 703–708. https://doi.org/10.1117/12.515847.

(124) Sharif Abdullah Al-Mamun; Reiko Nakajima; Takamasa Ishigaki. Effect of Liquid Level and Laser Power on the Formation of Spherical Alumina Nanoparticles by Nanosecond Laser Ablation of Alumina Target. *Thin Solid Films* **2012**, *523*, 46–51.
(125) Sattari, R.; Sajti, C. L.; Khan, S.; Barcikowski, S. Scale-up of Nanoparticle Production during Laser Ablation of Ceramics in Liquid Media. *27th Int. Congr. Appl. Lasers Electro-Optics* **2008**, *N204*. https://doi.org/10.2351/1.5061412.
(126) Wagener, P.; Schwenke, A.; Chichkov, B. N.; Barcikowski, S. Pulsed Laser Ablation of Zinc in Tetrahydrofuran: Bypassing the Cavitation Bubble. *J. Phys. Chem. C* **2010**, *114*, 7618–7625. https://doi.org/10.1021/jp911243a.
(127) Sebastian Kohsakowski; Antonio Santagata; Marcella Dell'Aglio; Alessandro de, G.; Stephan Barcikowski; Philipp Wagener; Bilal Gökce. High Productive and Continuous Nanoparticle Fabrication by Laser Ablation of a Wire-Target in a Liquid Jet. *Appl. Surf. Sci.* **2017**, *403*, 487–499.
(128) Daria Riabinina; Mohamed Chaker; Joelle Margot. Dependence of Gold Nanoparticle Production on Pulse Duration by Laser Ablation in Liquid Media. *Nanotechnology* **2012**, *23*, 135603–135606.
(129) Wang, J.; Blau, W. J.; Bärsch, N.; Jakobi, J.; Weiler, S.; Barcikowski, S. Pure Colloidal Metal and Ceramic Nanoparticles from High-Power Picosecond Laser Ablation in Water and Acetone. *IOP Publ. Nanotechnol. Nanotechnol.* **2009**, *20*, 445603–445611. https://doi.org/10.1088/0957-4484/20/44/445603.
(130) Preuss, S.; Demchuk, A.; Stuke, M. Sub-Picosecond UV Laser Ablation of Metals. *Appl. Phys. A* **1995**, *61*, 33–37.
(131) Men Endez-Manj, A.; Wagener, P.; Barcikowski, S. Transfer-Matrix Method for Efficient Ablation by Pulsed Laser Ablation and Nanoparticle Generation in Liquids. *J. Phys. Chem. C* **2011**, *115*, 5108–5114. https://doi.org/10.1021/jp109370q.
(132) B. Neuenschwander; B. Jaeggi; M. Schmid; G. Hennig. Surface Structuring with Ultra-Short Laser Pulses: Basics, Limitations and Needs for High Throughput. *Phys. Procedia* **2014**, *56*, 1047–1058.
(133) Anisimov, S.; Kapeliovich, B. L.; Perelman, T. Electron Emission from Metal Surfaces Exposed to Ultrashort Laser Pulses. *J. Exp. Theor. Phys.* **1974**, *66*, 375–377.
(134) Jiang, L.; Tsai, H.-L. A Plasma Model Combined with an Improved Two-Temperature Equation for Ultrafast Laser Ablation of Dielectrics. *J. Appl. Phys.* **2008**, *104*, 093101–093108. https://doi.org/10.1063/1.3006129.
(135) Tetsuo Sakka, Satoru Masai, Kazuhiro Fukami, Y. H. O. Spectral Profile of Atomic Emission Lines and Effects of Pulse Duration on Laserablation in Liquid. *Spectrochim. Acta Part B* **2009**, *64*, 981–985.
(136) Dittrich, S.; Streubel, R.; Cormac Mcdonnell, ·; Huber, H. P.; Barcikowski, S.; Gökce, · Bilal. Comparison of the Productivity and Ablation Efficiency of Different Laser Classes for Laser Ablation of Gold in Water and Air. *Appl. Phys. A* **2019**, *125*, 432–441. https://doi.org/10.1007/s00339-019-2704-8.
(137) Schille, J.; Schneider, L.; Lickschat, P.; Loeschner, U.; Ebert, R.; Exner, H. High-Pulse Repetition Frequency Ultrashort Pulse Laser Processing of Copper. *J. Laser Appl.* **2015**, *27*, S28007–S28012. https://doi.org/10.2351/1.4906482.
(138) B. Jaeggi; B. Neuenschwander; M. Schmid; M. Muralt; J. Zuercher; U. Hunziker. Influence of the Pulse Duration in the Ps-Regime on the Ablation Efficiency of Metals. *Phys. Procedia* **2011**, *12*, 164–171.
(139) Hashidaa, M.; A.F. Semeroka; O. Gobertb; G. Petitec; Y.Izawad; J.F-. Wagner. Ablation Threshold Dependence on Pulse Duration for Copper. *Appl. Surf. Sci.* **2002**, *197–198*, 862–867.
(140) Tünnermann, A.; Wellegehausen, B.; Chichkov, B. N.; Momma, C.; Jacobs, H.; Welling, H.; Nolte, S. Ablation of Metals by Ultrashort Laser Pulses. *J. Opt. Soc. Am. B* **1997**, *14* (10), 2716–2722. https://doi.org/10.1364/JOSAB.14.002716.
(141) Hanon, M. M.; Akman, E.; Oztoprak, B. G.; Gunes, M.; Taha, Z. A.; Hajim, K. I.; E. Kacar; Gundogdu, O.; Demir, A. Experimental and Theoretical Investigation of the Drilling of Alumina Ceramicusing Nd:YAG Pulsed Laser. *Opt. Laser Technol.* **2012**, *44*, 913–922.
(142) Liu, W.; Kosareva, O.; Golubtsov, I. S.; Iwasaki, A.; Becker, A.; Kandidov, V. P.; Chin, S. L. Applied Physics B Femtosecond Laser Pulse Filamentation versus Optical Breakdown in H2O. *Appl. Phys. B* **2003**, *76*, 215–229. https://doi.org/10.1007/s00340-002-1087-1.

(143) Alfred Vogel, Kester Nahen, Dirk Theisen, and J. N. Plasma Formation in Water by Picosecond and Nanosecond Nd:YAG Laser Pulses—Part I: Optical Breakdown at Threshold and Superthreshold Irradiance. *IEEE J. Sel. Top. Quantum Electron.* **1996**, *2* (4), 847–860.
(144) Hammer, D. X.; Jansen, E. D.; Frenz, M.; Noojin, G. D.; Thomas, R. J.; Noack, J.; Vogel, A.; Rockwell, B. A.; Welch, A. J. Shielding Properties of Laser-Induced Breakdown in Water for Pulse Durations from 5 Ns to 125 Fs. *Appl. Opt.* **1997**, *36* (22), 5630. https://doi.org/10.1364/ao.36.005630.
(145) Yoshino, K.; Fujii, H.; Inuishi, Y. Laser-Induced Breakdown in Organic Liquids. *J. Phys. D. Appl. Phys.* **1977**, *10*, 1975–1984.
(146) Kei Toyota; Satoru Nakashima; Tadashi Okada. Near-Infrared Laser-Induced Breakdown of Liquid Benzene. *Chem. Phys. Lett.* **2000**, *323*, 323–328.
(147) Tatiana Kovalchuk; Gregory Toker; Valery Bulatov; Israel Schechter. Laser Breakdown in Alcohols and Water Induced by 1064nm Nanosecond Pulses. *Chem. Phys. Lett.* **2010**, *500*, 242–250.
(148) Daniel X. Hammer, Robert J. Thomas, Gary D. Noojin, B. A. R.; Paul K. Kennedy, and W. P. R. Experimental Investigation of Ultrashort Pulse Laser-Induced Breakdown Thresholds in Aqueous Media. *IEEE J. Quantum Electron.* **1996**, *32* (4), 670–678.
(149) N.F. Bunkin, S. I. B. Role of a Dissolved Gas in the Optical Breakdown of Water. *Quantum Electron.* **2006**, *36* (2), 117–124. https://doi.org/10.1070/QE2006v036n02ABEH013113.
(150) Hahn, A.; Barcikowski, S.; Chichkov, B. N. Influences on Nanoparticle Production during Pulsed Laser Ablation. *ournal of Laser Micro/Nanoengineering* **2008**, *3* (2), 73–77. https://doi.org/10.2961/jlmn.2008.02.0003.
(151) M A Valverde-Alva, T García-Fernández, E Esparza-Alegría, M Villagrán-Muniz, C Sánchez-Aké, R Castañeda-Guzmán, M B de la Mora, C. E. M.-H. and J. L. S. L. Laser Ablation Efficiency during the Production of Ag Nanoparticles in Ethanol at a Low Pulse Repetition Rate (1–10 Hz). *Laser Phys. Lett.* **2016**, *13*, 106002–106007. https://doi.org/10.1088/1612-2011/13/10/106002.
(152) Resano-Garcia, A.; Battie, Y.; Koch, A.; Naciri, A. E.; Chaoui, N. Influence of the Laser Light Absorption by the Colloid on the Properties of Silver Nanoparticles Produced by Laser Ablation in Stirred and Stationary Liquid. *J. Appl. Phys.* **2015**, *117*, 113103–113109. https://doi.org/10.1063/1.4915277.
(153) Kalus, M.-R.; Bärsch, N.; Streubel, R.; Gökce, E.; Barcikowski, S.; Gökce, B. How Persistent Microbubbles Shield Nanoparticle Productivity in Laser Synthesis of Colloids – Quantification of Their Volume, Dwell Dynamics, and Gas Composition. *Phys. Chem. Chem. Phys.* **2017**, *19* (10), 7112–7123. https://doi.org/10.1039/C6CP07011F.
(154) Oliveira, M.; Nogueira, R.; MacHado, A. V. Synthesis of Aluminium Nanoparticles in a PP Matrix during Melt Processing: Effect of the Alkoxide Organic Chain. *React. Funct. Polym.* **2012**, *72* (10), 703–712. https://doi.org/10.1016/J.REACTFUNCTPOLYM.2012.06.022.
(155) Giacomo, A. De; Dell'Aglio, M.; Santagata, A.; Gaudiuso, R.; Pascale, O. De; Wagener, P.; Messina, G. C.; Compagnini, G.; Barcikowski, S. Cavitation Dynamics of Laser Ablation of Bulk and Wire-Shaped Metals in Water during Nanoparticles Production. *Phys. Chem. Chem. Phys.* **2013**, *15* (9), 3083–3092. https://doi.org/10.1039/C2CP42649H.
(156) Y. Jiang, P. Liu, Y. Liang, H.B. Li, G. W. Y. Promoting the Yield of Nanoparticles from Laser Ablation in Liquid. *Appl Phys A* **2011**, *105*, 903–907. https://doi.org/10.1007/s00339-011-6557-z.
(157) Cristoforetti, G.; Pitzalis, E.; Spiniello, R.; Ishak, R.; Giammanco, F.; Muniz-Miranda, M.; Caporali, S. Physico-Chemical Properties of Pd Nanoparticles Produced by Pulsed Laser Ablation in Different Organic Solvents. *Appl. Surf. Sci.* **2012**, *258* (7), 3289–3297. https://doi.org/10.1016/J.APSUSC.2011.11.084.
(158) Baladi, A.; Sarraf Mamoory, R. Investigation of Different Liquid Media and Ablation Times on Pulsed Laser Ablation Synthesis of Aluminum Nanoparticles. *Appl. Surf. Sci.* **2010**, *256* (24), 7559–7564. https://doi.org/10.1016/J.APSUSC.2010.05.103.
(159) Scaramuzza, S.; Zerbetto, M.; Amendola, V. Synthesis of Gold Nanoparticles in Liquid Environment by Laser Ablation with Geometrically Confined Configurations: Insights To Improve Size Control and Productivity. *J. Phys. Chem. C* **2016**, *120* (17), 9453–9463. https://doi.org/10.1021/ACS.JPCC.6B00161.
(160) Messina, G. C.; Wagener, P.; Streubel, R.; Giacomo, A. De; Santagata, A.; Compagnini, G.; Barcikowski, S. Pulsed Laser Ablation of a Continuously-Fed Wire in Liquid Flow for High-Yield

Production of Silver Nanoparticles. *Phys. Chem. Chem. Phys.* **2013**, *15* (9), 3093–3098. https://doi.org/10.1039/C2CP42626A.

Chapter 3

Investigation on Lead Iodide Perovskite Hysteresis and Degradation Mechanisms

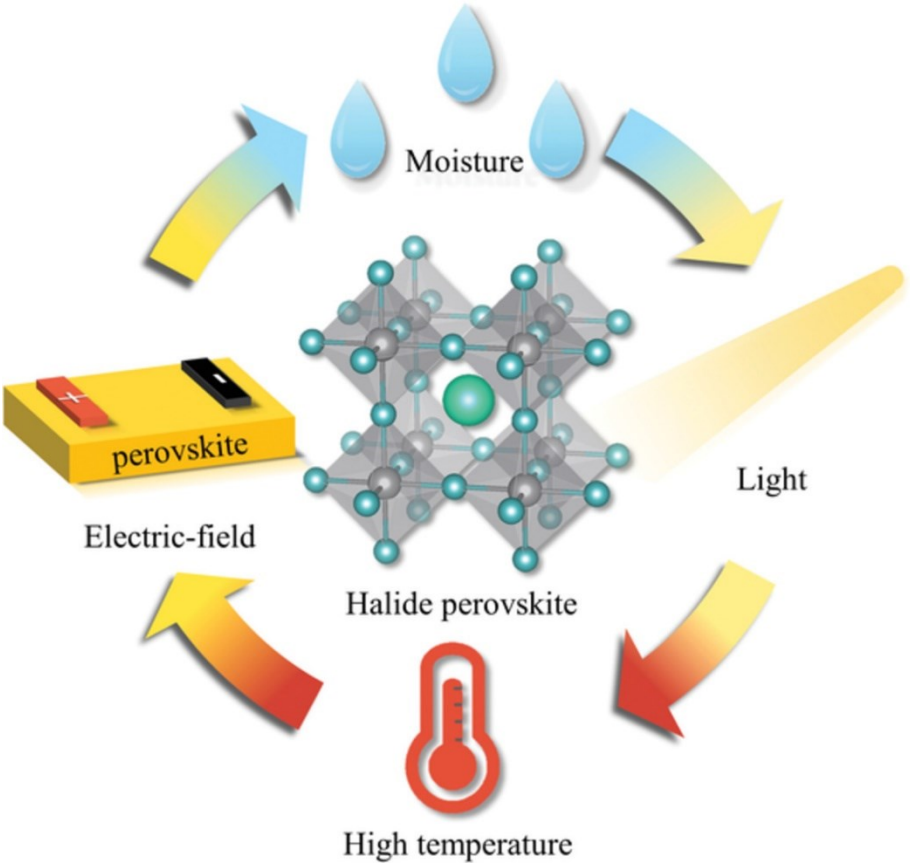

InfoMat (2020) 2(6) 1034-1056

3. Investigation on Lead Iodide Perovskite Hysteresis and Degradation Mechanisms[1]

3.1 The Aim of The Project

As elucidated in Section 1.4.1, stability and reliability of lead halide perovskite materials are still the bottleneck for their extensive industrial application. HOIPs exhibit several weaknesses, mostly related to their hybrid organic nature,[2] which require further research and solutions to make PSCs ready to enter the market. Moisture,[3] UV light,[4] temperature susceptibility[5] and I-V hysteresis are the main issues to address for more stable and reliable perovskite-based devices.[6–8] The underlying causes of I-V hysteresis in lead halide perovskites are still not clear. Several works agreed on explaining such hysteretic phenomena by means of ions moving within the perovskite layer,[9–12] while others concluded that the LHPs behave as a ferroelectric material.[13–15] Lead halide perovskites from solution-ablated precursors have recently proved high stability in ambient conditions and low hysteresis, constituting a promising route for more stable and less hysteretic LHPs.[16] Indeed, while standard solution-processed LHP could not survive extensive electrical characterization and showed irreversible degradation in a few hours, laser-ablated derived perovskite proved higher tolerance and resistance both to electric field and environmental exposure.

For this reason in the present work thesis I-V hysteresis, and electric field effects have been investigated by means of electrical and optical characterizations of planar devices on archetypal methylammonium lead triiodide perovskite $CH_3NH_3PbI_3$ ($MAPbI_3$) synthesized with laser-ablated precursors.[1] $MAPbI_3$ from laser-ablated precursors endures prolonged electric field application and extensive electrical characterizations, which were not possible for standard solution-processed $MAPbI_3$, were performed. In particular, these measurements allowed investigating whether the I-V hysteresis is due to ions and/or ferroelectric properties of LHP material by using extremely low scan rates. Besides, having $MAPbI_3$ derived from laser-ablated precursors a slower degradation dynamic, the effects of the hysteresis on the material were detected too. It was concluded that different mechanisms contribute to the I-V hysteresis observed in PSCs and that ion migration is responsible for both long term transitory effects and permanent structural changes in the $MAPbI_3$ layer, altering the electrical properties of the devices. A model based on the band bending made possible explaining the current injection/extraction into/from the hybrid organic-inorganic semiconductor, which suggested how these effects are important for the band alignment for a photovoltaics device.

These results are useful to better understand the degrading mechanisms in PSCs with different LHPs and/or different architectures.

3.2 Results and Discussion

Previous works showed that $MAPbI_3$ perovskite exhibits in dark a rectifying current-voltage behavior by keeping the devices pre-biased at positive or negative voltages before an I-V scan measurement, whereas it was found that such a phenomenon does not occur when the measurements are performed after storage or after a pre-biased step at 0 V for a long time.[16] Since $MAPbI_3$ perovskite synthesized from lead iodide nanoparticles obtained by laser ablation in solution (LASiS) showed higher resistance towards electric field induced degradation, stressful electrical characterizations were possible. In this work, $MAPbI_3$ underwent several cyclic current-voltage scans, both at fast and very low scan rates. Measuring several scan cycles at different orders of magnitude scan rates allowed investigating the temporary/permanent phenomena and testing the LHP robustness to the applied electric field. In particular, 0.3 mV/s current-voltage scans were used to detect the steady-state I-V curves of the device once all transient behaviors terminated. Optical characterizations were designed to support and to validate the results, in addition to provide further information for the model dynamics.

3.2.1 *Current-Voltage Measurements*

Figure 3.1 summarizes the typical current-voltage scans on interdigitated devices both in dark and light conditions (more details regarding the measurement conditions and device structure are reported in Section 3.4). Both the fast scan and steady-state curves show hysteresis, despite the very low scan rate used in steady-state measurements (Figure 3.1 a).

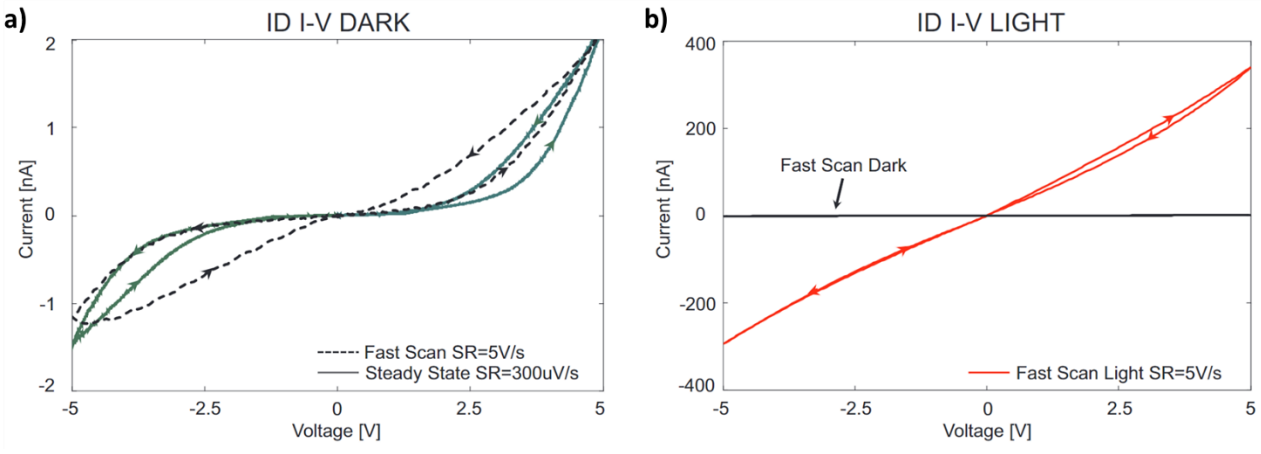

Figure 3.1 I-V scans at different scan rates made on interdigitated device a) in dark and b) in light conditions. The dark current was reported for comparison.

The different response to variable scan rates and the transient nature of the I-V curves eliminate the hypothesis of ferroelectric behavior (whether they exist, they are negligible), as it will be better explained below. The data at very low scan rate suggest that in addition to some ionic species there are others moving species within the material at a much slower pace. The photogeneration properties of the device are clearly evaluable in Figure 3.1 b, where the comparison of light and dark I-V curves highlighted a more than two orders of magnitude difference in currents. Furthermore, by comparing the two plots in Figure 3.1 it is possible to notice how curves measured under illumination can be approximated by linear fit, while those measured in dark conditions showed a non-linear shape.

The different currents indicate that photogenerated charge dominate the injected charge under light. Ion drift-diffusion within organic-inorganic semiconductors has been widely studied [17–19] and the rectifying phenomenon in LHP materials has been explained in several works as the consequence of ion drift-diffusion through the active layer, particularly on planar devices.[6,11] However, no one recorded before current-voltage scans with such a low scan rate, which constitutes a good approximation of the steady-state condition. Figure 3.2 focuses on the detail of the steady-state curve around 0 V captured both on cycle #1 (Figure 3.2 a) on a pristine device (i.e., not measured neither stressed before), and in cycle #2 (Figure 3.2 b). The insets in Figure 3.2 represent the absolute current values in logarithmic scale to emphasize the zero-current crossing voltage for each scan.

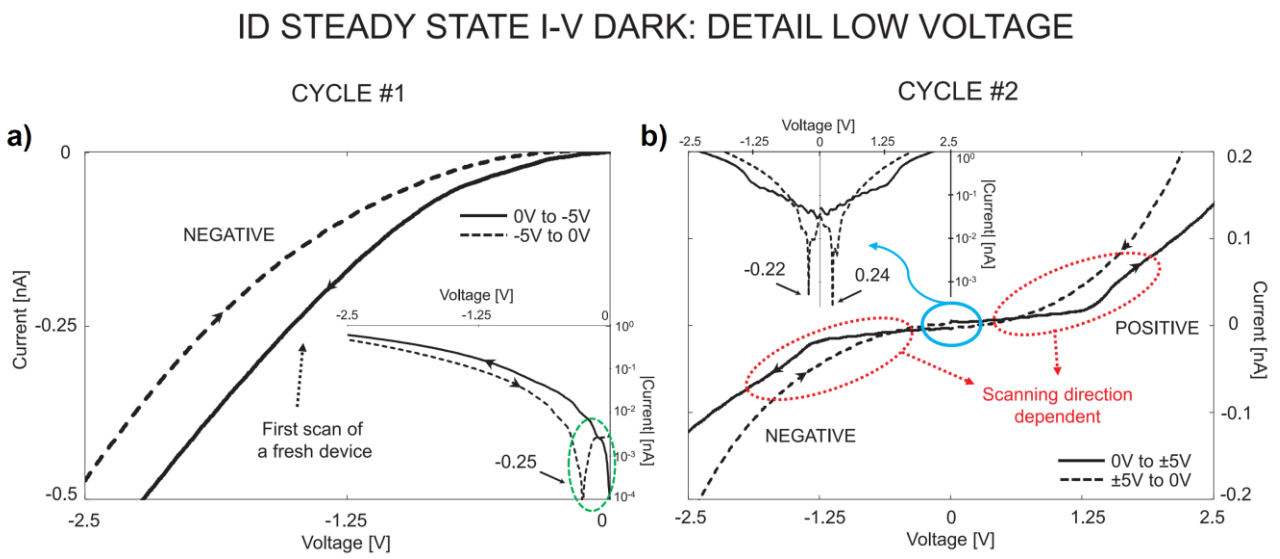

Figure 3.2 I-V steady-state scan detail at low voltages. a) The zero-current crossing voltage depends on the scanning direction. If the device scanned is fresh and unbiased, the current flex is not present, and the scan starts from 0 A (green dashed circle in the inset). b) From 5 to 0 V a positive voltage of 0.24 V remains at zero-crossing current, while a negative voltage of -0.22 V remains from −5 V to 0 V (inset highlighting the blue region). The red dotted circles envelop the current flexes that are scanning direction dependent.

Comparing I-V scans at different cycles, it can be noticed that the steady-state scan on cycle #1 from 0 V to -5 V on a pristine device has the zero-current crossing voltage at 0 V, while the backward scan from -5 V to 0 V crosses around −0.25 V. Then, in cycle #2, during the positive scan at 0 V the current is above zero, while the backward scan crosses zero-current at 0.24 V. The same repeats during the following cycles from #3 to #5, similarly to what observed in the work by Huang et al.[6] Only with cycle #7, after leaving the device in storage conditions and unbiased for 5 days, an I-V curve that starts with zero-current at zero at 0 V was recorded, showing that the residual voltage is a recoverable phenomenon. Such a "reset" of the device is understandable with a slow diffusion of ions within the $MAPbI_3$ layer. The storage, in fact, allows the ions accumulated at the interface with the electrodes to diffuse back to their initial isotropic distribution, eliminating the residual zero-current crossing voltage measured during the steady-state I-V scans. One can also conclude that V_{DIP} is not due to ferroelectric domains switching during the scan, since the domains should not reset unless there is a change in temperature or applied electric fields and in any case longer relaxation times should be present. Furthermore, ferroelectric domains should switch and produce the V_{DIP} voltage even with fast scans, which is not the case.

Thus, the effects due to ferroelectric domains contributing to the observed hysteresis can be considered, if present, negligible. This I-V data interpretation agrees with the considerations of Beilsten-Edmands et al.,[20] who suggested the movement of ions (Pb^{2+} and/or MA^{+}) within the $MAPbI_3$ layer. One also notes flexes around ± 1.25 V (red dotted circles in Figure 3.2 b) in cycle #2, while there are no flexes in cycle #1 (Figure 3.2 a). Like V_{DIP}, flexes are recoverable effects because they disappear after the devices are kept in storage conditions for enough time. One can also see that their weight on the I-V curves lowers repeating continuous steady-state measurements. These effects can be explained considering that, although the storage at 0 V allowed the ions distribution into the $MAPbI_3$ layer to be restored, the continuous measurements also induce a degradation of the $MAPbI_3$/Au interface.

3.2.2 *Morphological and Optical Analysis*

The top-view scanning electron microscopy (SEM) image of $MAPbI_3$ thin film onto Si substrate shows NCs with an average size of 200 nm, having the characteristic rectangular prism of tetragonal perovskite lattice (Figure 3.3 a). The cross-sectional SEM image of the same sample shows a compact thick film of approximatively 1.3 μm (Figure 3.3 b). No PbI_2 spherical particles can be observed in SEM images. This is confirmed by the low-intensity peak at 12.6° in XRD pattern related to PbI_2 phase

(Figure 3.3 c) which has a much lower intensity than the reflection of $MAPbI_3$ (100) plane at 14.1°.[16] Because of the grain size of the spray-coated $MAPbI_3$ thin film (about 200 nm), in an interdigitated device there are about a hundred NC (about 20 nm) between two electrodes. This morphology of the film favors, according to Huang et al,[21] ions migration, which shows smaller activation energy at the grain boundaries than within a single crystal. The migration stops when the drift-diffusion process is balanced and, when a bias is applied, ions accumulate close to the electrodes creating a charge accumulation at the gold fingers.

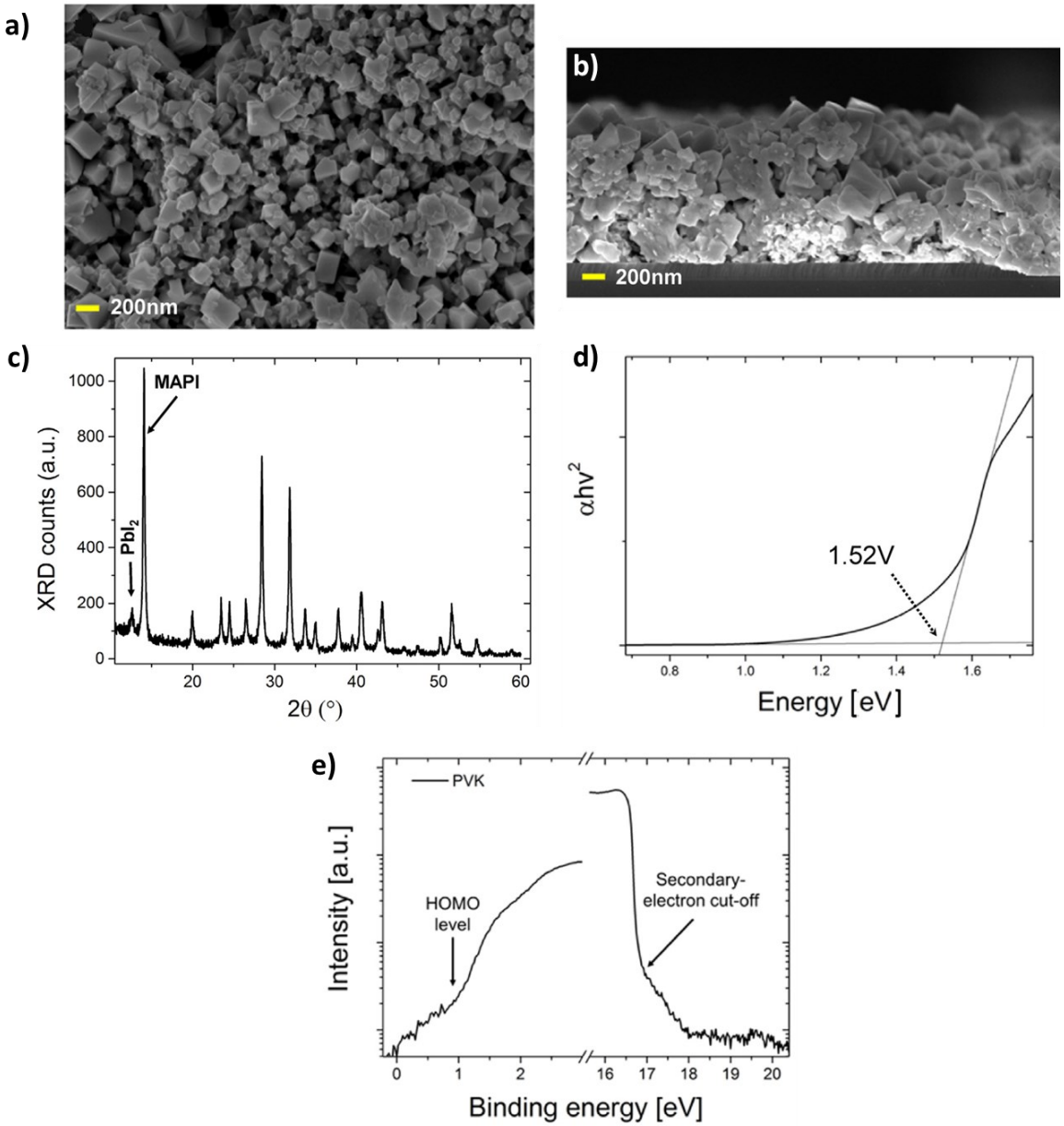

Figure 3.3 Morphological and optical characterization of $MAPbI_3$ film. a) Top view and b) cross-section SEM images. c) XRD pattern of $MAPbI_3$ film deposited on zero background silicon. d) Tauc plot made from $MAPbI_3$/glass absorbance spectra. e) Ultraviolet Photoelectron Spectroscopy spectrum of $MAPbI_3$/Au electrode highlighting HOMO level with respect to the Fermi level (4.53 eV) and higher binding energies region for work functions estimation.

Such migration related phenomena were evident in the interdigitated devices we used and were not be easily detected in a usual vertical device, where there are only few nanocrystals between electrodes, although the phenomenon of ion migration is always present and influences the performance of a PV cell .[22,23]

The measurements we produced were therefore interesting for giving evidence to a phenomenon which is present in PSC. The measurement of the optical property of $MAPbI_3$ deposited on glass allowed its phase characterization. The band gap was found to be 1.52 eV, using a Tauc plot (Figure 3.3 d), in agreement with the value of solution-processed tetragonal LHP materials.[24] From ultraviolet photoelectron spectroscopy characterization, the HOMO band level and the Fermi level of $MAPbI_3$ material were extrapolated (Figure 3.3 e). The HOMO level was found to be approximately 0.9 eV lower than the −4.53 eV estimated Fermi level, whereas the LUMO energy level at −3.91 eV. According to these values the material is n-doped, in contrast with values obtained from solution-processed perovskites reported in literature.[25] It is known that ablation in organic solvents determines the presence of graphene/graphite in the ablated materials and the estimated Fermi level agrees with this presence, since graphene/graphite shows a work function of 4.4–4.6 eV.[26,27] The introduction of such "doping" materials in $MAPbI_3$ derives from the PbI_2 NCs precursors by LASiS (Section 3.4.2). In view of the recent studies on carbon-based perovskite solar cells highlighting their good long-term stability due to the use of carbon electrodes,[28–30] the higher stability towards moisture and electric field effects of the present $MAPbI_3$ perovskite can be related to the presence of such carbon materials.[31–33]

3.2.3 *Perovskite Degradation due to Ion Migration*

In addition to give rise to reversible hysteretic behaviors such as the V_{DIP} and flexes in I-V curves, ion migration is also responsible for material degradation. The high ion concentration in proximity of the electrodes, upon application of a bias, generates a huge electric field that can influence the perovskite lattice.

Effects on I-V curve

Despite the inert atmosphere and the controlled temperature, the application of a prolonged electric field in dark conditions induces some permanent degradation observable both in dark and light curves. In Figure 3.4 a one can notice how the current decreases with time of measurement, and during the cycle #5 the injected current is lower than during cycles #2 and #1. The current decrease is permanent, and the current does not recover also after storage without a bias. Except

the fast scans and the first steady-state scan from 0 V to -5 V during cycle #1, in all the curves the V_{DIP} voltage related to the device history, was detected. One also observes that by increasing the cycles of characterization, the current flexes tend to vanish and disappear. This effect and the current reduction can be ascribed to electric field induced degradation.

In particular, the application of an electric field for a long time (as is the case for the steady-state I-V scans) allows ions to migrate and accumulate. The migration stops when drift-diffusion is balanced. However, this migration leads to a high concentration of ions in proximity of the electrodes. Such a high concentration of ions was suggested as the source of the $MAPbI_3$ degradation close to the Au contact since it generates a high electric field. The high density of ions has a negative effect on the $MAPbI_3$ perovskite, inducing a high stress on its lattice. Therefore, a lattice-degraded layer starts surrounding the gold electrodes limiting both the injected current (Figure 3.4 a) and the extracted photocharges (Figure 3.4 b). Indeed, the extracted photogenerated current is lower in cycle #5 than in fresh devices, but this difference is not comparable with the variations in the injected dark current during the respective cycles. Moreover, the extracted photocurrent from a fresh device can be approximated by a linear fit, while the photocurrent measured on the same device in cycle #5 is considerably different. Finally, the presence of a V_{DIP} voltage is still observed in fast I-V scans in light conditions (inset in Figure 3.4 b).

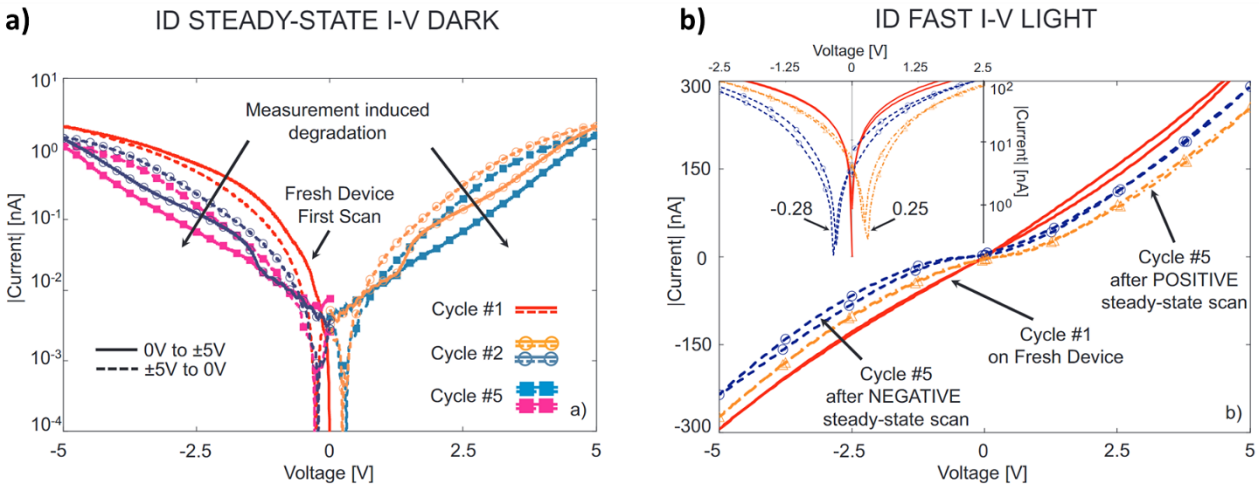

Figure 3.4 a) Steady-state scans of an ID sample in dark conditions during several cycles. Continuous lines stand for scans from 0 V to ± 5 V, while dashed lines for scans from ± 5–0 V. Circles indicate the positive and negative scans during cycle #2 measurements, after the first scan of the fresh device (red lines), while the filled squares curves indicate the steady-state I-V during cycle #5. b) Fast I-V curves of the same sample under light condition as in a) at different measurement steps. Red continuous line is the fresh device; blue dashed line with circles is after the cycle #5 negative steady-state scan; orange dot-dashed line is after the cycle #5 positive steady-state scan. The inset in b) underlines the presence of a residual built-in voltage in the curves when measuring in light after steady-state scans.

V_{DIP} was approximately −0.28 V (dashed blue line with empty circles) when the previous measurement was a negative steady-state scan and 0.25 V (orange dashed line with empty triangles) in case of a positive steady-state scan. On the contrary, the fast scan in light on a fresh device or after storage crosses the zero-current at 0 V. Although the planar structures of the interdigitated devices intensified this phenomenon, the presence of V_{DIP} is in accordance with well-observed long time V_{OC} decay occurring in PSCs and with pre-polarization affecting solar cell performance.[34] x

Electric field effects on perovskite lattice

To verify the hypothesis of the existence of a degraded layer surrounding the electrodes, Raman spectra were recorded in different regions of the IDs samples (Figure 3.5). The blue curve represents a sample measured on gold fingers after cycle #7 electrical characterization, whereas the red curve represents a fresh device measured in an equivalent region and stored unbiased for the same amount of time. Raman spectrum of $MAPbI_3$ film at standard conditions did not show any significant peaks and this is what can be also observed in the fresh perovskite sample.[35,36] On the other hand, several peaks appeared in the case of fully characterized device measured on gold electrodes. The appearance of such peaks is compatible with the presence of crystalline lead iodide.[37] Specifically, the peak at 94 cm^{-1} is due to Pb-I stretching,[38] while the peaks at 110 and 215 cm^{-1} are related to first- and second order Pb-I longitudinal modes vibrations, respectively.[39] Furthermore, the blue line shoulder at 110 cm^{-1} derives from both lead iodide (PbI_2) and methylammonium iodide (MAI).[35]

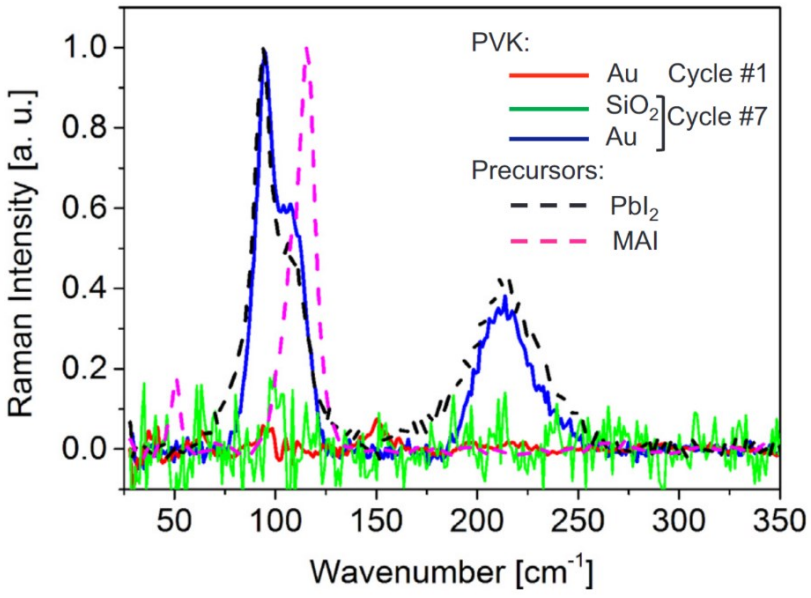

Figure 3.5 Raman characterization of $MAPbI_3$ sprayed on ID substrates on a fresh device and after the cycle #7. Raman spectra of PbI_2 and MAI precursor powders was added as reference.

Additionally, the Raman spectra were measured also between Au electrodes, where $MAPbI_3$ perovskite was grown on SiO_2. Such spectra (green curve) did not show the presence of $MAPbI_3$ precursors both on a fully characterized and on a fresh device. These results show that the effects of ion migration lead to the degradation of the perovskite near to the electrode where migrated ions accumulate and the precursors of LHP, namely PbI_2 and MAI, are present.[40]

3.2.4 *Model interpretation of the experiments*

The phenomena generated by the electric field can be understood with a qualitative model. Figure 3.6 a represents the fresh device unbiased. Here, ions (light blue and gray spheres) occupy their initial position in the lattice and are distributed uniformly within the LHP layer and the bands are flat. Figure 3.6 b shows the biased device in steady-state condition. In this condition, dipoles are generated at $MAPbI_3$/Au interfaces due to charge accumulation. Such dipoles are few nm thick (10–50 nm)[41] and they enhance holes/electrons injection via tunneling. The presence of such dipoles produces an effect similar to the functionalization usually adopted in organic devices to promote charge injection.[42–44] Once the dipoles width is in the order of nm, charges easily cross the potential barrier by tunneling. Therefore, the dipole potential barriers are not impeding but promoting the charge injection, since the dipole heights are equivalent to shifts of the electrode work functions (respectively called $\Delta\varphi_{B1}$ and $\Delta\varphi_{B2}$ in Figure 3.6 b-d). Figure 3.6 c represents the transient condition of temporary $MAPbI_3$ band bending occurring when applying a negative voltage (-2.5 V). In this transient condition, ions drift-diffusion is unbalanced and there is no tunneling of e^+/h^+, resulting in a lower overall current. This can explain the flexes in the current observed in Figure 3.4 a. These observations point to the fact that despite using such a low scan rate as 0.3 mV/s, the resulting scan does not represent the final steady-state condition of the device, since transitory phenomena persist. Probably, heavy ions (Pb^{2+} and/or MA^+) are responsible for the I-V hysteresis despite the low scan rate.

Finally, Figure 3.6 d shows what happens after the $MAPbI_3$ film is biased for a prolonged time. The ions accumulated at the $MAPbI_3$/Au interfaces are responsible for a permanent damage of the $MAPbI_3$ perovskite film, which converts back to PbI_2 and MAI original precursors. Such degraded layer around the gold electrodes limits the current injection. The presence of $MAPbI_3$ degraded layers explains the lowering of the dark current and the different shape and decrease of the light current with increasing measurement time, shown respectively in Figure 3.4 a,b.

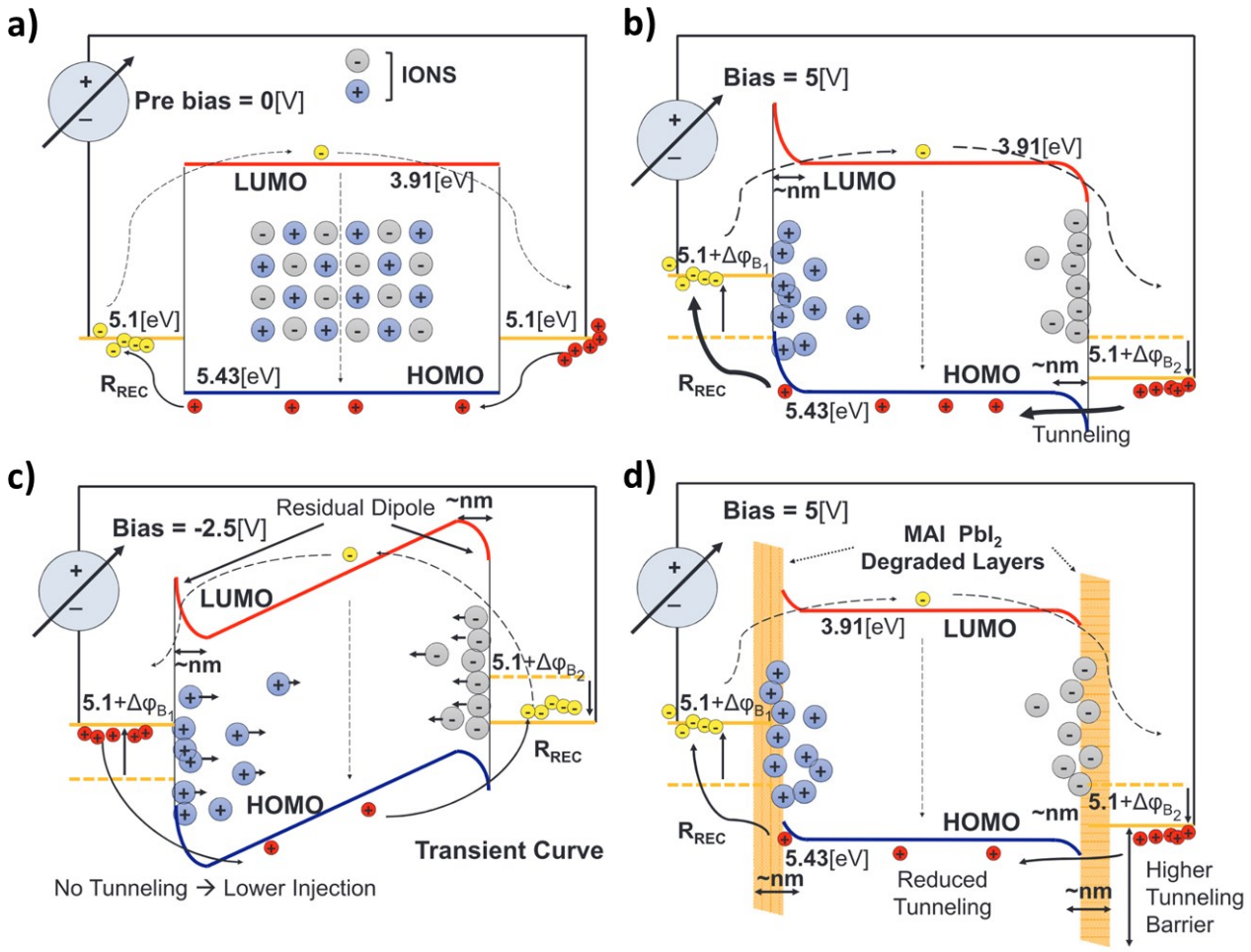

Figure 3.6 Qualitative model representation of the band diagram without (a) and with (b) biasing the interdigitated sample at steady-state conditions. c) Band banding during a transient measurement, in which the tunneling is reduced due to the persistence of a dipole generated during the positive steady-state scan. d) Situation occurring under biasing after prolonged exposure to high electric field near the contacts, in which the tunneling current is reduced due to higher barriers generated by degraded $MAPbI_3$ layers.

3.3 Summary

Methylammonium lead iodide perovskite material was synthetized starting from spray-coated lead iodide nanoparticles precursor obtained by laser ablation technique. From earlier studies, this perovskite material proved to be more stable than the standard spin-coated counterpart. Thanks to the electrical characterizations performed at different scan rates on interdigitated perovskite devices it was possible to recognize the causes at the base of the electrical hysteresis, distinguishing between temporary and permanent phenomena generated during the current-voltage measurements. Results indicated no (or negligible) ferroelectric phenomenon in methylammonium lead iodide perovskite, while ions migration at perovskite grain boundaries has several effects, leading to material degradation.

Following the drift-diffusion law under the effect of applied bias, the ions accumulate at the interfaces with the electrodes, generating dipoles in the device. Such dipoles change the band alignment of the semiconductor with the electrode work functions, thus changing the current injection dynamics. Despite the initial improvement in band alignment that dipoles might induce, the high electric field they generate at perovskite/electrode interfaces is destructive and induces a degradation mechanism which converts methylammonium lead iodide perovskite layer back to the initial precursors (methylammonium iodide and lead iodide). Therefore, insulating degraded layers generate around the electrodes, limiting the current injected in dark and extracted in light conditions. The presence of these layers was detected both in the current-voltage scans and by Raman spectroscopy measurements.

Finally, a qualitative model describing the bands bending under different conditions was presented to explain the dynamics observed in the devices during the current-voltage scans. Although all the characterization, observations and models were made on interdigitated devices with a planar structure, the same phenomena can also occur in the vertical structures extensively used in perovskite solar cells. Thus, this study gives a wiser view of the ion migration effects, providing that it must be suppressed to optimize both functionality and reliability of LHP materials, also extending perovskite solar cells lifetime.

3.4 Experimental Section

3.4.1 *Setup and Device Structure*

To limit the electric field induced degradation effects, all the characterization were performed in a chamber containing a nitrogen inert atmosphere, set at a controlled temperature of 25 °C. An additional external black box including the nitrogen one was used to avoid external light and electromagnetic radiation interferences (Figure 3.7 a); both boxes were grounded. A Peltier-based temperature controller allowed setting the device temperature from -20 to 80 °C. Planar interdigitated devices were fabricated using 10×10mm^2 crystalline Si substrates covered by silicon oxide and patterned with interdigitated golden electrodes (work-function Φ_{Au} = −5.1 eV). IDs had a 20 µm $MAPbI_3$ photoactive layer between golden electrodes (Figure 3.7 b). A 10×10mm^2 fluorine-doped tin oxide (FTO)/glass substrate (TEC 7, Sigma-Aldrich) was coated with $MAPbI_3$ perovskite for optical characterizations.

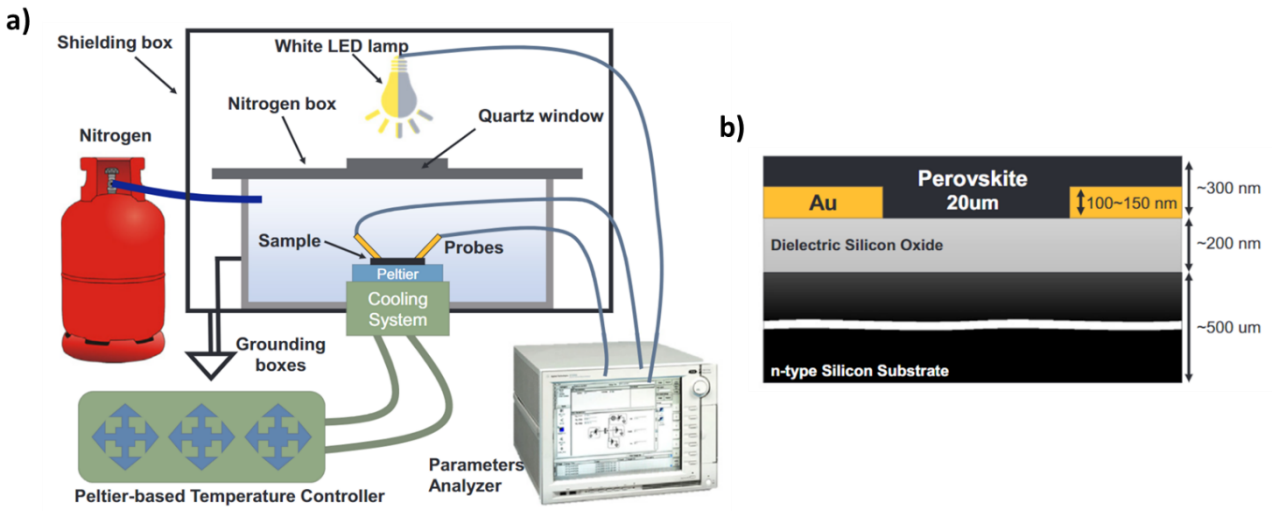

Figure 3.7 a) Sketch of the setup developed to run the electrical measurements. b) Representation of the planar structure used in this work.

3.4.2 *Device Preparation*

$MAPbI_3$ perovskite layers implemented in IDs and FTO/glass samples were obtained by a two-step process. Firstly, a precursor solution of PbI_2 nanoparticles (NPs) in anhydrous isopropyl alcohol (IPA) was deposited onto the respective substrates by spray coating. Secondly, the PbI_2 layers were converted into $MAPbI_3$ perovskite by dip coating in 10 mg/ml MAI solution in IPA for 3 minutes, then rinsed in anhydrous IPA, and finally in anhydrous dichloromethane. The resulting $MAPbI_3$ films thickness was in the order of 1 µm, as observed in SEM cross section profiles (Figure 3.3 b). Lead iodide nanoparticles were produced by LASiS. The second harmonic at 532 nm of a pulsed (10 Hz) Nd:YAG laser (Quantel) with 9 ns pulse duration was focused on the surface of a lead iodide compressed round powder tablet with a fluence of 2 J/cm^2. The tablet was placed in a glass vial and immersed in anhydrous iodobenzene. LASiS was performed in such conditions for 2 hours, obtaining a 70 µg/ml PbI_2 NPs colloidal solution. The NPs concentration was estimated via optical extinction, as previously reported.[16] Finally, the PbI_2 nanoparticles in iodobenzene were centrifuged and redispersed in anhydrous IPA before spray deposition. The spray coating depositions were performed via a home-made system (Figure 3.8) mounting a Professional Dual Action Airbrush Kit (nozzle diameter: 2 mm) with gravity feed (ExquizonEU), operating with nitrogen flow at 3 bar (20 °C) and moved by stepper motors system. The substrate was positioned vertically, 3 cm far from the nozzle tip and kept at 50 °C during the deposition. 1.0 ml of precursor ink was sprayed in air under extractor hood (20% relative humidity). The spray coating process was optimized by setting a 10x10mm^2 square pattern, with a step of 0.2 mm and a spray pattern width of about 4 mm.

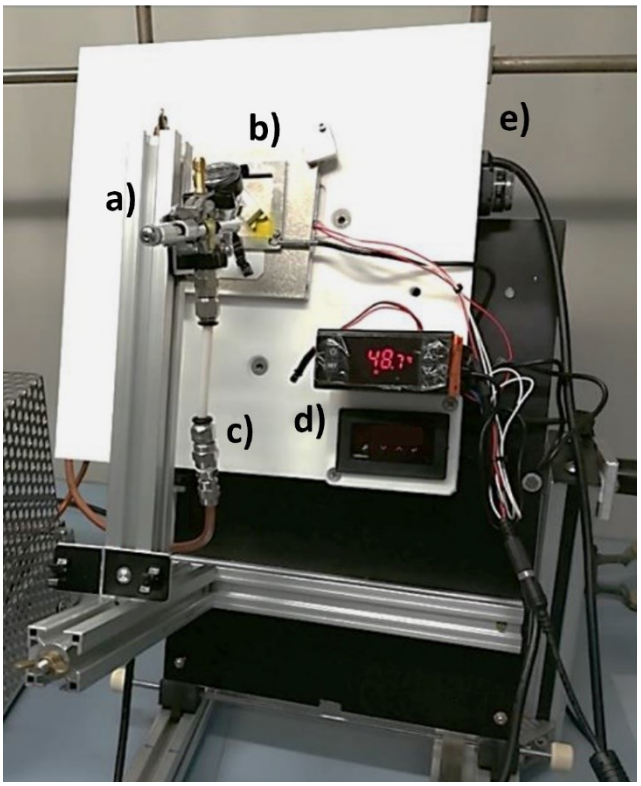

Figure 3.8 Picture of the home-made spray coating system employed in this work to deposit lead iodide precursors nanoparticles to be then converted into $MAPbI_3$ perovskite thin films. a) Airbrush, b) sample holder mounted on a hot-plate, c) nitrogen supply, d) hot-plate controller, e) stepper motors.

3.4.3 *Materials Characterization*

$MAPbI_3$ perovskite work function was estimated via Ultraviolet Photoelectron Spectroscopy analysis performed using a Kratos Axis UltraDLD spectrometer and a He I (21.22 eV) discharge lamp. The Ultraviolet Photoelectron Spectroscopy measurements were conducted on a 55 µm diameter area, at pass energy of 10 eV, and with a dwell time of 100 ms. The work function was measured from the threshold energy for the emission of secondary electrons during He I excitation. A −9.0 V bias was applied to the sample to precisely determine the low kinetic energy cut-off.[45] Raman spectroscopy measurements were collected by means of a custom setup equipped with an Ar^+/ Kr^+ gas laser (Coherent, Innova 70) tuned for emission at 514.5 nm. The laser was focused on the sample through an Olympus BX 41 microscope with a 20× objective (Olympus, MPlan FLN 20×, NA=0.40), while Raman scattering diffused by the sample was coupled into the slit of a three-stage subtractive spectrograph (Jobin Yvon S3000) and detected by a liquid nitrogen-cooled CCD (Jobin Yvon, Symphony, 1024×256 pixels, front illuminated). In this configuration, the laser spot diameter was about 5 µm. The laser power used during Raman measurements was 250 µW for PbI_2 powder, MAI powder and $MAPbI_3$ films on SiO_2, while 25 µW for $MAPbI_3$ on Au. All these measurements were

carried out in standard conditions (25°C, 1 atm). SEM analysis was performed with a Zeiss Sigma HD microscope, equipped with a Schottky FEG source and two detectors for secondary electrons (InLens and Everhart Thornley). A low accelerating voltage (1-5 kV) was used to delineate fine surface features without inducing conductive coatings that can deleteriously modify the perovskite surface morphology. X-ray diffraction (XRD) patterns were recorded in Bragg–Brentano geometry with a Bruker D8 Advance diffractometer equipped with a Cu $K_{\alpha 1}$ anode at operating voltage and current of 40 kV and 40 mA, respectively. All the diffraction patterns were measured at RT over an angular range between 6° and 60°, with a step size of 0.020° and an acquisition time of 1.0 s.

3.4.4 *Electrical Measurements*

An Agilent B1500 parameters analyzer was used for both the electrical characterizations of the devices and the control of the white LED lamp used as light source. High-resolution source measurement units were used to measure electrodes current, while a high-power one driven the light source. Light measurements were run under a white LED biased to give a light power density of about 50 mW/cm^2. Current voltage scans were performed with a scan rate of 5 V and 0.3m V/s for fast and steady-state scan, respectively. Figure 3.9 a summarizes the experimental conditions for the electrical characterization of the samples.

I-V scan was defined as positive when measured by a forward scan from 0 to 5 V, followed by a backward scan from 5 V to 0 V; negative when measured in opposite direction (from 0 to −5 V, then from −5 to 0 V). Positive and negative scans were repeated several times and at different scan rates to monitor any appreciable differences in the devices behavior related to the characterization itself and/or prolonged applied electric field. Figure 3.9 b shows the whole electrical characterization procedure followed in this study, including seven cycles of measurements. Starting and ending cycles (#1 and #7) are equivalent but were useful to compare the devices at the beginning and at the end of the complete characterization. The check cycles (#2, #3, and #4) comprehended only steady-state scans to monitor and to test the devices resistance to measurement-induced degradation. The full cycle (#5) measures consisted in fast scans, both in light and in dark, after a steady-state I-V scan in positive and negative directions. Finally, the storage cycle (#6) was intended to let the device rest such that relaxation phenomena could be detected within the ending cycle.

a)

	SR [V/s]	Scans direction & voltage range [V]	Light – LED (50 mW/cm^2)
I–V fast	5	Negative: 0 → −5; −5 → 0	OFF – ON
I–V steady-state	300E−6	Positive: 0 → +5; +5 → 0	OFF

b)

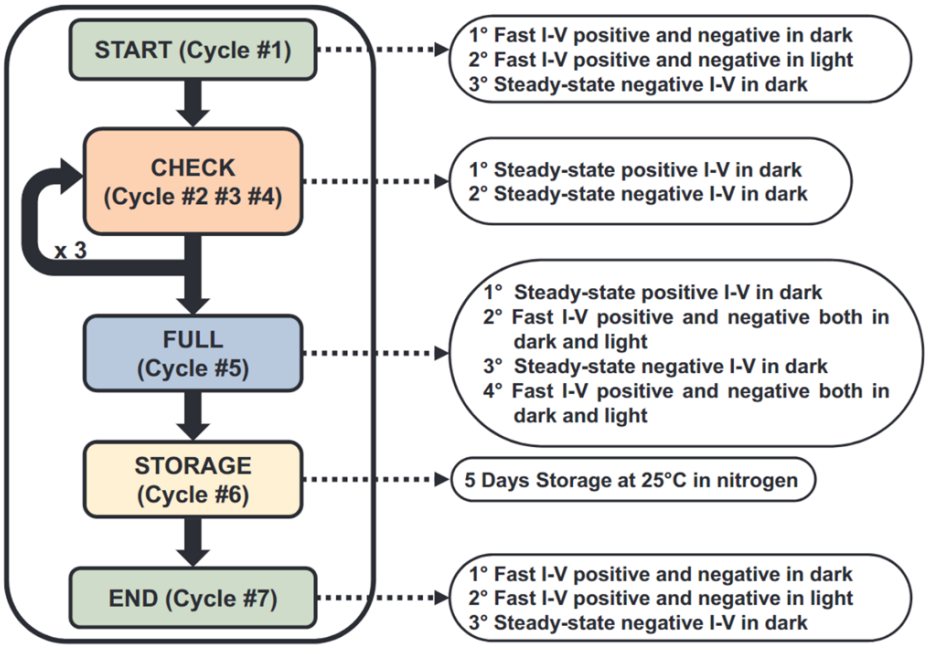

Figure 3.9 a) Specifications on the characterization timings, direction, voltage ranges and illumination used for the experiments. b) Type and order of the electrical measurements performed for the complete characterization of perovskite interdigitated devices.

References

(1) Rizzo, A.; Lamberti, F.; Buonomo, M.; Wrachien, N.; Torto, L.; Lago, N.; Sansoni, S.; Pilot, R.; Prato, M.; Michieli, N.; et al. Understanding Lead Iodide Perovskite Hysteresis and Degradation Causes by Extensive Electrical Characterization. *Sol. Energy Mater. Sol. Cells* **2019**, *189*, 43–52. https://doi.org/10.1016/j.solmat.2018.09.021.

(2) Niu, G.; Guo, X.; Wang, L. Review of Recent Progress in Chemical Stability of Perovskite Solar Cells. *J. Mater. Chem. A* **2015**, *3*, 8970–8980. https://doi.org/10.1039/c4ta04994b.

(3) Wang, Q.; Chen, B.; Liu, Y.; Deng, Y.; Bai, Y.; Dong, Q.; Huang, J. Scaling Behavior of Moisture-Induced Grain Degradation in Polycrystalline Hybrid Perovskite Thin Films. *Energy Environ. Sci* **2017**, *10*, 516–522. https://doi.org/10.1039/c6ee02941h.

(4) Abdelmageed, G.; Jewell, L.; Hellier, K.; Seymour, L.; Luo, B.; Bridges, F.; Zhang, J. Z.; Carter, S. Mechanisms for Light Induced Degradation in MAPbI3 Perovskite Thin Films and Solar Cells. *Appl. Phys. Lett.* **2016**, *109* (233905). https://doi.org/10.1063/1.4967840.

(5) Divitini, G.; Cacovich, S.; Matteocci, F.; Cinà, L.; Carlo, A. Di; Ducati, C. In Situ Observation of Heat-Induced Degradation of Perovskite Solar Cells. *Nat. Energy* **2016**, *1*. https://doi.org/10.1038/NENERGY.2015.12.

(6) Xiao, Z.; Yuan, Y.; Shao, Y.; Wang, Q.; Dong, Q.; Bi, C.; Sharma, P.; Gruverman, A.; Huang, J. Giant Switchable Photovoltaic Effect in Organometal Trihalide Perovskite Devices. *Nat. Mater.* **2015**, *14*. https://doi.org/10.1038/NMAT4150.

(7) Jeffrey A. Christians, Joseph S. Manser, and P. V. K. Best Practices in Perovskite Solar Cell Efficiency Measurements. Avoiding the Error of Making Bad Cells Look Good. *J. Phys. Chem. Lett.* **2015**, *6*, 852−857. https://doi.org/10.1021/acs.jpclett.5b00289.

(8) Calado, P.; Telford, A. M.; Bryant, D.; Li, X.; Nelson, J.; O'regan, B. C.; Barnes, P. R. F. Evidence for Ion Migration in Hybrid Perovskite Solar Cells with Minimal Hysteresis. *Nat. Commun.* **2016**, *7* (13831). https://doi.org/10.1038/ncomms13831.

(9) Bag, M.; Renna, L. A.; Adhikari, R. Y.; Karak, S.; Liu, F.; Lahti, P. M.; Russell, T. P.; Tuominen, M. T.; Venkataraman, D. Kinetics of Ion Transport in Perovskite Active Layers and Its Implications for Active Layer Stability. *JACS* **2015**, *137*, 13130−13137. https://doi.org/10.1021/jacs.5b08535.

(10) Van Reenen, S.; Kemerink, M.; Snaith, H. J. Modeling Anomalous Hysteresis in Perovskite Solar Cells. *J. Phys. Chem. Lett* **2015**, *6*, 3808–3814. https://doi.org/10.1021/acs.jpclett.5b01645.

(11) De Bastiani, M.; Dell'Erba, G.; Gandini, M.; D'Innocenzo, V.; Neutzner, S.; Kandada, A. R. S.; Grancini, G.; Binda, M.; Prato, M.; Ball, J. M.; et al. Ion Migration and the Role of Preconditioning Cycles in the Stabilization of the J-V Characteristics of Inverted Hybrid Perovskite Solar Cells. *Adv. Energy Mater.* **2016**, *6* (1501453). https://doi.org/10.1002/AENM.201501453.

(12) Courtier, N. E.; Cave, J. M.; Foster, J. M.; Walker, A. B.; Richardson, G. How Transport Layer Properties Affect Perovskite Solar Cell Performance: Insights from a Coupled Charge Transport/Ion Migration Model. *Energy Environ. Sci.* **2019**, *12* (1), 396–409. https://doi.org/10.1039/c8ee01576g.

(13) Butler, K. T.; Frost, J. M.; Walsh, A. Ferroelectric Materials for Solar Energy Conversion: Photoferroics Revisited. *Energy Environ. Sci.* **2015**, *8*, 838–848. https://doi.org/10.1039/c4ee03523b.

(14) Liu, S.; Zheng, F.; Koocher, N. Z.; Takenaka, H.; Wang, F.; Rappe, A. M. Ferroelectric Domain Wall Induced Band Gap Reduction and Charge Separation in Organometal Halide Perovskites. *J. Phys. Chem. Lett* **2015**, *6*, 693–699. https://doi.org/10.1021/jz502666j.

(15) Guo, H.; Liu, P.; Zheng, S.; Zeng, S.; Liu, N.; Hong, S. Re-Entrant Relaxor Ferroelectricity of Methylammonium Lead Iodide. *Curr. Appl. Phys.* **2016**, *16* (12), 1603–1606.

(16) Lamberti, F.; Litti, L.; De Bastiani, M.; Sorrentino, R.; Gandini, M.; Meneghetti, M.; Petrozza, A. High-Quality, Ligands-Free, Mixed-Halide Perovskite Nanocrystals Inks for Optoelectronic Applications. *Advanced Energy Materials*. 2017. https://doi.org/10.1002/aenm.201601703.

(17) Bernards, D. A.; Malliaras, G. G. Steady-State and Transient Behavior of Organic Electrochemical Transistors. *Adv. Funct. Mater.* **2007**, *17* (17), 3538–3544. https://doi.org/10.1002/ADFM.200601239.

(18) Laiho, A.; Herlogsson, L.; Forchheimer, R.; Crispin, X.; Berggren, M. Controlling the Dimensionality of Charge Transport in Organic Thin-Film Transistors. *PNAS* **2011**, *108* (37), 15069–15073. https://doi.org/10.1073/pnas.1107063108/-/DCSupplemental.

(19) Sebastian B.Meier, DanielT ordera, Antonio Pertegás, Cristina Roldán-Carmona, Enrique Ortí, H. J. B. Light-Emitting Electrochemical Cells: Recent Progress and Future Prospects. *Mater. Today* **2014**, *17*, 217–223.

(20) Beilsten-Edmands, J.; Eperon, G. E.; Johnson, R. D.; Snaith, H. J.; Radaelli, P. G. Non-Ferroelectric Nature of the Conductance Hysteresis in CH3NH3PbI3 Perovskite-Based Photovoltaic Devices. *Appl. Phys. Lett* **2015**, *106* (17), 173502–173507. https://doi.org/10.1063/1.4919109.

(21) Shao, Y.; Fang, Y.; Li, T.; Wang, Q.; Dong, Q.; Deng, Y.; Yuan, Y.; Wei, H.; Wang, M.; Gruverman, A.; et al. Grain Boundary Dominated Ion Migration in Polycrystalline Organic-Inorganic Halide Perovskite Films. *Energy Environ. Sci.* **2016**, *9*, 1752–1759. https://doi.org/10.1039/c6ee00413j.

(22) Liang, Z.; Zhang, S.; Xu, X.; Wang, N.; Wang, J.; Wang, X.; Bi, Z.; Xu, G.; Yuan, N.; Ding, J. A Large Grain Size Perovskite Thin Film with a Dense Structure for Planar Heterojunction Solar Cells via Spray Deposition under Ambient Conditions. *RSC Adv.* **2015**, *5* (74), 60562–60569. https://doi.org/10.1039/C5RA09110A.

(23) Singh, T.; Miyasaka, T. Stabilizing the Efficiency Beyond 20% with a Mixed Cation Perovskite Solar Cell Fabricated in Ambient Air under Controlled Humidity. *Adv. Energy Mater.* **2018**, *8* (3), 1700677–1700685. https://doi.org/10.1002/AENM.201700677.

(24) Baikie, T.; Fang, Y.; Kadro, J. M.; Schreyer, M.; Wei, F.; Mhaisalkar, S. G.; Graetzel, M.; White, T. J. Synthesis and Crystal Chemistry of the Hybrid Perovskite (CH3NH3)PbI3 for Solid-State Sensitised Solar Cell Applications. *J. Mater. Chem. A* **2013**, *1* (18), 5628–5641. https://doi.org/10.1039/C3TA10518K.

(25) Harwell, J. R.; Baikie, T. K.; Baikie, I. D.; Payne, J. L.; Ni, C.; Irvine, J. T. S.; Turnbull, G. A.; Samuel, I. D. W. Probing the Energy Levels of Perovskite Solar Cells via Kelvin Probe and UV Ambient Pressure Photoemission Spectroscopy. *Phys. Chem. Chem. Phys* **2016**, *18*, 19738--19745. https://doi.org/10.1039/c6cp02446g.

(26) Takahashi, T.; Tokailin, H.; Sagawa, T. Angle-Resolved Ultraviolet Photoelectron Spectroscopy of the Unoccupied Band Structure of Graphite. *Phys. Rev. B* **1985**, *32* (12), 8317–8324.

(27) Feng, Y.; Zhang, K.; Li, H.; -, A.; Hartmann, G.; Hwang, G. S. The Work Function of Few-Layer Graphene. *J. Phys. Condens. Matter* **2017**, *29* (035003). https://doi.org/10.1088/0953-8984/29/3/035003.

(28) ARoldán-Carmona, C.; Zimmermann, I.; Mosconi, E.; Lee, X.; Martineau, D.; Narbey, S.; Oswald, F.; De Angelis, F.; Graetzel, M.; Nazeeruddin, M. K. One-Year Stable Perovskite Solar Cells by 2D/3D Interface Engineering. *Nat. Commun.* **2017**, *8* (15684). https://doi.org/10.1038/ncomms15684.

(29) Hu, Y.; Si, S.; Mei, A.; Rong, Y.; Liu, H.; Li, X.; Han, H. Stable Large-Area (10x10 Cm2) Printable Mesoscopic Perovskite Module Exceeding 10% Efficiency. *Sol. RRL* **2017**, *1* (2), 2–7. https://doi.org/10.1002/solr.201600019.

(30) Fagiolari, L.; Bella, F. Carbon-Based Materials for Stable, Cheaper and Large-Scale Processable Perovskite Solar Cells. *Energy Environ. Sci.* **2019**, *12* (12), 3437–3472. https://doi.org/10.1039/c9ee02115a.

(31) Amendola, V.; Polizzi, S.; Meneghetti, M. Laser Ablation Synthesis of Silver Nanoparticles Embedded in Graphitic Carbon Matrix. *Sci. Adv. Mater.* **2012**, *4* (3–4), 497–500. https://doi.org/10.1166/SAM.2012.1308.

(32) Reyes, D.; Camacho, M.; Camacho, M.; Mayorga, M.; Weathers, D.; Salamo, G.; Wang, Z.; Neogi, A. Laser Ablated Carbon Nanodots for Light Emission. *Nanoscale Res. Lett.* **2016**, *11* (424). https://doi.org/10.1186/s11671-016-1638-8.

(33) Zhang, X.; Zeng, Q.; Xiong, Y.; Ji, T.; Wang, C.; Shen, X.; Lu, M.; Wang, H.; Wen, S.; Zhang, Y.; et al. Energy Level Modification with Carbon Dot Interlayers Enables Efficient Perovskite Solar Cells and Quantum Dot Based Light-Emitting Diodes. *Adv. Funct. Mater.* **2020**, *30* (11), 1910530–1910538. https://doi.org/10.1002/ADFM.201910530.

(34) O'regan, B. C.; Barnes, P. R. F.; Li, X.; Law, C.; Palomares, E.; Marin-Beloqui, J. M. Optoelectronic Studies of Methylammonium Lead Iodide Perovskite Solar Cells with Mesoporous TiO2: Separation

of Electronic and Chemical Charge Storage, Understanding Two Recombination Lifetimes, and the Evolution of Band Offsets during J−V Hysteresis. *JACS* **2015**, *137*, 5087–5099. https://doi.org/10.1021/jacs.5b00761.

(35) Zhou, Y.; Garces, H. F.; Padture, N. P. Challenges in the Ambient Raman Spectroscopy Characterization of Methylammonium Lead Triiodide Perovskite Thin Films. *Front. Optoelectron.* **2016**, *9* (1), 81–86. https://doi.org/10.1007/s12200-016-0573-8.

(36) Quarti, C.; Grancini, G.; Mosconi, E.; Bruno, P.; Ball, J. M.; Lee, M. M.; Snaith, H. J.; Petrozza, A.; De Angelis, F. The Raman Spectrum of the CH3NH3PbI3 Ybrid Perovskite: Interplay of Theory and Experiment. *J. Phys. Chem. Lett.* **2014**, *5*, 279–284. https://doi.org/10.1021/jz402589q.

(37) N. A. Davydova, J. Baran, M. K. Marchewka, H. R. Interface Vibrational Modes in Layered Crystals with Stacking Faults. *J. Mol. Struct.* **1997**, *404*, 163–165.

(38) Khilji, M. Y.; Sherman, W. F.; Wilkinson, G. R. Raman Study of Three Polytypes of PbI2. *J. Raman Spectrosc.* **1982**, *13* (2), 127–133. https://doi.org/10.1002/JRS.1250130206.

(39) Condeles, J. F.; Ando, A. R. A.; Mulato, A. M. Optical and Structural Properties of PbI 2 Thin Films. *J. Mater. Sci.* **2008**, *43*, 525–529. https://doi.org/10.1007/s10853-007-1854-9.

(40) Yang, Y.; Pei, Q. Efficient Blue-Green and White Light-Emitting Electrochemical Cells Based on Poly[9,9-Bis(3,6-Dioxaheptyl)-Fluorene-2,7-Diyl]. *J. Appl. Phys.* **1997**, *81* (7), 3294–3296. https://doi.org/10.1063/1.364313.

(41) Bergmann, V. W.; Guo, Y.; Tanaka, H.; Hermes, I. M.; Li, D.; Klasen, A.; Bretschneider, S. A.; Nakamura, E.; Berger, D.; L Weber, S. A. Local Time-Dependent Charging in a Perovskite Solar Cell. *ACS Appl. Mater. Interfaces* **2016**, *8*, 19402−19409. https://doi.org/10.1021/acsami.6b04104.

(42) Hill, I. G.; Rajagopal, A.; Kahn, A.; Hu, Y. Molecular Level Alignment at Organic Semiconductor-Metal Interfaces. *Appl. Phys. Lett.* **1998**, *73* (5), 662–665.

(43) Hill, I. G.; Kahn, A. Energy Level Alignment at Interfaces of Organic Semiconductor Heterostructures. *J. Appl. Phys.* **1998**, *84* (10), 5583–5589.

(44) Xu, Z.; Chen, L.-M.; Chen, M.-H.; Li, G.; Yang, Y. Energy Level Alignment of Poly(3- Hexylthiophene): [6,6]-Phenyl C61 Butyric Acid Methyl Ester Bulk Heterojunction. *Appl. Phys. Lett* **2009**, *95*, 013301–013303. https://doi.org/10.1063/1.3163056.

(45) M.G. Helander, M.T. Greiner, Z.B. Wang, Z. H. L. Pitfalls in Measuring Work Function Using Photoelectron Spectroscopy. *Appl. Surf. Sci.* **2010**, *256*, 2602–2605.

Chapter 4

PbI_2 Nanoparticles as Porous Precursor-Buffer Layer for Carbon-Perovskite Solar Cells

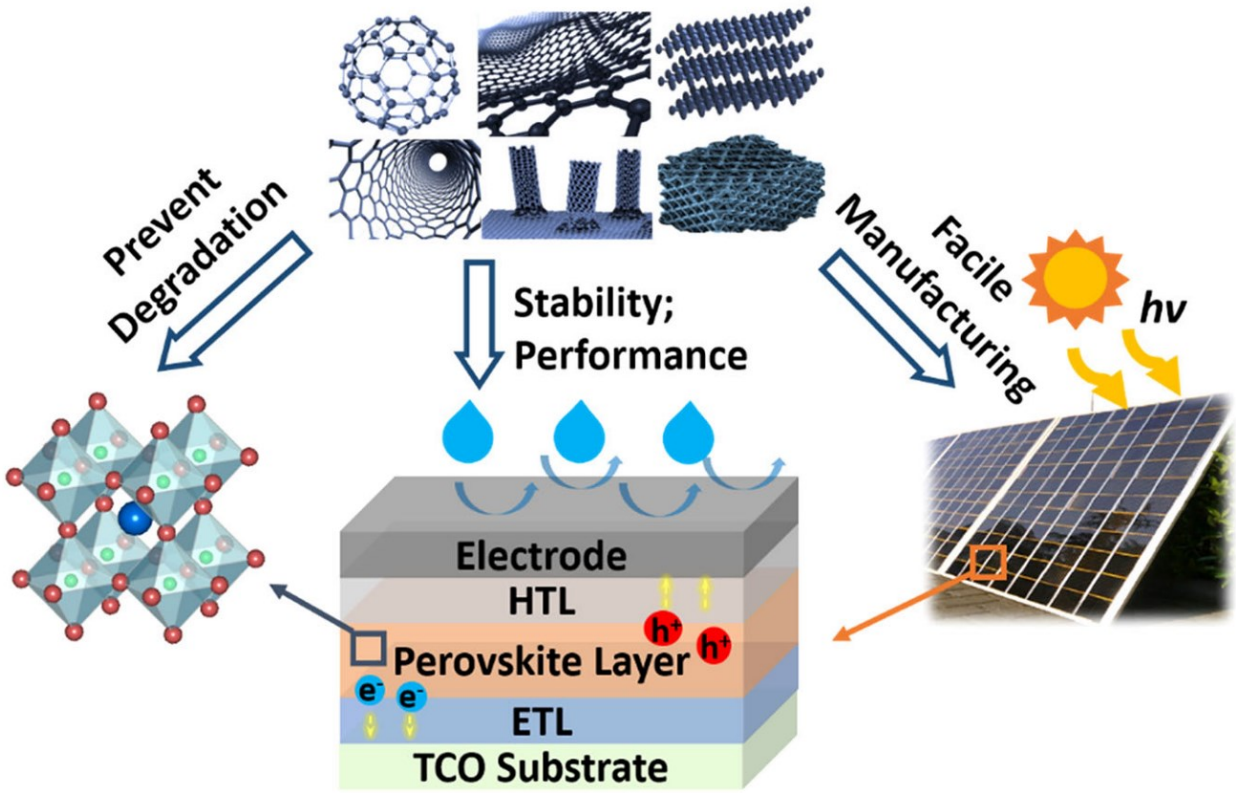

Carbon Energy. 2019;1:109–123

4. PbI_2 Nanoparticles as Porous Precursor–Buffer Layer for Carbon–Based Perovskite Solar Cells

4.1 The Aim of The Project

As previously stated in Section 1.4, long term stability of perovskite–based solar cells has been extremely improved by adopting "hole–conductor free" architectures, more commonly referred to as mesoporous carbon–based perovskite solar cells (mC–PSCs), which proved device stabilities over thousands hours [1,2] even at module scale (10^2 cm^2).[3,4] In these configurations, a LHP precursor solution is infiltrated into thick (≈ 10 µm) mesoporous scaffold made of carbon, the negative contact, insulating oxides, acting as spacer between electrodes, and titanium dioxide, the electron transport layer (Figure 4.1 a,b). Besides stability, another advantage of mC–PSCs is the possibility to pre–fabricate large amount of mesoporous scaffolds on glass and then complete the solar cells, by infiltrating the perovskite precursors solution from the top, when needed allowing to produce devices "on demand".[5] This, together with the low production cost and the full processability of stable mesoporous carbon-based PSCs have recently shown the great potential for the development of large–scale production processes (Figure 4.1 c).[6–9] The capability of mC–PSCs to operate without a selective hole transporting layer (HTL) is an advantage over conventional PSCs, often employing HTLs fabricated with expensive and unstable organic materials such as spiro–OMeTAD.

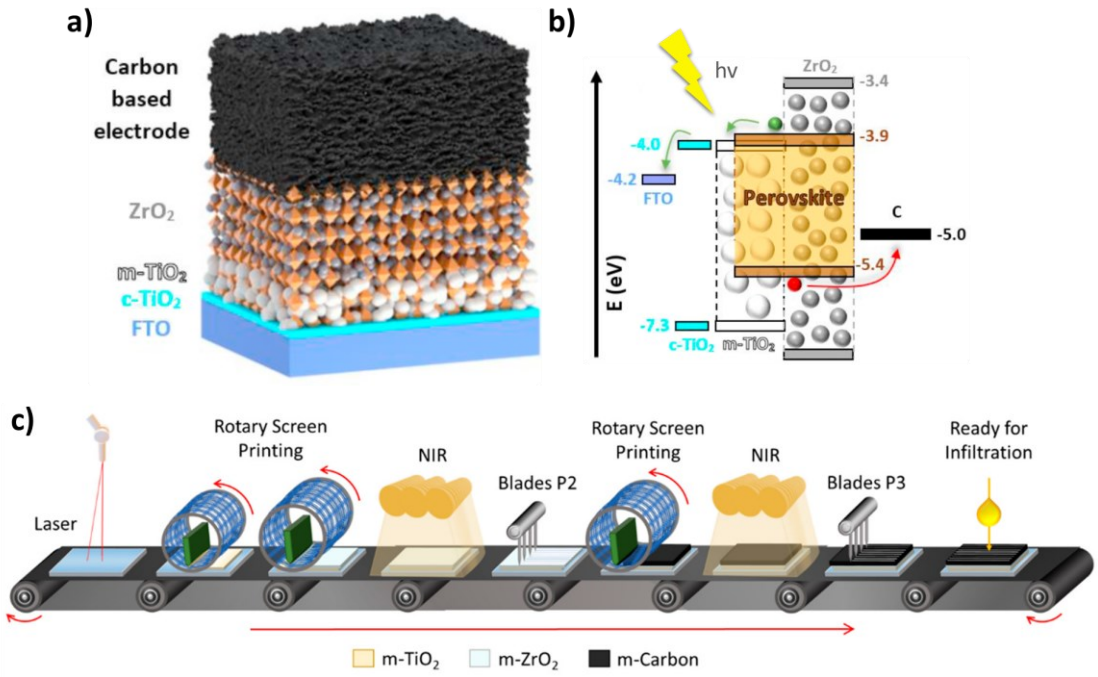

Figure 4.1 a) Structure and b) energy band diagram of mesoscopic carbon–based PSC.[10] c) Representation of a roll–to–roll production line of mC–PSCs using screen–printing, scribing methods, and near–infrared annealing.[5]

However, the hole quasi–Fermi level (E_{Fp}), which is predominantly determined by the interaction between the perovskite and the carbon electrode, is higher in carbon–based PSCs than in traditional planar PSCs due to the higher Femi level of C than the HOMO of the HTM in planar PSCs. A list of abbreviations is reported in an appendix (pp. 242) at the end of the dissertation. This causes the lower open–circuit voltage (V_{OC}) measured for carbon-based PSCs than that of HTM–based PSCs.[9] In addition, the poor charge selectivity of carbon electrode and the high thickness of the mesoporous C layer inevitably lead to lower efficiencies than those of planar PSCs architectures, due to a higher probability of photo–generated charges to recombine along and/or at the carbon electrode.[5] Several optimizations have been made in the last years, mostly aimed at improving the perovskite/C interface [10] and the carbon paste formulation for the top electrode fabrication.[11,12] Nevertheless, mC–PSCs efficiencies are still below 16 %,[13] far behind the planar counterpart showing PCEs up to 25 %.[14] Moreover, the constrain of using high T (> 450 °C) for the sintering of mesoporous oxide make difficult the deposition of mesoporous carbon–based PSCs over flexible substrates.[11,15]

The aim of the project presented in this chapter was to mitigate the above–mentioned obstacles by depositing, via spray coating, thin films of PbI_2 NPs synthesized by laser ablation synthesis (LASiS) in isopropanol (IPA) to be used both as buffer layer, to separate charge transport layers, and precursor layer, to be converted into methylammonium lead triiodide ($MAPbI_3$) perovskite photoactive material by infiltration of MAI solution in IPA (Figure 4.2). $MAPbI_3$ from ablated–precursors recently shown the presence of a graphitic/graphene phase (formed during LASiS) linked to the perovskite phase, which proved to reduce both $MAPbI_3$ sensitivity towards humidity and the current density–voltage (J–V) hysteresis due to ions migration.[16,17] With this approach, both perovskite morphology and mC–PSCs scalability could be improved thanks to: (i) the possibility to produce $MAPbI_3$ photoactive layers with bigger grains than those obtained in conventional mC–PSCs;[18–21] (ii) a simplification of the overall fabrication process of carbon–based PSCs (i.e., mesoporous spacer oxide layers are no more needed); (iii) the avoidance of the infiltration step of the perovskite precursor solution through the stack (which usually require a robotic mesh deposition technique).[22,23] The non–use of oxide buffer layers would also help in reducing the number of high–temperature fabrication steps to produce mC–PSCs, by avoiding the mesoporous oxide sintering. In addition, the sustainability of the whole process would be ensured by avoiding the use of DMF/DMSO toxic solvents during the precursors deposition/perovskite conversion, usually necessary to dissolve lead halide precursors.

In the following paragraphs, optimization processes for laser ablation synthesis and spray coating deposition of lead iodide nanoparticles will be presented, up to their implementation in mesoporous carbon–based PSCs as spacer/perovskite precursor layer.

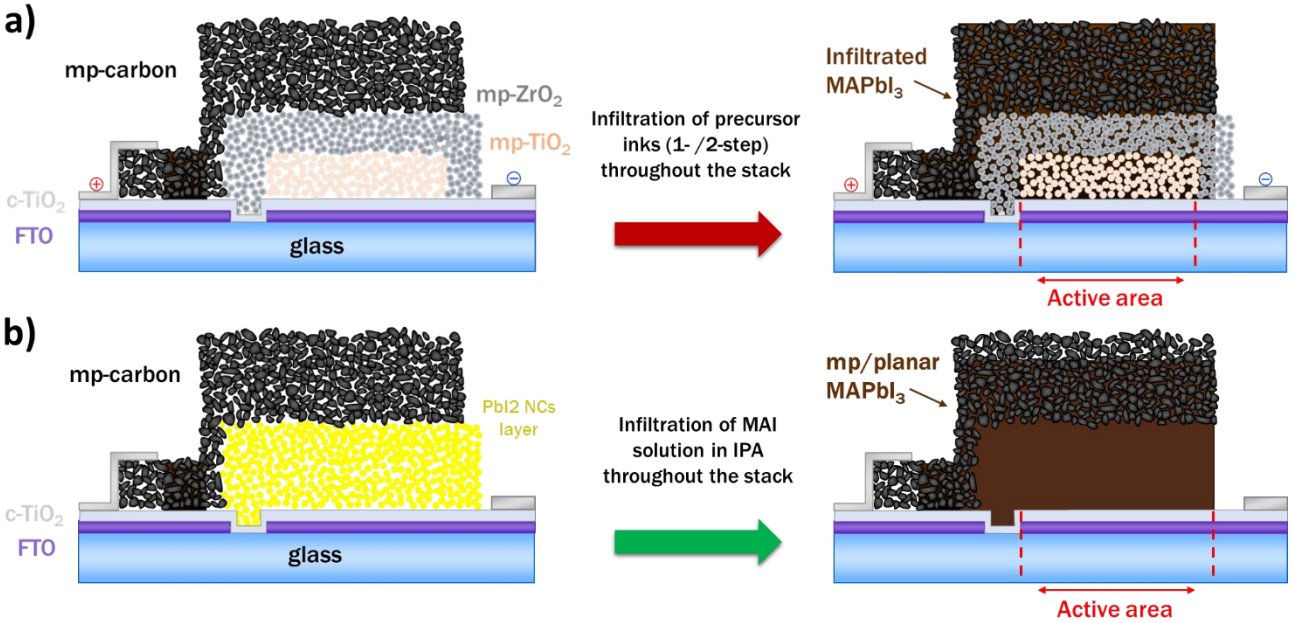

Figure 4.2 Schematic comparison (not in scale) between a) the typical $MAPbI_3$ synthesis adopted for mC–PSCs, obtained by infiltrating a perovskite precursors solution through the stack;[6] b) the proposed approach in which $MAPbI_3$ is obtained converting a precursor porous layer made of PbI_2 NPs by infiltrating MAI solution in alcohol.

4.2 Results and Discussion

4.2.1 *Preliminary Validation Tests*

A high temperature (300–400 °C) annealing step of carbon–film electrode is usually required to remove the non–conductive binders contained in the organic paste,[6,15] as well as to effectively produce a carbon mesoporous layer.[24] Consequently, the underlying PbI_2 NPs layer must bear these conditions without affecting its morphology since a good porosity is required for a good penetration of MAI solution (i.e., a good conversion into $MAPbI_3$ perovskite).[25–29] Since the melting point of bulk lead iodide (of about 402 °C, presumably lower for the case of nanoparticles)[30–32] is close to the annealing temperature required for mesoporous carbon electrodes, PbI_2 nanoparticles thin film must undergo preliminary annealing treatments before proceeding with the subsequent experiments. For this reason, PbI_2 NPs alcoholic solution, prepared by LASiS in isopropanol, was spray–coated onto four 1x1 cm^2 FTO/glass substrates to get thin films ≈ 0.5 µm thick. Such films were annealed at different temperatures, in the range of 300–400 °C as required for the deposition of mesoporous carbon electrode, then characterized to evaluate their optical and morphological

properties. The $MAPbI_3$ perovskite layers produced by dip coating the annealed PbI_2 precursor films into a 10 mg/ml methylammonium iodide (MAI) solution in isopropanol were characterize as well (Figure 4.3). Further details on PbI_2 spray coating depositions and perovskites conversion are reported in Section 4.4.1. Figure 4.4 shows the UV–Vis spectra of the so–obtained PbI_2 thin films and the $MAPbI_3$ perovskite layers produced from them. No variations in the UV–Vis profile of not–annealed spray–coated PbI_2 NPs thin film was observed (Figure 4.4 a), while its upward shift compared to the precursor ink UV–Vis spectrum was attributed to a higher NPs light scattering once deposited over the substrate. A decrease in the typical lead iodide absorption edge, around 500 nm, was registered for the annealed precursor films, up to the complete disappearance of the contribution at 400°C.

A similar trend was noticed in the UV–Vis spectra of perovskite layers obtained from the corresponding former samples with an attenuation of $MAPbI_3$ absorption edge, around 780 nm, when converted from PbI_2 precursor films annealed at high temperatures (Figure 4.4 b). Coherently with the trends observed for the UV–Vis absorption edges, a decrease of the typical yellow lead iodide coloration was noticed at increasing annealing temperatures (Figure 4.4 c). The same phenomenon was reflected in their perovskite counterpart showing a dark brown collared $MAPbI_3$ when converted from not–annealed PbI_2 film, while perovskites with pale colorations were produced from precursor layers annealed at higher temperatures (Figure 4.4 d). The yellowish regions in the $MAPbI_3$ film obtained by converting precursor films annealed at 350 and 400 °C highlighted the presence of PbI_2 underneath perovskite. This, together with the disappearance of $MAPbI_3$ absorption edge in UV–Vis spectra, pointed out that non–optimal perovskite conversions are obtained in these conditions. The perovskite conversion times (i.e., the minimum time require for dip coating conversion), reported below each sample in Figure 4.4 d, increased up to the 350 °C sample and then decreased in the case of the 400 °C one.

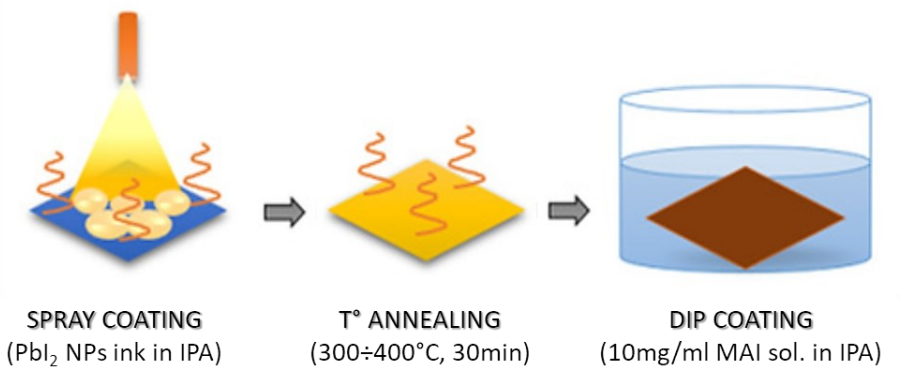

Figure 4.3 Diagram showing the sequential steps followed for the deposition, the thermal annealing, and the conversion of PbI_2 and $MAPbI_3$ perovskite thin films, respectively.[29]

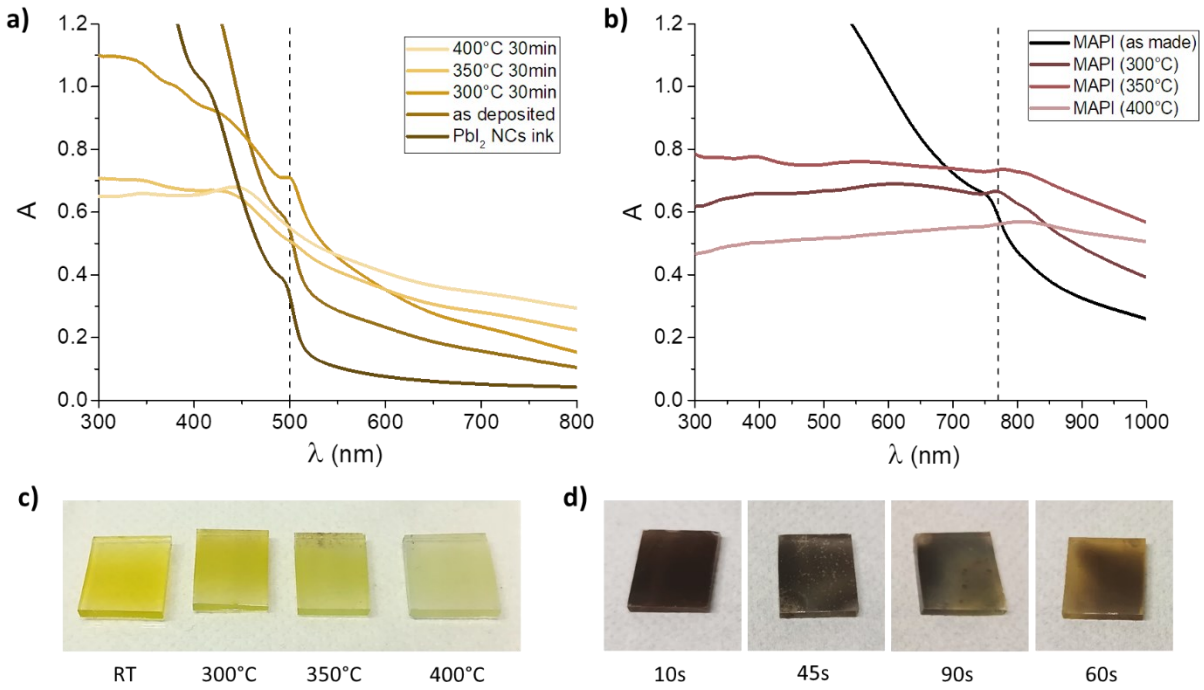

Figure 4.4 UV–Vis spectra of a) spray–coated PbI_2 NPs precursor thin films obtained at increasing annealing temperature and b) the $MAPbI_3$ perovskite layers obtained from the formers. The typical absorption of PbI_2, at about 500 nm, and of $MAPbI_3$ perovskite, around 780 nm, are indicated by dash lines in each UV–Vis plot. Pictures of c) lead iodide precursor films and d) $MAPbI_3$ layers obtained from their conversion. Longer perovskite conversion times, reported underneath each sample in (d), were register when synthesized from PbI_2 precursor layers annealed at higher temperatures.

This trend was ascribed to a decreased porosity in the PbI_2 films annealed at high temperature, due to the possible sintering of nanoparticles, with the consequent increase in the infiltration time between of MAI precursor during dip coating. The decrease in the perovskite conversion time in the case of 400 °C sample was ascribed to the thinning of the lead iodide layer (i.e., a faster conversion due to a lower amount of precursor material) due to evaporation processes that start to occur at temperature close to the melting point of the material. SEM analysis provided an insight on the thermally induced change in morphology of both the precursor thin films and the $MAPbI_3$ perovskite layers produced from their conversion (Figure 4.5). Both spray–coated PbI_2 NPs and $MAPbI_3$ crystals showed an increase in size with the annealing temperature. Lead iodide nanoparticles, with an average size of 20–50 nm in untreated samples, increased in size up to 200 nm when annealed at 300 °C. A poor uniformity and the appearance of uncovered FTO regions were observed for samples treated at higher temperatures, with the formation of micrometric clusters (Figure 4.5 a). A similar trend, both in size and in substrate coverage was noticed in $MAPbI_3$ layers as well. Perovskite nanoparticles of 100–200 nm and 300–400 nm were observed when converted from untreated and 300 °C PbI_2 precursor films, respectively, in line with previous studies.[25,33] Both these samples showed a good coverage of the FTO/glass without uncovered regions.

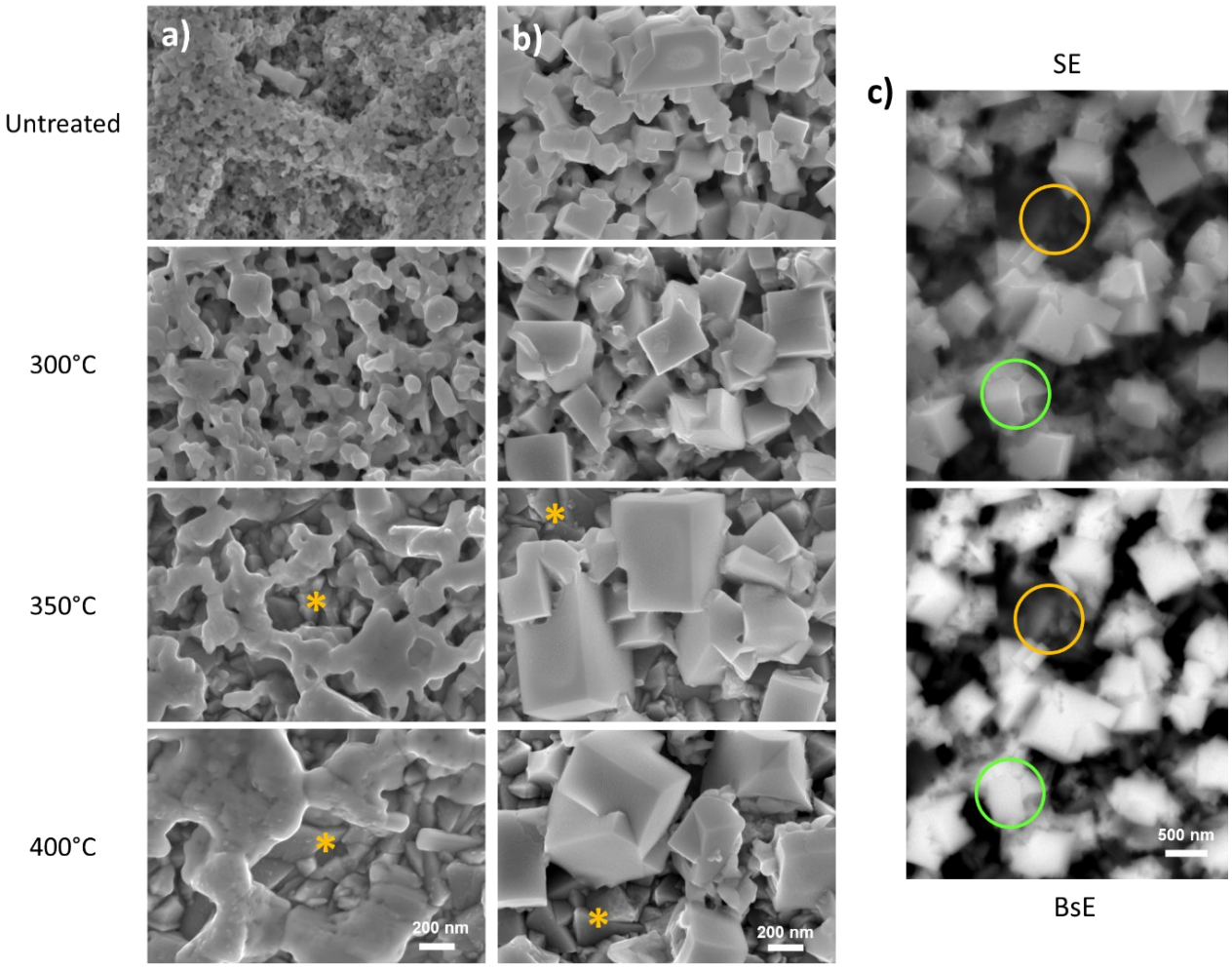

Figure 4.5 Top–view SEM images of a) PbI_2 NPs spray–coated onto FTO/glass substrates and b) $MAPbI_3$ crystals obtained from their conversion. The annealing temperatures of precursor PbI_2 films are reported on the left while asterisks highlight uncovered FTO regions. c) Secondary electrons (SE) and back–scattered electrons (BsE) images showing the different contrast between $MAPbI_3$ perovskite crystals (green circles) and FTO (orange circles), through which it was possible to distinguish between covered and uncovered regions of the substrate.

On the contrary, a poor substrate coverage was noticed for $MAPbI_3$ layers converted from precursors films annealed at 350 and 400 °C, with the formation of bigger perovskite crystals up to 1 µm lateral size (Figure 4.5 b). Thus, perovskite crystal size is affected by the precursor NPs one where bigger PbI_2 crystal lead to bigger $MAPbI_3$ crystals, in line with previous reports.[34,35] Secondary electrons (SE) and back–scattered electrons (BsE) imaging were employed to better distinguish between the covered/uncovered regions in perovskite samples (Figure 4.5 c). Photoluminescence (PL) measurements are widely used to analyze the quality of lead halide perovskite materials.[36–38] Figure 4.6 a shows the steady–state PL spectra of $MAPbI_3$ films, produced as previously reported samples but using glass as substrate to avoid alterations of $MAPbI_3$ emissive properties induced by FTO conductive oxide.[39,40]

A strong emission peak around 780 nm, corresponding to the 1.6 eV bandgap expected for $MAPbI_3$,[41,42] was registered for perovskite produced from the untreated PbI_2 film (black line), close to the one obtained for a reference sample (with comparable thickness) prepared by 2–step spin coating deposition.[43] Details regarding the preparation of the reference spin–coated sample are reported in Section 4.4.2. This highlighted the good quality of both the PbI_2 precursor NPs produced by LASiS in IPA and the $MAPbI_3$ perovskite material synthesized from them. A lower, yet still intense PL emission was measured for the $MAPbI_3$ layer converted from the PbI_2 NPs annealed at 300°C, while poor emissive properties were observed for $MAPbI_3$ synthesized from 350 and 400 °C treated precursor samples, respectively.

No significant differences were observed by comparing the XRD patterns of $MAPbI_3$ perovskites obtained from untreated and 300 °C treated PbI_2 NPs precursor layers, showing the typical sharp reflections of tetragonal perovskite phase (peak at 23.7° related to the (211) reflection)[44,45] and just a slight increase in the lead iodide contribute (indicated by the (001) reflection at 12.7 °) for the case of 300 °C treated sample Figure 4.6 b.[46,47]

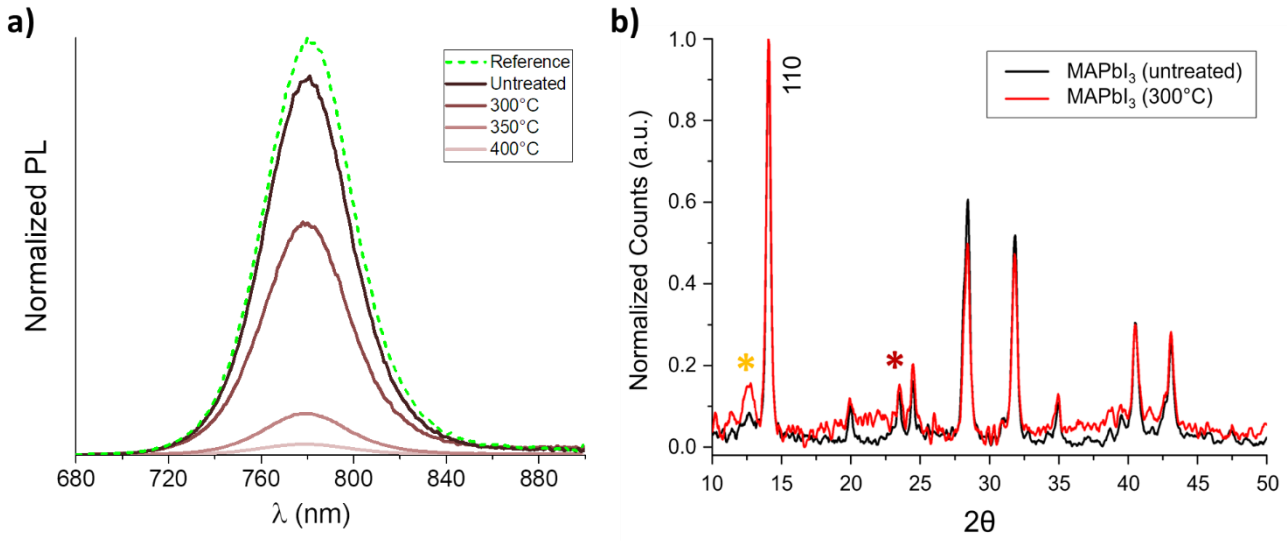

Figure 4.6 a) Steady–state PL spectra of $MAPbI_3$ layers on glass obtained by converting spray–coated thin films of PbI_2 NPs annealed at different temperatures. All spectra were normalized over the maximum intensity of a reference $MAPbI_3$ sample (dash green line), prepared by spin coating deposition. b) Comparison between XRD patterns of $MAPbI_3$/FTO/glass samples obtained from untreated and 300 °C treated PbI_2 NPs. Orange asterisk indicates the (001) reflection of PbI_2, while the brown asterisk is related to the (211) typical reflection of tetragonal $MAPbI_3$ phase. Both spectra were normalized over the main perovskite (110) reflection at 14.1°.

Based on the optical and morphological results reported above, the annealing treatment at 300 °C were selected as a compromise to get uniform and good quality $MAPbI_3$ perovskite films from spray–coated PbI_2 NPs in conditions compatible with mesoporous C electrode depositions.

4.2.2 *LASiS of High–Volume PbI_2 Nanoparticles Colloidal Solutions*

LASiS usually produce low volumes (a few ml) of poor concentrated (µg/ml) colloidal solution of nanoparticles (Section 2).[48] Even if recent studies showed how the initial low productivity of LASiS can been remedied, reaching NPs production rates up to grams per hour,[49] the harsh conditions required for such high concentrations were not suitable for our purposes. This required an appropriate optimization of LASiS procedure to produce higher volumes (>10^1 ml) of more concentrated (≈ mg/ml) PbI_2 nanoparticles, a prerogative to spray coating larger–area thin films to implement into mC–PSCs and convert into $MAPbI_3$ photoactive material. By standard LASiS procedure for obtaining PbI_2 nanoparticles inks, [16] 4.0 ml of PbI_2 NPs ink in IPA with a concentration of about 0.2 mg/ml are obtained by LASiS within 20 minutes. Details regarding LASiS setup and the followed procedure for the estimation of lead iodide NPs colloidal solutions concentration are reported in Section 4.4.3. Higher yields can be achieved by increasing the ablation time, the solvent volume, and/or the laser fluence. However, high fluences can both damage the target and cause laser ablation of the low–boiling high–vapor pressure alcoholic solvent (e.g., flames), reducing the safety of LASiS process. The appearance of a contribute between 20–30° was observed in the XRD pattern of PbI_2 NPs when a fluence of 8 J/cm^2 was employed for the synthesis (Figure 4.7).

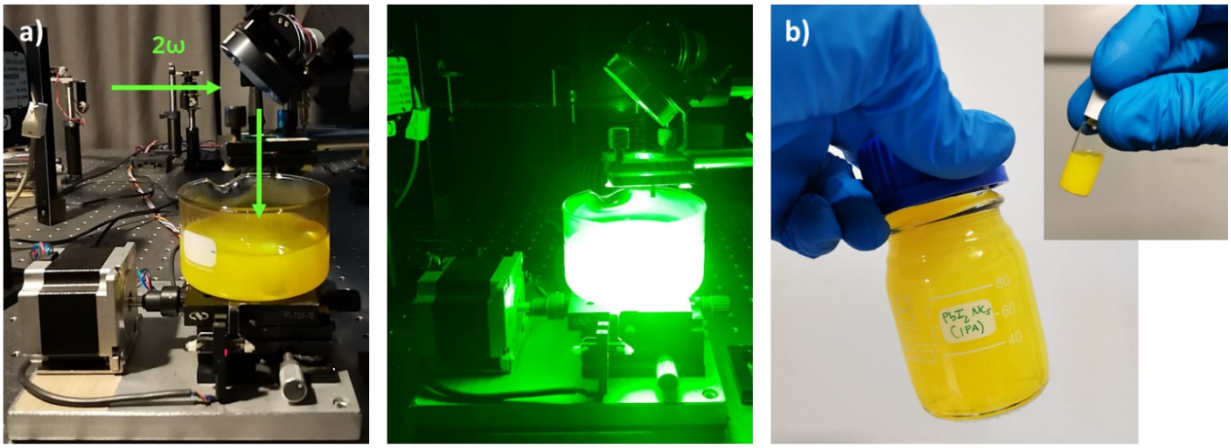

c)

LASiS Conditions

Conditions	λ_{exc}	Laser Fluence	Solvent Volume	Solvent Height	Focal Lenght	Ablated Area	Ablation Time	Ablation Yield
Standard procedure	532 nm	2 J/cm^2	4 ml	2.5 cm	5.0 cm	5x5 mm^2	20 mins	2 mg/hour
Optimized Conditions	532 nm	4 J/cm^2	160 ml	2.8 cm	7.5 cm	8x8 mm^2	4 hours	20 mg/hour

Figure 4.7 XRD patterns of PbI_2 nanoparticles produced by laser ablation in isopropanol at difference laser fluence values. The red circle highlights the appearance of a contribute between 20–30° when an 8 J/cm^2 fluence is set for the synthesis. Such contribute was attributed to the formation of amorphous PbI_2 and/or carbonaceous species due to solvent degradation when LASiS is performed at high laser fluence.[50-52]

Such contribute was attributed to the possible formation of carbonaceous materials due to the solvent degradation when LASiS is performed at too high fluences.[50–52] This set 4 J/cm^2 as the maximum fluence to use to get PbI_2 NPs with crystallinity and/or amorphous carbon species. After several attempts in which the ablation time, the solvent volume, and the container type (affecting the length of the laser optical path to reach the target) were varied, a suitable condition was identified for the designated applications.

Figure 4.8 shows the setup and the conditions used for obtaining 160 ml of 0.6 mg/ml concentrated PbI_2 NPs ink by LASiS in IPA for 4 hours. The increase in PbI_2 NPs solution concentration over time was monitored as described in Section 4.4.3, related to the trend of PbI_2 absorption edge at 500 nm in the UV–Vis spectra (Figure 4.9 a). Even higher concentration, of more than 0.7 mg/ml, was achieved by LASiS for 6 hours in the above–mentioned conditions. However, such a high concentration led to colloidal solutions with poor stability showing, within 10–15 minutes, fast PbI_2 NPs aggregation. This can be observed with an increase in the scattering contribution at 600–800 nm in UV–Vis spectra (Figure 4.9 a). This made the sample a non–valuable candidate for the subsequent spray coating depositions and set the upper concentration limit for the ligands–free PbI_2 NPs colloidal solutions. On the contrary, good ink stabilities were appreciated for the solutions ablated for up to 4 hours (> 48 hours), which just required a 5–minutes bath sonication before depositions.

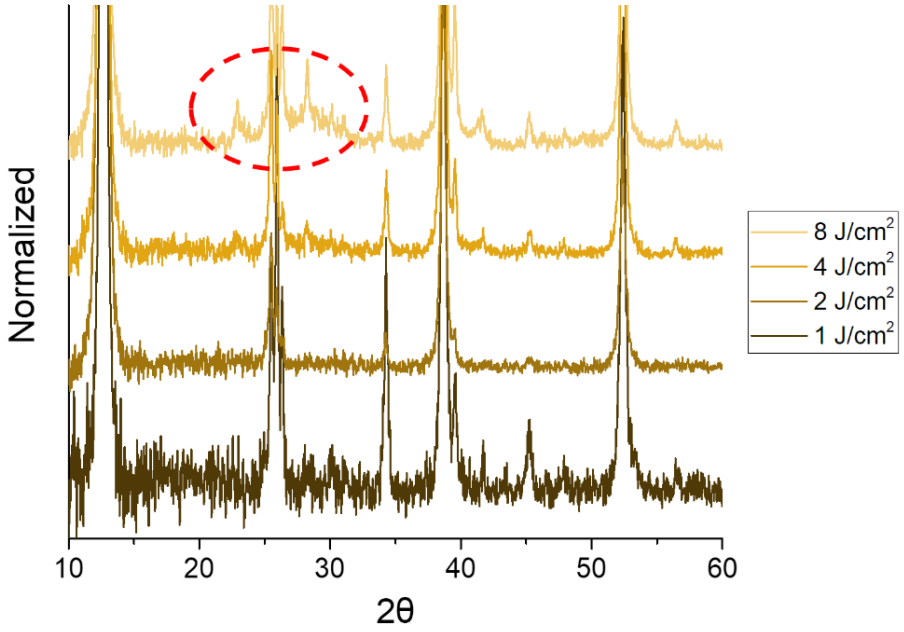

Figure 4.8 Pictures a) under visible light and b) in dark of the LASiS setup employed for the synthesis of high volume PbI_2 NPs colloidal solutions. b) Volume comparison between the 160 ml colloidal solution obtained in optimized conditions and the initial low–volume ink obtained in standard conditions (inset). c) Table summarizing the experimental conditions employed for the standard and the optimized high–volume LASiS.

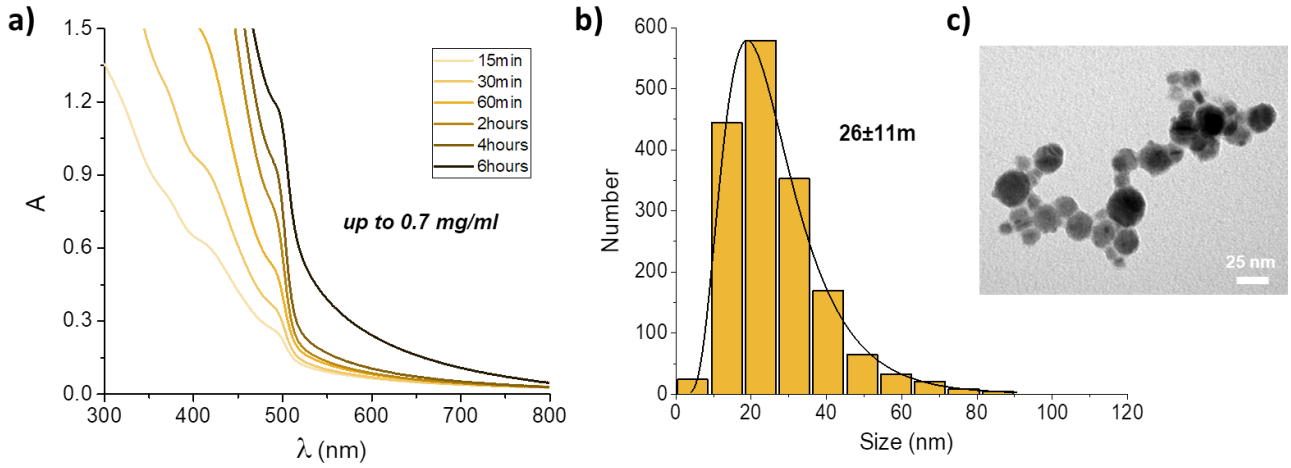

Figure 4.9 a) UV–Vis spectra showing the increase in PbI_2 absorption edge with the ablation time. The upward shift in 600–800 nm range for the 6 hours profile was associated to an increase of scattered light due to NPs aggregation. b) NPs size distribution estimated from c) TEM images of the colloidal solution ablated for 4 hours. The black curve in (b) indicates the lognormal fit through which it was estimated an average size of 15–40 nm.

A sharp size distribution of lead iodide nanoparticles, in the range of 15–40 nm, was estimated from TEM analysis of the ink (Figure 4.9 b,c). These dimensional values are in line with previous SEM analysis (Figure 4.5 a) and are optimal for getting porous PbI_2 NPs precursor films to implement in mC–PSCs. In this way it was possible to increment the ablation yield of one order of magnitude by optimizing LASiS conditions, from about 2 mg/hour (4ml of 0.2 mg/ml ink in 20 minutes) to 20 mg/hour (160 ml of 0.5–0.6 mg/ml ink in 4 hours), paving the way for producing large–area spray–coated PbI_2 nanoparticles thin films.

4.2.3 *Large–area Spray–coated PbI_2 NPs precursor thin films*

As remarked in Section 4.1, a thick, porous lead iodide film is needed to effectively act both as perovskite precursor layer as well as to separate the contacts of a carbon–based perovskite solar cell (Figure 4.2 b). For this reason, the high–volume PbI_2 NPs concentrated ink (Section 4.2.2) was spray–coated over 2.7x2.7 cm^2 FTO/glass to produce thick, uniform, and porous film (Figure 4.10 a). Further details on the large–area spray coating conditions of PbI_2 NPs are reported in Section 4.4.4. Film thickness was determined by combining profilometry and cross–sectional SEM analyses, through which an optimal average thickness of about 2 µm was measured by spray coating 20 ml of precursor ink (Figure 4.10 b,c). The porosity of PbI_2 NPs precursor films, a requirement for its subsequent conversion to $MAPbI_3$ perovskite,[25–28] was evaluated by Atomic Force Microscopy (AFM) and top–view SEM measurements.

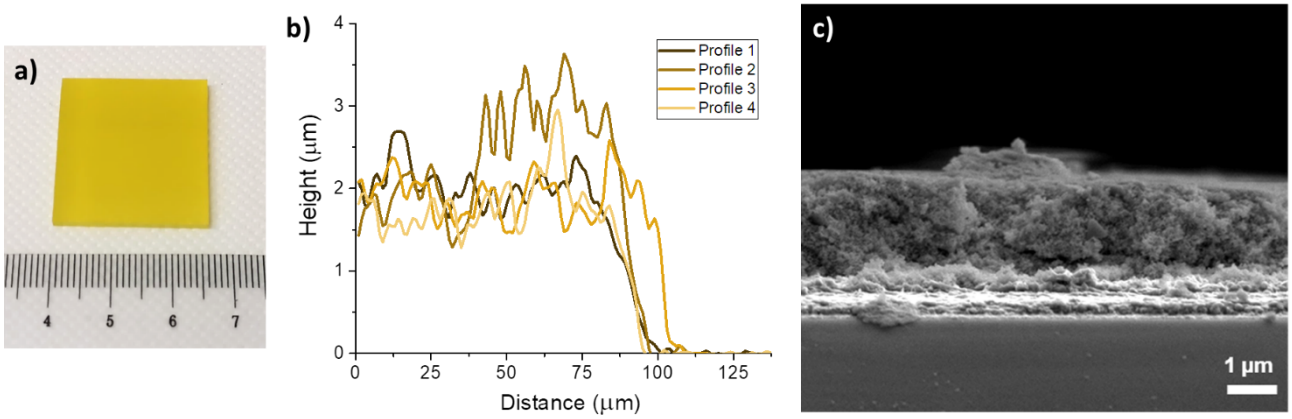

Figure 4.10 a) Picture of a 2.7x2.7 cm^2 PbI_2/FTO/glass sample obtained after spray coating 20 ml of the high–volume concentrated PbI_2 NPs ink. Film thickness estimation by b) profilometry and c) cross–sectional SEM.

From Figure 4.11 a it is possible to appreciate the peculiar morphology of the spray–coated lead iodide films, highly porous and characterized by micrometric craters on the surface. The formation of such craters was ascribed to the coffee ring effect,[53] expected for low temperature deposition processes (as the spray coatings of this work are). Wide range (20x20 µm) AFM analysis confirmed the morphology of PbI_2 film observed through SEM, allowing to better analyze the craters depth (up to 400 nm) thanks to the high resolution in Z–direction. AFM images were analyzed with WSxM software, through with an average roughness of 0.23 µm and a root mean square roughness of 0.28 µm were calculated. Figure 4.11 b shows the AFM 3D color map of the 20 ml spray–coated PbI_2 NPs precursor film (Figure 4.11 a). UV–Vis spectra were also evaluated to get an indication about thin thickness, proportional to the PbI_2 absorption edge at 500 nm. In this way it was possible to correlate profilometry and SEM data with the UV–Vis edges to calibrate the spray coating deposition (Figure 4.12 a,c). After a thermal annealing at 300 °C, the precursor films were converted into $MAPbI_3$ layers by dip coating in 10 mg/ml MAI solution in IPA for 1 minute.

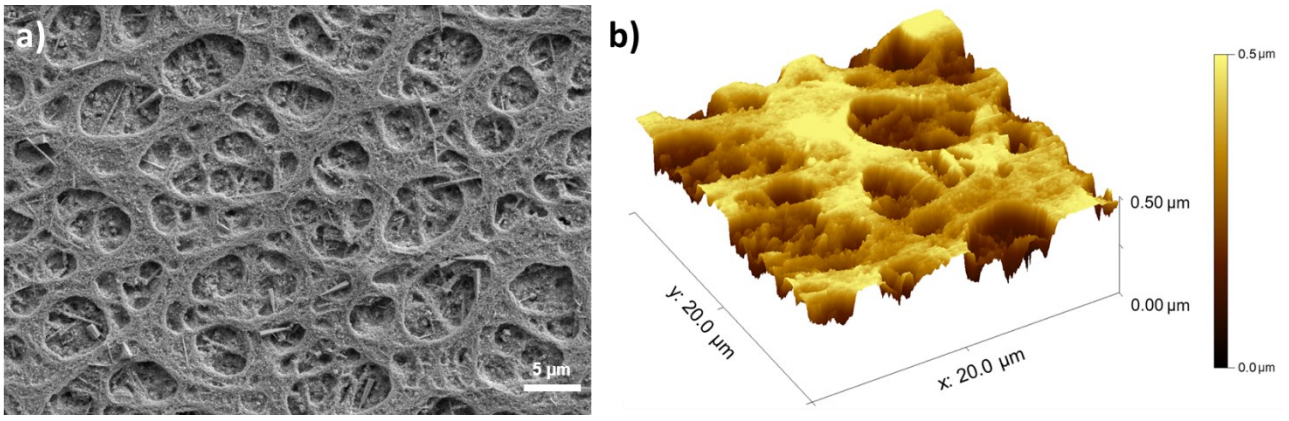

Figure 4.11 a) Top–view SEM image and b) 3D AFM colour map of the PbI_2 NPs film obtained by spray coating 20 ml of precursor ink in IPA over FTO/glass.

As for PbI_2 films, the same thickness analysis by profilometry, SEM and UV–Vis measurements was adopted for these samples as well (Figure 4.12 b,d). SEM cross–sectional images showed a thickening (of about 2 times) of $MAPbI_3$ film after PbI_2 precursor layer conversion, typical of multi–step perovskite films processing (Figure 4.12 c,d).[34,35,54] All these results proved how the adopted procedure (Figure 4.3) to effectively produce thick, and homogenous $MAPbI_3$ perovskite layer over large areas (Figure 4.12 e).

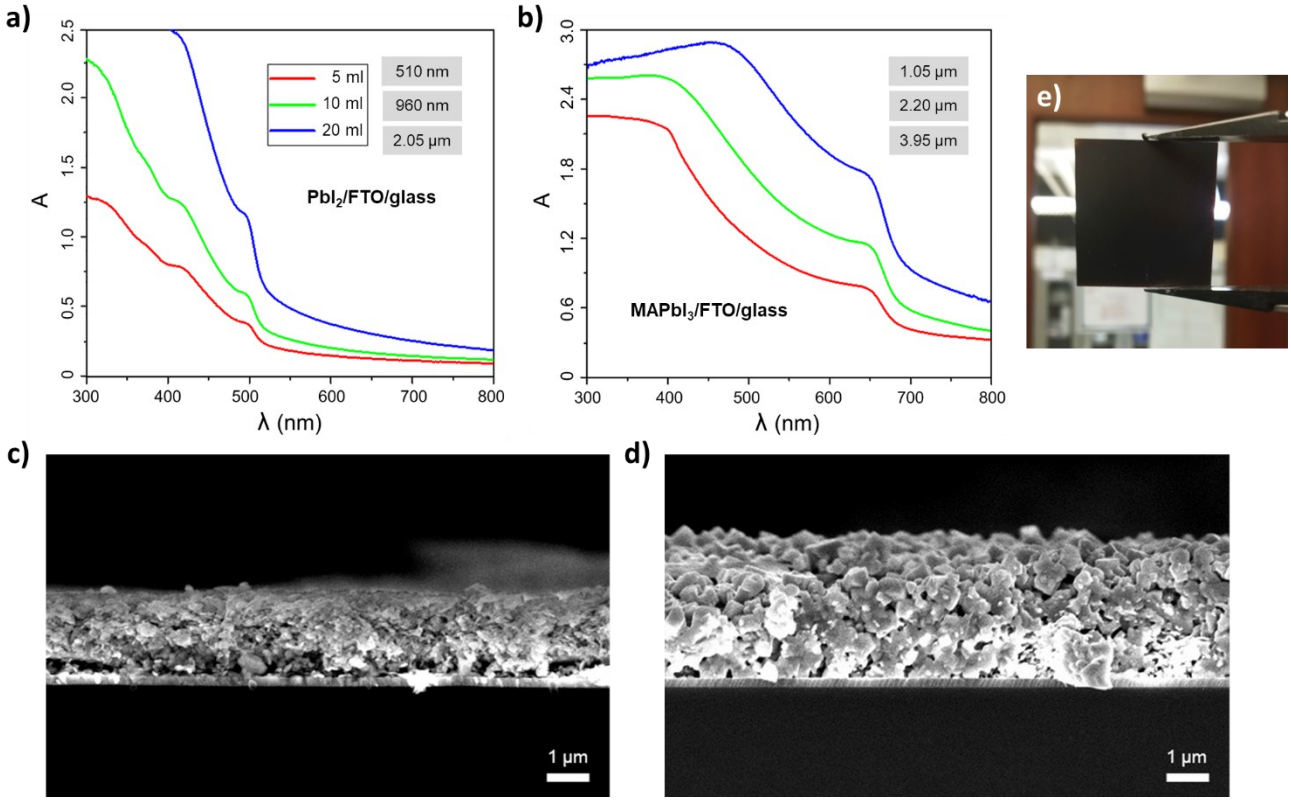

Figure 4.12 UV–Vis spectra of a) lead iodide precursor thin films produced by spray coating different volumes of PbI_2 NPs ink over FTO/glass and b) $MAPbI_3$ perovskite layer obtained by converting the former samples by dip coating. The film thicknesses measured by profilometry are reported for each sample in both plots. Cross–sectional SEM image of c) lead iodide precursor layer produced by spray coating 20 ml of PbI_2 NPs over SiO_2/Si substrate (to get a better contrast and avoid charging during SEM analysis) and d) $MAPbI_3$ perovskite film obtained by converting the former sample by dip coating in MAI solution. The PbI_2 precursor films were annealed at 300 °C before perovskite conversions and UV–Vis and SEM analyses. e) Photograph of the 2.7x2.7 cm^2 $MAPbI_3$/FTO/glass sample obtained by converting the 20 ml PbI_2 precursor layer.

4.2.4 *Carbon–based Perovskite Solar Cells Assembly*

Once optimized the PbI_2 NPs deposition and $MAPbI_3$ conversion (Section 4.2.3) the next, final step was to test the effect of applying the C–paste over the stack. As previously reported in Section 4.1, the lower efficiencies of mesoporous carbon-based PSCs than traditional planar architectures is generally attributed to a higher recombination rate of photo–generated charges along the carbon electrode and/or at the perovskite/carbon interface.[5,10] For this reason, the carbon paste

formulation and deposition is crucial for the top electrode fabrication.[11,12] Based on a previous studies,[22,23] a carbon paste by Gwent electronic materials (GEM) was selected as candidate to be screen printed onto the lead iodide s precursor layers. A compact TiO_2 (c–TiO_2) thin layer (≈50 nm) was deposited over 2.7x2.7 cm^2 FTO/glass by spray pyrolysis using a 10% solution of titanium diisopropoxide bis(acetylacetonate) solution in isopropanol and heated at 550 °C for 30 minutes on a hotplate.[23] 2 µm thick lead iodide precursor layer was deposited on c–TiO_2/FTO/glass by spray coating 20 ml of PbI_2 NPs colloidal solution in IPA, as previously described in Section 4.2.3. The resulting sample was cut in half using a diamond tip cutter to get 2 pixels out of it. Finally, the GEM carbon paste was screen printed onto the middle of the PbI_2 NPs/c–TiO_2/FTO/glass stack, then sintered at 300 °C for 30 minutes (Figure 4.13 a). In this way, mesoporous carbon electrodes of about 10 µm thickness were produced.[22] The so–obtained carbon electrode/PbI_2 NPs interface was analyzed by Raman mapping, following the procedure of a previous study.[23]

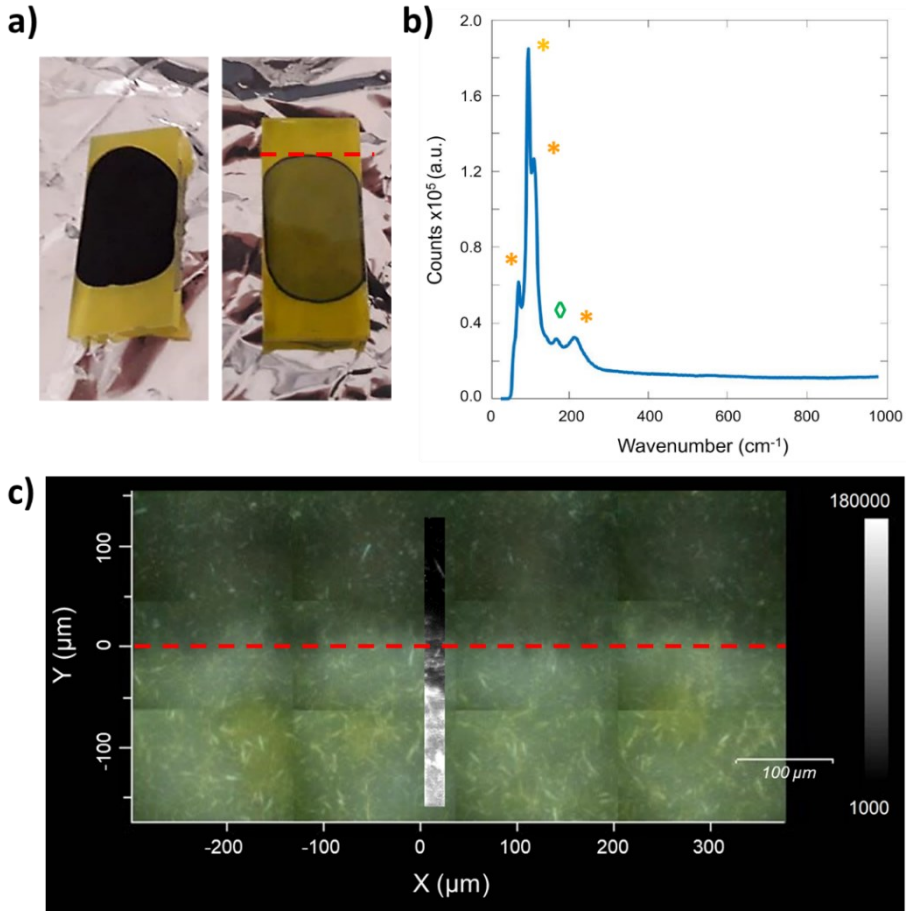

Figure 4.13 a) Face–up (left) and face–down (right) pictures of a C(GEM paste)/PbI_2 NPs/c–TiO_2/FTO/glass sample. b) Typical Raman spectrum of a PbI_2/c–TiO_2/glass sample. The orange asterisk indicates lead iodide contributes, respectively at 73, 96, 110 and 214 cm^{-1}, while the green rhombus highlights the titania peak around 198 cm^{-1}. c) Raman map of the Carbon/PbI_2 NPs/c–TiO_2/FTO/glass sample obtained by measuring the maximal intensity between 80 and 120 cm^{-1} over a reference baseline. The measurements were carried out through the glass side of the sample, in the region indicated with the red dash line in (a). The PbI_2 NPs/carbon interface corresponds to the zero value of Y–axis, with the region underneath the C electrode placed over the red line.

Figure 4.13 b shows the typical Raman spectrum of a PbI_2/c–TiO_2/glass sample with the lead iodide contributes, at 73, 96, 110 and 214 cm^{-1}, and the titania peak at 198 cm^{-1} (the one at 144 cm^{-1} is convolute within PbI_2 peak at 100 cm^{-1}) indicated by orange asterisks and the green rhombus, respectively. The Raman map, with the associated color scale bar, is reported in Figure 4.13 c. The analysis was carried out through the glass side of the sample around the carbon/PbI_2 interface, indicated with the red dash line in Figure 4.13 a and corresponding to the zero value of Y–axis in the 2D map. No lead iodide signals in the Raman shift range between 80 and 120 cm^{-1} were detected underneath the carbon electrode (the region above the red dash line). This suggested a damage of lead iodide precursor layer and/or PbI_2 NPs dissolution inside the carbon paste during its deposition. The same procedure was repeated without treating the C layer at 300 °C for 30 minutes, obtaining similar results. For this reason, GEM paste was rejected as non–suitable for our purposes. Based on recent studies,[55,56] an alternative way for the carbon electrode deposition, in which the carbon paste can be directly deposited on the perovskite absorbing layer, was pursued.

An alternative carbon ink containing ethyl cellulose as highly soluble, low toxic, and cheap polymeric binder was used for low temperature carbon top electrode fabrication.[57] The prepared ink contained 12.5% ethyl cellulose resin in 1 g of 1–butanol, with a 29.4% carbon loading. To better investigate the impact of the carbon paste deposition on the morphology of the PbI_2 NPs precursor layer, 2 batches were prepared in different conditions by: (i) depositing the carbon electrode on top of the PbI_2 layer, before $MAPbI_3$ conversion by dip coating; (ii) depositing the carbon contact after the perovskite conversion. The low–temperature carbon paste was annealed at 70 °C for 5 minutes under the extractor hood after its blade–coating deposition. All other conditions were kept constant, as previously described. A poor perovskite conversion was observed for those stacks obtained by depositing the carbon paste directly on PbI_2 NPs, with visible yellow regions underneath the carbon electrode highlighting unreacted lead iodide precursor (Figure 4.14 a).

Better results were achieved by depositing the carbon ink after perovskite conversion, without no yellow regions and the typical dark brown color of $MAPbI_3$ perovskite phase all over the surface (Figure 4.14 b). This comparison sanctioned the impossibility, in the presented conditions, to obtain good samples when the C paste is applied prior the perovskite conversion. As a first batch to analyze, 10 devices were assembled following this procedure and current density–voltage (J–V) scans were registered for each device under AM 1.5 standard illumination conditions.

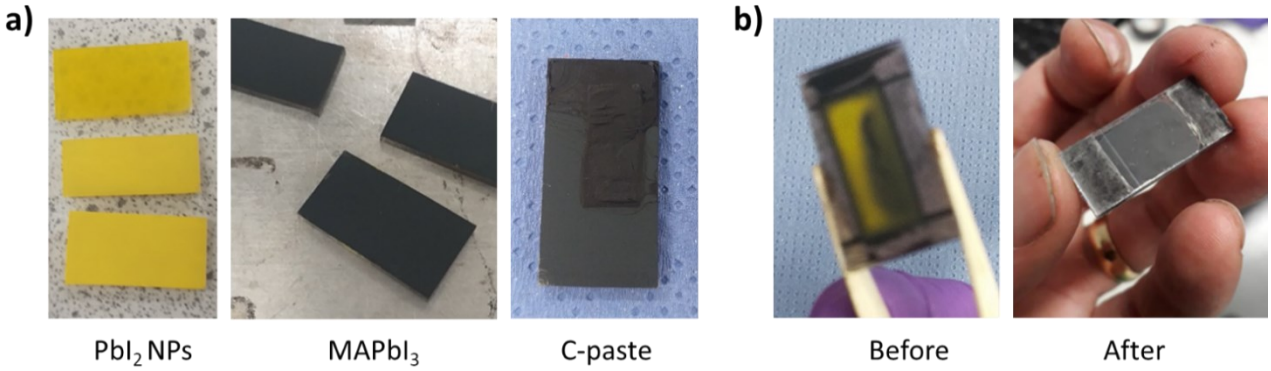

Figure 4.14 a) Top–side pictures showing the samples obtained by sequential depositions of PbI_2 NPs precursor layers, $MAPbI_3$ perovskites, and carbon electrode onto c–TiO_2/FTO/glass substrates. b) Bottom–side picture of the final stacks obtained by blade–coating the carbon paste before/after $MAPbI_3$ perovskite conversion by dip coating. Wide yellow regions, attributed to unreacted lead iodide precursor, are visible in samples obtained with the former procedure.

Further details regarding the electrical characterizations are reported in Section 4.4.5. The figures of merit calculated from the collected J–V curves are summarized in Figure 4.15 a, while Figure 4.15 b shows the forward/reverse scans of the best pixel. The lowest photo–conversion efficiency (PCE) calculated for these devices was attributed to the low fill factor (FF), in the range of 20–30, and the negligible short–circuit current density (J_{SC}), below 0.5 mA/cm^2. FF in the range of 65–75 and J_{SC} above 20 mA/cm^2 are usually measured for carbon-based PSCs. On the other hand, the measured open–circuit voltage values, of about 0.9 V on average, and carbon electrode sheet resistance (R_{SHEET}), of about 15 Ω/sq, are in line with those reported for efficient carbon-based PSCs in previous works.[5,8,57] These results highlighted the good quality of the $MAPbI_3$ absorbing layer (i.e., high V_{OC})[58,59] and the good conductivity of the carbon top contact (generally comprises between 10–20 Ω/sq for these architectures), suggesting that the low FF and J_{SC} values are mainly related to issues concerning the dynamics of photo–generated charges and/or the carbon/perovskite interface.

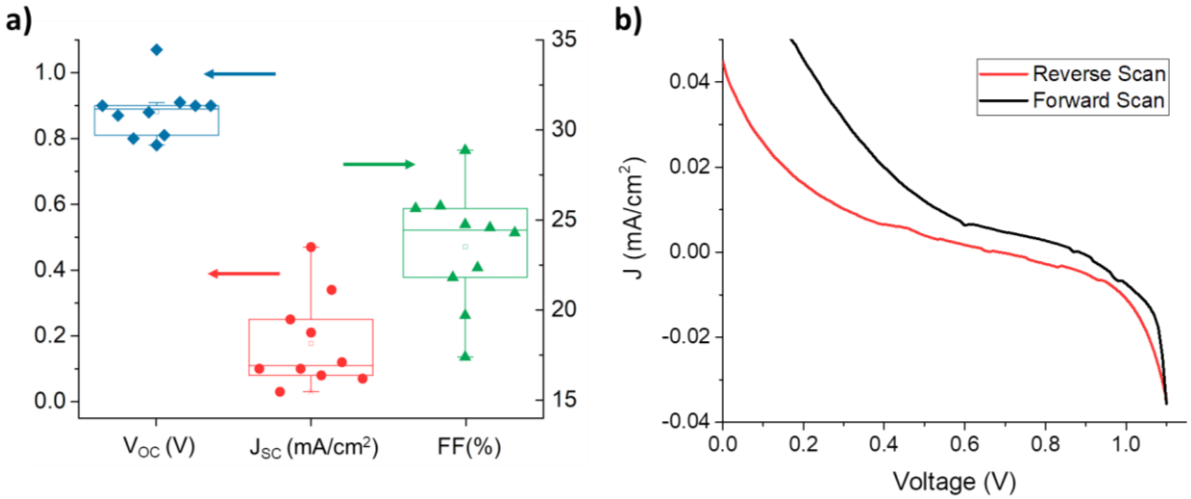

Figure 4.15 a) Box chart reporting the figures of merit (open–circuit voltage V_{OC}, short–circuit current density J_{SC}, fill factor FF) extrapolated from the reverse J–V curves of 10 devices assembled in the first batch. Arrows indicate the reference axis for each data set. b) Forward and reverse J–V curves of the best pixel.

Cross–sectional SEM analysis was performed on the carbon/$MAPbI_3$/c–TiO_2/FTO/glass stack to inspect the carbon/perovskite top interface, indicated by the green dash line in Figure 4.16. A uniform and continuous $MAPbI_3$perovskite film of 2–3 µm was observed underneath the thick carbon layer, of about 20 µm.

No relevant thickness variations were observed along the perovskite film by cross–sectional SEM statical analysis, confirming the good conditions in which the spray coating depositions of PbI_2 NPs were performed (Section 4.2.3). On the contrary, a non–optimal morphology was observed for the blade–coated carbon top layer, characterized by micrometric voids in the region close to the perovskite interface and a structural inhomogeneity between the top and the bottom side (Figure 4.16). Based on this observation and by assuming a good charges photo–generation within the $MAPbI_3$ absorbing layer, since the good PL emission registered (Figure 4.6 a), the reasons behind the low FF and J_{SC} values can be laid on dominant charges recombination phenomena and/or on high R_{SERIES} caused by the poor carbon/perovskite interface. The former is responsible for the negligible short–circuit current density, thus the negligible photo–generated current density, measured in all devices.[60,61] The latter is inversely proportional to charge extraction and causes the flattening of the J–V curve, resulting in a net decrease of the FF but without affecting the open–circuit voltage.[62–64] Moreover, a S–shaped profile can be noticed in both the forward and reverse scan reported in Figure 4.15 b. This non–optimal diode behaviour is generally caused by charge extraction/transport barriers at the interface between the absorber and the top selective contact [65–68] (i.e., the carbon electrode in the specific case). These barriers can also lead to J–V hysteresis phenomena, occuring when moving and/or accumulated ionic species are present within the perovskite layer under bias.[17,69–72] This can explain as well the high hysteresis index,[73] in the range of 50–65%, calculated for the devices assembled in the first batch.

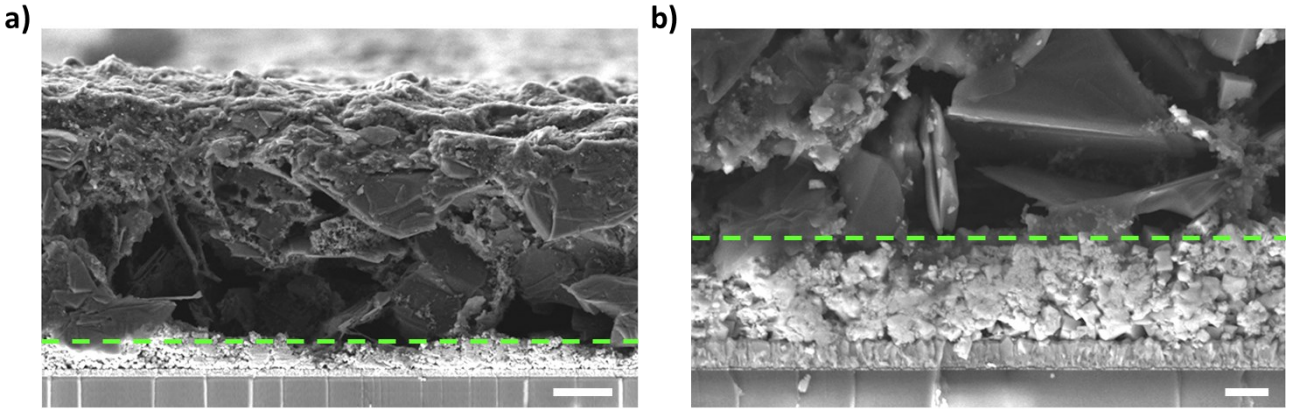

Figure 4.16 Cross–sectional SEM images showing the mesoporous Carbon/$MAPbI_3$/c–TiO_2/FTO/glass stack at different magnifications. 5 µm and 1 µm scale bars are reported in (a) and (b) images, respectively. The green dash lines highlight the carbon/perovskite interface.

Most of the efficiency losses described so far can be traced back to the poor perovskite/interface (Figure 4.16 b),[18,74] rather than to the perovskite absorbing layer itself. The bad carbon layer morphology can be ascribed first to the carbon ink formulation, based on 1–butanol solvent. During the thermal annealing of the blade–coated carbon electrode, the low–boiling, high vapor pressure alcohol can have exerted micro–pressures at local level while quickly evaporating and escaping the carbon layer, generating the crack, micro–cavities and voids observed in cross–sectional SEM images. Moreover, since a downward temperature gradient is generated when the sample is placed on the hotplate, the micro–cavities generation due to the quick evaporation of 1–butanol is predominant in the bottom part of the carbon electrode. This could explain why these voids are concentrated in the region close to the perovskite interface (Figure 4.16 a).

A pre–heat treatment, performed at lower temperature, and a further optimization of the carbon paste formulation, employing higher boiling solvents (compatible with the perovskite underneath layer) and deposition, lowering the thickness of the whole carbon top contact (still maintaining a low R_{SHEET}), could be valuable solutions to reduce this phenomenon and improve the morphology of the carbon top electrode. Different perovskite conversion conditions and/or post–treatments could be evaluated as well to improve the morphology of the $MAPbI_3$ layer, further increasing the perovskite crystals dimension and/or induce a partially dissolving/re–crystallizing $MAPbI_3$ to reduce the film roughness and the number of grain boundaries within it [75,76] (which constitute, together with a poor C/perovskite interface, another possible cause for the high charge recombination observed in all the assembled stacks).

4.3 Summary

In this study, the implementation of lead iodide nanoparticles synthesized by laser ablation in isopropanol into mesoporous carbon–based perovskite solar cells (mC–PSCs) was investigated. The aim was to deposit, via spray coating, thin films of PbI_2 NPs to be used both as buffer layer, to separate the charge transport layers, and as a precursor layer, to convert into methylammonium lead triiodide ($MAPbI_3$) perovskite photoactive film. With this strategy, both the perovskite morphology and the mC–PSCs scalability could be improved, thanks to: (i) the deposition of $MAPbI_3$ layers with bigger grains than those produced in conventional mC–PSCs; (ii) a simplification of the overall fabrication process of carbon–based PSCs by removing the mesoporous oxide spacers, which require thermal sintering at high temperatures; (iii) the avoidance of the infiltration step of the perovskite precursor solutions through the stack, which usually require a robotic mesh deposition

technique. After the preliminary validation tests, the LASiS procedure was optimized to produce high–volume concentrated PbI_2 NPs colloidal solutions in IPA to be then spray–coated over large–area (2–7x2.7 cm^2) substrates, forming porous precursor films. The $MAPbI_3$ film obtained by their dip coating conversion showed a good crystallinity and good emissive properties, comparable to those of perovskite materials synthesized by conventional synthetic routes. The first carbon electrode depositions using a commercial carbon paste showed an incompatibility with the underline PbI_2 NPs layer, causing its irreversible degradation. Better results were obtained by using a low–temperature carbon paste containing ethyl cellulose resin as non–toxic polymeric binder, which proved to be suitable for its blade–coating deposition onto both the PbI_2 NPs precursor layer and the $MAPbI_3$ perovskite film. The electrical characterization of the first batch of carbon–based PSCs obtained with this procedure pointed out good open–circuit voltage (V_{OC}) values, while poor fill factors (FF) and negligible short–circuit current densities (J_{SC}). By analyzing the current density–voltage (J–V) curves and the cross–sectional SEM images of the stacks, the lowest photo–conversion efficiencies (PCE) registered in all devices were ascribed to a non–optimal perovskite/carbon interface, leading to high R_{SERIES}, poor photo–generated charges extraction and high charges recombination/accumulation. Different carbon paste formulations, deposition techniques, and/or post–treatment conditions, need to be further investigated and optimized to improve the carbon top electrode morphology and the carbon/perovskite interface. Different perovskite conversion and/or post–treatment conditions could be evaluated as well to reduce the roughness and the grain boundaries density in the $MAPbI_3$ perovskite layer, which constitute the other possible cause for the high charge recombination observed in all the assembled stacks.

4.4 Experimental Section

4.4.1 *2–Step Deposition of $MAPbI_3$ Perovskite Films*

For the preliminary validation tests, the PbI_2 NPs colloidal solution prepared by LASiS in isopropanol was spray–coated onto four 1x1 cm^2 FTO/glass substrates (TEC 7, Ossila) using a home–made spray coating system. The substrates were cleaned before depositions following a widely used procedure reported in literature[77] which involves four ultrasonic bath cleaning steps in 2% v/v Hellmanex water solution (15 mins), distilled water (2 x 15 mins), acetone (15 mins), and isopropanol (15 mins), respectively, then dried with a nitrogen stream. The home–made spray coater used for deposition processes is depicted in Figure 4.17. The system was based on Professional Dual Action MicroAirbrush Kit with gravity feed (ExquizonEU), operating with a nitrogen flow heated at 40 °C

and at a pressure of 3 bar. Stepper motors, remotely controlled by a LabView software, were used for regulating the horizontal and vertical handling of the airbrush, moved at a constant speed of 0.4 cm/s. The spray tip (0.25 mm nozzle diameter) was located 4 cm far from the substrates, heated at 100 °C during depositions by a hot plate integrated in the spray coater stage.

4.0 ml of a 0.2 mg/ml PbI_2 NPs ink in IPA was spray coated over the four cleaned substrates, with an ink flow of 0.15 ml/min and a 1.5x1.5 cm^2 square pattern were set for all the spray–coated samples. After depositions, the so–obtained lead iodide precursor films were annealed for 30 minutes at different temperatures, respectively of 300, 350, and 400 °C. The reference films did not undergo this treatment. Finally, $MAPbI_3$ films were obtained by dip coating the PbI_2 samples into a 10 mg/ml MAI solution in anhydrous isopropanol for 30–120 seconds, depending on the sample. Each film was left immersed for other 20 seconds after that the complete change in color of $MAPbI_3$ was achieved (from yellow to dark brown). The perovskite samples were then rinsed in anhydrous isopropanol and chlorobenzene. Finally, all the $MAPbI_3$ layers underwent a thermal annealing at 100 °C for 10 minutes under Argon flow. The whole process was performed under extractor hood at 20°C and 50 % relative humidity. Both PbI_2 and $MAPbI_3$ samples were stored under nitrogen atmosphere in a dryer before the subsequent characterizations.

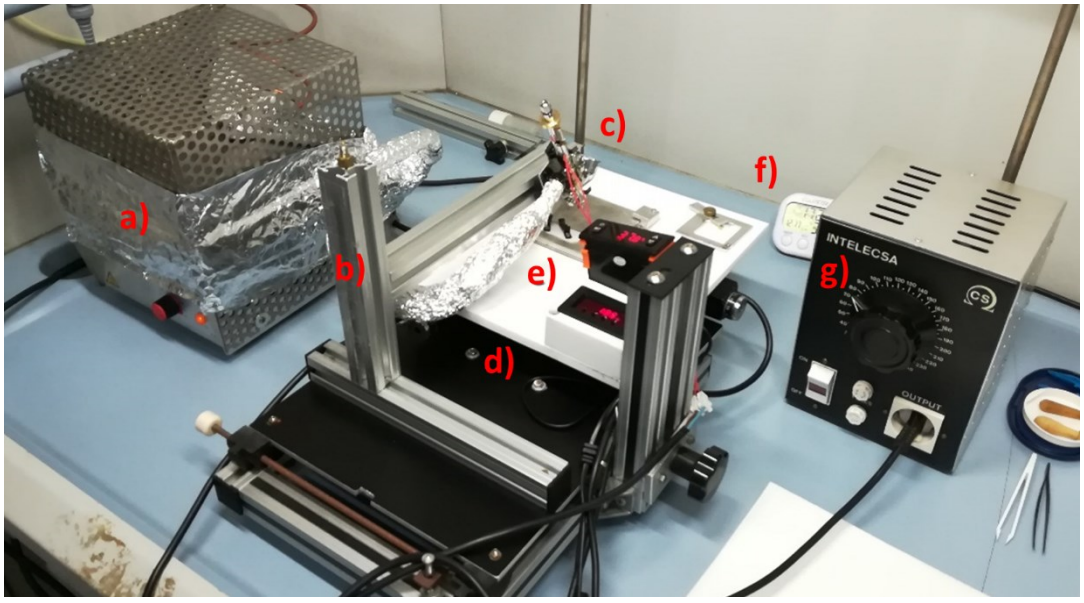

Figure 4.17 Picture of the home–made spray coating tool employed for the spray coating deposition. a) Nitrogen inlet pre–heated by a copper coil placed on a hot plate, b) Mobile support for spray tip positioning, c) micro–airbrush (8 ml tank), d) moving stage on x–y axis by stepper motors, e) hot–plate controllers, f) hygrometer with temperature sensor, g) AC controller of the resistance place on the airbrush as heating system for the sprayed ink. The setup was located under extractor hood, with stepper motors remotely controlled via LabView program.

4.4.2 *Reference 2–Step Spin–Coated $MAPbI_3$ Thin Films*

The reference $MAPbI_3$ sample depicted in Figure 4.6 (dashed line) was prepared by 2–step spin coating deposition following a recent recipe reported in literature.[43] 1 M PbI_2 solution was prepared by dissolving 922 mg into 2.0 ml DMF, put on a magnetic stirrer at 800 rpm and heated at 75 °C for 6 hours. 40 µL of PbI_2 solution was spin–coated on 1x1 cm^2 FTO/glass substrate at 3000 rpm/min for 50 s, followed by thermal annealing at 100 °C for 5 minutes. Once cooled down to room temperature, 200 µL of a 0.25 M MAI solution in isopropanol was dropped onto the PbI_2 precursor film (in the middle) and immediately spin–coated at 1200 rpm/min for 20 seconds. MAI solution was prepared before perovskite spin coating conversion by dissolving 80 mg of MAI powders into 2ml IPA, stirred at 1000 rpm while kept at 60 °C by a hot plate for 30 minutes. The so–obtained perovskite film was finally thermally annealed at 100 °C for 10 mins under Argon flow. The whole process was performed under extractor hood in laboratory conditions.

4.4.3 *PbI_2 Nanoparticles ink via Laser Ablation in Solution*

The standard LASiS procedure for obtaining PbI_2 nanoparticles inks [16] foresees the focalization, at a fluence of 2 J/cm^2, of a pulsed beam of 9 ns at 532 nm by a 20 Hz Nd:YAG laser (Quantel Q–Smart 450 mJ) on the surface of a lead iodide round target place in a glass vial and immersed in 4.0 ml isopropanol (Figure 4.18 a). The round pellet target of 1.3 cm diameter was obtained by compressing PbI_2 powders with a table maker (uniaxial hydraulic press) under a pressure of 10 tons for 10 minutes. To ensure a uniform erosion of the target by the laser, the PbI_2 target was moved at a constant speed of 0.5 mm/s by a double–axis (x,y) stepper motors system during LASiS procedure.

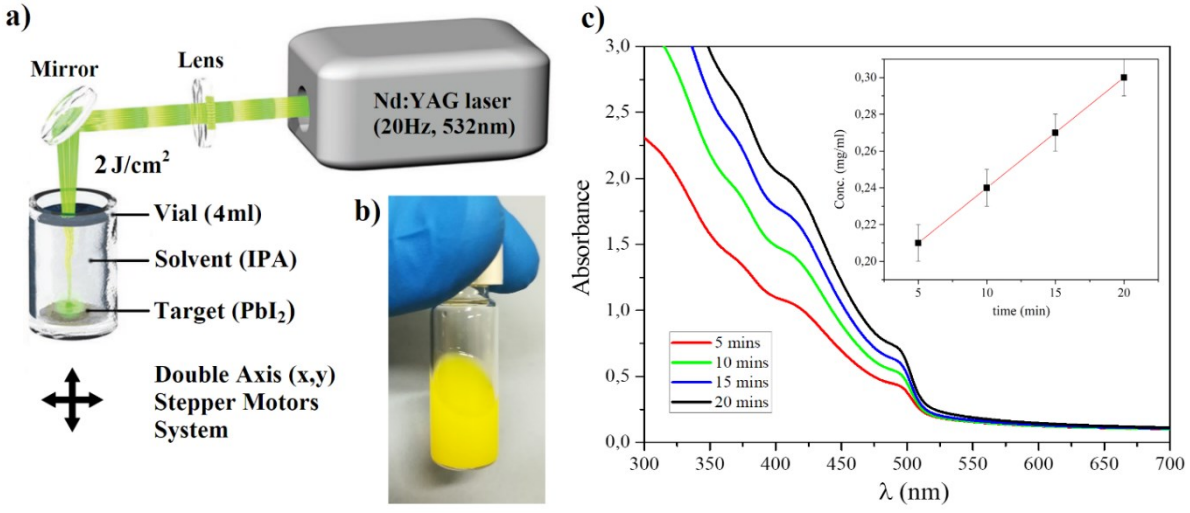

Figure 4.18 a) Sketch diagram of the LASiS process for preparation of the PbI_2 NCs ink. b) 4.0 ml vial containing the PbI_2 NCs colloidal solution is isopropanol. c) UV–Vis spectra of PbI_2 NCs inks with increasing concentration, obtained at increasing ablation time in the same experimental conditions.

In this starting conditions, 4.0 ml of PbI_2 NPs ink in IPA with a concentration up to 0.3 mg/ml can be obtained by LASiS within 20 minutes (Figure 4.18 b,c). The concentration of PbI_2 NPs was estimated by centrifuging and digesting an aliquot of the ink in DMF, then calculating the concentration value through the Lambert–Beer law by evaluating the absorbance peak at 322 nm. The molar absorptivity of lead iodide, equal to 7700 $M^{-1}cm^{-1}$, was estimated using a calibration line made with standard solutions of commercial PbI_2 powders in DMF.[16]

4.4.4 *Large–Area Spray–Coated PbI_2 NPs precursor films*

The large–area lead iodide precursor films reported in Figure 4.1 a were prepared by spray coating the high volume concentrated PbI_2 NPs ink in IPA (Section 4.2.2) with the home–made spray coater previously described (Figure 4.17). 5, 10, and 20 ml of a 0.6 mg/ml PbI_2 NPs precursor colloidal solution were spray–coated over 2.7x2.7 cm^2 FTO/glass substrates, opportunely cleaned before depositions (Section 4.4.1). An ink flow of 0.2 ml/min and a 3x3 cm^2 square pattern were set for all the spray–coated samples. After spray depositions, the PbI_2 precursor films were annealed in the optimized conditions at 300 °C for 30 minutes (Section 4.2.1). $MAPbI_3$ films were obtained by dip coating the so–obtained PbI_2 samples into a 10 mg/ml MAI solution in anhydrous isopropanol for 60 seconds, followed by a thermal annealing at 100 °C for 10 minutes under dry atmosphere (Argon continuous flow). All other unspecified experimental conditions were the same as those reported in Section 4.4.1.

4.4.5 *Electrical Device Characterization*

Current density–voltage scans were measured using a class AAA solar simulator (Newport Oriel Sol3A) at AM 1.5 100 mW/cm^{-2} illumination, calibrated using a KG5 filtered reference cell. The solar cells area was determined by applying a 0.49 cm^2 mask. All devices were light soaked for 3 minutes before the J–V sweeps, registered from open–circuit voltage to short–circuit current density (forward scan) and vice versa (reverse scan) at a rate of 330 mV/s using a Keithley 2400 source meter. CERASOLZER active solder alloy, a lead–free material for low temperature soldering (150 °C),[78] was applied onto the carbon electrode to constitute the top contact for the J–V scans measurement. Sheet resistances were measured using a JANDEL RM 3000 Four–Point Probe System.[57]

References

(1) ARoldán-Carmona, C.; Zimmermann, I.; Mosconi, E.; Lee, X.; Martineau, D.; Narbey, S.; Oswald, F.; De Angelis, F.; Graetzel, M.; Nazeeruddin, M. K. One-Year Stable Perovskite Solar Cells by 2D/3D Interface Engineering. *Nat. Commun.* **2017**, *8*, 15684–15693. https://doi.org/10.1038/ncomms15684.

(2) Mei, A.; Li, X.; Liu, L.; Ku, Z.; Liu, T.; Rong, Y.; Xu, M.; Hu, M.; Chen, J.; Yang, Y.; et al. A Hole-Conductor-Free, Fully Printable Mesoscopic Perovskite Solar Cell with High Stability. *Science (80-.).* **2014**, *345* (6194), 295–298. https://doi.org/10.1126/science.1254763.

(3) De Rossi, F.; Baker, J. A.; Beynon, D.; Hooper, K. E. A.; Meroni, S. M. P.; Williams, D.; Wei, Z.; Yasin, A.; Charbonneau, C.; Jewell, E. H.; et al. All Printable Perovskite Solar Modules with 198 Cm2 Active Area and Over 6% Efficiency. *Adv. Mater. Technol.* **2018**, *3* (11), 1800156–1800164. https://doi.org/10.1002/admt.201800156.

(4) Hu, Y.; Si, S.; Mei, A.; Rong, Y.; Liu, H.; Li, X.; Han, H. Stable Large-Area (10x10 Cm2) Printable Mesoscopic Perovskite Module Exceeding 10% Efficiency. *Sol. RRL* **2017**, *1* (2), 1600019–1600025. https://doi.org/10.1002/solr.201600019.

(5) Meroni, S. M. P.; Worsley, C.; Raptis, D.; Watson, T. M. Triple-Mesoscopic Carbon Perovskite Solar Cells: Materials, Processing and Applications. *Energies* **2021**, *14*, 386–424. https://doi.org/10.3390/en14020386.

(6) Jenny Baker, Katherine Hooper, Simone Meroni, a Adam Pockett, James McGettrick, Zhengfei Wei, Renan Escalante, Gerko Oskam, M. C. and T. W. High Throughput Fabrication of Mesoporous Carbon Perovskite Solar Cells. *J. Mater. Chem. A* **2017**, *5*, 18643–18650. https://doi.org/10.1039/c7ta05674e.

(7) Duan, M.; Hu, Y.; Mei, A.; Rong, Y.; Han, H. Printable Carbon-Based Hole-Conductor-Free Mesoscopic Perovskite Solar Cells: From Lab to Market. *Mater. Today Energy* **2018**, *7*, 221–231. https://doi.org/10.1016/j.mtener.2017.09.016.

(8) Fagiolari, L.; Bella, F. Carbon-Based Materials for Stable, Cheaper and Large-Scale Processable Perovskite Solar Cells. *Energy Environ. Sci.* **2019**, *12* (12), 3437–3472. https://doi.org/10.1039/c9ee02115a.

(9) Chen, H.; Yang, S. Carbon-Based Perovskite Solar Cells without Hole Transport Materials: The Front Runner to the Market? *Adv. Mater.* **2017**, *29* (24), 1603994–1604009. https://doi.org/10.1002/ADMA.201603994.

(10) Bogachuk, D.; Tsuji, R.; Martineau, D.; Narbey, S.; Herterich, J. P.; Wagner, L.; Suginuma, K.; Ito, S.; Hinsch, A. Comparison of Highly Conductive Natural and Synthetic Graphites for Electrodes in Perovskite Solar Cells. *Carbon N. Y.* **2021**, *178*, 10–18. https://doi.org/10.1016/j.carbon.2021.01.022.

(11) Bogachuk, D.; Zouhair, S.; Wojciechowski, K.; Yang, B.; Babu, V.; Wagner, L.; Xu, B.; Lim, J.; Mastroianni, S.; Pettersson, H.; et al. Low-Temperature Carbon-Based Electrodes in Perovskite Solar Cells. *Energy Environ. Sci* **2020**, *13*, 3880–3916. https://doi.org/10.1039/d0ee02175j.

(12) Que, M.; Zhang, B.; Chen, J.; Yin, X.; Yun, S. Carbon-Based Electrodes for Perovskite Solar Cells. *Mater. Adv.* **2021**, *2*, 5560–5579. https://doi.org/10.1039/d1ma00352f.

(13) Liu, C.; He, Z.; Li, Y.; Liu, A.; Cai, R.; Gao, L.; Ma, T. Sulfur Contributes to Stable and Efficient Carbon-Based Perovskite Solar Cells. *J. Colloid Interface Sci.* **2021**, *605*, 54–59.

(14) NREL Best Research-Cell Efficiency Chart https://www.nrel.gov/pv/assets/pdfs/best-research-cell-efficiencies.20200104.pdf.

(15) Liu, Z.; Shi, T.; Tang, Z.; Sun, B.; Liao, G. Using a Low-Temperature Carbon Electrode for Preparing Hole-Conductor-Free Perovskite Heterojunction Solar Cells under High Relative Humidity. *Nanoscale* **2016**, *8* (13), 7017–7023. https://doi.org/10.1039/C5NR07091K.

(16) Lamberti, F.; Litti, L.; De Bastiani, M.; Sorrentino, R.; Gandini, M.; Meneghetti, M.; Petrozza, A. High-Quality, Ligands-Free, Mixed-Halide Perovskite Nanocrystals Inks for Optoelectronic Applications. *Advanced Energy Materials*. 2017, pp 1601703–1601707. https://doi.org/10.1002/aenm.201601703.

(17) Rizzo, A.; Lamberti, F.; Buonomo, M.; Wrachien, N.; Torto, L.; Lago, N.; Sansoni, S.; Pilot, R.; Prato,

M.; Michieli, N.; et al. Understanding Lead Iodide Perovskite Hysteresis and Degradation Causes by Extensive Electrical Characterization. *Sol. Energy Mater. Sol. Cells* **2019**, *189*, 43–52. https://doi.org/10.1016/j.solmat.2018.09.021.

(18) Wei, Z.; Chen, H.; Yan, K.; Zheng, X.; Yang, S. Hysteresis-Free Multi-Walled Carbon Nanotube-Based Perovskite Solar Cells with a High Fill Factor . *J. Mater. Chem. A* **2015**, *3*, 24226–24231. https://doi.org/10.1039/c5ta07714a.

(19) Chen, H. N.; Wei, Z. H.; He, H. X.; Zheng, X. L.; Wong, K. S.; Yang, S. H. Solvent Engineering Boosts the Efficiency of Paintable Carbon-Based Perovskite Solar Cells to beyond 14%. *Adv. Energy Mater.* **2016**, *6* (8), 1502087–1502096. https://doi.org/10.1002/AENM.201502087.

(20) Xu, X.; Liu, Z.; Zuo, Z.; Zhang, M.; Zhao, Z.; Shen, Y.; Zhou, H.; Chen, Q.; Yang, Y.; Wang, M. Hole Selective NiO Contact for Efficient Perovskite Solar Cells with Carbon Electrode. *Nano Lett.* **2015**, *15*, 2402–2408. https://doi.org/10.1021/nl504701y.

(21) Ku, Z.; Rong, Y.; Xu, M.; Liu, T.; Han, H. Full Printable Processed Mesoscopic CH3NH3PbI3/TiO2 Heterojunction Solar Cells with Carbon Counter Electrode. *Sci. Rep.* **2013**, *3*, 3132–3136. https://doi.org/10.1038/srep03132.

(22) Meroni, S. M. P.; Hooper, K. E. A.; Dunlop, T.; Baker, J. A.; Worsley, D.; Charbonneau, C.; Watson, T. M. Scribing Method for Carbon Perovskite Solar Modules. *Energies* **2020**, *13*, 1589–1604. https://doi.org/10.3390/en13071589.

(23) Meroni, S. M. P.; Mouhamad, Y.; Rossi, F. De; Baker, J.; Escalante, R.; Searle, J.; Carnie, M. J.; Jewell, E.; Oskam, G.; Watson, T. M.; et al. Homogeneous and Highly Controlled Deposition of Low Viscosity Inks and Application on Fully Printable Perovskite Solar Cells. *Sci. Technol. Adv. Mater.* **2018**, *19* (1), 1–9. https://doi.org/10.1080/14686996.2017.1406777.

(24) Mishra, A.; Ahmad, Z.; Zimmermann, I.; Martineau, D.; Shakoor, R. A.; Touati, F.; Riaz, K.; Al-Muhtaseb, S. A.; Nazeeruddin, M. K. Effect of Annealing Temperature on the Performance of Printable Carbon Electrodes for Perovskite Solar Cells. *Org. Electron.* **2019**, *65*, 375–380. https://doi.org/10.1016/J.ORGEL.2018.11.046.

(25) Wang, M.; Feng, Y.; Bian, J.; Liu, H.; Shi, Y. A Comparative Study of One-Step and Two-Step Approaches for MAPbI3 Perovskite Layer and Its Influence on the Performance of Mesoscopic Perovskite Solar Cell. *Chem. Phys. Lett.* **2018**, *692*, 44–49.

(26) Shao, F.; Xu, L.; Tian, Z.; Xie, Y.; Wang, Y.; Sheng, P.; Wang, D.; Huang, F. A Modified Two-Step Sequential Deposition Method for Preparing Perovskite CH3NH3PbI3 Solar Cells. *RSC Adv.* **2016**, *6*, 42377–42381. https://doi.org/10.1039/c6ra05718g.

(27) Hwang, K.; Jung, Y. S.; Heo, Y. J.; Scholes, F. H.; Watkins, S. E.; Subbiah, J.; Jones, D. J.; Kim, D. Y.; Vak, D. Toward Large Scale Roll-to-Roll Production of Fully Printed Perovskite Solar Cells. *Adv. Mater.* **2015**, *27* (7), 1241–1247. https://doi.org/10.1002/ADMA.201404598.

(28) Yan, J. J.; Li, Y.; Chang, Y.; Jiang, P.; Wang, C. W. The Effect of Porous Lead Iodide Precursor Film on Perovskite Film Formation and Its Photovoltaic Property after an Effective Pretreatment. *Superlattices Microstruct.* **2016**, *94*, 196–203. https://doi.org/10.1016/J.SPMI.2016.03.045.

(29) Habibi, M.; Ahmadian-Yazdi, M.-R.; Eslamian, M. Optimization of Spray Coating for the Fabrication of Sequentially Deposited Planar Perovskite Solar Cells. *J. Photonics Energy* **2017**, *7* (2), 022003–022019. https://doi.org/10.1117/1.jpe.7.022003.

(30) Li, H.; Han, P. D.; Zhang, X. B.; Li, M. Size-Dependent Melting Point of Nanoparticles Based on Bond Number Calculation. *Mater. Chem. Phys.* **2013**, *137* (3), 1007–1011. https://doi.org/10.1016/J.MATCHEMPHYS.2012.11.016.

(31) Zhang, Z.; Zhao, M.; Jiang, Q. Melting Temperatures of Semiconductor Nanocrystals in the Mesoscopic Size Range. *Semicond. Sci. Technol.* **2001**, *16*, L33–L35.

(32) Goldstein, A. N.; Echer, C. M.; Alivisatos, A. P. Melting in Semiconductor Nanocrystals. *Science (80-.).* **1992**, *256*, 1425–1427. https://doi.org/10.1126/SCIENCE.256.5062.1425.

(33) Wu, K.-L.; Kogo, A.; Sakai, N.; Ikegami, M.; Miyasaka, T. High Efficiency and Robust Performance of Organo Lead Perovskite Solar Cells with Large Grain Absorbers Prepared in Ambient Air Conditions. *Chem. Lett* **2015**, *44*, 321–323. https://doi.org/10.1246/cl.140919.

(34) Chen, H.; Wei, Z.; Zheng, X.; Yang, S. A Scalable Electrodeposition Route to the Low-Cost, Versatile and Controllable Fabrication of Perovskite Solar Cells. *Nano Energy* **2015**, *15*, 216–226.

https://doi.org/10.1016/j.nanoen.2015.04.025.
(35) Sutherland, B. R.; Hoogland, S.; Adachi, M. M.; Kanjanaboos, P.; Wong, C. T. O.; McDowell, J. J.; Xu, J.; Voznyy, O.; Ning, Z.; Houtepen, A. J.; et al. Perovskite Thin Films via Atomic Layer Deposition. *Adv. Mater.* **2015**, *27* (1), 53–58. https://doi.org/10.1002/ADMA.201403965.
(36) Krückemeier, L.; Krogmeier, B.; Liu, Z.; Rau, U.; Kirchartz, T. Understanding Transient Photoluminescence in Halide Perovskite Layer Stacks and Solar Cells. *Adv. Energy Mater.* **2021**, *11*, 2003489–2003507. https://doi.org/10.1002/aenm.202003489.
(37) Mahon, N. S.; Korolik, O. V; Khenkin, M. V; Arnaoutakis, G. E.; Galagan, Y.; Soriūtė, V.; Litvinas, D.; Ščajev, P.; Katz, E. A.; Mazanik, A. V. Photoluminescence Kinetics for Monitoring Photoinduced Processes in Perovskite Solar Cells. *Sol. Energy* **2020**, *195*, 114–120. https://doi.org/10.1016/j.solener.2019.11.050.
(38) Kirchartz, T.; Márquez, J. A.; Stolterfoht, M.; Unold, T. Photoluminescence-Based Characterization of Halide Perovskites for Photovoltaics. *Adv. Energy Mater.* **2020**, 1904134–1904154. https://doi.org/10.1002/aenm.201904134.
(39) You, J.; Meng, L.; Song, T.-B.; Guo, T.-F.; Yang, Y.; Chang, W.-H.; Hong, Z.; Chen, H.; Zhou, H.; Chen, Q.; et al. Improved Air Stability of Perovskite Solar Cells via Solution-Processed Metal Oxide Transport Layers. *Nat. Nanotechnol.* **2016**, *11*, 75–82. https://doi.org/10.1038/NNANO.2015.230.
(40) Climent-Pascual, E.; Hames, B. C.; Moreno-Ramírezramírez, J. S.; Luis´alvarez, A.; Luis´alvarez, L.; Juarez-Perez, E. J.; Mas-Marza, E.; Mora-Seró, I.; Seró, S.; De Andrés, A.; et al. Influence of the Substrate on the Bulk Properties of Hybrid Lead Halide Perovskite Films. *J. Mater. Chem. A* **2016**, *4*, 18153–18163. https://doi.org/10.1039/c6ta08695k.
(41) Yin, W.-J.; Yang, J.-H.; Kang, J.; Yan, Y.; Wei, S.-H. Halide Perovskite Materials for Solar Cells: A Theoretical Review. *J. Mater. Chem. A* **2015**, *3* (17), 8926–8942. https://doi.org/10.1039/C4TA05033A.
(42) Cui, D.; Yang, Z.; Yang, D.; Ren, X.; Liu, Y.; Wei, Q.; Fan, H.; Zeng, J.; Frank, S. (; Liu,). Color-Tuned Perovskite Films Prepared for Efficient Solar Cell Applications. *J. Phys. Chem. C* **2016**, *120*, 42–47. https://doi.org/10.1021/acs.jpcc.5b09393.
(43) Panzer, F.; Chauhan, M.; Yu Zhong, A.; Konstantin SchötzSch, A.; Tripathi, B.; Sven Huettner, A. Investigating Two-Step MAPbI3 Thin Film Formation during Spin Coating by Simultaneous in Situ Absorption and Photoluminescence Spectroscopy. *J. Mater. Chem. A* **2020**, *8*, 5086–5095. https://doi.org/10.1039/c9ta12409h.
(44) Qin, L.; Lv, L.; Li, C.; Zhu, L.; Cui, Q.; Hu, Y.; Lou, Z.; Teng, F.; Hou, Y. Temperature Dependent Amplified Spontaneous Emission of Vacuum Annealed Perovskite Films. *RSC Adv.* **2017**, *7* (26), 15911–15916. https://doi.org/10.1039/C7RA01155E.
(45) Oku, T. Crystal Structures of CH3NH3PbI3 and Related Perovskite Compounds Used for Solar Cells. In *Solar Cells - New Approaches and Reviews (Chapter 3)*; Kosyachenko, L. A., Ed.; InTech, 2015; pp 78–91. https://doi.org/10.5772/59284.
(46) Reinoso, M. Á.; Otálora, C. A.; Gordillo, G. Improvement Properties of Hybrid Halide Perovskite Thin Films Prepared by Sequential Evaporation for Planar Solar Cells. *Materials (Basel).* **2019**, *12* (9), 1394. https://doi.org/10.3390/ma12091394.
(47) Luo, S.; Daoud, W. A. Crystal Structure Formation of CH3NH3PbI3-XClx Perovskite. *Mater. 2016, Vol. 9, Page 123* **2016**, *9* (3), 123–135. https://doi.org/10.3390/MA9030123.
(48) Zeng, H.; Du, X. W.; Singh, S. C.; Kulinich, S. A.; Yang, S.; He, J.; Cai, W. Nanomaterials via Laser Ablation/Irradiation in Liquid: A Review. *Adv. Funct. Mater.* **2012**, *22* (7), 1333–1353. https://doi.org/10.1002/adfm.201102295.
(49) Streubel, R.; Bendt, G.; Gökce, B. Pilot-Scale Synthesis of Metal Nanoparticles by High-Speed Pulsed Laser Ablation in Liquids. *Nanotechnology* **2016**, *27*, 205602. https://doi.org/10.1088/0957-4484/27/20/205602.
(50) Shaikh, A. F.; Tamboli, M. S.; Patil, R. H.; Bhan, A.; Ambekar, J. D.; Kale, B. B. Bioinspired Carbon Quantum Dots: An Antibiofilm Agents. *J. Nanosci. Nanotechnol.* **2018**, *19* (4), 2339–2345. https://doi.org/10.1166/JNN.2019.16537.
(51) Puvvada, N.; Kumar, P.; Konar, S.; Kalita, H.; Mandal, M.; Pathak, A.; Prashanth Kumar, B. N. Synthesis of Biocompatible Multicolor Luminescent Carbon Dots for Bioimaging Applications

Synthesis of Biocompatible Multicolor Luminescent Carbon Dots for Bioimaging Applications. *Sci. Technol. Adv. Mater.* **2012**, *13*, 045008–045014. https://doi.org/10.1088/1468-6996/13/4/045008.
(52) De, B.; Karak, N. A Green and Facile Approach for the Synthesis of Water Soluble Fluorescent Carbon Dots from Banana Juice. *RSC Adv.* **2013**, *3*, 8286–8290. https://doi.org/10.1039/c3ra00088e.
(53) Mampallil, D.; Eral, H. B. A Review on Suppression and Utilization of the Coffee-Ring Effect. *Adv. Colloid Interface Sci.* **2018**, *252*, 38–54. https://doi.org/10.1016/j.cis.2017.12.008.
(54) Gozalzadeh, S.; Nasirpouri, F.; Seok, S. Il. Towards Environmental Friendly Multi-Step Processing of Efficient Mixed-Cation Mixed Halide Perovskite Solar Cells from Chemically Bath Deposited Lead Sulphide. *Sci. Rep.* **2021**, *11*, 18561–18571. https://doi.org/10.1038/s41598-021-97633-5.
(55) Yang, F.; Dong, L.; Jang, D.; Saparov, B.; Tam, K. C.; Zhang, K.; Li, N.; Brabec, C. J.; Egelhaaf, H. J. Low Temperature Processed Fully Printed Efficient Planar Structure Carbon Electrode Perovskite Solar Cells and Modules. *Adv. Energy Mater.* **2021**, *11* (28), 2101219–2101227. https://doi.org/10.1002/AENM.202101219.
(56) Zhang, F.; Yang, X.; Wang, H.; Cheng, M.; Zhao, J.; Sun, L. Structure Engineering of Hole−Conductor Free Perovskite-Based Solar Cells with Low-Temperature-Processed Commercial Carbon Paste As Cathode. *ACS Appl. Mater. Interfaces* **2014**, *6*, 16140–16146. https://doi.org/10.1021/am504175x.
(57) Raptis, D.; Stoichkov, V.; Meroni, S. M. P.; Pockett, A.; Worsley, C. A.; Carnie, M.; Worsley, D. A.; Watson, T. Enhancing Fully Printable Mesoscopic Perovskite Solar Cell Performance Using Integrated Metallic Grids to Improve Carbon Electrode Conductivity. *Curr. Appl. Phys.* **2020**, *20* (5), 619–627. https://doi.org/10.1016/j.cap.2020.02.009.
(58) Qiu, F.; Chu, J.; Liu, Z.; Xiang, J.; Yang, J.; Wang, C. Insight into the Origins of Figures of Merit and Design Strategies for Organic/Inorganic Lead-Halide Perovskite Solar Cells. *Sol. RRL* **2020**, *4*, 2000452–2000480. https://doi.org/10.1002/SOLR.202000452.
(59) Krückemeier, L.; Rau, U.; Stolterfoht, M.; Kirchartz, T. How to Report Record Open-Circuit Voltages in Lead-Halide Perovskite Solar Cells. *Advanced Energy Materials*. 2019. https://doi.org/10.1002/aenm.201902573.
(60) Short-Circuit Current | PVEducation https://www.pveducation.org/pvcdrom/solar-cell-operation/short-circuit-current.
(61) Kitai, A. *Principles of Solar Cells, Principles of Solar Cells, LEDs and Related Devices - The Role of the PN Junction*, 2nd Editio.; Wiley, Ed.; 2019.
(62) Cheng, Y.; Peng, Y.; Jen, A. K.-Y.; Yip, H.-L. Development and Challenges of Metal Halide Perovskite Solar Modules. *Sol. RRL* **2021**, 2100560. https://doi.org/10.1002/SOLR.202100545.
(63) Equivalent circuit calculator |PV Lighthouse https://www.pvlighthouse.com.au/equivalent-circuit.
(64) *Physics of Semiconductor Devices, 3rd Edition | Wiley*; 2006.
(65) Khalf, A.; Gojanović, J.; Ćirović, N.; Živanović, S. Two Different Types of S-Shaped J-V Characteristics in Organic Solar Cells. *Opt. Quantum Electron.* **2020**, *52* (2). https://doi.org/10.1007/S11082-020-2236-7.
(66) Saive, R. S-Shaped Current–Voltage Characteristics in Solar Cells: A Review. *IEEE J. Photovoltaics* **2019**, *9* (6), 1477–1484. https://doi.org/10.1109/jphotov.2019.2930409.
(67) M. K. Koopmans and J. A. A Numerical Study of the Implications of S-Shaped JV Characteristics in Perovskite Solar Cells. In *Physics at Veldoven*; 2019.
(68) Sundqvist, A.; Sandberg, O. J.; Nyman, M.; Smått, J. H.; Österbacka, R. Origin of the S-Shaped JV Curve and the Light-Soaking Issue in Inverted Organic Solar Cells. *Adv. Energy Mater.* **2016**, *6*, 1502265–1502271. https://doi.org/10.1002/AENM.201502265.
(69) Bag, M.; Renna, L. A.; Adhikari, R. Y.; Karak, S.; Liu, F.; Lahti, P. M.; Russell, T. P.; Tuominen, M. T.; Venkataraman, D. Kinetics of Ion Transport in Perovskite Active Layers and Its Implications for Active Layer Stability. *JACS* **2015**, *137*, 13130−13137. https://doi.org/10.1021/jacs.5b08535.
(70) Van Reenen, S.; Kemerink, M.; Snaith, H. J. Modeling Anomalous Hysteresis in Perovskite Solar Cells. *J. Phys. Chem. Lett* **2015**, *6*, 3808–3814. https://doi.org/10.1021/acs.jpclett.5b01645.
(71) Courtier, N. E.; Cave, J. M.; Foster, J. M.; Walker, A. B.; Richardson, G. How Transport Layer Properties Affect Perovskite Solar Cell Performance: Insights from a Coupled Charge Transport/Ion Migration Model. *Energy Environ. Sci.* **2019**, *12* (1), 396–409. https://doi.org/10.1039/c8ee01576g.
(72) Jiang, H.; Liu, X.; Chai, N.; Huang, F.; Peng, Y.; Zhong, J.; Zhang, Q.; Ku, Z.; Cheng, Y.-B. Alleviate the J-

V Hysteresis of Carbon-Based Perovskite Solar Cells via Introducing Additional Methylammonium Chloride into MAPbI 3 Precursor. *RSC Adv.* **2018**, *8*, 35157–35161. https://doi.org/10.1039/c8ra04347g.

(73) Hysteresis Index: A Figure without Merit for Quantifying Hysteresis in Perovskite Solar Cells. *ACS Energy Lett.* **2018**, *3*, 2472–2476. https://doi.org/10.1021/acsenergylett.8b01627.

(74) Xu, W.-K.; Chen, F.-X.; Cao, G.-H.; Wang, J.-Q.; Wang, L.-S. Factors Influencing the Performance of Paintable Carbon-Based Perovskite Solar Cells Fabricated in Ambient Air. *Chinese Phys. B* **2018**, *27* (3), 038402–038408. https://doi.org/10.1088/1674-1056/27/3/038402.

(75) Zhou, Z.; Wang, Z.; Zhou, Y.; Pang, S.; Wang, D.; Xu, H.; Liu, Z.; Padture, N. P.; Cui, G. Methylamine-Gas-Induced Defect-Healing Behavior of CH3NH3PbI3 Thin Films for Perovskite Solar Cells. *Angew. Chemie - Int. Ed.* **2015**, *54* (33), 9705–9709. https://doi.org/10.1002/ANIE.201504379.

(76) Guo, F.; He, W.; Qiu, S.; Wang, C.; Liu, X.; Forberich, K.; Brabec, C. J.; Mai, Y. Sequential Deposition of High-Quality Photovoltaic Perovskite Layers via Scalable Printing Methods. *Adv. Funct. Mater.* **2019**, *29* (24), 1900964–1900972. https://doi.org/10.1002/ADFM.201900964.

(77) Taylor, A. D.; Sun, Q.; Goetz, K. P.; An, Q.; Schramm, T.; Hofstetter, Y.; Litterst, M.; Paulus, F.; Vaynzof, Y. A General Approach to High Efficiency Perovskite Solar Cells by Any Antisolvent. *Nat. Commun.* **2021**, 1–11. https://doi.org/10.1038/s41467-021-22049-8.

(78) Cerasolzer active solder alloy - MBR Electronics http://www.cerasolzer.com/cerasolzer/cerasolzer_gb.html.

Chapter 5

Eco-Friendly Spray Deposition of Perovskite Thin Films on Textured Surfaces

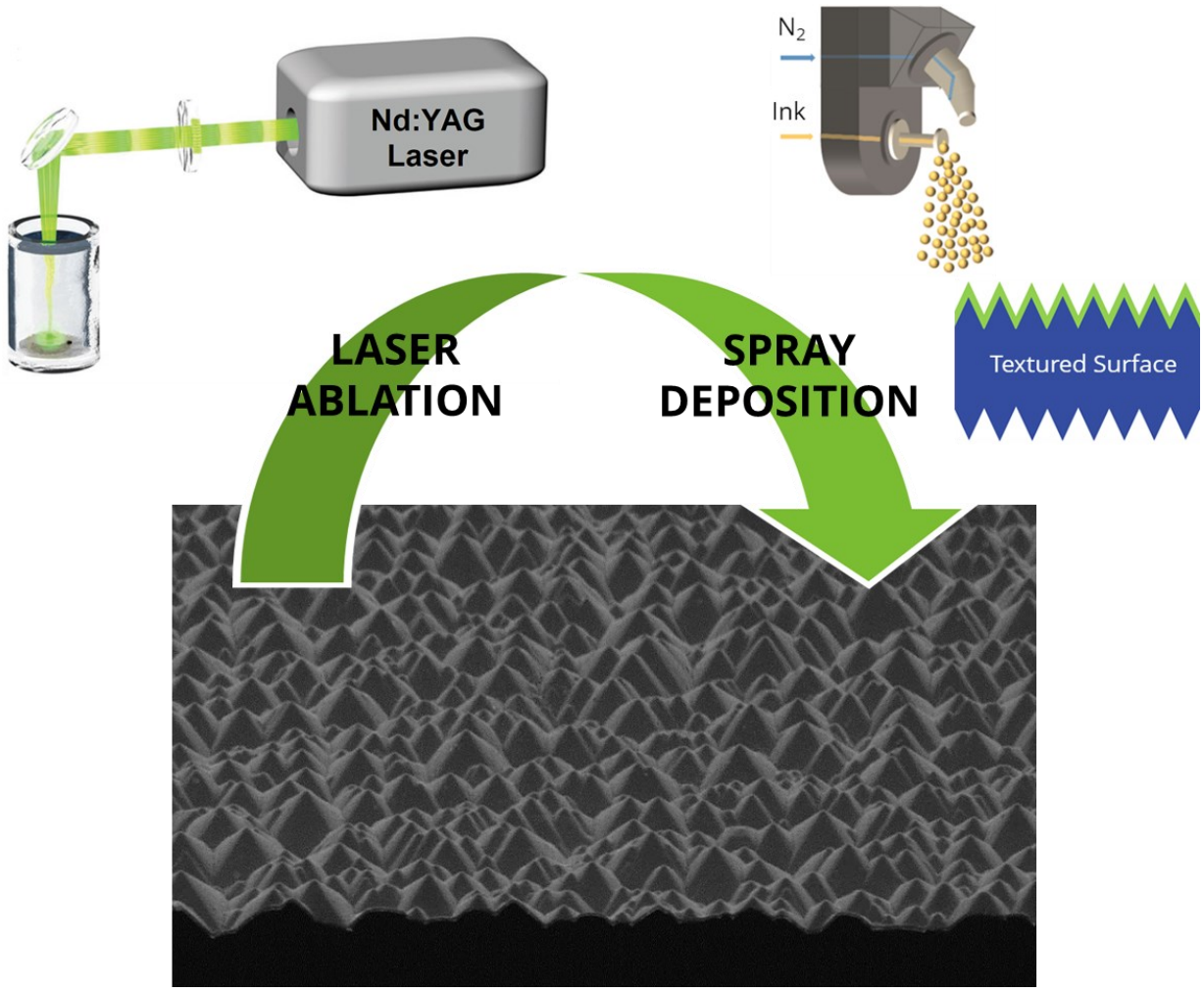

Adv. Mater. Technol. ***2020****, 1901009*

5. Eco-Friendly Spray Deposition of Perovskite Thin Films on Textured Surfaces[1]

5.1 The Aim of The Project

The combination of lead halide perovskite photoactive materials with the silicon solar cells technology enabled the realization of monolithic perovskite-Si tandem devices with photo-conversion efficiencies (PCEs) nowadays above 29%,[2,3] constituting an effective and promising way for perovskite technology entrance into the PV market.[4,5] In the monolithic tandem configuration, also referred as two-terminal tandem, the PSC is assembled directly on top of a Si bottom cell. Since the perovskite top device needs to be fabricated on wafers that feature micron-scale randomly distributed pyramidal texture, necessary to minimize reflection losses in tandems,[6,7] the use of commercial crystalline silicon (c-Si) wafers represents a technological challenge. The PSCs owe their great success to their high PCE obtained via solution–deposition techniques, which are cheaper and simpler than vacuum-based process for conventional PV device fabrication. Thus, solution-based processing of perovskite solar cells compatible with textured substrates is required. Among solution processing techniques, spin coating is the most widely employed due to its low cost, ease of access, and simplicity in getting high-quality polycrystalline perovskite films.[8] However, this technique is not suitable for large-scale production and results in high material consumption, not compatible with sustainable low-cost processes. Moreover, spin coating the perovskite layer onto textured silicon bottom cells represents a challenge by itself which, to date, led to poor coverage of the films resulting in low-performing tandems.[9,10] At present, two-terminal perovskite-Si tandems are realized following two main approaches. In the first case, the perovskite film of the top cell is spin-coated onto c-Si bottom cell with a mirror-polished flat surface. However, as previously stated this causes reflection losses in the device which reduce the overall PCE and require the use of additional antireflective coating.[11] In the second case, the perovskite layer is deposited on textured Si bottom cell via hybrid conversion where the inorganic perovskite precursors, namely lead iodide (PbI_2) and cesium bromide (CsBr), are thermally evaporated on textured bottom cell and then converted into perovskite by spin coating the organic perovskite precursors (formamidinium iodide/bromide, FAI and FABr, respectively).[10,12] In hybrid conversion, the main obstacle is represented by fine-tuning the conversion process. Both the approaches reported above still rely on spin coating as a deposition and/or conversion method, a technique with intrinsic low reproducibility and poor coverage control once implemented for large-area surfaces. This represents a roadblock for the perovskite-Si tandem

commercialization. Indeed, for a successful entry into the PV market, two-terminal tandems need to be produced with the standard size of commercial cells (and modules), which for high-efficiency c-Si solar cells are currently of 6 inches (pseudo-) squared c-Si wafers.[13]

In this work, a sequential eco-friendly (SEF) spray coating technique is presented as an innovative method to deposition lead halide perovskite thin films on micron-scale textured Si bottom cells for two-terminal tandem applications. The proposed approach completely avoids the use of hazardous solvents, commonly used in previously reported studies on spray-coated PSCs.[14,15] Spray coating is already an established scalable deposition technique which can be easily adopted for many applications.[16] In this study, such technique was adapted for the deposition of methylammonium lead triiodide ($MAPbI_3$) and mixed-cation lead mixed-halide perovskite ($CsFAMAPbI_{3-x}Br_x$) in ambient conditions, demonstrating both the versatility and the suitability of the methodology for the realization of perovskite films for two-terminal textured tandem devices through bandgap tuning.

5.2 Results and Discussion

5.2.1 *The Sequential Spray Coating Method*

Textured silicon heterojunction (SHJ) solar cells were fabricated as test platforms for the SEF spray coating technique (Figure 5.1 a). c-Si wafers were immersed into KOH alkaline solution to obtain 7÷10 µm randomly distributed pyramids via etching processes, obtaining textured surfaces both at the front and back sides (Figure 5.1 b).[17] Intrinsic (i) and doped (p,n) amorphous silicon layers were deposited via plasma enhanced chemical vapor deposition (PECVD). Indium-tin oxide (ITO) thin films were then deposited via sputtering to form the passivating heterojunction contacts at front and back sides, as well as the recombination junction[18] necessary to electrically couple the top and bottom cells in a monolithic tandem device.[19] A list of abbreviations is reported in an appendix (pp. 242) at the end of the dissertation. The SHJ was fabricated in rear-junction configuration to accommodate a monolithic two-terminal tandem design, i.e., electrons are collected at the illuminated side of the device.[20] Finally, a NiO_x thin layer was deposited via sputtering onto the sunward ITO layer of the textured SHJ bottom cell, to simulate the hole transport layer for the inverted (p–i–n) perovskite top cell. More details about the SHJ fabrication are reported in Section 5.5.2.

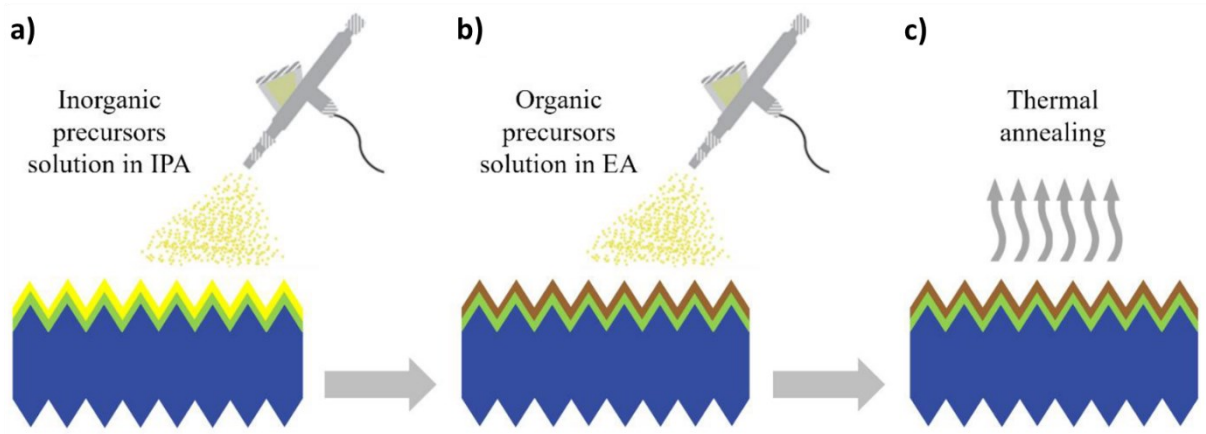

Figure 5.1 a) Schematic representation (not in scale) of the textured Si heterojunction bottom cell. b) Cross-sectional SEM image of the textured surface of the randomly distributed silicon pyramids.

Sequential eco-friendly spray coating technique consists of two consecutive depositions. Firstly, a PbI_2 NCs colloidal solution (ink) synthesized by laser ablation in IPA[21–26] was spray-coated onto the NiO_x/SHJ textured bottom cells. Secondly, the so-obtained inorganic precursor layer was then converted into $MAPbI_3$ perovskite with a subsequent spray coating of a methylammonium iodide solution in ethyl acetate (EA). A similar procedure was adopted also for $CsFAMAPbI_{3-x}Br_x$ perovskite. In this case, a CsBr aqueous solution was added to the PbI_2 NCs ink in IPA as a source of Cs^+, with a volume ratio of 1:100 between CsBr and PbI_2 solutions and a molar ratio of 1:20 between CsBr and PbI_2 inorganic precursors. Then, the resulting PbI_2 NCs-CsBr solution was deposited via spray coating on textured SHJ bottom cell. The mixed inorganic precursors layer was finally converted into mixed-cation lead mixed-halide $CsFAMAPbI_{3-x}Br_x$ perovskite by spraying coating a mixed organic precursors (namely FAI, FABr, and methylammonium bromide, MABr) solution in EA (Figure 5.2 a,b).

Both the organic precursors solutions used for $MAPbI_3$ and $CsFAMAPbI_{3-x}Br_x$ were prepared by dissolving the salts in IPA, then diluting the resulting solutions 1:50 (v:v) in EA. After the SEF spray coating process, both $MAPbI_3$ and $CsFAMAPbI_{3-x}Br_x$ samples were annealed at 100 °C for 10 min under inert conditions (Argon flux) to complete perovskite conversion (Figure 5.2 c). All the experiments were performed under extractor hood in ambient condition (25 °C, 50 % relative humidity). More details regarding the SEF spray coating procedure are reported in Section 5.5.3. With this protocol, the limitations of spin coating deposition technique were avoided without losing the benefits of solution processing or relying on expensive vacuum deposition equipment. Remarkably, this methodology is compatible with the current industrial PV manufacturing standards, paving the way to a scalable, sustainable, and low-cost process required for two-terminal tandem commercialization.

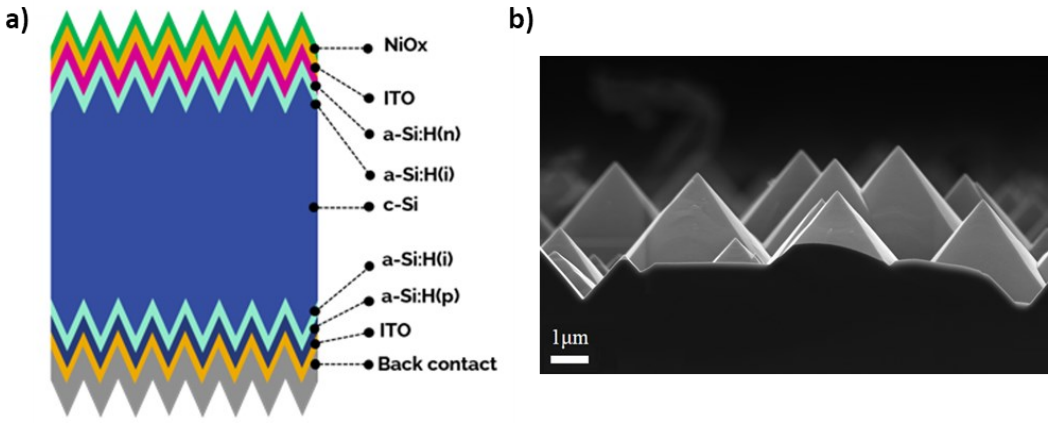

Figure 5.2 Sketch of the sequential eco-friendly spray coating process. Spray coating of a) inorganic precursors ink in isopropanol, and b) organic precursors solution in ethyl acetate over NiO_x/textured SHJ bottom cell (thicknesses not in scale). c) Thermal annealing for 10 minutes at 100 °C. Colours: blue for textured SHJ bottom cell, green for NiO_x layer, yellow for PbI_2 NCs/PbI_2 NCs-CsBr films, and brown for perovskite films.

5.2.2 *The lead iodide NCs precursor ink*

To get a perovskite fully coverage of the textured surface of NiO_x/SHJ bottom cell, a uniform precursor layer must be obtained first. The main advantages in using PbI_2 NCs by laser ablation in solution (LASiS) are the environmental-friendly solvents used in the process, such as low-boiling isopropanol, and the absence of ligands and/or surfactants to stabilize the nanocrystals. On the contrary, the use of toxic and hazard high-boiling, aprotic, polar solvents (such as DMF, DMSO and N-methyl-2-pyrrolidone) in traditional spray coating of perovskite precursor solutions hinders the potential of the technique. Moreover, the PbI_2 NCs inks in IPA are stable over days, just requiring a sonication treatment before spray depositions if stored for long time (Figure 5.3). Additionally, there is no need of any secondary post-treatment processes due to the absence of stabilizers in solution,[27,28] which greatly simplify the overall deposition process. Further details regarding the LASiS setup and the ablation conditions are reported in Section 5.5.1. The typical ultraviolet–visible (UV–Vis) absorbance spectrum profile of PbI_2 NCs is preserved after spray coating step, showing the characteristic absorption edge at 500 nm (Figure 5.4 a).[29] In the near infrared (NIR) region, a scattering contribution can be observed in the spectrum of the colloidal solution since the average dimensions of the PbI_2 NCs are several tens of nm (40–60 nm), as estimated from the transmission electron microscopy (TEM) and dynamic light scattering analysis (Figure 5.4 b-d).The scattering contribution further increases once the lead iodide NCs are spray-coated onto a substrate (Figure 5.4 a), since larger structures are formed. Figure 5.4 b depicts a TEM image of PbI_2 NCs by LASiS highlighting their hexagonal shape, typical of PbI_2 crystals,[29] which testifies their good crystallinity.

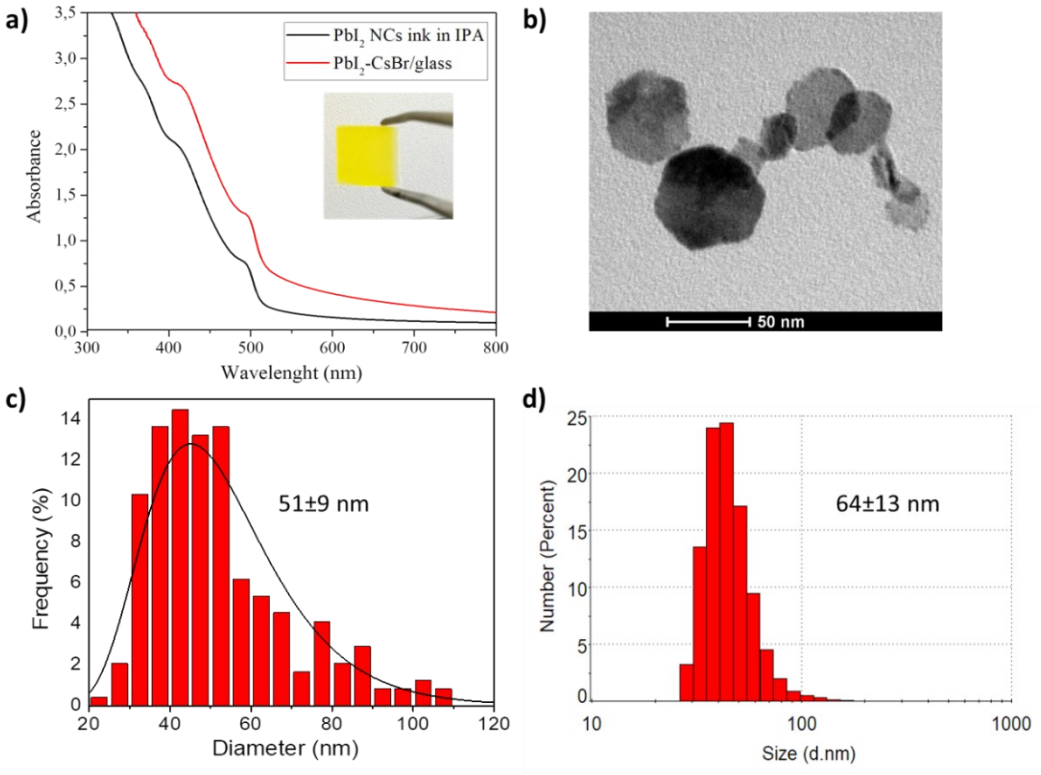

Figure 5.3 PbI_2 NCs ink stability over time. Pictures of the ink a) as made, b) after 2 weeks and c) after 2 weeks ultrasonicated for 10 minutes. d) UV-Vis spectra of PbI_2 NCs ink in the same cases. It is possible to notice how ultrasonic treatment can effectively restore both the initial dispersion and UV-Vis profile of PbI_2 NCs ink. Such ink recovery is also confirmed by looking at the top-view SEM images of e) fresh PbI_2 NCs ink, f) PbI_2 NCs ink aged for 2 weeks, and g) PbI_2 NCs ink aged for 2 weeks after 10 minutes ultrasonication.

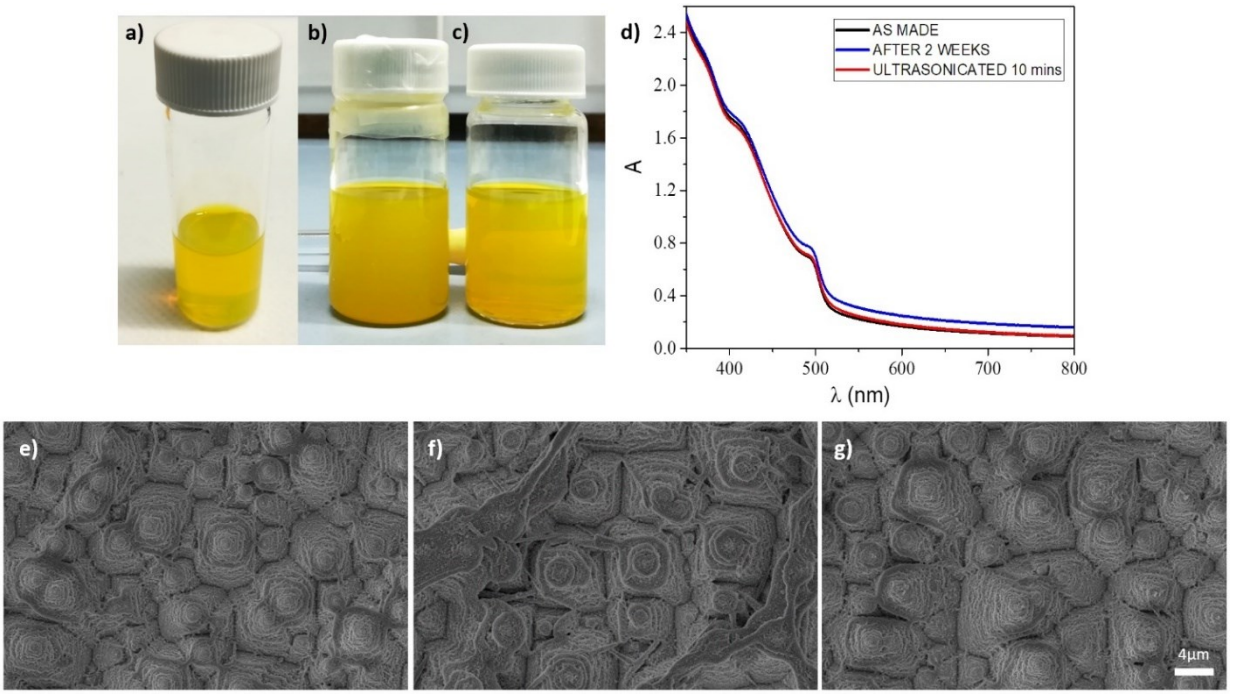

Figure 5.4 a) UV–vis absorbance spectra of the PbI_2 NCs ink in IPA and the mixed PbI_2–CsBr ink thin film obtained by spray coating such ink on soda-lime glass. b) TEM image of the PbI_2 NCs obtained by laser ablation synthesis in isopropanol. c) Size distribution of PbI_2 NCs by laser ablation in IPA obtained from the analysis of 250 nanoparticles observed in TEM images. An average NCs size of 51±9 nm was estimated through lognormal fit. d) Dynamic light scattering data, reporting an average size of PbI_2 NCs of 64±13 nm with a polydispersity index (PdI) < 0.5. The PbI_2 NCs

5.2.3 *Optimization of Perovskite Conversion and Deposition*

To form a uniform and continuous inorganic precursor thin film on top of the textured surfaces, PbI_2 NCs/PbI_2–CsBr ink spray coating first step was optimized. Figure 5.5 a,b respectively show the top-view and cross-sectional SEM images of the spray-coated PbI_2 NCs ink over the textured surfaces of NiO_x/SHJ bottom cells in optimized conditions . Both tips and valleys of the pyramids were well covered by spraying 2.0 ml of 0.3 mg/ml PbI_2 NCs ink in IPA, revealing a conformal coverage of the c-Si pyramids. Uncovered areas, particularly on pyram id tips, were observed when using lower solution-loading amounts (Figure 5.5 c-e). On the contrary, higher solution-loading films lead to the formation of accumulations and/or micrometric thick bridges between pyramids (Figure 5.5 f-h).

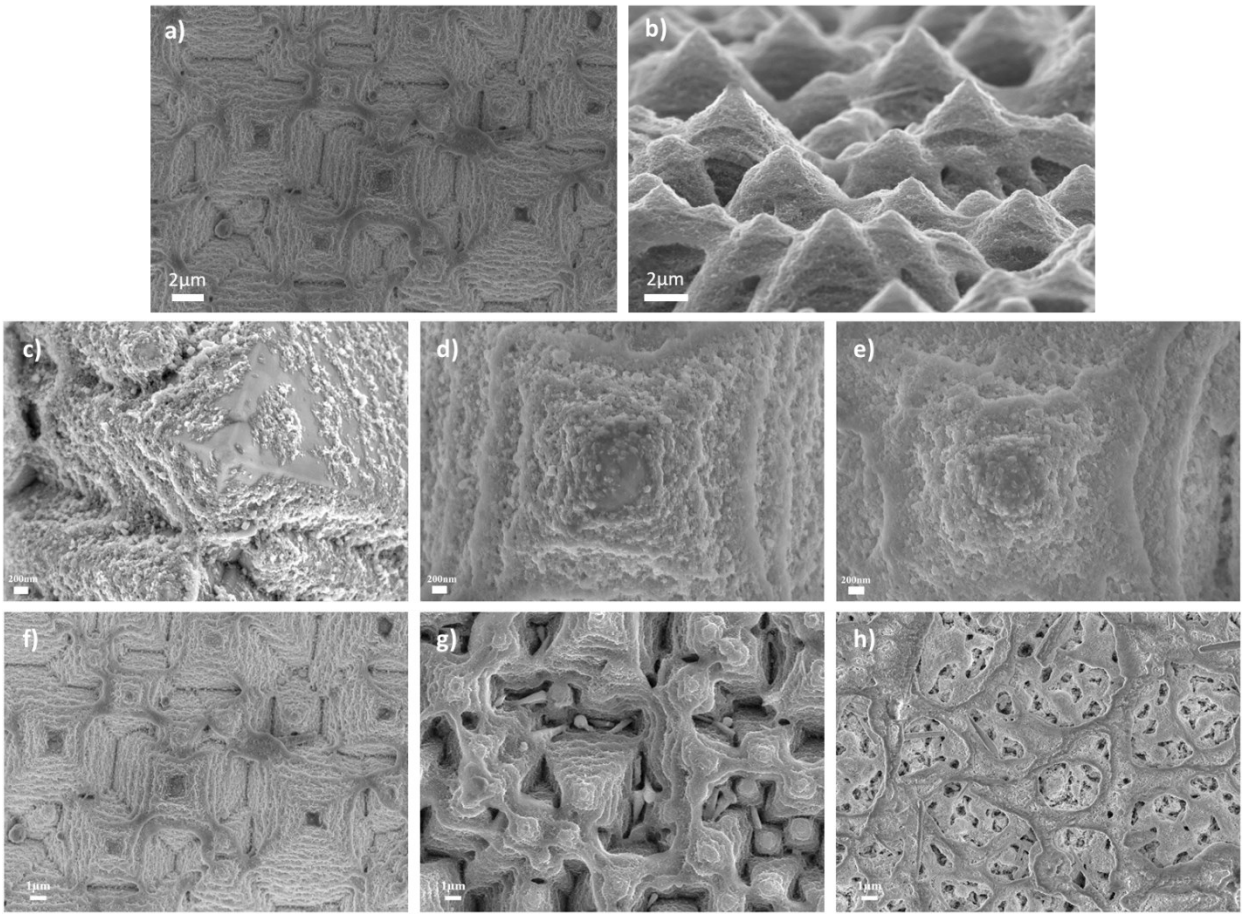

Figure 5.5 Top-view and cross-section SEM images of the spray-coated PbI_2 NCs thin films onto textured NiO_x/ textured SHJ bottom cells in various conditions. PbI_2 NCs ink concentration was 0.3 mg/ml for all samples. a,b) Uniform and conformal coating obtained in optimized conditions. c-e) Degree of coverage of pyramids tip obtained spray coating (c) 0.5 ml, (d) 1.0 ml and (e) 2.0 ml of PbI_2 NCs ink. f-h) Morphology obtained by spray coating (f) 2.0 ml, (g) 3.0ml and (h) 4.0 ml of 0 PbI_2 NCs ink.

The latter must be avoided since they complicate the subsequent perovskite conversion, thus hampering the performance of the two-terminal perovskite-Si tandem solar cell. Similar results were obtained for the case of PbI_2–CsBr ink deposition too, in which 2.0 ml solution was confirmed as the best ink volume to spray for obtaining a uniform coating of the perovskite precursor film over the textured NiO_x/SHJ substrates (Figure 5.6). Both the concentration and the volume of the organic precursor solutions sprayed over the PbI_2/PbI_2–CsBr thin films was varied to find out the optimal perovskite conversion conditions. The volume loading seemed not to be a relevant parameter by itself. What turned out to be more critical was the number of spray coating cycles adopted to deposit the organic precursor solutions in EA. To avoid a nonconformal perovskite coating of the textured substrate, one-cycle spraying must be adopted to prevent dissolution and recrystallization of the perovskite crystals.

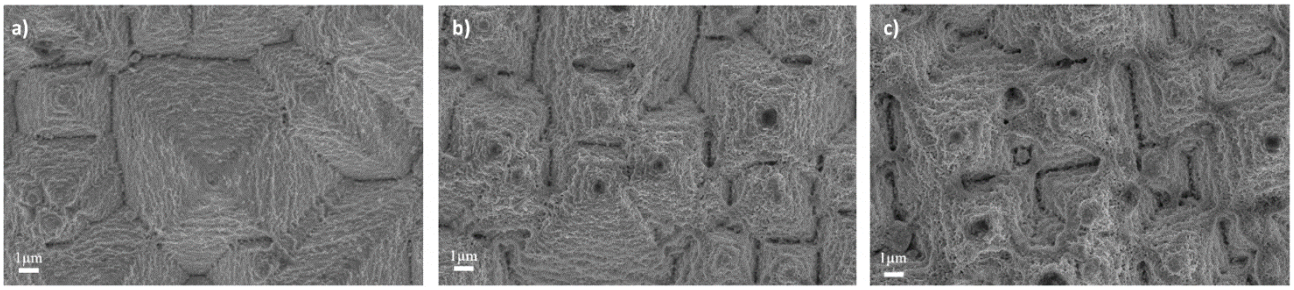

Figure 5.6 Top-view SEM images of a) 1.0 ml, b) 2.0 ml and c) 2.5 ml of PbI_2 NCs-CsBr ink (0.3 mg/ml) sprayed over NiO_x/textured SHJ bottom cells. It can be noticed how spray coating ink volumes > 2.0 ml produces bridges between pyramids (leading to a non-conformal coverage of the substrate), while lower volumes lead to poor coverage of silicon pyramids (especially on pyramids tip).

In fact, best perovskite conversions were obtained when the ink flow was calibrated to guarantee a complete second spray deposition step in just one cycle. As expected, at a fixed volume, unconverted PbI_2 layer at the $MAPbI_3$/NiO_x interface (Figure 5.7 a) was observed when spray coating MAI organic solutions with a too low concentration (PbI_2-MAI molar ratio 2:1), while over stoichiometric solutions (PbI_2-MAI molar ratio 1:5) resulted in the crystallization of the organic precursors excess onto the perovskite films (Figure 5.7 b). The best $MAPbI_3$ perovskite film, showing a uniform coating on the textured substrate without any MAI accumulations (Figure 5.7 c), was obtained in stoichiometric conditions (PbI_2-MAI molar ratio 1:1). In this case, 2.0 ml of 0.3 mg/ml PbI_2 NCs ink in IPA was spray coated over the NiO_x/SHJ substrate and then converted into $MAPbI_3$ perovskite by a subsequent spray deposition of 1.0 ml of 0.2 mg/ml MAI solution in EA. Interestingly, it was noticed how the concentration of MAI solutions can play a role in determining the quality of the final $MAPbI_3$ perovskite film. Particularly, $MAPbI_3$ layer with a good precursor conversion and bigger grains (up to 700 nm) was obtained by spraying a MAI solution in ethyl acetate with a molar

ratio of about 1:1.5 between PbI_2-MAI precursors over the PbI_2 NCs layer (Figure 5.7 d). Despite this improvement in perovskite film morphology, thick bridges among silicon pyramids are present in this sample, highlighting the requirement of a lower concentration for the MAI organic precursor solution to deposit in the second spray coating step of sequential eco-friendly spray coating method. As observed for $MAPbI_3$ thin films by SEF spray coating, a good perovskite conversion and conformal coverage of textured substrate was obtained in stoichiometric conditions between inorganic-organic precursors also for the mixed-cation lead mixed-halide $CsFAMAPb_{I3-x}Br_x$ perovskite (Figure 5.8 c,d). Such film was obtained by spray coating 2.0 ml of 0.3 mg/ml PbI_2 NCs–CsBr ink onto NiO_x/SHJ textured substrate, then converted into perovskite by spraying 2.0 ml of 0.1 mg/ml FAI-FABr-MABr (3.3:2:1 molar ratio) solution in EA (previously prepared by diluting 1:50 v:v the 5.5 mg/ml mother solution in IPA). The $CsFAMAPb_{I3-x}Br_x$ films obtained by spray coating lower or higher volumes (i.e., under or over stoichiometric solutions) of the mixed organic precursors solution led to a poor coverage of the pyramids (Figure 5.8 a,b) and thick bridges among pyramid tips (Figure 5.8 e,f), respectively.

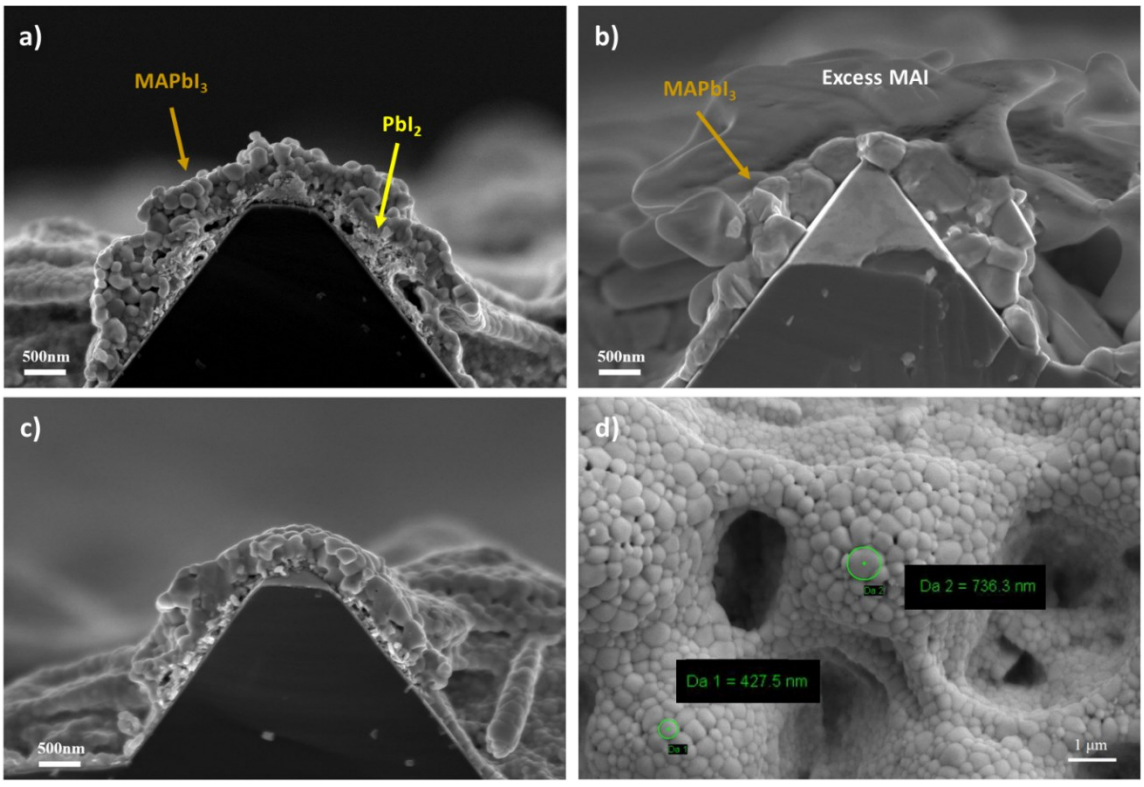

Figure 5.7 Cross-section SEM images of $MAPbI_3$ perovskite thin films deposited over the NiO_x/textured SHJ substrates. The samples were obtained converting the PbI_2 NCs precursor films (2.0 ml, 3.0 mg/ml) by spray coating 1.0 ml of MAI solution in ethyl acetate with different concentrations: a) 0.1 mg/ml, b) 1.0 mg/ml, and c) 0.2 mg/ml. It is possible to notice how to obtain both a good perovskite conversion and a conformal coverage of the textured substrate, the 0.2 mg/ml MAI solution represents the optimal concentration (1:1 precursor molar ratio). d) Top view SEM image of the $MAPbI_3$ film obtained by spraying an over-stoichiometric MAI solution (1.0 ml, 0.3 mg/ml). Bigger perovskite crystal grains were obtained in this condition, but with thick bridges among silicon pyramids (to be avoided for perovskite-Si tandem applications).

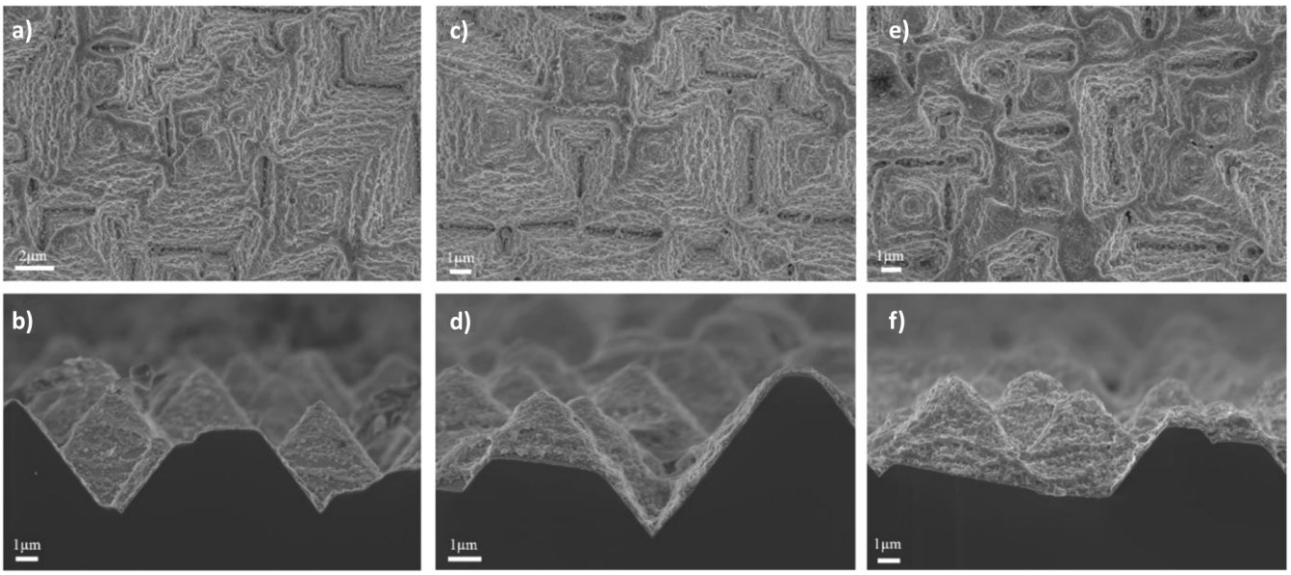

Figure 5.8 Top-view and cross-section SEM images of $CsFAMAPbI_{3-x}Br_x$ thin films deposited over NiO_x/textured SHJ substrates. The samples were obtained converting the PbI_2 NCs-CsBr precursor films deposited in optimized conditions (Figure 5.5 b) by spray coating a,b) 1.0ml, c,d) 2.0ml, and e,f) 3.0ml of FAI-FABr-MABr organic precursor solutions in ethyl acetate (0.1 mg/ml). It can be noticed how the $CsFAMAPbI_{3-x}Br_x$ obtained by spraying 2.0 ml (c,d) was the best in terms of uniform coverage of the textured silicon substrate. Lower amounts of organic precursors led to poor coverage (a-d), while higher led to thick bridges between silicon pyramids (c-f).

Both the $MAPbI_3$ and $CsFAMAPbI_{3-x}Br_x$ optimized thin films did not present any residual reflections related to PbI_2/CsBr precursors in XRD patterns (Figure 5.9), proving a complete precursors conversion into perovskite phases. Moreover, all the spray-coated perovskite films showed smaller crystal grains in SEM images than those reported in literature.[30–32] This fact was ascribed to the large amount of perovskite nucleation centers provided by the PbI_2 precursor NCs used in this study. In addition, the use of low-boiling volatile solvents (i.e., IPA and EA) for the SEF spray coating deposition processes highly hinders the dissolution and the recrystallization of precursors and perovskite, respectively.[30] If, on one side, this fact limits the perovskite grain dimensions that one can reach with this methodology, on the other side avoiding dissolution/recrystallization processes is very useful to get a uniform and conformal perovskite coating of micron-scale textured surfaces.

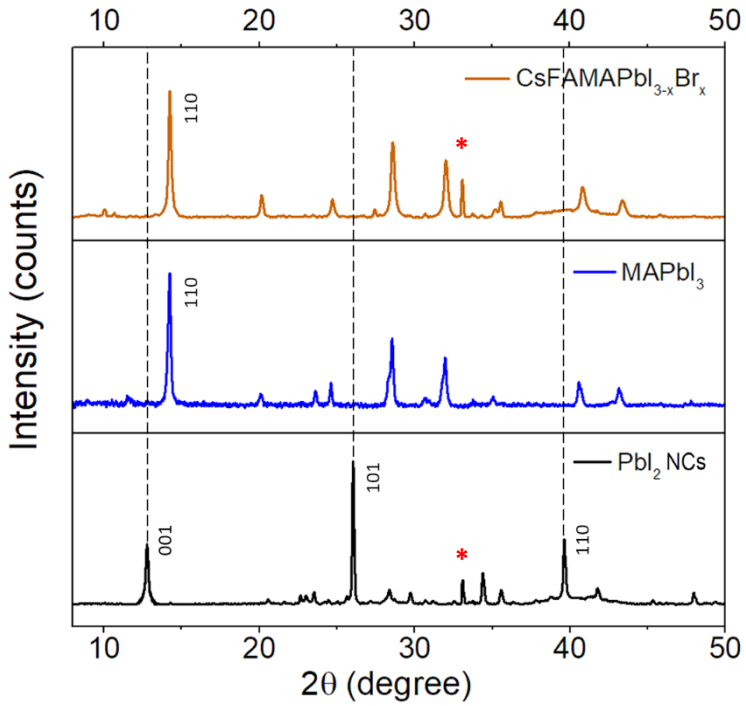

Figure 5.9 XRD diffraction pattern of $CsFAMAPbI_{3-x}Br_x$ (orange), $MAPbI_3$ (blue), and PbI_2 NCs (black) thin films obtained by spray coating deposition onto textured SHJ substrates. The sharp reflection peaks at 33° (red asterisk) are related to the textured substrates. The variations in relative intensities of reflection peaks in PbI_2 NCs XRD pattern (001 reflection is not the most intense, as expected for crystalline PbI_2) can be ascribed to preferential orientation effects of the NCs onto the substrate.[32]

5.2.4 *Optical Characterization*

A set of spray-coated perovskite films on textured Si wafers covered by 300 nm of silicon nitride (SiN_x), deposited via PECVD, was prepared to investigate the optical properties of the samples. To isolate the perovskite films from possible electronic interaction with c-Si wafers, the dielectric SiN_x layer is required. Time-resolved photoluminescence (TRPL) spectroscopy was performed with a streak camera on these samples, to collect the spectral shape and time evolution of the PL at once for both for $MAPbI_3$ and $CsFAMAPbI_{3-x}Br_x$ perovskite films. Figure 5.10 shows the 2D pseudo-color graphs for each sample. As a reference sample, a $MAPbI_3$ film spin-coated on quartz substrate was prepared. Figure 5.11 a shows the normalized steady-state PL (SSPL) spectra of reference spin-coated $MAPbI_3$ perovskite (black), spray-coated $MAPbI_3$ (blue), and optimized (orange) spray-coated $CsFAMAPbI_{3-x}Br_x$ perovskite. Both the spray- and spin-coated $MAPbI_3$ perovskite films exhibited emissions centered at 770 nm, which is indicative of a bandgap of 1.61 eV, in agreement with the expected value for $MAPbI_3$ polycrystalline films.[33,34]

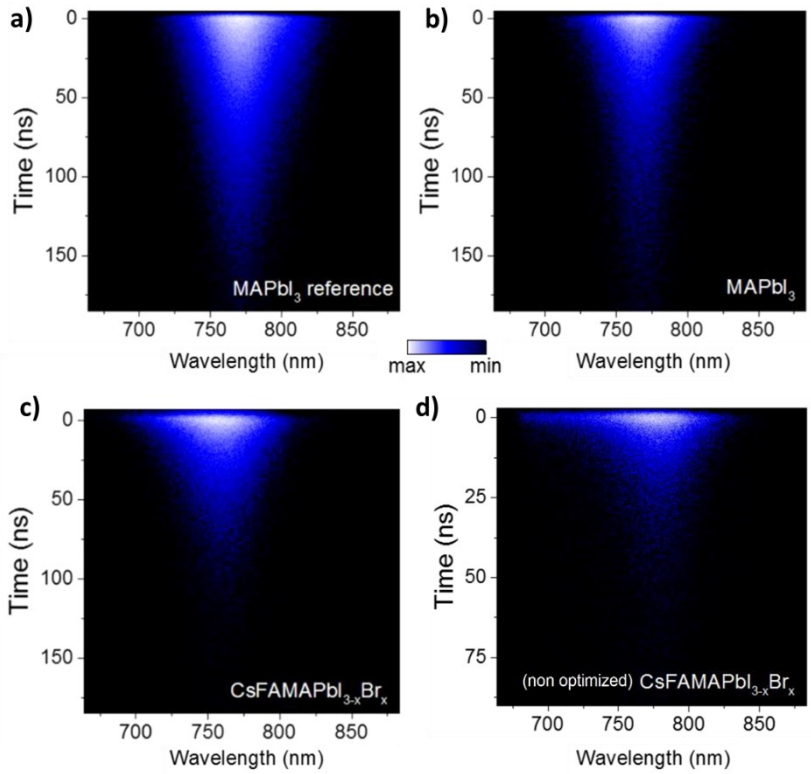

Figure 5.10 2D pseudo-colour streak camera images of a) spin-coated $MAPbI_3$ on quartz (reference), b) spray coated $MAPbI_3$, c) optimized and d) non-optimized $CsFAMAPbI_{3-x}Br_x$ perovskite films deposited on textured SiN_x/Si substrates. The samples were excited at 532 nm.

The $CsFAMAPbI_{3-x}Br_x$ perovskite film showed a broader and blue-shifted emission, centered at 736 nm. This wavelength corresponds to a higher bandgap of about 1.68 eV, typical of mixed-halide perovskites with a Br^- ratio of about 25 % with respect to I^-.[35] Such bandgap value is very close to the best one (around 1.70 eV) predicted for perovskite-silicon tandem application.[36–38] Moreover, in agreement with previous results from mixed halide perovskites obtained via LASiS,[26,39] the $CsFAMAPbI_{3-x}Br_x$ emission was stable even after keeping the perovskite sample in ambient conditions for many hours without any evidence of dominant phase segregation. On the contrary, such a good stability was not observed for non-optimized $CsFAMAPbI_{3-x}Br_x$ samples (orange line, Figure 5.11 c). The photoluminescence lifetimes of the three samples obtained with a laser excitation at 532 nm are shown in Figure 5.11 b. A biexponential fit was used to extrapolate the average PL lifetime (τ_{AVG}) from the transient decays (more details are reported in Section 5.5). Average PL lifetimes of 33 and 21 ns was estimated for the spin- and spray-coated $MAPbI_3$ films, respectively.

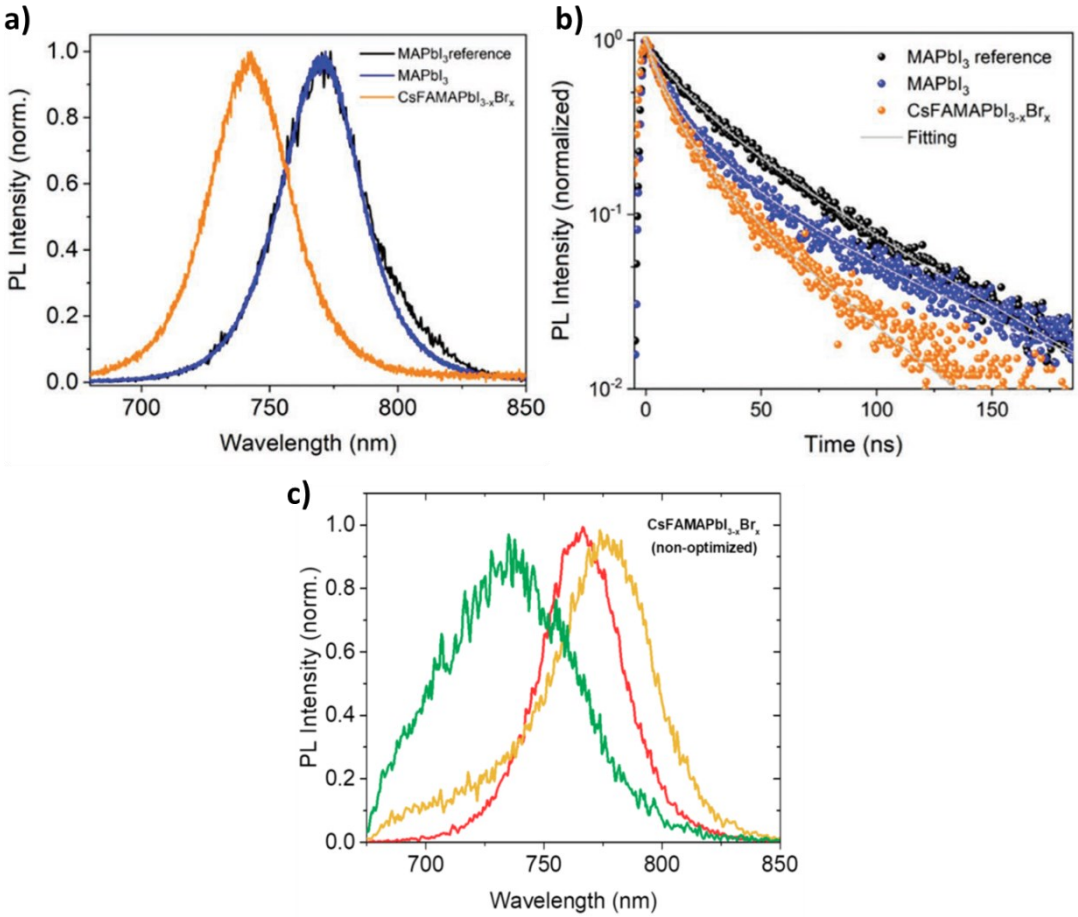

Figure 5.11 Normalized a) steady-state PL spectra and b) transient PL decay of reference spin-coated $MAPbI_3$ perovskite film on quartz substrate (black), spray-coated $MAPbI_3$ (blue), and spray-coated $CsFAMAPbI_{3-x}Br_x$ (orange) perovskite films on textured SiN_x/Si substrates. All samples were excited at 532 nm with a fluence of 0.5 μJ/cm^2. c) Examples of non-optimized $CsFAMAPbI_{3-x}Br_x$ perovskite resulted to phase segregation (yellow), PL broadening (green), and formation of a lower bandgap phase (red).

This reduction of the average lifetime was ascribed to the reduced crystals dimensions in the spray-coated $MAPbI_3$ sample (as previously elucidated), which increase the recombination rates of photogenerated charges at the grain boundaries.[40] PL lifetime was further reduced in the $CsFAMAPbI_{3-x}Br_x$ perovskite sample, with a τ_{AVG} of 17 ns. This shortening in PL lifetimes in mixed perovskite phases is generally attributed to halides segregation under illumination.[41,42] In fact, even if mixed cations (Cs^+, FA^+, MA^+) can stabilize the perovskite lattice, increasing the Br^- ratio in the structure (i.e., widening the perovskite bandgap) reduces the overall PL lifetime. Despite this, the optimized $CsFAMAPbI_{3-x}Br_x$ perovskite samples showed no evident halides segregation during SSPL measurement (Figure 5.11 a,c). To investigate the effects of different perovskite conversion conditions on its emissive properties, SSPL and TRPL measurements were performed on samples prepared with different spray-coated volume and concentrations of precursor solutions, as previously discussed in section 5.2.3. Mixed-cation lead mixed-halide perovskite films made by SEF spray coating using a 1:1 molar ratio between inorganic-organic precursors resulted in longer

lifetimes (Figure 5.12 a,b), confirming the better perovskite conversion yield and the higher quality of the perovskite films obtained in stoichiometric conditions already observed from SEM analysis. Additionally, higher volume loading seemed to be beneficial for $CsFAMAPbI_{3-x}Br_x$ perovskite, by increasing its PL lifetimes (Figure 5.12 c,d). This could be linked to a better and/or more uniform coverage of the PbI_2/CsBr inorganic precursor layer by the organic precursors spray-coated in the second step of SEF spray coating process, confirming that the volume of precursor solution is important to get a complete conversion from PbI_2 NCs-CsBr to $CsFAMAPbI_{3-x}Br_x$ perovskite. In parallel, full coverage of the film and higher crystal quality yield to longer PL lifetime.

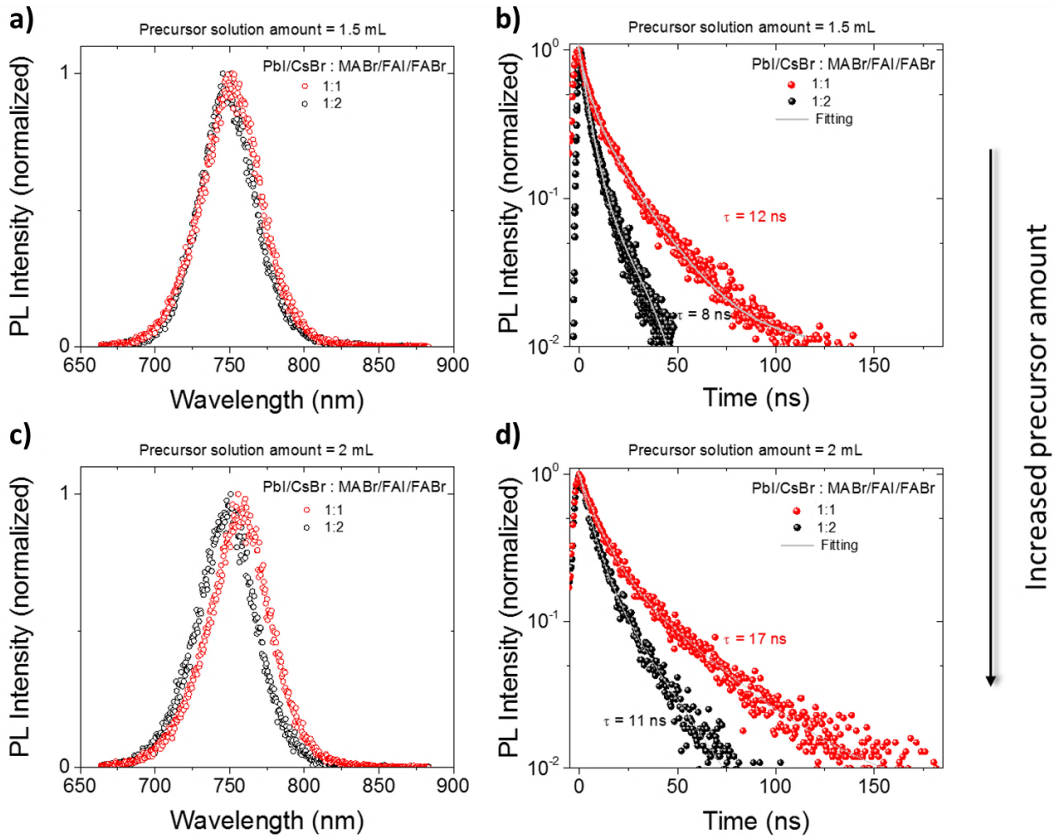

Figure 5.12 PL spectra and kinetics of $CsFAMAPbI_{3-x}Br_x$ perovskite thin films with different inorganic/organic precursors molar ratio (i.e., PbI_2-CsBr : MABr-FAI-FABr) and precursors amount (i.e., different volume loading) used for the conversion. SSPL and TRPL spectra obtained with a,b) 1.5 and c,d) 2.0 ml organic precursors amount respectively. PL spectra show a slight blue shifted emission peak of the perovskite obtained using a higher amount of organic precursors (red line), while TRPL measurements confirm that the volume of precursor solution is important to complete the conversion from PbI_2/CsBr to $CsFAMAPbI_{3-x}Br_x$ perovskite.

5.3 Further Developments

5.3.1 *The Ultrasonic Spray Coating Technique*

To fully exploit the potential of the SEF spray coating technique, an automated ultrasonic spray coating (USC) system was employed for the deposition of large area LHP thin films onto textured surfaces. In the next sections, USC depositions of PbI_2 NCs-CsBr thin films and their conversion into $CsFAMAPbI_{3-x}Br_x$ perovskite by SEF ultrasonic spray coating approach will be reported. First results regarding the implementation of such $CsFAMAPbI_{3-x}Br_x$ photoactive layers inside two-terminal textured perovskite-silicon tandem solar cells will be shown as well. Finally, the hybrid perovskite conversion approach (i.e., an evaporation deposition, followed by a spray coating one) will be introduced, reporting the first attempts to employ this technique for the scalable production of efficient two-terminal textured perovskite-silicon tandem devices.

Ultrasonic spray coating system by Sono-Tek[43] was employed for automated large area depositions of LHP thin films (further details regarding USC tool and deposition conditions are reported in Section 5.5.5). The main difference from the previous home-made airbrush setup relies in the way the ultrasonic spray coating tool generates droplets. In micro airbrush the spray plume is generated by Venturi effect, forcing the liquid through a small orifice (≈0.1 mm) using high pressure to produce spray. A thin needle (0.2-0.3 mm diameter) is moved inward/outward a nozzle, formed by a filled cone contained inside a hollow one (Figure 5.13 a). As the needle retracts from its rest position, opening the orifice, the ink is sucked inside the nozzle and mixes the with a nitrogen inlet to form a cone-shaped aerosol made of sub-millimetric droplets (10^2 µm diameter).[44,45]On the other hand, in USC system the spray plume is generated by a ultrasonic nozzle which, without high pressure effects or small orifice, atomize the ink due to ultrasonic vibrations (60-120 KHz).

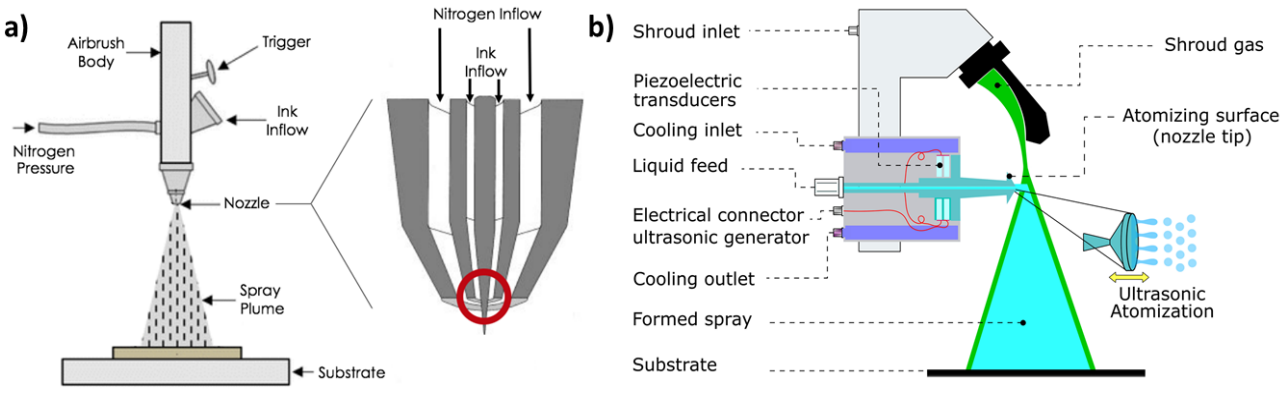

Figure 5.13 a) Schematic of the airbrush system showing a magnification of nozzle in which the needle retraction (red circle), actuated by trigger, allows the ink to mix with the N_2 gas to form the aerosol. b) Scheme of ultrasonic nozzle and spray plume obtained by intersecting the atomized liquid with a deflected gas stream during ultrasonic spray coating.

Spray shaping is then achieved by intersecting an atomized liquid plume with a defined gas stream (Figure 5.13 b). In this way, the kinetic energy of the spray plume can be controlled independently of flow rate. This technology allows to get a more defined spray cone shape and a better atomization of the liquid than airbrush, producing micro droplets (10^1 µm diameter) with a size distribution depending on the resonant frequency of the ultrasonic nozzle.[15,46]

5.3.2 *Spray Deposition of Large-Area Perovskite Films*

Due to bigger substrate area to cover and, above all, the different technical features than micro-airbrush, a re-optimization of PbI_2–CsBr/CsFAMA$PbI_{3-x}Br_x$ thin films deposition by ultrasonic spray coating over textured NiO_x/SHJ bottom cell was necessary. SEM analysis was widely adopted to investigate the degree of coverage of the spray-coated samples. Among all the experimental parameters of the automated ultrasonic spray tool, the main ones to tune to get a uniform and conformal coverage were found to be: (i) the volume loading of the precursors ink, (ii) the height of the spray head moving above the substrate, and (iii) the temperature of the substrate. The results are resumed in Figure 5.14. The same PbI_2 NCs–CsBr precursors ink used in the previous experiments made with the airbrush (Section 5.2.3) was employed for the USC depositions as well. The spray head speed (20 mm/s), the ink flow rate (1.0 ml/min), and the nitrogen output pressure (6.0 psi) were kept fixed for all depositions. Further details about ultrasonic spray coating depositions are reported in Section 5.5.5. As shown in top-view SEM images of PbI_2 NCs–CsBr thin films by USC, high ink volume loadings led to accumulations on pyramid tips, while low ones led to uncovered valleys (Figure 5.14 a).

When the spray head is close to the substrate, precursor NPs accumulations formed on top and in between the Si pyramids. A similar effect, but in a minor extent, is observed when the spray head is far from the textured surface. An intermediate distance was found to be optimal (Figure 5.14 b). Temperature is one of the most important parameters for USC depositions. Substrates are commonly heated during USC deposition as a strategy to improve surface-wetting.[47] This reduces the surface tension of the fluid and thus reduces its contact angle.[15] As depicted in Figure 5.14 c, a non-conformal coverage was obtained both at low and at high temperatures, with big NPs clusters onto the tips and thick bridges between pyramids, respectively. A poor coverage at the pyramid sides was noticed in both cases, especially in the valleys. Contrary to expectations, no accumulations in the valleys were observed even at low temperature.

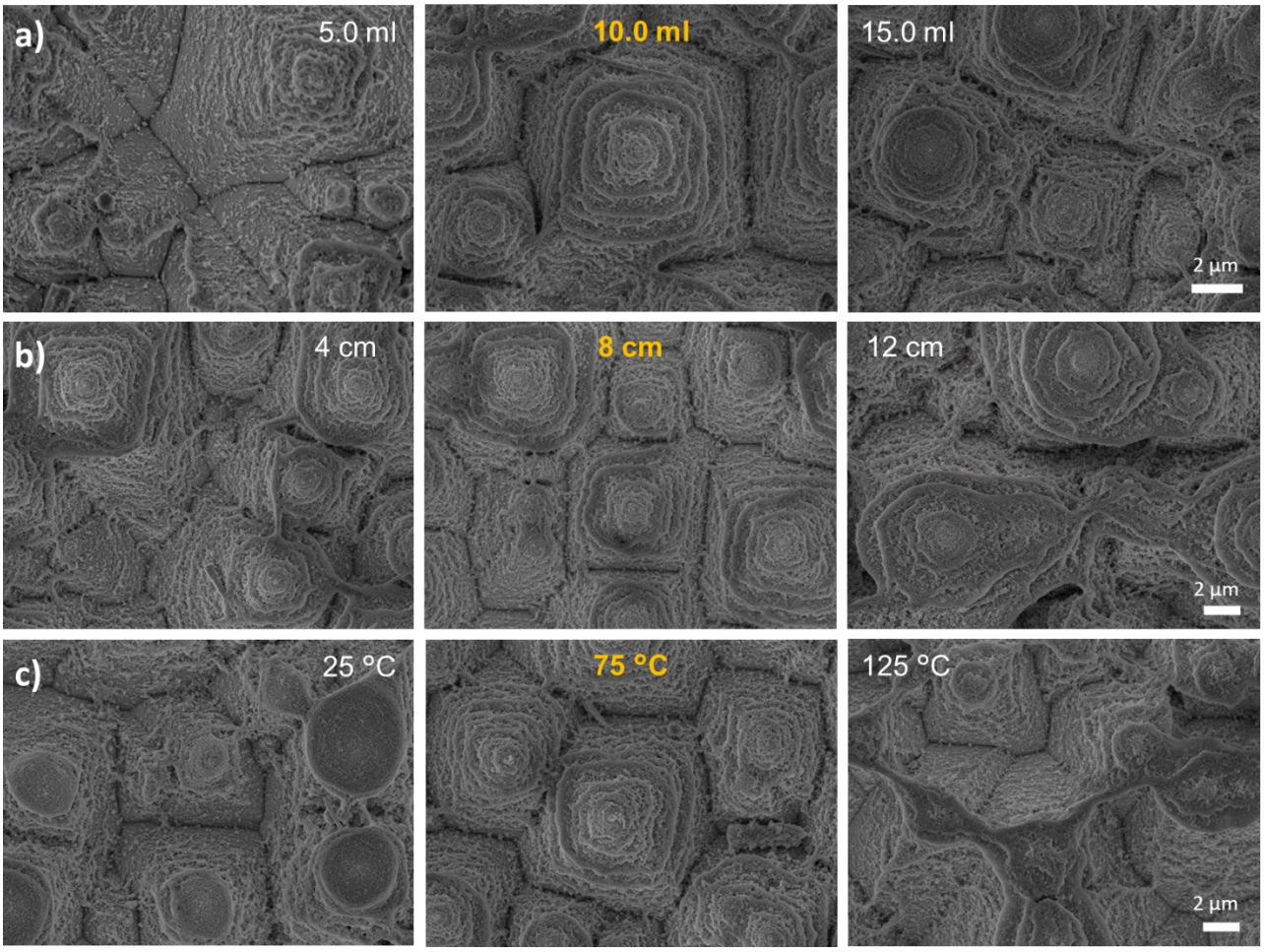

Figure 5.14 Optimization of the USC deposition of PbI_2–CsBr thin films over textured Si heterojunction solar cells. The top-view SEM images show the effect of (a) ink volume loading, (b) distance between spray head and the substrate, and (c) the temperature at which the substrate is heated on the morphology of the deposited PbI_2–CsBr thin films. The highlighted parameters indicate the optimal conditions. Each parameter was opportunely optimized by changing one parameter per time, following the same chronological order of the figures (i.e., volume, height, and finally temperature). All other parameters were fixed for all samples.

When a mid-range temperature value, close to the boiling point of isopropanol (equal to 82.5 °C) was set on the hot plate heating the substrate, a uniform and conformal PbI_2 NCs-CsBr coverage was achieved. These results suggest that other than the substrate temperature, the surface morphology affects USC deposition as well. In the specific case, it was assumed that texturing can induce the ink microdroplets pinning on pyramid tips, leading to a poor coverage if a non-optimal temperature is set. Plasma treatments are known to increase the surface energy (i.e., its wettability) of the substrates, helping the formation of uniform layers.[48–50] Following this indication, further improvements were achieved by treating the substrates via O_2-Ar plasma etching for 5 minutes before USC depositions. As shown in Figure 5.15, this pre-treatment ensured a uniform coverage over wide regions, with negligible NPs accumulations on tips and no bridges among Si pyramids of the textured SHJ solar cell. Once uniform and conformal PbI_2 NCs-CsBr precursor layers of about

300 nm were obtained by optimizing the USC parameters discussed above, $CsFAMAPbI_{3-x}Br_x$ perovskite thin films were produced from them by a subsequent ultrasonic spray coating of organic precursors (FAI-FABr-MABr) solution in ethyl acetate.

As previously reported in Section 5.2.3, one-cycle spraying is necessary to prevent dissolution and recrystallization of the perovskite crystals. Moreover, perovskite conversion by SEF spray coating was optimal when 1:1 molar ratio between inorganic-organic precursors is employed. For these reasons, volume loading and concentration of the organic precursors solution were calibrated to guarantee a complete spray deposition of equimolar organic precursors solution in one cycle. The ink flow was calibrated coherently. Further details on perovskite conversion by SEF ultrasonic spray coating are reported in Section 5.5.5. Figure 5.16 shows the cross-sectional SEM images of $CsFAMAPbI_{3-x}Br_x$ thin films obtained right after USC of organic precursors over optimized PbI_2 NCs-CsBr precursor layers at different ink concentrations and substrate temperatures.

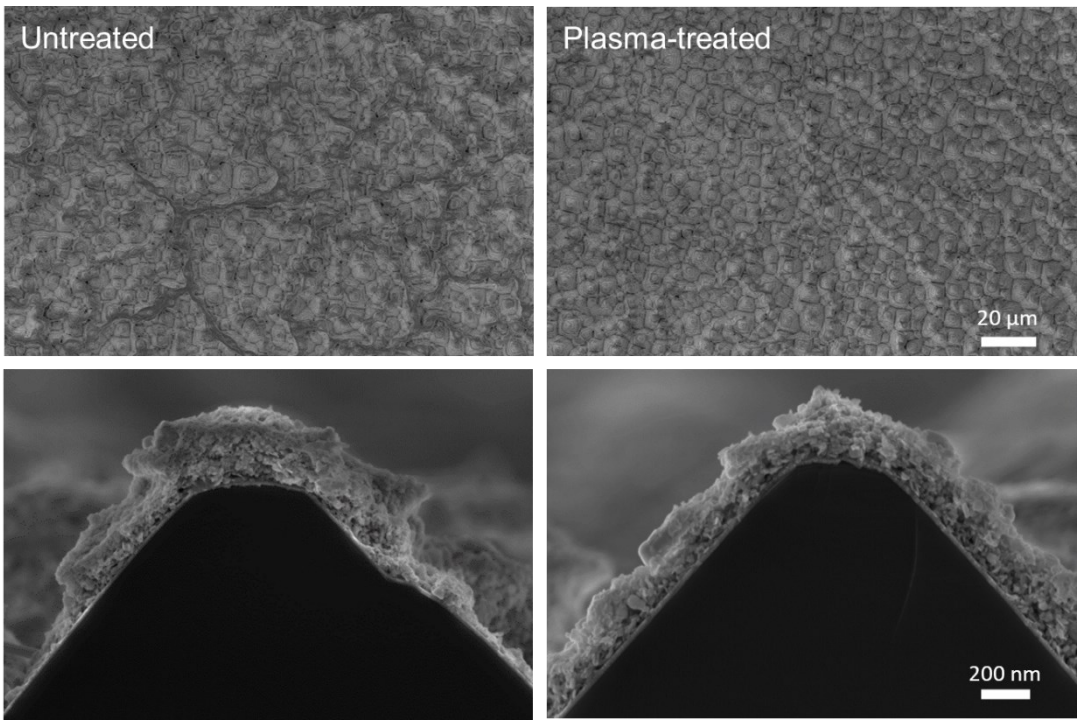

Figure 5.15 Top-view (up) and cross-sectional (bottom) SEM images showing the ultrasonic spray coated PbI_2–CsBr thin films onto textured SHJ solar cells when the substrate is untreated (left) and treated by O_2-Ar plasma etching before the precursors deposition (right).

2 mg/ml was found as optimal ink concentration to get good perovskite conversion, leadi ng to big perovskite grains and a uniform and conformal coverage of the textured NiO_x/SHJ bottom cell (Figure 5.16 a). On the contrary, incomplete perovskite conversions were noticed when lower ink concentrations were employed, leading to unreacted inorganic and organic precursors at the bottom and at the top of the perovskite layer, respectively.

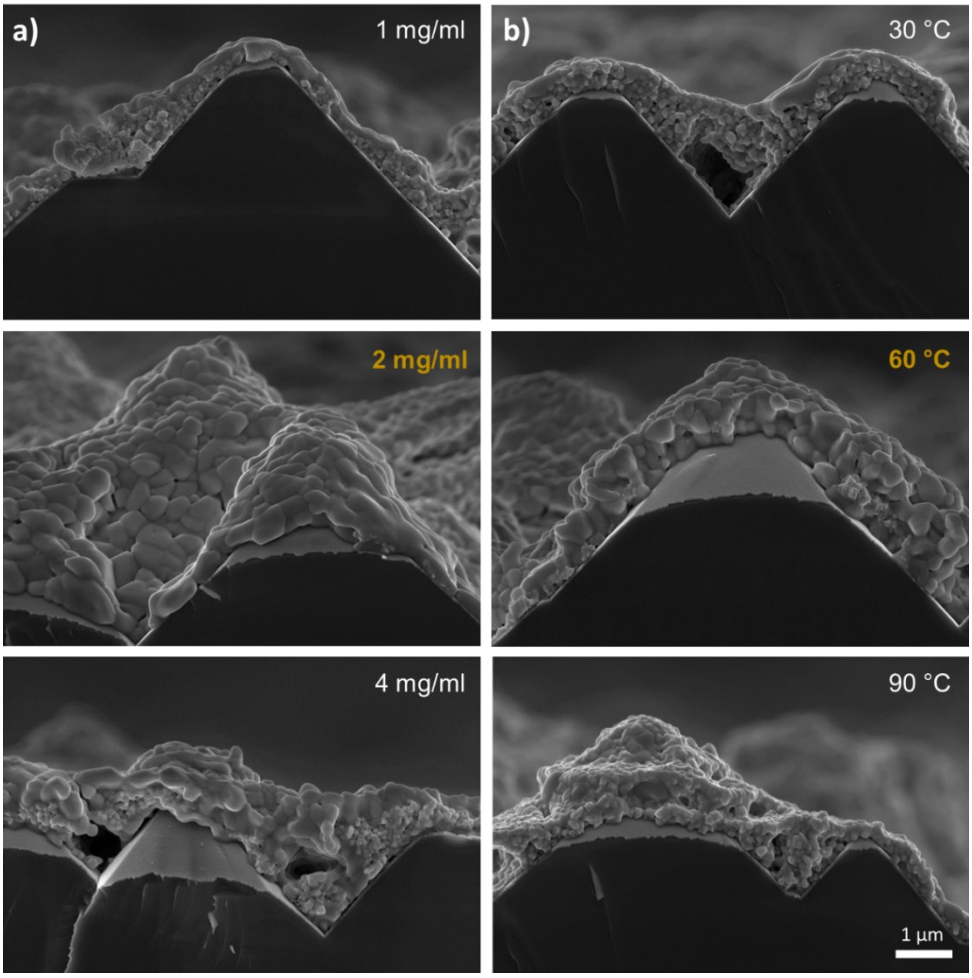

Figure 5.16 Optimization of CsFAMAPbI$_{3-x}$Br$_x$ perovskite conversion by USC deposition of FAI-FABr-MABr solution in ethyl acetate over optimized PbI_2 NCs–CsBr precursors layers. Cross-sectional SEM images showing the effect of: (a) concentration of the organic precursors solution, (b) the temperature at which the substrate is heated during depositions on the morphology of the perovskite thin films. The two parameters were optimized, following the same chronological order of the figures (i.e., ink concentration at first, then substrate temperature), keeping all the other parameters fixed. The highlighted parameters indicate the optimal conditions.

Higher ink concentrations caused the formation of organic precursors accumulations at the top of the perovskite layer, with a loss of layer uniformity. Temperature played a key role in the CsFAMAPbI$_{3-x}$Br$_x$ conversion as well. The USC depositions performed at low temperature (30 °C) led to non-optimal perovskite conversions, with organic precursors accumulations on top (Figure 5.16 b). Conversions executed at temperatures above the boiling point of ethyl acetate (90 °C) led to perovskites with small grains and a morphology resembling the one of PbI_2 NCs-CsBr precursors films. CsFAMAPbI$_{3-x}$Br$_x$ perovskite with big grains and good coverage of textured surfaces was achieved by heating the substrate at an intermediate value of temperature. These results suggested that a too low temperature causes a poor penetration of FAI-FABr-MABr organic precursors into PbI_2 NCs-CsBr layer, while a too high temperature (albeit improving the precursors diffusion) led to a poor perovskite morphology due to the fast ethyl acetate evaporation.

A mid-range temperature (60 °C) ensures both a good conversion of precursors into perovskite phase and a good film morphology over the textured NiO_x/SHJ bottom cell. This was confirmed by XRD analysis (Figure 5.17 a) performed before thermal annealing on same samples reported in Figure 5.16 b. The XRD pattern of $CsFAMAPbI_{3-x}Br_x$ perovskite film converted at 30 °C highlighted the presence of unreacted PbI_2 and hydrated perovskite phases, which can be linked to the coordination of unreacted/accumulations of organic species (i.e., MA^+, FA^+) with moisture (Figure 5.17 b).[51–53] Moreover, the presence of a sharp peak around 33°, related to the textured substrate (Figure 5.17 a), indicated a non-optimal perovskite film coverage in these conditions. A lower $CsFAMAPbI_{3-x}Br_x$ perovskite crystallinity, testified by a decrease in intensity of the main perovskite peak (related to the 110 reflection) at 14.1°, was noticed when converted by heating the substrate at 90 °C. This is in line with the smaller perovskite grains observed for this sample (Figure 5.16 b). No unreacted precursors/hydrated phases were observed in the XRD pattern of the $CsFAMAPbI_{3-x}Br_x$ perovskite layer converted at 60 °C, nor contributes related to the textured substrate. Thus, 50° C represented the optimal temperature condition to get a good perovskite conversion by sequential USC depositions. In this way, 0.5 - 1 µm thick niform and conformal coatings of $CsFAMAPbI_{3-x}Br_x$ perovskite by SEF ultrasonic spray coating over textured surfaces were achieved.

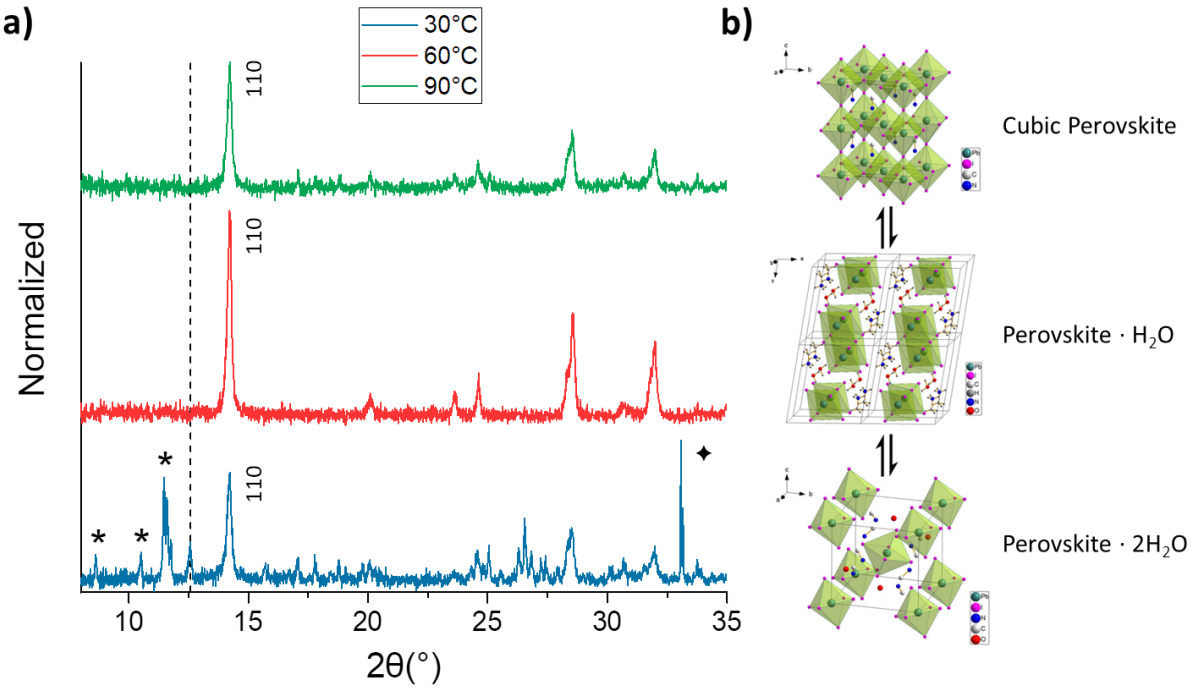

Figure 5.17 a) XRD pattern of $CsFAMAPbI_{3-x}Br_x$ perovskite thin films by USC at different temperatures over textured SHJ bottom cells. The dash line indicates the contribute at 12.6°, which is attributed to the main (100) reflection of PbI_2. The contributes at low angles (✱) in 30 °C sample testify the presence of hydrated perovskite phases, while the sharp reflection peak at 33° (✦) is related to the textured substrate. Data were normalized with respect to the (110) reflection of 60 °C sample. b) Representation of hybrid organic-inorganic perovskite structure in its cubic phase (top), monohydrate phase (middle), and dihydrate phase (bottom).[51]

5.3.3 *Application in Perovskite-Silicon Tandem Devices*

The final step of the project consisted in testing the $CsFAMAPbI_{3-x}Br_x$ perovskite thin films by sequential USC into two-terminal fully-textured perovskite-silicon tandem solar cells and in verifying their resulting performance. Pictures of the optimized PbI_2 NCs-CsBr and $CsFAMAPbI_{3-x}Br_x$ thin films deposited by USC over textured NiO_x/SHJ bottom cell are reported in Figure 5.18 a. Schematics in Figure 5.18 b shows the tandem device architecture, highlighting the thickness, the function, and the deposition method employed for each layer.

The perovskite top cell structure was completed as previously reported.[38] A thin film (25 nm) of C_{60} molecules were deposited on top of the $CsFAMAPbI_{3-x}Br_x$ perovskite absorbing layer by thermal evaporation, constituting the electron transporting layer. Then, a thin layer (20 nm) of tin (II) oxide was deposited by atomic layer deposition as buffer layer, to protect the previous layers from subsequent depositions. 100 nm of indium-zinc oxide (IZO), acting as transparent conductive oxide, were deposited onto tin oxide by sputtering. 300 nm of silver, the metallic top contact, and 100 nm of magnesium fluoride anti-reflective coating were deposited by electron beam evaporation.[38] Figure 5.18 c shows the cross-sectional SEM image of the complete perovskite top cell built onto the textured SHJ bottom one.

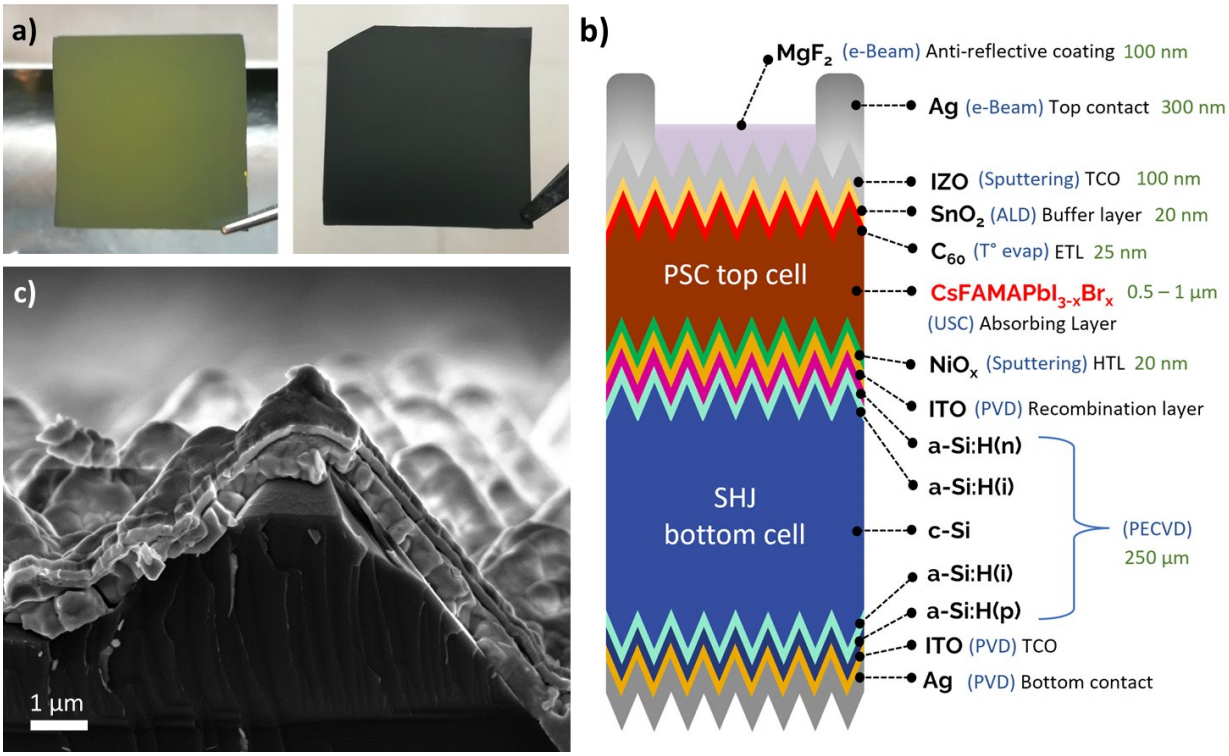

Figure 5.18 a) Pictures of optimized PbI_2 NCs-CsBr (right) and the $CsFAMAPbI_{3-x}Br_x$ (left) thin films deposited by USC over 4x4 cm^2 textured NiO_x/SHJ bottom cells. b) Schematics (not in scale) showing the textured perovskite-silicon tandem device architecture.[38] The thickness (green), the function (black), and the deposition method (blue) employed for each layer. c) Cross-sectional SEM image of textured perovskite-Si tandem device.

An active area of 1 cm^2 was set by masking the devices before Ag and MgF_2 depositions. A picture of 4x4cm^2 two-terminal fully-textured perovskite-silicon tandem device is shown in Figure 5.19 a. Five tandem devices of one single pixel each were assembled and characterized as first batch, which figures of merit are summarized in Figure 5.19 b. The best device showed a PCE equal to 9 %, which J-V curve measured under illumination is reported in Figure 5.19 c. More details regarding the characterization of the photovoltaic performance are reported in Section 5.5.8. The low performance of tandem devices was principally attributed to the low FF (the ratio between the green and the hatched area in Figure 5.19 c), in the range of 40-53, and the low J_{SC}, of 8-12 mA/cm^2. FF > 75 and J_{SC} of 19-20 mA/cm^2 are expected for efficient two-terminal perovskite-silicon tandem devices.[3,54,55] The issues behind this discrepancy are not simple to identify (especially in multi-junction solar cells) and can be ascribed to several aspects, which require a deep electrical and optical characterization of the devices.[56–62] Based on the previous characterizations and on the interpretation of J-V curves, an explanation of the factors that can have affected the tandem devices, leading to poor PCE, will be provide in the following discussion. Equivalent circuits are usually employed for the description of the electrical beviour of a PV devices.[63–67] Figure 5.19 d reports the equivalent circuit used to interpret the J-V curves measured for the monolithic fully-textured perovskite-silicon tandem solar cells.

The SHJ bottom cell, which has been extensively tested and optimized in previous studies,[12,68,69] was excluded from the discussion since its contribution to performance losses was considered negligible. Variations in terms of compoisition, thickness, and of interface between layers of the perovskite top cell, even in a few isolated spots, can heavily influence the J-V curve of the whole tandem and, consequently, its resulting performance. Locally inhomogeneities of the precursor layer thickness and/or of the organic precursors distribution during USC steps can result in regions with a non-optimal perovskite conversion. These regions can both increase the series resistance,[70] e.g. by forming layers with a low conducibility, and decrease the extracted photocurrent density (J_{Ph}), due to a reduced capability of the perovskite absorbing material to convert light into free charges and/or a higher probability of photogenerated charges recombination at trap/defect sites.[71,72] A high R_S is testified by the bending in the second part of the J-V curve (from V_M up to V_{OC}, Figure 5.19 c), with is responsible of a reduction of the FF value, yet not affecting the V_{OC}.[73,74] On the other hand, a decrease of J_{Ph} inevitably lead to a reduced short-circuit current density (J_{SC}), without altering the shape of the J-V curve.[67,75] In the specific case, the low measured J_{SC} was mainly ascribed to the smaller perovskite grain size than those reported in literature (Section 5.2.3).[30–32]

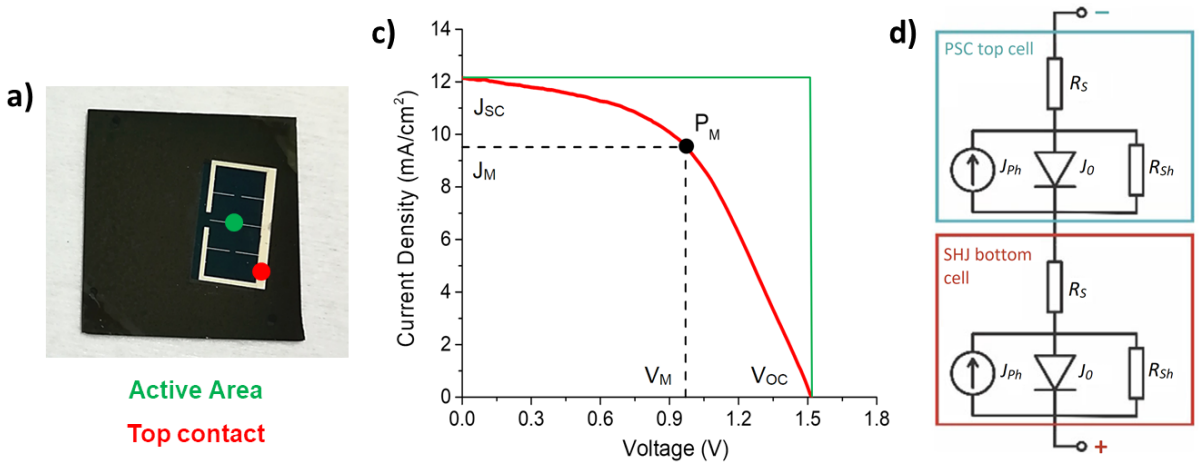

b)

PCE (%)	V_{OC} (mV)	J_{SC} (mA/cm^2)	FF	V_M (mV)	I_M (mA)	P_M (mW)
8.99	1516	12.15	50.33	970	9.56	9.3
7.47	1559	11.49	41.68	860	8.95	7.7
6.05	1588	7.46	51.11	1100	5.67	6.2
6.72	1562	8.63	49.85	1000	6.92	6.9
7.63	1538	9.39	52.85	1060	7.42	7.9

Figure 5.19 a) Picture of the 4x4cm^2 two-terminal textured perovskite-silicon tandem device, highlighting the 2x0.5 cm^2 active area (green dot) and the silver top contact (red dot) regions. The bottom contact was underneath the device. b) Table reporting the figures of merit of the devices, together with the maximum voltage (V_M), current (I_M), and power (P_M). c) Current density-voltage scan of the best tandem device, highlighting the related figures of merit and the maximum power point (P_M). The curve was measured under illumination in reverse bias (from 1.8 to 0 V), highlighting the related figures of merit and maximum power point (P_M). d) Equivalent circuit model used to describe the electrical behaviour of the two-terminal perovskite-silicon tandem devices, comprising two one-diode models for each sub cell.[56]

Smaller crystal domains, i.e. higher density of grain boundaries in the perovskite absorbing layer increase the non-radiative recombination probability of photogenerated charges.[40,76,77] The non-flat region in the first part of the J-V curve (from 0 V to V_M, Figure 5.19 c), the second contribute to the reduction in the FF, is generally attributed to low shunt resistance (R_{SHUNT}). R_{SHUNT} causes power losses in solar cells by providing alternative pathways for the light-generated current, leading to the reduction of both the amount of current flowing through the solar cell junction and the voltage measured at the extremities of the PV device.[78,79] A low R_{SHUNT} can be attributed both to damages of the underlying layers during the perovskite top cell processing, as well as to a non-optimal perovskite coverage in some regions (presumably in the valleys among Si pyramids of the textured SHJ bottom cell). An extensive SEM and XRD investigation could provide further information regarding these hypotheses. The V_{OC} measured for the devices (1.5-1.6 V) were lower than those expected for two-terminal perovskite-silicon tandem (1.8-1.9 V), equal to the sum of the V_{OC} of the sub cells connected in series.[54] This loss in V_{OC} can be attributed to a combination of a low R_{SHUNT}

and a high dark recombination current density (J_0).[80] J_0 is a measure of the leakage of carriers across a p-n junction under reverse bias, caused by carriers recombination in the neutral regions on either side of the junction.[81] Additionally, the V_{OC} is sensitive towards energy misalignment between the perovskite absorbing layer and the charge-transport layers sandwiching it.[66,82] Thus, fluctuations in perovskite composition, i.e. in electrons and holes quasi-Fermi levels,[83] can have a negative impact of the V_{OC} measured for the whole tandem device.

5.4 Summary

In this study, an innovative sequential eco-friendly spray coating method to deposit metal halide perovskite thin films on textured surfaces was presented. By completely avoiding the use of hazardous solvents, the SEF spray coating protocol can solve an important step toward the commercialization of the perovskite-based solar cell technology. Starting from lead iodide nanocrystals precursor solution by laser ablation in isopropanol, it was demonstrated how $MAPbI_3$ and $CsFAMAPbI_{3-x}Br_x$ thin layers can be obtained by spray coating such nanocrystals on textured substrates, then converted into perovskite phases by a subsequent spray coating of the organic precursors in ethyl acetate. To achieve a uniform and conformal perovskite coating of textured Si heterojunction bottom solar cells, used as substrates to mimic the architecture of monolithic perovskite-silicon tandem, SEM analysis was widely adopted. Good perovskite coverage was obtained once optimized the deposition conditions, with smaller crystal grains than those reported in literature. This was ascribed both to the use of PbI_2 NCs as perovskite precursors, as well as to the low-boiling volatile solvent used in the sequential eco-friendly spray coating process. Different conversion conditions and/or perovskite post-treatments could be evaluated to improve the morphology of the perovskite thin films while maintaining a conformal and uniform coverage of textured substrates, especially to decrease the amount of grain boundaries and increase the grain size.[84–89] A complete conversion of precursors into perovskite phases was testified by XRD patterns.

Photoluminescence measurements confirmed the increased bandgap of $CsFAMAPbI_{3-x}Br_x$ (1.68 eV) respect to $MAPbI_3$ (1.61 eV) due to Br^- incorporation into perovskite lattice, which is crucial to get efficient perovskite-silicon tandem application.[36,37] The innovative deposition approach here presented well suits the industrial standards and can be interesting for future large-area monolithic perovskite-Si textured tandem fabrication, even by optimizing the spray coating of other layers needed in the device architecture. First attempts in this direction were obtained by using an automated ultrasonic spray coating system, which was employed for the deposition of large area

$CsFAMAPbI_{3-x}Br_x$ perovskite thin films by SEF spray coating approach. Preliminary results of working fully-textured monolithic perovskite-silicon tandem devices implementing the spray-coated $CsFAMAPbI_{3-x}Br_x$ absorbing layers, proving the potential of the method, were also presented, and interpreted.

5.5 Experimental Section

5.5.1 *PbI_2 NCs ink via Laser Ablation in Solution*

The colloidal solution of PbI_2 nanocrystals were produced by LASiS in isopropanol as previously reported in Chapter 4 (Section 4.4.3). For the purposes of this work, experimental conditions were tuned to produce 4.0 ml of PbI_2 NCs ink in IPA with a concentration of 0.3 mg/ml within 20 minutes (Figure 4.18 c). The concentration of PbI_2 NCs inks were estimated by optical extinction, calculating the concentration values through Lambert-Beer law of PbI_2 digested in DMF (Section 4.4.3).[39]

5.5.2 *Silicon Heterojunction Bottom Cell Fabrication*

SHJ solar cells were realized on float zone double-side-textured four inches wafers (250–280 µm thick) as reported in a previous study.[68] KOH alkaline solution was used for the etching of the raw c-Si wafers, obtaining randomly distributed pyramidal texturing (Figure 5.1 b).[90] The textured wafers were then cleaned in RCA1 and RCA2 solutions. PECVD by Indeotec Octopus 2 was employed to deposit amorphous intrinsic and doped Si layers. ITO and Ag thin films (150 and 250 nm thick, respectively) were sequentially sputtered in the physical vapor deposition (PVD) side of the Octopus 2 cluster, forming the back contact of the SHJ. To mimic a perovskite-silicon tandem configuration, ITO (25 nm) and NiO_x (20 nm) thin layers were sequentially deposited by Angstrom EvoVac as recombination junction and hole transport layer of the top cell, respectively (Figure 5.1 a).

5.5.3 *The Home-made Micro-Airbrush Spray Coating System*

The sequential spray coating depositions represented in Figure 5.2 were performed by using the same home-made spray coating system previously reported in Chapter 4 (Section 4.4.1). An optimized ink flow of 0.2 and 0.4 ml/min was set for the first (Figure 5.20 a) and the second (Figure 5.20 b) spray coating step, respectively. All depositions were performed under extractor hood (20 °C, 50 % relative humidity), over an area of 1.5×1.5 cm^2. After spray depositions, all samples underwent a thermal annealing for 10 min at 100 °C under Ar flow.

5.5.4 *PbI_2 NC–CsBr Thin Film on Soda-Lime Glass*

To produce the PbI_2 -CsBr thin film reported in Figure 5.4 a, 2.0 ml of PbI_2 NCs ink in IPA (0.3 mg/ml) mixed with 20 µl of CsBr aqueous solution (0.7 mg/ml) were spray-coated over a soda-lime glass (1.5×1.5 cm^2) substrate, then heated at 100 °C by a hot plate. The PbI_2 NCs–CsBr ink was sonicated for 5 minutes before spraying. A constant ink flow of 0.3 ml/min was set for the deposition, performed under extractor hood in ambient condition.

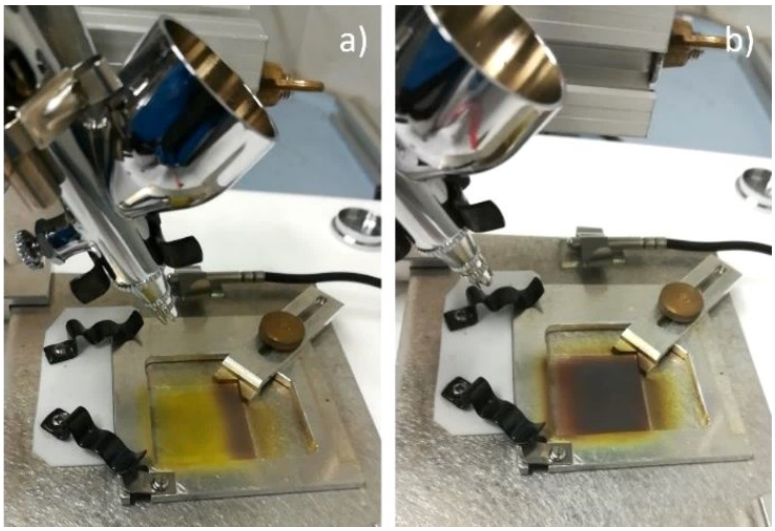

Figure 5.20 Pictures showing the conversion of a PbI_2 NCs-CsBr thin film over soda-lime glass to $CsFAMAPbI_{3-x}Br_x$ perovskite by spray coating a FAI-FABr-MABr solution in ethyl acetate. The photographs were taken a) during and b) at the end of perovskite conversion.

5.5.5 *The Ultrasonic Spray Coating Automated Tool*

Figure 5.21 a reports the picture of the ExactaCoat OP2 automated, programmable benchtop coating system by Sono-Tek with coordinated XYZ motion control using Windows-based software and user-friendly teach pendant with trackball. The versatile system is aimed from R&D to mid-volume production thin film coatings. The main experimental parameters to tune for ultrasonic spray coating deposition of thin films are listed in Figure 5.21 b, with the parameters kept fixed for all experiments inside brakets. To ensure a full coverage of the substrates, the spray head was moved by following a square grid spray pattern (4x4 cm^2) with a line spacing of 4 mm, set by the Sono-Tek software interface for all samples (Figure 5.21 c). To work in safe and controlled conditions, the ultrasonic spray depositions were performed in a glovebox, filled with a nitrogen atmosphere at 5 mbar overpressure and continuously purified by a circulating system. As for the previous depositions by home-made airbrush system (Section 5.5.3), the same PbI_2 NCs-CsBr solutions were employed as precursor inks for USC depositions as well.

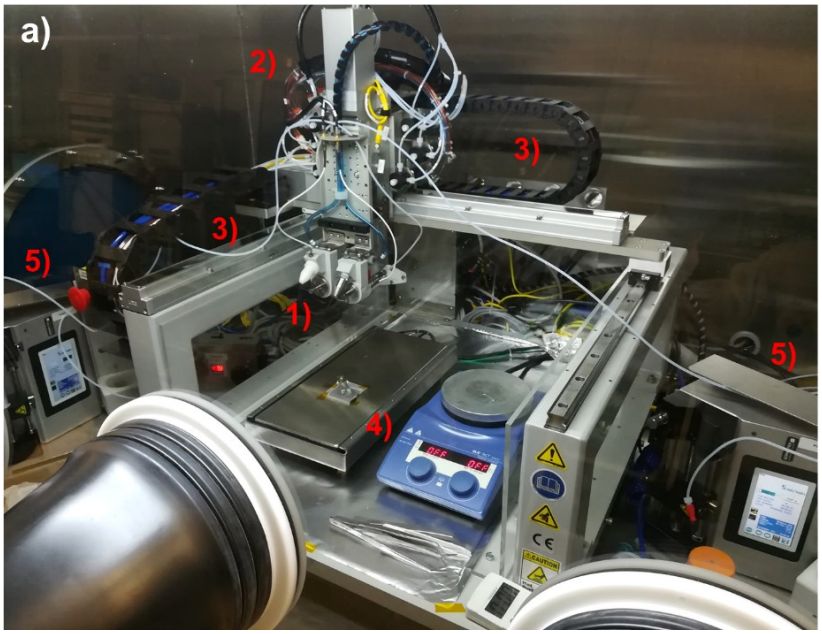

b)

PARAMETER	RANGE
N_2 pressure	5.0 – 9.0 psi (6)
Height	3.0 – 12.0 cm
Speed	0.1 – 30 cm/s
Spray Plume	1 – 10 cm
Line spacing	down to 0.1 mm (4)
Nozzle Power	1.0 – 5.5 W (2.0)
Piezo frequency	48 / 120 KHz (120)
Deposition area	up to 30x30 cm^2 (4x4)
Ink flow rate	0.1 – 10.0 ml/min
Hot plate T°	up to 150°C

c)

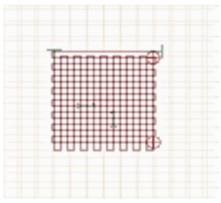

Figure 5.21 a) Picture of the ultrasonic spray coating automated system located into a glovebox, showing (1) ultrasonic Impact nozzles, (2) feeding tubes carrying the nitrogen gas, the ink, and the power supply to the nozzles, (3) XYZ handling automated system, moved by brushless DC motors, (4) hot plates used to heat the substrates during/after the spray depositions, and (5) syringe pumps connected to the nozzles for the ink supply. b) Table listing the main instrumental parameters of the machine with the respective range of values. Values in brackets indicate the fixed parameters employed in all experiments. c) Spray pattern used in this work, set using the Sono-Tek software interface.

To avoid clogging of the ultrasonic nozzles due to the possible formation of aggregates, PbI_2 NCs-CsBr precursor inks were sonicated for 5 minutes before depositions. The ink concentration (0.3 mg/ml), the spray head speed (20 mm/s) and the ink flow rate (1.0 ml/min) were kept fixed for all USC depositions of inorganic precursors thin films, while volume loading, height of spray head, and substrate temperature were chosen as main parameters to tune (Figure 5.14). The optimized PbI_2 NCs-CsBr layers were then converted into $CsFAMAPbI_{3-x}Br_x$ perovskites by a subsequent USC deposition of FAI-FABr-MABr solution in ethyl acetate, prepared following the procedure reported in Section 5.2.3. The spray head speed (10 mm/s) and height (6 cm) were fixed, while organic precursors concentration and substrate temperature were tuned during the perovskite conversion optimization (Figure 5.16). All samples underwent a thermal annealing for 10 min at 100 °C inside the glovebox after SEF spray coating procedure.

5.5.6 *Morphological Characterizations*

SEM measurements were performed with a Zeiss Auriga CrossBeam workstation based on a Gemini field emission-scanning electron microscope column. The column was equipped with in-lens secondary electron and back scattered electron detectors for high resolution and contrast imaging, and with an airlock for fast and convenient sample transfer. All SEM measurements were performed

with an accelerating voltage of 5 kV and a working distance of 5 mm. XRD patterns were recorded in grazing incidence geometry using a BRUKER AXS D8 ADVANCE Plus diffractometer working with a Cu $K_{\alpha 1}$ anode. The X-Ray source position was fixed to get an incidence angle of 1° and a motorized anti-air-scatter screen was mounted during the measurements. All diffraction patterns were recorded at room temperature.

5.5.7 *Optical Characterizations*

A Renishaw InVia micro-Raman instrument, equipped with a CCD detector (100 µm slits) and a piezoelectric xyz scanning stage, was used to perform steady-state photoluminescence (SSPL) measurements. Using a 50× objective, a 633 nm line of He-Ne laser (Renishaw RL63, 13 mW) excitation beam was focused on the sample with an output power of 1 µW. To account for small intensity fluctuations of the laser output (< 5%), a c-Si internal reference was used before and after each SSPL measurement. All SSPL measurements were performed in ambient conditions. A high-resolution streak camera system (Hamamatsu, C10910) was used for recording time-resolved photoluminescence (TRPL) measurements. A 532 nm excitation beam (HELIOS 532-4-125, Coherent Inc.) was focused to pump the perovskite samples, which were mounted inside a sealed nitrogen chamber to prevent any changes due to exposure to oxygen and humidity. A spectrograph and streak camera system were employed to resolve the associated PL emissions spectrally and temporally. Data were acquired in photon counting mode using the streak camera software (HPDTA), then exported to Origin Pro 2015 for further analysis. All TRPL measurements were registered at room temperature.

5.5.8 *Photovoltaic Performance*

Current density-voltage (J-V) measurements were performed at room temperature using WaveLabs Sinus 220 LED-based solar simulator with AM 1.5G irradiance spectrum. The light intensity was calibrated using a reference Fraunhofer ISE CalLab certified c-Si solar cell. Device measurements were performed at 200 mV/s scan speed using a Keithley 2400 source meter, performing a forward scan (from -0.1 to 1.8 V) followed by a reverse scan (from 1.8 to -0.1 V). The illumination area of the devices was 1.03 cm^2, determined by the application of a laser cut shadow mask over the devices during the electrical J-V scans. The stabilized power measurements were recorded via a homemade LabView-based software.

References

(1) Sansoni, S.; De Bastiani, M.; Aydin, E.; Ugur, E.; Isikgor, F. H.; Al-Zahrani, A.; Lamberti, F.; Laquai, F.; Meneghetti, M.; De Wolf, S. Eco-Friendly Spray Deposition of Perovskite Films on Macroscale Textured Surfaces. *Adv. Mater. Technol.* **2020**, *5* (2), 1901009–1901014. https://doi.org/10.1002/admt.201901009.

(2) NREL Best Research-Cell Efficiency Chart https://www.nrel.gov/pv/assets/pdfs/best-research-cell-efficiencies.20200104.pdf.

(3) Al-Ashouri, A.; Köhnen, E.; Li, B.; Magomedov, A.; Hempel, H.; Caprioglio, P.; Márquez, J. A.; Belen, A.; Vilches, M.; Kasparavicius, E.; et al. Monolithic Perovskite/Silicon Tandem Solar Cell with >29% Efficiency by Enhanced Hole Extraction. *Science (80-.).* **2020**, *370*, 1300–1309.

(4) Oxford PV - Leaders in perovskite solar technology https://www.oxfordpv.com/.

(5) Galagan, Y. Perovskite Solar Cells from Lab to Fab: The Main Challenges to Access the Market. *Oxford Open Mater. Sci.* **2020**, *1* (1), 1–9. https://doi.org/10.1093/oxfmat/itaa007.

(6) Altazin, S.; Stepanova, L.; Werner, J.; Niesen, B.; Ballif, C.; Ruhstaller, B. Design of Perovskite/Crystalline-Silicon Monolithic Tandem Solar Cells. *Opt. Express* **2018**, *26* (10), A579. https://doi.org/10.1364/oe.26.00a579.

(7) Qarony, W.; Hossain, M. I.; Jovanov, V.; Salleo, A.; Knipp, D.; Tsang, Y. H. Influence of Perovskite Interface Morphology on the Photon Management in Perovskite/Silicon Tandem Solar Cells. *ACS Appl. Mater. Interfaces* **2020**, *12* (13), 15080–15086. https://doi.org/10.1021/acsami.9b21985.

(8) Zheng, X.; Chen, B.; Wu, C.; Priya, S. Room Temperature Fabrication of CH3NH3PbBr3 by Anti-Solvent Assisted Crystallization Approach for Perovskite Solar Cells with Fast Response and Small J-V Hysteresis. *Nano Energy* **2015**, *17*, 269–278. https://doi.org/10.1016/j.nanoen.2015.08.023.

(9) Sahli, F.; Werner, J.; Kamino, B. A.; Bräuninger, M.; Monnard, R.; Paviet-Salomon, B.; Barraud, L.; Ding, L.; Diaz Leon, J. J.; Sacchetto, D.; et al. Fully Textured Monolithic Perovskite/Silicon Tandem Solar Cells with 25.2% Power Conversion Efficiency. *Nat. Mater.* **2018**, *17* (9), 820–826. https://doi.org/10.1038/s41563-018-0115-4.

(10) Werner, J.; Sahli, F.; Fu, F.; Diaz Leon, J. J.; Walter, A.; Kamino, B. A.; Niesen, B.; Nicolay, S.; Jeangros, Q.; Ballif, C. Perovskite/Perovskite/Silicon Monolithic Triple-Junction Solar Cells with a Fully Textured Design. *ACS Energy Lett.* **2018**, *3* (9), 2052–2058. https://doi.org/10.1021/acsenergylett.8b01165.

(11) Jiang, Y.; Almansouri, I.; Huang, S.; Young, T.; Li, Y.; Peng, Y.; Hou, Q.; Spiccia, L.; Bach, U.; Cheng, Y. B.; et al. Optical Analysis of Perovskite/Silicon Tandem Solar Cells. *J. Mater. Chem. C* **2016**, *4* (24), 5679–5689. https://doi.org/10.1039/c6tc01276k.

(12) Hou, Y.; Aydin, E.; Bastiani, M. De; Xiao, C.; Isikgor, F. H.; Xue, D.; Baek, S.; Huang, Z.; Wei, M.; Dong, Y.; et al. Efficient Tandem Solar Cells with Solution-Processed Perovskite on Textured Crystalline Silicon. *Science (80-.).* **2020**, *367* (6482), 1135–1140.

(13) Battaglia, C.; Cuevas, A.; De Wolf, S. High-Efficiency Crystalline Silicon Solar Cells: Status and Perspectives. *Energy Environ. Sci.* **2016**, *9* (5), 1552–1576. https://doi.org/10.1039/c5ee03380b.

(14) Bishop, J. E.; Smith, J. A.; Lidzey, D. G. Development of Spray-Coated Perovskite Solar Cells. *ACS Appl. Mater. Interfaces* **2020**, *12*, 48237–48245. https://doi.org/10.1021/acsami.0c14540.

(15) Bishop, J. E.; Routledge, T. J.; Lidzey, D. G. Advances in Spray-Cast Perovskite Solar Cells. *J. Phys. Chem. Lett.* **2018**, *9* (8), 1977–1984. https://doi.org/10.1021/acs.jpclett.8b00311.

(16) Tiwari, A.; Uzun, L. *Advanced Functional Materials*; Wiley, Ed.; Scrivener Publisher, 2015.

(17) Baker-Finch, S. C.; McIntosh, K. R. Reflection Distributions of Textured Monocrystalline Silicon: Implications for Silicon Solar Cells. *Prog. Photovoltaics Res. Appl.* **2013**, *21* (5), 960–971. https://doi.org/10.1002/PIP.2186.

(18) Aydin, E.; Troughton, J.; De Bastiani, M.; Ugur, E.; Sajjad, M.; Alzahrani, A.; Neophytou, M.; Schwingenschlögl, U.; Laquai, F.; Baran, D.; et al. Room-Temperature-Sputtered Nanocrystalline Nickel Oxide as Hole Transport Layer for p-i-n Perovskite Solar Cells. *ACS Appl. Energy Mater.* **2018**, *1* (11), 6227–6233. https://doi.org/10.1021/acsaem.8b01263.

(19) Allen, T. G.; Bullock, J.; Yang, X.; Javey, A.; De Wolf, S. Passivating Contacts for Crystalline Silicon

Solar Cells. *Nat. Energy* **2019**. https://doi.org/10.1038/s41560-019-0463-6.
(20) Descoeudres, A.; Holman, Z. C.; Barraud, L.; Morel, S.; De Wolf, S.; Ballif, C. >21% Efficient Silicon Heterojunction Solar Cells on N-and P-Type Wafers Compared. *IEEE J. Photovoltaics* **2013**, *3* (1), 83–89. https://doi.org/10.1109/JPHOTOV.2012.2209407.
(21) Yang, G. *Laser Ablation in Liquids: Principles and Applications in the Preparation of Nanomaterials (1st Edition)*; Pan Stanford Publishing, 2012.
(22) Semaltianos, N. G. Nanoparticles by Laser Ablation. *Crit. Rev. Solid State Mater. Sci.* **2010**, *35* (2), 105–124. https://doi.org/10.1080/10408431003788233.
(23) Zeng, H.; Du, X. W.; Singh, S. C.; Kulinich, S. A.; Yang, S.; He, J.; Cai, W. Nanomaterials via Laser Ablation/Irradiation in Liquid: A Review. *Adv. Funct. Mater.* **2012**, *22* (7), 1333–1353. https://doi.org/10.1002/adfm.201102295.
(24) Amendola, V.; Polizzi, S.; Meneghetti, M. Laser Ablation Synthesis of Gold Nanoparticles in Organic Solvents. *J. Phys. Chem. B* **2006**, *110* (14), 7232–7237. https://doi.org/10.1021/jp0605092.
(25) Ismail, R. A.; Mousa, A. M.; Khashan, K. S.; Mohsin, M. H.; Hamid, M. K. Synthesis of PbI2 Nanoparticles by Laser Ablation in Methanol. *J. Mater. Sci. Mater. Electron.* **2016**, *27* (10), 10696–10700. https://doi.org/10.1007/s10854-016-5169-y.
(26) Rizzo, A.; Lamberti, F.; Buonomo, M.; Wrachien, N.; Torto, L.; Lago, N.; Sansoni, S.; Pilot, R.; Prato, M.; Michieli, N.; et al. Understanding Lead Iodide Perovskite Hysteresis and Degradation Causes by Extensive Electrical Characterization. *Sol. Energy Mater. Sol. Cells* **2019**, *189*, 43–52. https://doi.org/10.1016/j.solmat.2018.09.021.
(27) Wang, R.; Shang, Y.; Kanjanaboos, P.; Zhou, W.; Ning, Z.; Sargent, E. H. Colloidal Quantum Dot Ligand Engineering for High Performance Solar Cells. *Energy Environ. Sci.* **2016**, *9* (4), 1130–1143. https://doi.org/10.1039/c5ee03887a.
(28) Yuan, J.; Bi, C.; Wang, S.; Guo, R.; Shen, T.; Zhang, L.; Tian, J. Spray-Coated Colloidal Perovskite Quantum Dot Films for Highly Efficient Solar Cells. *Adv. Funct. Mater.* **2019**, *1906615*, 1–7. https://doi.org/10.1002/adfm.201906615.
(29) Klein, E.; Lesyuk, R.; Klinke, C. Insights into the Formation Mechanism of Two-Dimensional Lead Halide Nanostructures. *Nanoscale* **2018**, *10* (9), 4442–4451. https://doi.org/10.1039/c7nr09564c.
(30) Heo, J. H.; Lee, M. H.; Jang, M. H.; Im, S. H. Highly Efficient CH3NH3PbI3−xClx Mixed Halide Perovskite Solar Cells Prepared by Re-Dissolution and Crystal Grain Growth via Spray Coating. *J. Mater. Chem. A* **2016**, *4* (45), 17636–17642. https://doi.org/10.1039/c6ta06718b.
(31) Park, M.; Cho, W.; Lee, G.; Hong, S. C.; Kim, M. cheol; Yoon, J.; Ahn, N.; Choi, M. Highly Reproducible Large-Area Perovskite Solar Cell Fabrication via Continuous Megasonic Spray Coating of CH3NH3PbI3 (SI). *Small* **2019**, *15* (1). https://doi.org/10.1002/smll.201804005.
(32) Chou, Y. S.; Chou, L. H.; Guo, A. Z.; Wang, X. F.; Osaka, I.; Wu, C. G.; Liu, C. L. Ultrasonic Spray-Coated Mixed Cation Perovskite Films and Solar Cells. *ACS Sustain. Chem. Eng.* **2019**, *7* (16), 14217–14224. https://doi.org/10.1021/acssuschemeng.9b03058.
(33) D'Innocenzo, V.; Srimath Kandada, A. R.; De Bastiani, M.; Gandini, M.; Petrozza, A. Tuning the Light Emission Properties by Band Gap Engineering in Hybrid Lead Halide Perovskite. *J. Am. Chem. Soc.* **2014**, *136* (51), 17730–17733. https://doi.org/10.1021/ja511198f.
(34) Isikgor, F. H.; Li, B.; Zhu, H.; Xu, Q.; Ouyang, J. High Performance Planar Perovskite Solar Cells with a Perovskite of Mixed Organic Cations and Mixed Halides, MA1-XFAxPbI3-YCly. *J. Mater. Chem. A* **2016**, *4* (32), 12543–12553. https://doi.org/10.1039/c6ta03381d.
(35) Bush, K. A.; Frohna, K.; Prasanna, R.; Beal, R. E.; Leijtens, T.; Swifter, S. A.; McGehee, M. D. Compositional Engineering for Efficient Wide Band Gap Perovskites with Improved Stability to Photoinduced Phase Segregation. *ACS Energy Lett.* **2018**, *3* (2), 428–435. https://doi.org/10.1021/acsenergylett.7b01255.
(36) Jošt, M.; Köhnen, E.; Morales-Vilches, A. B.; Lipovšek, B.; Jäger, K.; Macco, B.; Al-Ashouri, A.; Krč, J.; Korte, L.; Rech, B.; et al. Textured Interfaces in Monolithic Perovskite/Silicon Tandem Solar Cells: Advanced Light Management for Improved Efficiency and Energy Yield. *Energy Environ. Sci.* **2018**, *11* (12), 3511–3523. https://doi.org/10.1039/c8ee02469c.
(37) Jacobs, D. A.; Langenhorst, M.; Sahli, F.; Richards, B. S.; White, T. P.; Ballif, C.; Catchpole, K. R.; Paetzold, U. W. Light Management: A Key Concept in High-Efficiency Perovskite/Silicon Tandem

Photovoltaics. *J. Phys. Chem. Lett.* **2019**, *10* (11), 3159–3170. https://doi.org/10.1021/acs.jpclett.8b03721.

(38) Aydin, E.; Allen, T. G.; Bastiani, M. De; Xu, L.; Ávila, J.; Salvador, M.; Kerschaver, E. Van; Wolf, S. De. Interplay between Temperature and Bandgap Energies on the Outdoor Performance of Perovskite/Silicon Tandem Solar Cells. *Nat. Energy* **2020**. https://doi.org/10.1038/s41560-020-00687-4.

(39) Lamberti, F.; Litti, L.; De Bastiani, M.; Sorrentino, R.; Gandini, M.; Meneghetti, M.; Petrozza, A. High-Quality, Ligands-Free, Mixed-Halide Perovskite Nanocrystals Inks for Optoelectronic Applications. *Advanced Energy Materials*. 2017, pp 1601703–1601707. https://doi.org/10.1002/aenm.201601703.

(40) Castro-Méndez, A. F.; Hidalgo, J.; Correa-Baena, J. P. The Role of Grain Boundaries in Perovskite Solar Cells. *Adv. Energy Mater.* **2019**, *9* (38), 1901489–1901498. https://doi.org/10.1002/aenm.201901489.

(41) Jaysankar, M.; Raul, B. A. L.; Bastos, J.; Burgess, C.; Weijtens, C.; Creatore, M.; Aernouts, T.; Kuang, Y.; Gehlhaar, R.; Hadipour, A.; et al. Minimizing Voltage Loss in Wide-Bandgap Perovskites for Tandem Solar Cells. *ACS Energy Lett.* **2019**, *4* (1), 259–264. https://doi.org/10.1021/acsenergylett.8b02179.

(42) Hoke, E. T.; Slotcavage, D. J.; Dohner, E. R.; Bowring, A. R.; Karunadasa, H. I.; McGehee, M. D. Reversible Photo-Induced Trap Formation in Mixed-Halide Hybrid Perovskites for Photovoltaics. *Chem. Sci.* **2015**, *6* (1), 613–617. https://doi.org/10.1039/c4sc03141e.

(43) ExactaCoat | Sono-Tek https://www.sono-tek.com/product/exactacoat/.

(44) Kelly, A. G. Printed Electronics from Solution-Processed 2D Materials, School of Physics, Trinity College Dublin, 2018.

(45) Parramon, J. M.; Ferron, M. *The Big Book of Airbrush Technique and Materials - Vol. 1*; Watson-Guptill, Ed.; 1994.

(46) How Ultrasonic Nozzles Work |Sono-Tek https://www.sono-tek.com/ultrasonic-coating/how-ultrasonic-nozzles-work/.

(47) Gittens, G. J. Variation of Surface Tension of Water with Temperature. *J. Colloid Interface Sci.* **1969**, *30* (3), 406–412. https://doi.org/10.1016/0021-9797(69)90409-3.

(48) Homola, T.; Shekargoftar, M.; Pospíšil, J. Atmospheric Plasma Treatment of ITO Thin Films for Rapid Manufacturing of Perovskite Solar Cells. *NANOCON Conf. Proc. - Int. Conf. Nanomater.* **2020**, 43–47. https://doi.org/10.37904/NANOCON.2019.8645.

(49) Lok, B. K.; Ng, P. Y.; Hu, X.; Low, H. P. Effect of Plasma Treated ITO Substrate on Inkjet Printing of Conductive Ink. *8th Electron. Packag. Technol. Conf.* **2006**, 154–160. https://doi.org/10.1109/EPTC.2006.342708.

(50) Kim, J. S.; Friend, R. H.; Cacialli, F. Surface Energy and Polarity of Treated Indium–Tin–Oxide Anodes for Polymer Light-Emitting Diodes Studied by Contact-Angle Measurements. *J. Appl. Phys.* **1999**, *86* (5), 2779–2785. https://doi.org/10.1063/1.371124.

(51) Leguy, A. M. A.; Hu, Y.; Campoy-Quiles, M.; Alonso, M. I.; Weber, O. J.; Azarhoosh, P.; Van Schilfgaarde, M.; Weller, M. T.; Bein, T.; Nelson, J.; et al. Reversible Hydration of CH3NH3PbI3 in Films, Single Crystals, and Solar Cells. *Chem. Mater.* **2015**, *27* (9), 3397–3407. https://doi.org/10.1021/acs.chemmater.5b00660.

(52) Docampo, P.; Bein, T. A Long-Term View on Perovskite Optoelectronics. *Acc. Chem. Res.* **2016**, *49*, 339–346. https://doi.org/10.1021/acs.accounts.5b00465.

(53) Huang, J.; Tan, S.; Lund, P. D.; Zhou, H. Impact of H2O on Organic-Inorganic Hybrid Perovskite Solar Cells. *Energy Environ. Sci.* **2017**, *10*, 2284–2311. https://doi.org/10.1039/c7ee01674c.

(54) Li, H.; Zhang, W. Perovskite Tandem Solar Cells: From Fundamentals to Commercial Deployment. *Chem. Rev.* **2020**, *120* (18), 9835–9950. https://doi.org/10.1021/acs.chemrev.9b00780.

(55) Jošt, M.; Kegelmann, L.; Korte, L.; Albrecht, S. Monolithic Perovskite Tandem Solar Cells: A Review of the Present Status and Advanced Characterization Methods Toward 30% Efficiency. *Adv. Energy Mater.* **2020**, *10* (26). https://doi.org/10.1002/aenm.201904102.

(56) Krishnan, U. Factors Affecting the Stability of Perovskite Solar Cells: A Comprehensive Review. *J. Photonics Energy* **2019**, *9* (02), 1. https://doi.org/10.1117/1.jpe.9.021001.

(57) Kim, M.; Ham, S.; Cheng, D.; Wynn, T. A.; Jung, H. S.; Meng, Y. S. Advanced Characterization

Techniques for Overcoming Challenges of Perovskite Solar Cell Materials. *Adv. Energy Mater.* **2020**, *2001753*, 1–26. https://doi.org/10.1002/aenm.202001753.

(58) Farooq, A.; Khan, M. R.; Abzieher, T.; Voigt, A.; Lupascu, D. C.; Lemmer, U.; Richards, B. S.; Paetzold, U. W. Photodegradation of Triple-Cation Perovskite Solar Cells: The Role of Spectrum and Bias Conditions. *ACS Appl. Energy Mater.* **2021**, *4*, 3083–3092. https://doi.org/10.1021/acsaem.0c02813.

(59) Graint San, Michal Balber, Jedrzej Jedrzejewski, and I. B. The Phototransport in Halide Perovskites: From Basic Physics to Applications. *J. Appl. Phys.* **2020**, *127*, 085013. https://doi.org/10.1063/1.5095190.

(60) Knight, A. J.; Patel, J. B.; Snaith, H. J.; Johnston, M. B.; Herz, L. M. Trap States, Electric Fields, and Phase Segregation in Mixed-Halide Perovskite Photovoltaic Devices. *Adv. Energy Mater.* **2020**, *10* (9), 1–11. https://doi.org/10.1002/aenm.201903488.

(61) Stolterfoht, M.; Le Corre, V. M.; Feuerstein, M.; Caprioglio, P.; Koster, L. J. A.; Neher, D. Voltage-Dependent Photoluminescence and How It Correlates with the Fill Factor and Open-Circuit Voltage in Perovskite Solar Cells. *ACS Energy Lett.* **2019**, *4* (12), 2887–2892. https://doi.org/10.1021/acsenergylett.9b02262.

(62) Da, Y.; Xuan, Y.; Li, Q. Quantifying Energy Losses in Planar Perovskite Solar Cells. *Sol. Energy Mater. Sol. Cells* **2018**, *174*, 206–213. https://doi.org/10.1016/J.SOLMAT.2017.09.002.

(63) Jošt, M.; Matič, G.; Köhnen, E.; Li, B.; Glažar, B.; Jankovec, M.; Albrecht, S.; Topič, M. Subcell Operation and Long-Term Stability Analysis of Perovskite-Based Tandem Solar Cells Using a Bichromatic Light Emitting Diode Light Source. *Sol. RRL* **2021**, *2100311*. https://doi.org/10.1002/solr.202100311.

(64) Blaga, C.; Christmann, G.; Boccard, M.; Ballif, C.; Nicolay, S.; Kamino, B. A. Palliating the Efficiency Loss Due to Shunting in Perovskite/Silicon Tandem Solar Cells through Modifying the Resistive Properties of the Recombination Junction. *Sustain. Energy Fuels* **2021**, *5* (7), 2036–2045. https://doi.org/10.1039/D1SE00030F.

(65) Köhnen, E.; Jošt, M.; Morales-Vilches, A. B.; Tockhorn, P.; Al-Ashouri, A.; Macco, B.; Kegelmann, L.; Korte, L.; Rech, B.; Schlatmann, R.; et al. Highly Efficient Monolithic Perovskite Silicon Tandem Solar Cells: Analyzing the Influence of Current Mismatch on Device Performance. *Sustain. Energy Fuels* **2019**, *3* (8), 1995–2005. https://doi.org/10.1039/c9se00120d.

(66) Wu, N.; Wu, Y.; Walter, D.; Shen, H.; Duong, T.; Grant, D.; Barugkin, C.; Fu, X.; Peng, J.; White, T.; et al. Identifying the Cause of Voltage and Fill Factor Losses in Perovskite Solar Cells by Using Luminescence Measurements. *Energy Technol.* **2017**, *5* (10), 1827–1835. https://doi.org/10.1002/ENTE.201700374.

(67) Equivalent circuit calculator |PV Lighthouse https://www.pvlighthouse.com.au/equivalent-circuit.

(68) Aydin, E.; De Bastiani, M.; Yang, X.; Sajjad, M.; Aljamaan, F.; Smirnov, Y.; Hedhili, M. N.; Liu, W.; Allen, T. G.; Xu, L.; et al. Zr-Doped Indium Oxide (IZRO) Transparent Electrodes for Perovskite-Based Tandem Solar Cells. *Adv. Funct. Mater.* **2019**, *29* (25), 1–10. https://doi.org/10.1002/adfm.201901741.

(69) Bastiani, M. De; Mirabelli, A. J.; Hou, Y.; Gota, F.; Aydin, E.; Allen, T. G.; Troughton, J.; Subbiah, A. S.; Isikgor, F. H.; Liu, J.; et al. Efficient Bifacial Monolithic Perovskite/Silicon Tandem Solar Cells via Bandgap Engineering. *Nat. Energy* **2021**, *6*, 167–175. https://doi.org/10.1038/s41560-020-00756-8.

(70) Rietwyk, K. J.; Tan, B.; Surmiak, A.; Lu, J.; McMeekin, D. P.; Raga, S. R.; Duffy, N.; Bach, U. Light Intensity Modulated Photoluminescence for Rapid Series Resistance Mapping of Perovskite Solar Cells. *Nano Energy* **2020**, *73* (March), 104755. https://doi.org/10.1016/j.nanoen.2020.104755.

(71) Wolff, C. M.; Caprioglio, P.; Stolterfoht, M.; Neher, D. Nonradiative Recombination in Perovskite Solar Cells: The Role of Interfaces. *Adv. Mater.* **2019**, *31*, 1902762–1902781. https://doi.org/10.1002/adma.201902762.

(72) Dequilettes, D. W.; Frohna, K.; Emin, D.; Kirchartz, T.; Bulovic, V.; Ginger, D. S.; Stranks, S. D. Charge-Carrier Recombination in Halide Perovskites. *Chem. Rev.* **2019**, *119* (20), 11007–11019. https://doi.org/10.1021/acs.chemrev.9b00169.

(73) Muhammad, F. F.; Yahya, M. Y.; Hameed, S. S.; Aziz, F.; Sulaiman, K.; Rasheed, M. A.; Ahmad, Z. Employment of Single-Diode Model to Elucidate the Variations in Photovoltaic Parameters under Different Electrical and Thermal Conditions. *PLoS One* **2017**, 1–20.

https://doi.org/10.1371/journal.pone.0182925.
(74) Cheng, Y.; Peng, Y.; Jen, A. K.-Y.; Yip, H.-L. Development and Challenges of Metal Halide Perovskite Solar Modules. *Sol. RRL* **2021**, 2100560. https://doi.org/10.1002/SOLR.202100545.
(75) Short-Circuit Current | PVEducation https://www.pveducation.org/pvcdrom/solar-cell-operation/short-circuit-current.
(76) Wang, Z.; Lin, Q.; Chmiel, F. P.; Sakai, N.; Herz, L. M.; Snaith, H. J. Efficient Ambient-Air-Stable Solar Cells with 2D–3D Heterostructured Butylammonium-Caesium- Formamidinium Lead Halide Perovskites. *Nat. Energy* **2017**, *2*. https://doi.org/10.1038/nenergy.2017.135.
(77) Gutierrez-Partida, E.; Hempel, H.; Caicedo-Dávila, S.; Raoufi, M.; Peña-Camargo, F.; Grischek, M.; Gunder, R.; Diekmann, J.; Caprioglio, P.; Brinkmann, K. O.; et al. Large-Grain Double Cation Perovskites with 18μs Lifetime and High Luminescence Yield for Efficient Inverted Perovskite Solar Cells. *ACS Energy Lett.* **2021**, *6*, 1045–1054.
(78) Dhass, A. D.; Natarajan, E.; Lakshmi, P. Influence of Shunt Resistance on the Performance of Solar Photovoltaic Cell. *2012 Int. Conf. Emerg. Trends Electr. Eng. Energy Manag.* **2012**, 382–386. https://doi.org/10.1109/ICETEEEM.2012.6494522.
(79) Lombardero, I.; Algora, C. Impact of Shunt Resistance on the Assessment of Multijunction I-V. *AIP Conf. Proc.* **2012**, 060001–060007. https://doi.org/10.1063/1.5053525.
(80) Mahesh, S.; Ball, J. M.; Oliver, R. D. J.; McMeekin, D. P.; Nayak, P. K.; Johnston, M. B.; Snaith, H. J. Revealing the Origin of Voltage Loss in Mixed-Halide Perovskite Solar Cells. *Energy Environ. Sci.* **2020**, *13* (1), 258–267. https://doi.org/10.1039/c9ee02162k.
(81) *Physics of Semiconductor Devices, 3rd Edition | Wiley*; 2006.
(82) Stolterfoht, M.; Caprioglio, P.; Wolff, C. M.; Kegelmann, L.; Amir, Y.; Redinger, A.; Zu, F.; Albrecht, D. S.; Koch, N.; Kirchartz, D. T. The Impact of Energy Alignment and Interfacial Recombination on the Internal and External Open-Circuit Voltage of Perovskite Solar Cells. *Energy Environ. Sci.* **2019**, *12*, 2778–2788. https://doi.org/10.1039/c9ee02020a.
(83) Mora-Seró, I. How Do Perovskite Solar Cells Work? *Joule* **2018**, *2* (4), 585–587. https://doi.org/10.1016/j.joule.2018.03.020.
(84) Zhou, Z.; Wang, Z.; Zhou, Y.; Pang, S.; Wang, D.; Xu, H.; Liu, Z.; Padture, N. P.; Cui, G. Methylamine-Gas-Induced Defect-Healing Behavior of CH3NH3PbI3 Thin Films for Perovskite Solar Cells. *Angew. Chemie - Int. Ed.* **2015**, *54* (33), 9705–9709. https://doi.org/10.1002/ANIE.201504379.
(85) Brenes, R.; Guo, D.; Osherov, A.; Noel, N. K.; Eames, C.; Hutter, E. M.; Pathak, S. K.; Niroui, F.; Friend, R. H.; Islam, M. S.; et al. Metal Halide Perovskite Polycrystalline Films Exhibiting Properties of Single Crystals. *Joule* **2017**, *1* (1), 155–167. https://doi.org/10.1016/j.joule.2017.08.006.
(86) Wang, F.; Bai, S.; Tress, W.; Hagfeldt, A.; Gao, F. Defects Engineering for High-Performance Perovskite Solar Cells. *npj Flex. Electron.* **2018**, *2* (22), 1–14. https://doi.org/10.1038/s41528-018-0035-z.
(87) Hou, W.; Xiao, Y.; Han, G.; Qin, C.; Xiao, L.; Chang, Y.; Li, H. Dimethyl Sulfoxide and Bromide Methylamine Co-Treatment Inducing Defect Healing for Effective and Stable Perovskite Solar Cells. *Mater. Res. Bull.* **2019**, *112* (December 2018), 165–173. https://doi.org/10.1016/j.materresbull.2018.12.013.
(88) Guo, F.; He, W.; Qiu, S.; Wang, C.; Liu, X.; Forberich, K.; Brabec, C. J.; Mai, Y. Sequential Deposition of High-Quality Photovoltaic Perovskite Layers via Scalable Printing Methods. *Adv. Funct. Mater.* **2019**, *29* (24), 1900964–1900972. https://doi.org/10.1002/ADFM.201900964.
(89) Yang, J. A.; Qin, T.; Xie, L.; Liao, K.; Li, T.; Hao, F. Methylamine-Induced Defect-Healing and Cationic Substitution: A New Method for Low-Defect Perovskite Thin Films and Solar Cells. *J. Mater. Chem. C* **2019**, *7* (35), 10724–10742. https://doi.org/10.1039/c9tc03490k.
(90) Subhan, F. E.; Aimal, A.; Khan, D.; Daud Khan, A.; Ullah, N.; Imran, M.; Noman, M. Optical Optimization of Double-Side-Textured Monolithic Perovskite-Silicon Tandem Solar Cells for Improved Light Management. *RSC Adv.* **2020**, *10*, 26631–26638. https://doi.org/10.1039/d0ra04634e.

Chapter 6

Synthesis of $CsPbBr_3$ Nanocrystals by Laser Ablation in Alcohol for More Sustainable Perovskite-based Optoelectronics

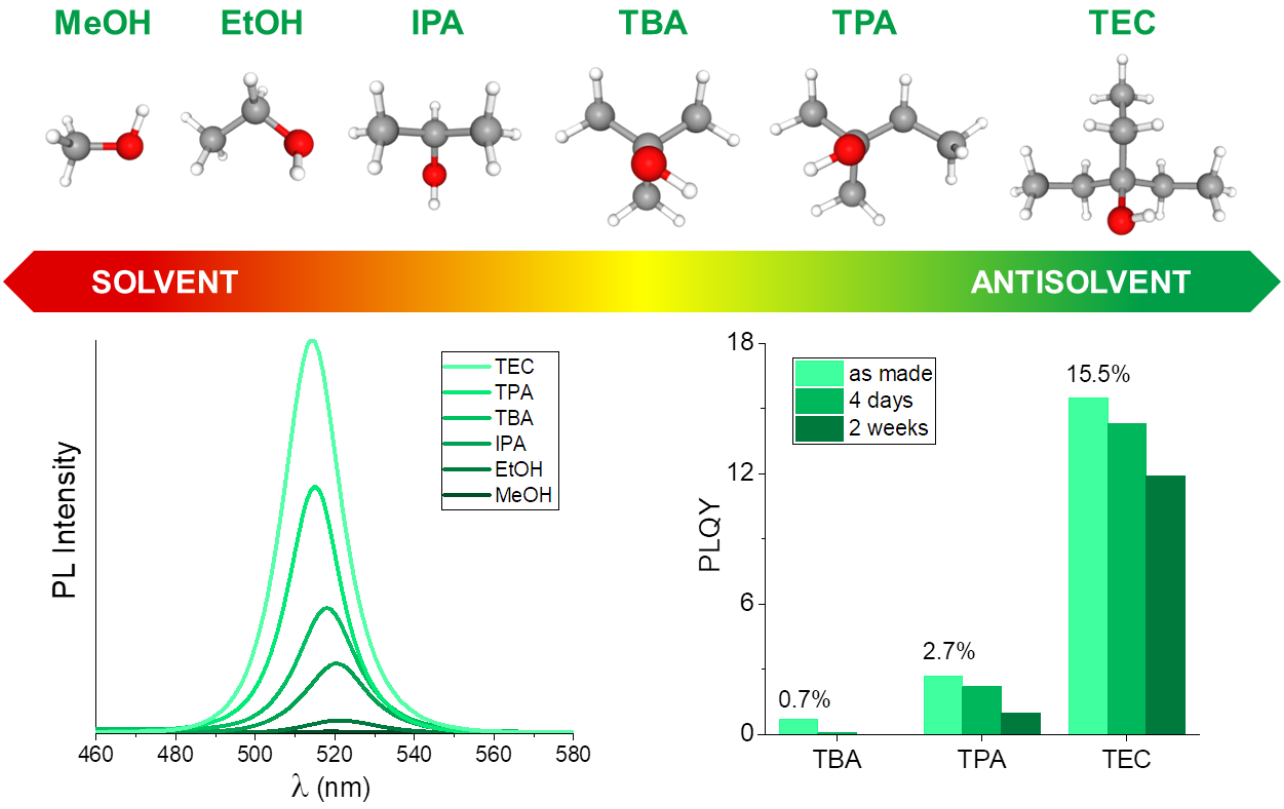

Under submission to ACS Sustain. Chem. & Eng.

6. Synthesis of $CsPbBr_3$ Nanocrystals by Laser Ablation in Alcohol for More Sustainable Perovskite-based Optoelectronics[1]

6.1 The Aim of The Project

As reported in Section 1.3, lead halide perovskite nanocrystals have attracted great attention in the last years, finding application in a variety of optoelectronic devices like light-emitting diodes, solar cells, white phosphors, solar concentrators, transistors, photo- and X-ray detectors, gas sensors, and quantum information.[2–11] In addition, the low cost of the perovskite precursor salts contributed to the substantial commercial appeal recently gained by perovskite-based optoelectronics. However, the commercial attraction of a new material is also influenced by the synthetic method employed for its production. The most widely used approach to produce perovskite NCs in solution is the high-temperature, in-vacuum "hot-injection" synthesis, which is challenging to scale up (Section 1.2.1).[12–14] Far more economically attractive proposals are represented by room temperature processes, performed without environmental control.[15–19] Furthermore, the identification of suitable green solvents and deposition methods for large-scale processing are other relevant aspects to consider.[20–23]

In the last decade, many large pharmaceutical and chemical firms have conducted several solvent selections based on environmental, health and safety (EHS) evaluations, which have been evaluated and collected by researcher to create unified guides.[24–26] This sensitivity towards sustainable chemical processes led to the creation of the innovative medicines initiative (IMI)-CHEM21 selection guide,[27] which has been consulted for the solvent selection of this work. Beyond scalability and sustainability of the synthetic processes, low-dimensionality and colloidal stability of perovskite NCs solutions (referred to as "inks") are fundamental to get stable and high-emissive inks. The former enhances the PLQY, a parameter which could help light-emitting applications, due to the spatial charge confinement afforded by nanocrystals dimension.[28,29] The latter is usually maintained by a shell of organic ligands, whose binding groups interactions with the nanocrystals surface are crucial both to colloidal stability as well as surface defect passivation.[30–33] However, the conductivity of perovskite NCs is strongly affected by the length and branching of the ligand tails when deposited as thin films to implement in optoelectronic devices.[34,35] Despite short-chain liquid- and solid-state ligand-exchange procedures have been proposed to overcome this issue,[36–38] the low stability of

lead halide perovskite nanocrystals in such post-synthetic processes still hinders their effectiveness and further complicate the integration of conductive layer to implement in optoelectronics.[33,39–42]

As recalled in the previous chapters, laser ablation synthesis in solution (LASiS) has proven to be a viable ligand-free, top-down method to synthesize lead halide perovskite nanocrystals in ambient conditions.[43–46] In this study, LASiS process was optimized for the synthesis of all-inorganic cesium lead tribromide ($CsPbBr_3$) perovskite NCs in eco-sustainable solvents. The effects of different commercially available branched aliphatic alcohols on the optical and morphological properties of $CsPbBr_3$ nanocrystals colloidal solutions were investigated. Although alcohols are usually found to be not beneficial for perovskite NCs in traditional bottom-up synthesis,[47–49] in this work it was demonstrated how high-emissive $CsPbBr_3$ nanocrystals can be obtained by opportunely selecting the dielectric constant and polarity of the alcohol employed for the synthesis. In addition, the lower surface tension (i.e., good wettability) and higher vapor pressure of alcohols compared to traditional high boiling toxic solvents used for LHP processing could be exploited in sustainable and fast roll-to roll compatible solution processing.[50–52] Finally, LASiS approach was investigated in other eco-friendly perovskite antisolvents, including acetates and anisole.

6.2 Results and Discussion

6.2.1 *The Choice of the Solvents to Employ for the Synthesis*

EHS guidelines were followed to select the green solvents to employ for LASiS,[24–27] and the most relevant physicochemical solvent properties for perovskite synthesis/processing were evaluated too (Figure 6.1).[22,53–58] In addition, dielectric constant and relative polarity were considered as main parameters when the solvent- or the antisolvent-like behavior towards the lead halide perovskite nanocrystals were considered.[59–67] The Innovative Medicines Initiative (IMI)-CHEM21 partnership,[27] a European consortium which promotes sustainable biological and chemical methodologies, has recently classified alcohols as recommended solvent to use due to their low impact on both human health and environment. Moreover, this class of solvents allows to investigate a wide range of dielectric constant and polarity values, moving from the solvent- to antisolvent-regime (Figure 6.2). For these reasons, methanol (MeOH), ethanol (EtOH), isopropanol (IPA), tert-butanol (TBA), tert-pentanol (TPA) and triethyl carbinol (TEC) aliphatic alcohols were selected as non-hazardous solvents to use for the synthesis of all-inorganic $CsPbBr_3$ NCs colloidal solutions. Such perovskite NCs were obtained by two different approaches, namely “2-step” and “in-situ” conversions.

	SAFETY & HEALTH			INK PROCESSABILITY			INTERACTION w. PEROVSKITE			
SOLVENT	BP (°C)	FP (°C)	TLV (ppm)	η (mPa·s, 25°C)	P_V (kPa, 25°C)	σ (dyn/cm, 20°C)	Relative polarity	ε (20°C)	D_N (kcal/mol)	USED IN THIS WORK
Acetonitrile	82	6	20	0.36	11.83	29.1	0.460	38.0	14.1	
γ-Butyrolactone	204	98	20	1.75	0.06	44.6	0.420	41.0	17.8	
N,N-Dimethylformammide	153	58	10	0.79	0.52	36.4	0.386	36.1	26.6	
N,N-Dimethylpropyleneurea	246	120	20	3.41	0.20	41.0	0.350	36.1	33.0	
1,3-dimethyl-2-imidazolidinone	222	114	20	1.43	<0.1	41.0	0.352	37.6	27.7	
Dimethyl sulfoxide	189	95	50	1.98	0.08	43.5	0.444	45.0	29.8	
N-metil-2-pirrolidone	202	91	20	1.65	0.05	40.7	0.355	32.8	27.3	
Anisole	154	43	10	0.79	0.47	35.0	0.198	4.3	9.0	x
Chlorobenzene	132	23	10	0.81	1.60	33.5	0.188	5.6	10.0	
Chloroform	61	/	10	0.54	26.27	27.2	0.259	4.8	4.0	
Ethyl acetate	77	- 4	400	0.43	12.43	23.8	0.228	6.0	17.1	x
Butyl acetate	126	22	200	0.74	1.53	25.1	0.178	5.1	15.0	x
Diethyl ether	35	- 45	400	0.22	70.92	17.0	0.120	4.3	19.2	
Toluene	111	4	20	1.17	3.79	28.4	0.099	2.4	0.1	
Methanol	65	12	200	0.54	16.93	22.5	0.762	32.6	19.0	x
Ethanol	78	13	1000	1.07	7.91	22.4	0.654	24.5	19.2	x
Isopropanol	82	12	400	2.04	6.05	21.8	0.546	19.9	21.1	x
tert-Butanol	82	11	100	3.77	5.43	20.7	0.389	10.9	21.9	x
tert-Pentanol	102	20	200	3.79	2.22	23.6	0.318	5.8	>22	x
Triethylcarbinol	143	38	100	>3.85	0.24	26.9	0.290	3.2	>23	x
Water	100	/	/	0.89	3.17	72.8	1.000	81.0	33.0	

Figure 6.1 Solvent evaluation based on EHS guidelines.[53,54] The table reports the main physicochemical properties of commonly used perovskite solvents (red) and antisolvents (blue), as well as those of alcohols used in this work (green). Solvent properties were classified based on their impact on safety and health, ink processability and their interaction with metal halide perovskite materials (boiling point BP, flash point FP, threshold limit value TLV,[55,56] viscosity η, vapor pressure P_V, surface tension σ, dielectric constant ε, donor number D_N [57,58]). Ranges of values were reported when no reference parameters have been identified in literature.

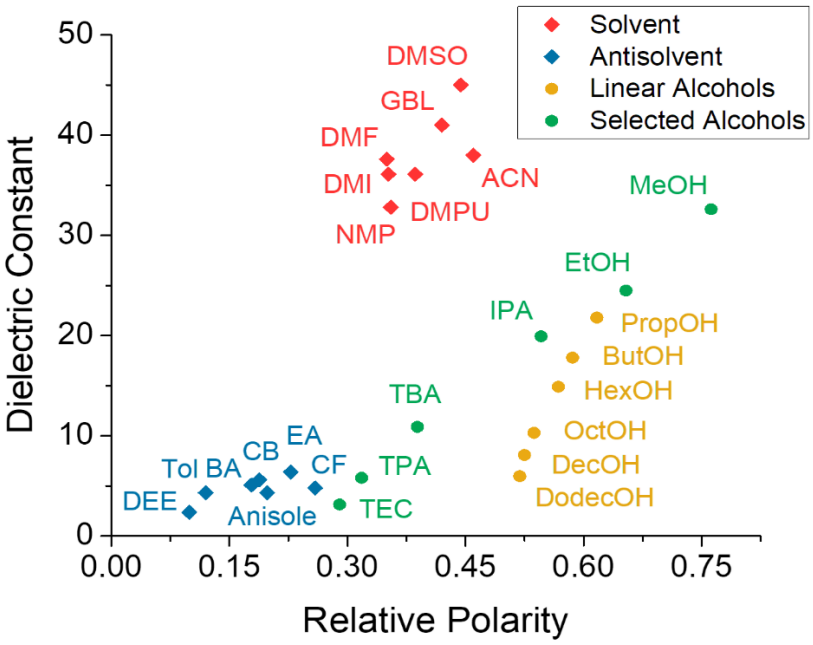

Figure 6.2 Graph reporting the dielectric constant as a function of relative polarity of most used solvents (red) and antisolvents (blue) for lead halide perovskite synthesis. It is noticeable that, contrary to linear chain alcohols (yellow), the use of branched alcohols (green) enables to reach low values of both dielectric constant and polarity.

6.2.2 *Perovskite Nanocrystals by Two-Step Conversion*

$CsPbBr_3$ perovskite NCs by "2-step conversion" approach were obtained by producing $PbBr_2$ precursors NCs solutions via laser ablation in alcohol at first, then converted into perovskite NCs by adding equimolar (i.e., 1:1 molar ratio) CsBr solutions in EtOH. Ethanol was chosen as solvent to use for all conversions (both "2-step" and "in-situ" ones) due to the poor solubility of CsBr in less polar alcohols. More details regarding the 2-step synthesis are reported in the Section 6.5.2. Following the trend reported in Figure 6.2, the best results were obtained using TPA and TEC, the alcohols with the lowest polarity and dielectric constant (i.e., having the most antisolvent-like behavior) among those investigated.[67] In these alcohols, $CsPbBr_3$ NCs with good optical and morphological properties were produced, showing sharp $CsPbBr_3$ perovskite excitonic peaks around 520 nm in the UV-Vis spectra (Figure 6.3 a). Narrow and intense PL emission peaks were registered in the steady-state PL measurements, having full width at half maximum (FWHM) of 18 and 16.5 nm for TPA and TEC samples, respectively.

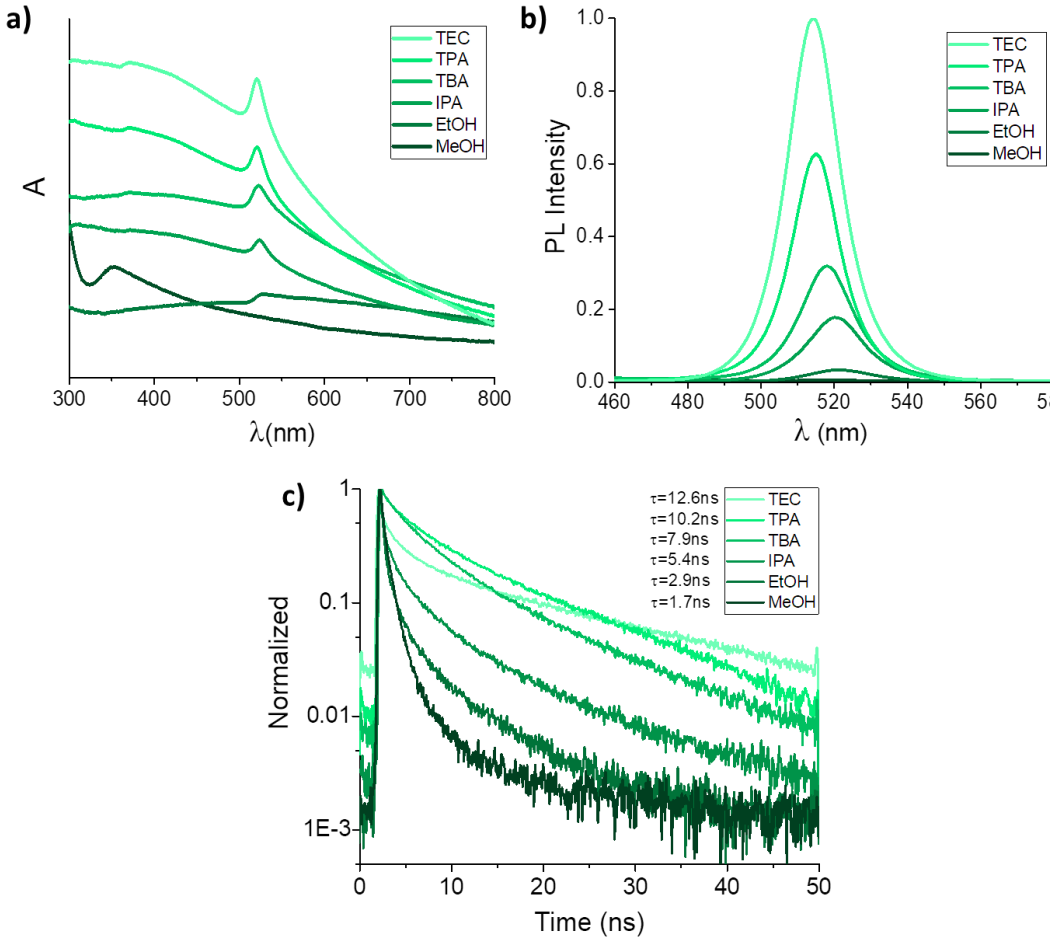

Figure 6.3 Optical properties of $CsPbBr_3$ NCs synthesized by "2-step conversion" in different alcohols. a) UV-Vis spectra, b) steady-state PL measurements, and c) time-resolved PL decays. The reported intensity-averaged lifetimes were estimated by three-exponential fit.

As previously reported for these perovskite NCs,[47,68–70] PL average lifetimes were calculated by three-exponential fit of the TRPL decays, equal to 10.2 and 12.6 ns for TPA and TEC samples, respectively (Figure 6.3 b,c). More details regarding TRPL decays fit are reported in Section 6.5.3. The orthorhombic $CsPbBr_3$ crystal phase was identified in XRD patterns of both samples, without contributes associated with unreacted precursors and/or non-perovskite phases (Figure 6.4 a).[71,72] Cubic-shaped NCs with average size of 120−200 nm were observed in TEM images (Figure 6.4 b).

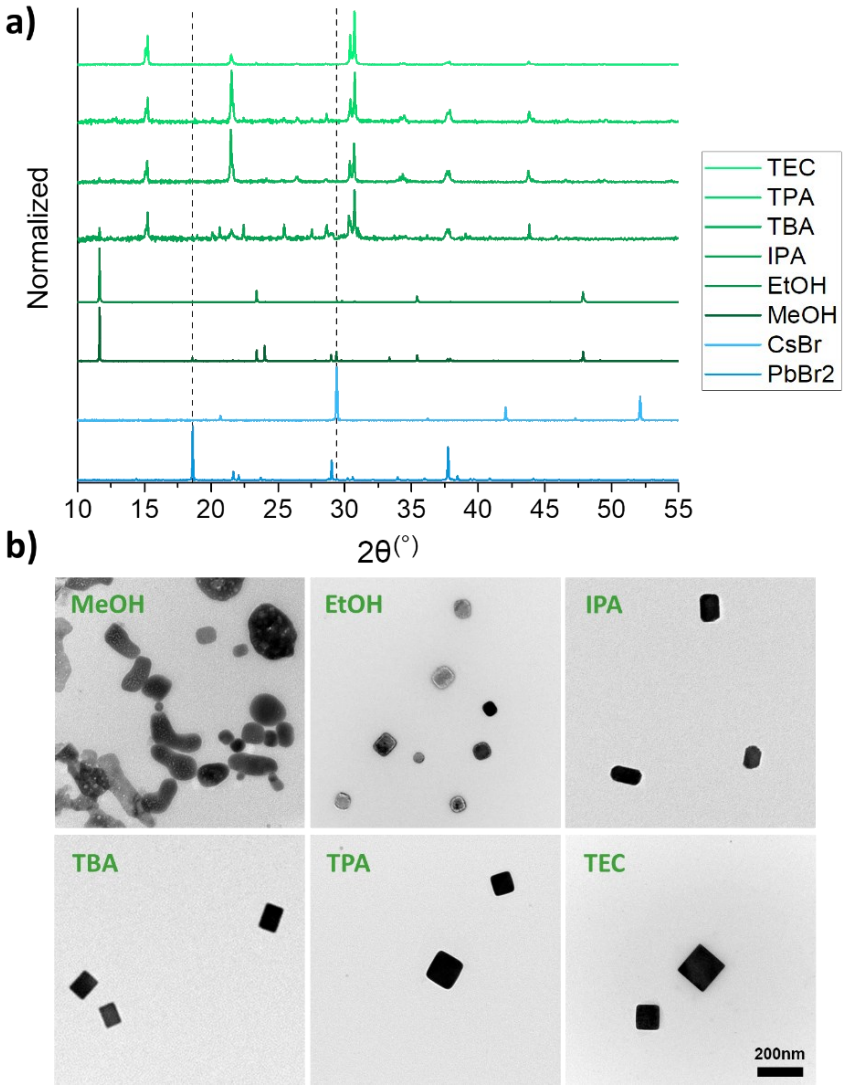

Figure 6.4 a) XRD patterns of $CsPbBr_3$ NCs synthesized by LASiS in different in alcohols. Diffractograms of $PbBr_2$ NCs by LASiS in alcohol and CsBr powders are also reported. b) TEM images of CsPbBr3 NCs synthesized by "2-step conversion" in different alcohols. Nanoparticles with more amorphous shapes are observed in alcohols with higher polarity and dielectric constants (i.e., methanol and ethanol), while cubic-shaped nanocrystals are obtained in alcohols with a more antisolvent-like behavior (i.e., tert-pentanol and triethyl carbinol).

Moreover, a good colloidal stability was observed in $CsPbBr_3$ nanocrystals in TPA and TEC alcohols despite the absence of any ligands in solution. A zeta potential value of 13.2 and 14.1 mV was measured for perovskite NCs in TPA and TEC, respectively. This positive surface charge of NCs can be attributed to laser-induced surface phenomena. [73,74] In addition, the higher viscosity (η) and donor number (D_N) of TPA and TEC alcohols compared to the antisolvents commonly used for perovskite synthesis (Figure 6.1) help the good colloidal stability of these samples. In fact the former is inversely proportional to the nanoparticles precipitation time in solution,[75] while the latter represents the solvent ability to coordinate Pb^{2+} Lewis's acid and, consequently, to passivate the surface of LHP nanocrystals.[76]

Contrary to TPA and TEC samples, $CsPbBr_3$ perovskite NCs obtained by the "2-step conversion" in MeOH and EtOH, the alcohols with most solvent-like behavior towards LHP phase of the set,[47,67] showed poor optical and morphological properties (a list of abbreviations is reported in an appendix at the end of the dissertation). No perovskite excitonic peaks were observed in their UV-Vis spectra and their emissive properties were very poor (Figure 6.3 a,b). PL emission peaks showed a broader FWHM of about 22 and 21 nm for MeOH and EtOH samples, respectively, and quickly faded after the addition of CsBr solution in EtOH to the $PbBr_2$ NCs. Accordingly, $CsPbBr_3$ NCs conversion struggled to take place in these solvents, showing a fast color change of the solutions from orange (the typical color of these perovskite phase) to milky-transparent in a few tens of seconds. From TRPL decays, average lifetimes of 1.7 and 2.9 ns were calculated for MeOH and EtOH samples, respectively (Figure 6.3 c). TEM analysis showed smaller and amorphous structures compared to TPA and TEC samples (Figure 6.4 b), while reflections in the XRD patterns highlighted the formation of extraneous Cs-Pb-Br phases (e.g., $CsPb_2Br_5$, Cs_4PbBr_6),[77–79] which presence is testified by the reflections at low angles (Figure 6.4 a). The poor properties of $CsPbBr_3$ perovskite NCs solutions in MeOH and EtOH, can be also related to the $PbBr_2$ precursor NCs in the same alcohols, which also showed poor optical and morphological properties (Figure 6.5).[80,81] These observations pointed out that methanol and ethanol are not good candidates for the eco-sustainable synthesis by LASiS of $CsPbBr_3$ NCs colloidal solution. Due to aggregation and precipitation phenomena, it was not possible to estimate the zeta potential values for these samples. $CsPbBr_3$ perovskite NCs obtained by the "2-step conversion" in IPA and TBA showed optical and morphological properties in between the two couples of samples previously discussed, showing rectangular-shaped nanocrystals, PL average lifetimes of 5.4 and 7.9 ns, PL emission peaks having FWHM of 20 and 18.5 nm, and zeta potential values of 11.8 and 13.5 mV, respectively (Figure 6.3 and Figure 6.4).

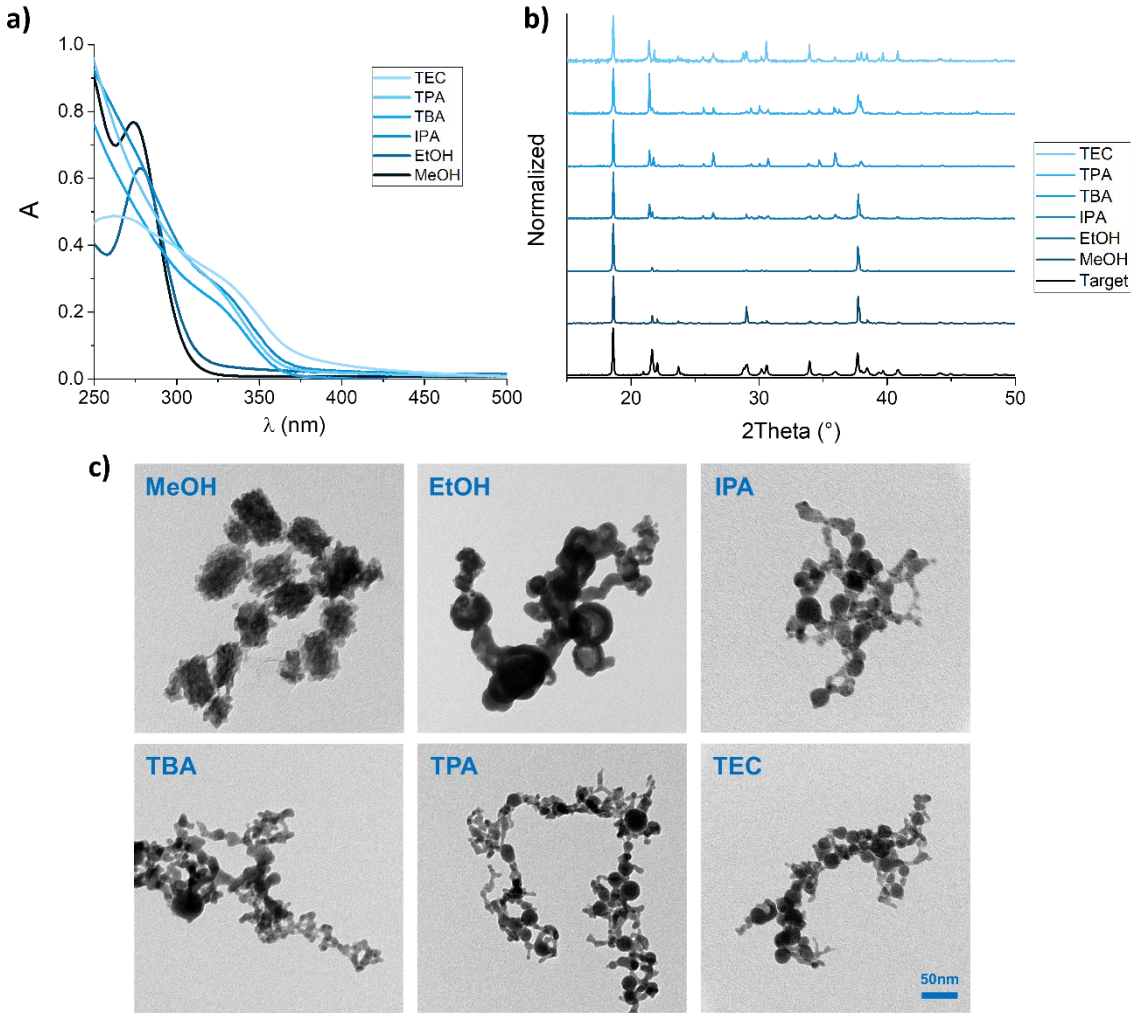

Figure 6.5 Optical and morphological characterization of $PbBr_2$ NCs precursor solutions by LASiS in alcohols. The typical $PbBr_2$ absorption edge at 350 nm can be observed in UV-Vis spectra (a),[84] while peaks around 275 nm in MeOH and EtOH spectra were attributed to bromo-plumbate complexes in solution.[85] The different relative intensities in XRD patterns (b) were ascribed to preferential orientation of the NCs onto the substrate and/or to different NCs morphologies, as noticed by TEM analysis (c).

6.2.3 *Perovskite Nanocrystals by In-Situ Conversion*

The "in-situ conversion" of $CsPbBr_3$ NCs is a direct synthesis of the perovskite NCs during LASiS, which is obtained by mixing the CsBr EtOH solution together with the ablation solvent before the synthesis. The "in-situ conversion" synthesis was not investigated and optimized in MeOH and EtOH since poor results were obtained with $CsPbBr_3$ NCs by "2-step conversion" in such alcohols. Compared to the "2-step" $CsPbBr_3$ NCs in the same alcohols, the "in-situ" ones showed improvements for all parameters. In particular, sharper and more intense perovskite excitonic peaks were observed in the UV-Vis spectra and a significant increase in intensity was noticed in the PL emissions (Figure 6.6 a,b).

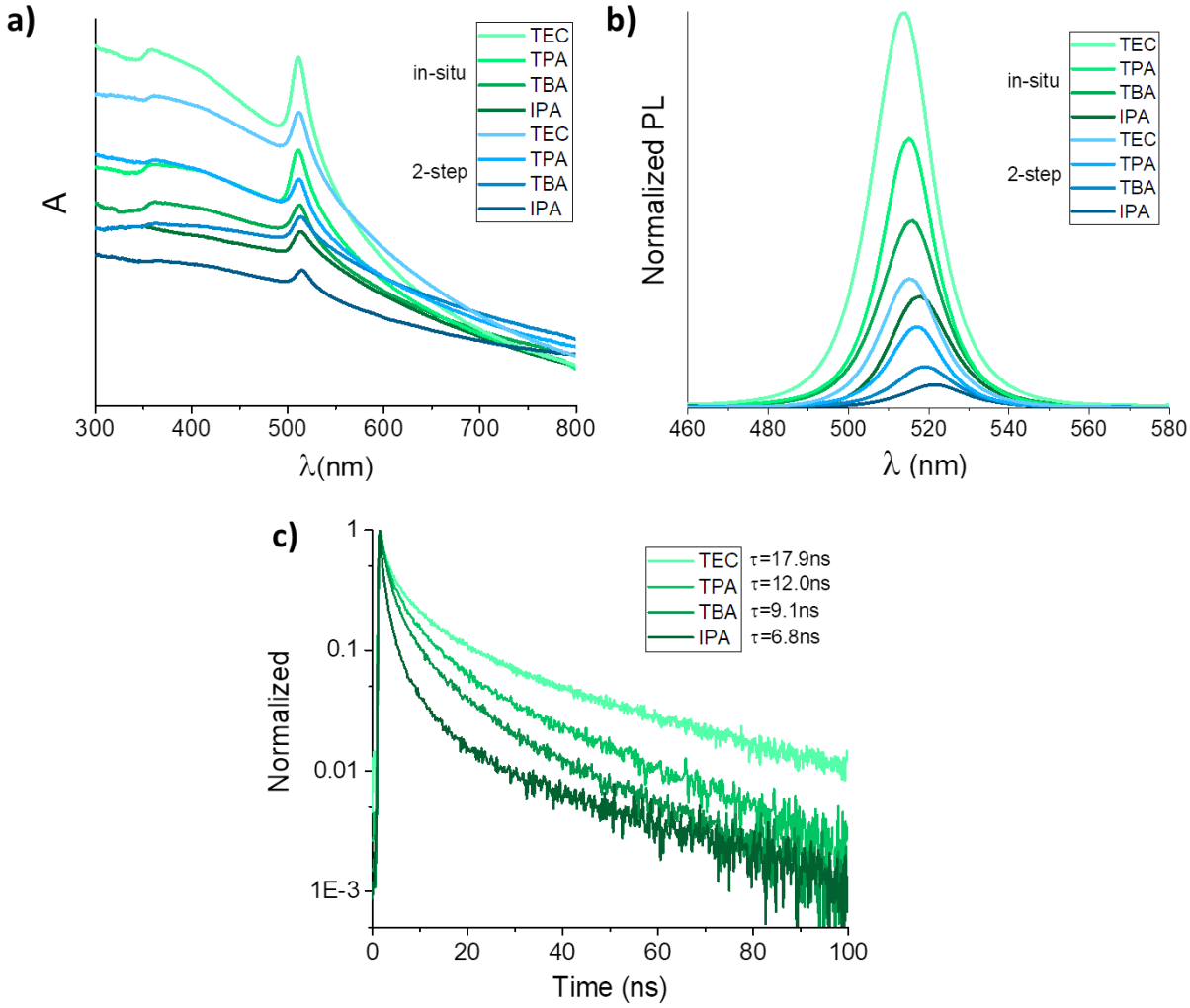

Figure 6.6 Comparison between a) UV-Vis spectra, b) steady-state PL emissions, and c) time-resolved PL decays of $CsPbBr_3$ NCs by "2-step" and "in-situ" conversion in different alcohols. The average lifetimes reported in TRPL decays were calculated by three-exponential fit.

A slight blueshift can be observed in both Abs edge and PL peak positions when compared to those of the respective "2-step" ones (Figure 6.7 a). This observation can be attributed to differences in the NCs size, as reported in previous studies.[43,82] Longer average PL lifetimes, equal to 12.0 and 17.9 ns for the syntheses in TPA and TEC, respectively, were estimated from TRPL measurements (Figure 6.6 c). While the "2-step" samples showed negligible PL quantum yields, a PLQY of 0.7, 2.7 and 15.5% was measured for perovskite NCs by "in-situ conversion" in TBA, TPA and TEC, respectively. Importantly, the latter sample showed a good PLQY stability over several days under ambient conditions, proving the wide time window in which one can process the colloidal solution (Figure 6.7 b).

a)

SOLVENT	Abs_{MAX} (nm)	PL_{MAX} (nm)	FWHM (nm)	τ_1 (ns)	τ_2 (ns)	τ_3 (ns)	τ_{AVG} (ns)
MeOH*	--- ---	522 ---	>22 ---	0.36 ---	1.13 ---	6.09 ---	**1.73** **---**
EtOH	515 ---	522 ---	21 ---	0.49 ---	1.72 ---	8.81 ---	**2.89** **---**
IPA	514 513	521 518	20 19	0.33 0.25	1.93 2.21	9.09 12.13	**5.38** **6.80**
TBA	513 512	519 516	18.5 17.5	0.59 0.31	2.47 3.04	10.34 16.71	**7.92** **9.12**
TPA	511 510	517 515	18 17	0.37 0.34	2.67 3.50	12.90 19.32	**10.18** **12.02**
TEC	510 510	515 514	16.5 16	0.42 0.31	2.74 3.55	16.25 25.22	**12.64** **17.94**

* PL intensity quickly faded right after measurement

b)

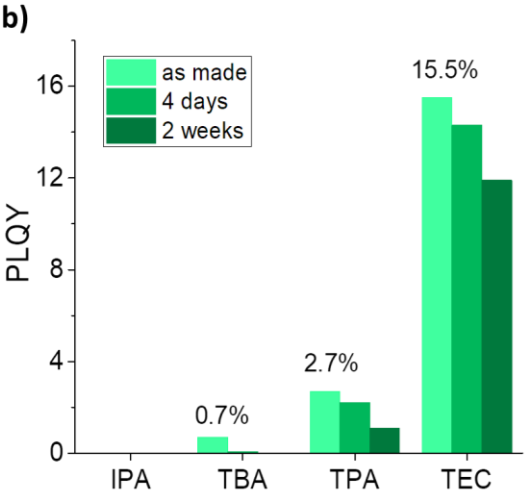

Figure 6.7 a) Table summarizing the results of optical characterizations performed on $CsPbBr_3$ NCs by laser ablation in alcohols. The excitonic peak positions (Abs_{MAX}), the PL emissions wavelength (PL_{MAX}) and full width half maximum (FWHM), and the intensity-averaged lifetimes (τ_{AVG}) calculated by three-exponential fit (τ_i) of the TRPL decays are listed. Data related to $CsPbBr_3$ NCs by "2-step conversion" synthesis are reported with a lighter font. b) PLQY values measured over time for the $CsPbBr_3$ NCs by "in-situ conversion" method in different alcohols. All samples were kept in ambient conditions under extractor wood during aging.

Both lifetimes and PLQY values are in line with previous works on orthorhombic $CPbBr_3$ nanocrystals.[69,72] The negligible PLQY of the "in-situ" sample synthesized in isopropanol can be understood as a consequence of the intermediate solvent- and antisolvent behavior of this alcohol (Figure 6.2). Higher zeta potential values than those of "2-step" samples were measured for "in-situ" $CsPbBr_3$ NCs ones (Figure 6.8 a), showing a good colloidal stability over time and a complete NPs precipitation in more than 48 hours. Rosa-Pardo et al. employed laser ablation to induce the photofragmentation of bulk hybrid lead halide perovskites, proving that laser irradiation can effectively be beneficial for NCs emissive properties.[83] Following this observation one can suggest that during the "in-situ" synthesis the laser beam, not only produces $PbBr_2$ NCs, but also fragments the $CsPbBr_3$ NCs that gradually form in solution as a consequence of the reaction between $PbBr_2$ precursor NCs and CsBr (Figure 6.8 b,c). This "in-situ" process gave smaller perovskite NCs than those obtained by "2-step conversion", with an average size ranging from 30 to 50 nm and narrower size distributions as observed in TEM and dynamic light scattering analysis (Figure 6.9). In contrast, the size of $CsPbBr_3$ NCs by "2-step conversion" synthesis were in the range of 80–200 nm, depending on the alcohol used for the ablation (Figure 6.4).

a)

SOLVENT	Z Pot (2-step)	Z Pot (in-situ)
IPA	11.8 mV	16.3 mV
TBA	13.5 mV	15.9 mV
TPA	13.2 mV	17.7 mV
TEC	14.1 mV	18.2 mV

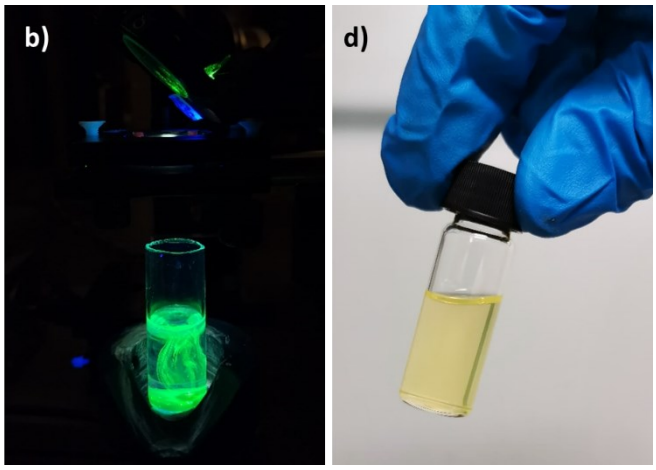

Figure 6.8 a) Table reporting the Z-potential values estimated for $CsPbBr_3$ NCs colloidal solutions by "2-step" and "in-situ" conversion in alcohols. b) Picture showing the "in-situ" formation of $CsPbBr_3$ NCs during laser ablation in triethyl carbinol. c) Picture of the $CsPbBr_3$ NCs colloidal solutions obtained after the synthesis.

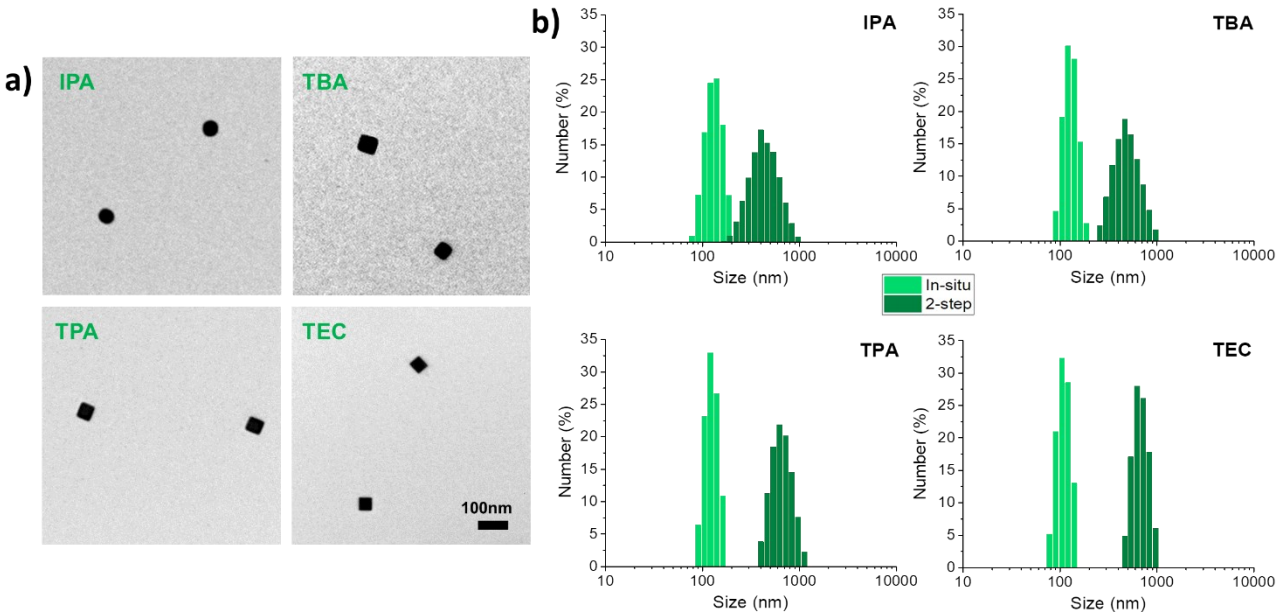

Figure 6.9 a) TEM images of $CsPbBr_3$ NCs by "in-situ conversion" in alcohols. A more defined NCs cubic shape can be appreciated moving from IPA to TEC samples. b) Comparison between dynamic light scattering measurements of "2-step" and "in-situ" $CsPbBr_3$ NCs solutions in alcohols. Each size distribution was averaged over 10 measurements. All the perovskite NCs solutions were placed in a sonication bath for 5 min before measurements. An average polydispersity index (PdI) of 0.14 and 0.25 was reported for "in-situ" and "2-step" samples, respectively.

6.3 Further Investigation

6.3.1 *Synthesis in Other Solvents*

LASiS production of $CsPbBr_3$ perovskite NCs was further investigated using other eco-sustainable perovskite antisolvents, namely ethyl acetate (EA), butyl acetate (BA) and anisole (Figure 6.1).[59,63,64,84] As observed for samples in alcohols, also in acetates, $CsPbBr_3$ NCs with superior optical properties are obtained when synthesized "in-situ" rather than by the "2-step" conversion. As shown in Figure 6.10 a, the characteristic $CsPbBr_3$ perovskite excitonic peak around 520 nm is present in the UV-Vis spectra of "in-situ" samples in EA and BA, while less visible and red-shifted in those of "2-step" samples. The PL emission peaks, centered at 524-525 nm, showed an increase in intensity of more than 2 times in "in-situ" $CsPbBr_3$ NCs compared to "2-step" ones (Figure 6.10 b). In parallel, a reduction in the FWHM was observed, from 20.5 to 20 nm for "2-step" and "in-situ" $CsPbBr_3$ NCs in EA, and from 18 to 17.5 nm for the same samples in BA, respectively.

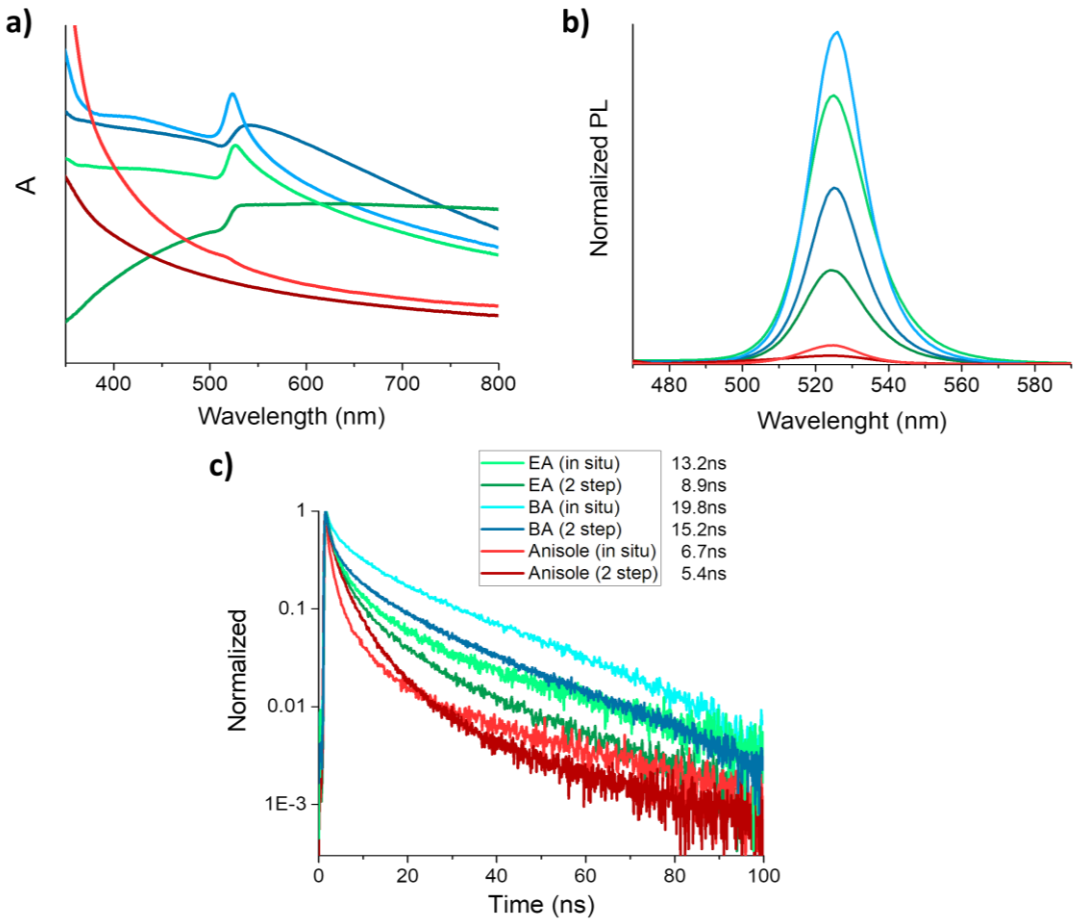

Figure 6.10 Comparison among a) UV-Vis spectra, b) SSPL measurements, and c) TRPL decays registered for $CsPbBr_3$ perovskite NCs by "2-step" and "in-situ" conversion in ethyl acetate, butyl acetate, and anisole. Colours of the lines shown for TRPL also indicate the spectra of a) and b).

Consistently with the PL intensities trend, an increase in the average PL lifetimes calculated from TRPL decays was observed when $CsPbBr_3$ NCs were synthesized by "in-situ conversion" in acetates, from 8.9 to 13.2 ns for "2-step" and "in-situ" samples in EA, and from 15.2 to 19.8 ns for the same samples in BA, respectively (Figure 6.10 c). However, despite the longer τ_{AVG} of $CsPbBr_3$ NCs colloidal solution in acetates than those of samples in alcohols (Figure 6.7 a), lower PL quantum yields were registered for the formers. PLQY values below 2% were measured for the "in-situ" samples in EA and BA, while negligible in the case of "2-step" samples in the same solvents. Following the XRD analysis, this can be attributed to the lower crystallinity of orthorhombic $CsPbBr_3$ perovskite crystals synthesized in acetates (Figure 6.11 a) with respect to those obtained in alcohols (Figure 6.4 a). TEM images showed a reduction in nanocrystals size of samples by "in-situ conversion" in EA and BA, in the range of 40-80 nm, compared to those produced by "2-step conversion", of 100-200 nm. (Figure 6.11 b).

Contrary to the previous samples synthesized in alcohols and acetates, both "2-step" and in "situ" $CsPbBr_3$ NCs made in anisole showed poor optical and morphological properties. UV-Vis spectra with negligible perovskite absorption edge, PL emission peaks with low intensities, and short average PL lifetimes of 5.4 and 6.7 ns for "2-step" and "in-situ", respectively, were observed for the syntheses in anisole (Figure 6.10). TEM analysis highlighted the presence of nanoparticles with amorphous shapes in both "2-step" and "in situ" samples synthesized in anisole (Figure 6.11 b), differing from perovskite NCs by LASiS in alcohols and acetates. The intense reflection peaks of $PbBr_2$ and CsBr in the XRD pattern of $CsPbBr_3$ NCs obtained in anisole testifies a poor conversion of precursors into perovskite (Figure 6.11 a).

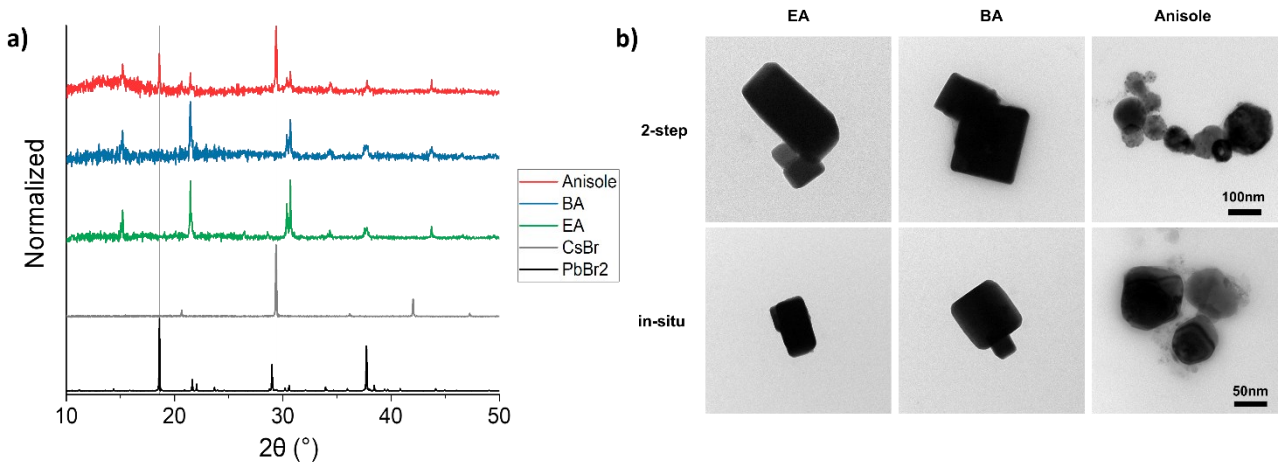

Figure 6.11 a) XRD patterns of the $CsPbBr_3$ NCs by LASiS in ethyl acetate, butyl acetate, and anisole. CsBr and $PbBr_2$ perovskite precursors are reported for comparison. b) TEM images of $CsPbBr_3$ NCs by "2-step" and "in-situ" conversion approaches in the same solvents.

This was ascribed to the immiscibility of CsBr solution in EtOH into anisole, limiting the perovskite conversion yield in this solvent. A non-flat background can be also noticed in the XRD pattern of anisole sample, showing a contribute around 15°. Such a broad peak at low diffraction angles is typically attributed to amorphous carbon nanomaterials.[85–87] It is known that LASiS can lead to the formation of carbon nanostructures when organic solvents are employed for the synthesis.[88–90] This can be considered another source of difference of the synthesis in anisole and those in other solvents.

In addition, the XRD analysis of $PbBr_2$ precursor NPs by LASiS in anisole highlighted a lower crystallinity compared to those synthesized in alcohols (Figure 6.4 a) and acetates (Figure 6.12 a) which, consequently, has a negative impact on the final properties of the perovskites. No relevant differences were observed in TEM images (Figure 6.12 b) while an increase in the scattering contribute in the 400-600 nm region, linked to a worst NPs dispersion (e.g., faster NPs aggregation, clusters formation), was observed in the UV-Vis of $PbBr_2$ NCs obtained in anisole (Figure 6.12 c).

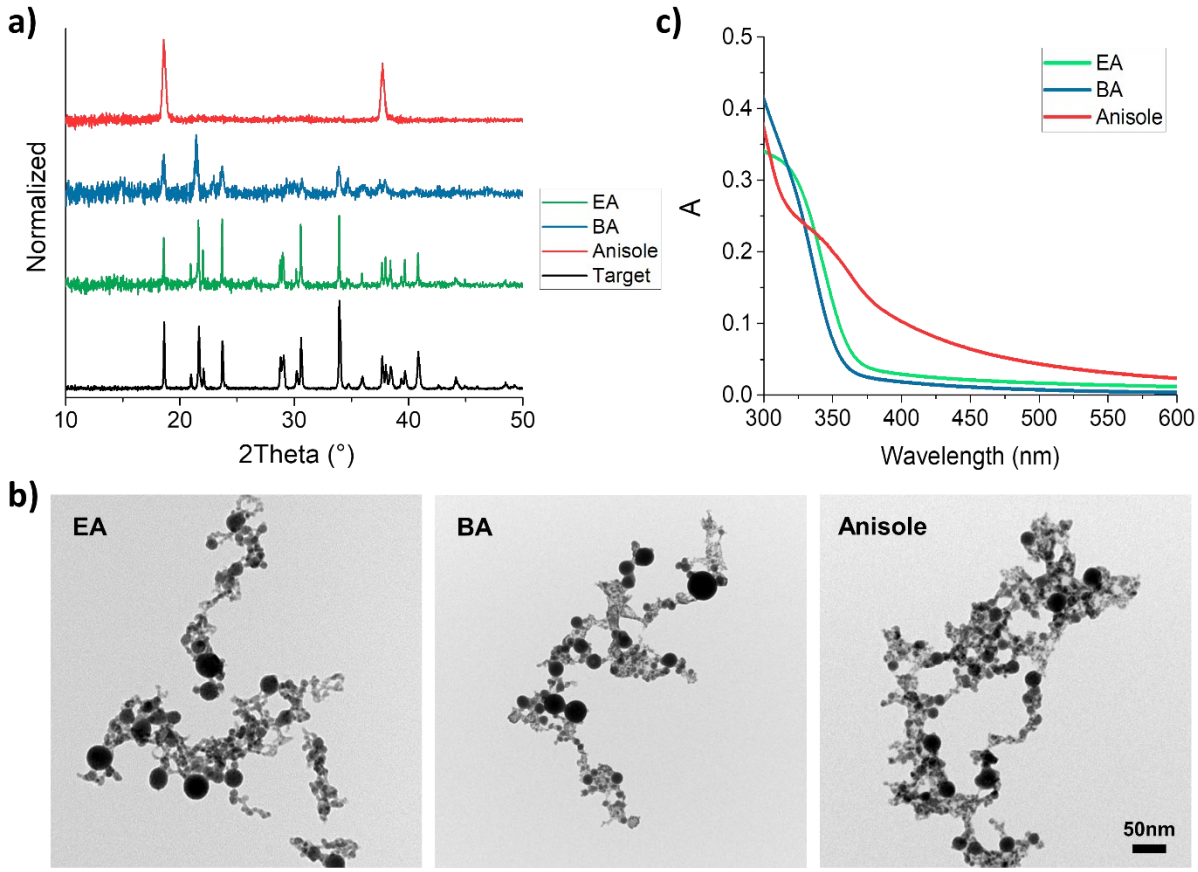

Figure 6.12 a) XRD patterns of $PbBr_2$ precursor NPs by LASiS in ethyl acetate (EA), butyl acetate (BA), and anisole. The XRD pattern of $PbBr_2$ target is also reported for comparison. b) TEM images and c) UV-Vis spectra of the same $PbBr_2$ NPs solutions. An increase in the scattering contribute between 400-600 nm can be noticed the UV-Vis spectrum of $PbBr_2$ NCs by LASiS in anisole.

6.3.2 *PL Quenching due to the Presence of Carbon Dots*

To verify the hypothesis of LASiS-generated C NPs, laser ablation of bare anisole, without the $PbBr_2$ target, was performed in the same experimental conditions used for the synthesis of $CsPbBr_3$ perovskite NCs. The characteristic yellow color and absorbance features of carbon dots (CDs) colloidal solutions were observed in the UV-Vis spectra (Figure 6.13 a).[88,91] The peaks in the 250–280 region are generally assigned to π–π* transitions due to the presence of the aromatic C=C framework, while the contribute around 350 nm corresponds to n–π* transitions as a result of the presence of various surface functional groups.[92]

The XRD analysis highlighted the same contribute around 15° and 30°, related to amorphous C material (as mentioned in the previous paragraph),[85–87] in both XRD patterns of $CsPbBr_3$ NCs in anisole and the bare ablated solvent, whereas this signals are absent in $CsPbBr_3$ NCs synthesized in other solvents (Figure 6.13 b). The confirmation of the presence of LASiS-generated carbon dots inside the anisole solutions was obtained by comparing the results of different spectroscopy and microscopy techniques. Carbon dots display excitation-wavelength dependent emission, since their fluorescence is affected by the electronic bandgap transitions of conjugated π-domains, surface defect states, local fluorophores, nanoparticles size, and element doping.[93–97] In accordance to this, a coherent shift of the PL emission peaks with the excitation wavelength was observed in SSPL spectra of the solution obtained ablating anisole (Figure 6.14 a).

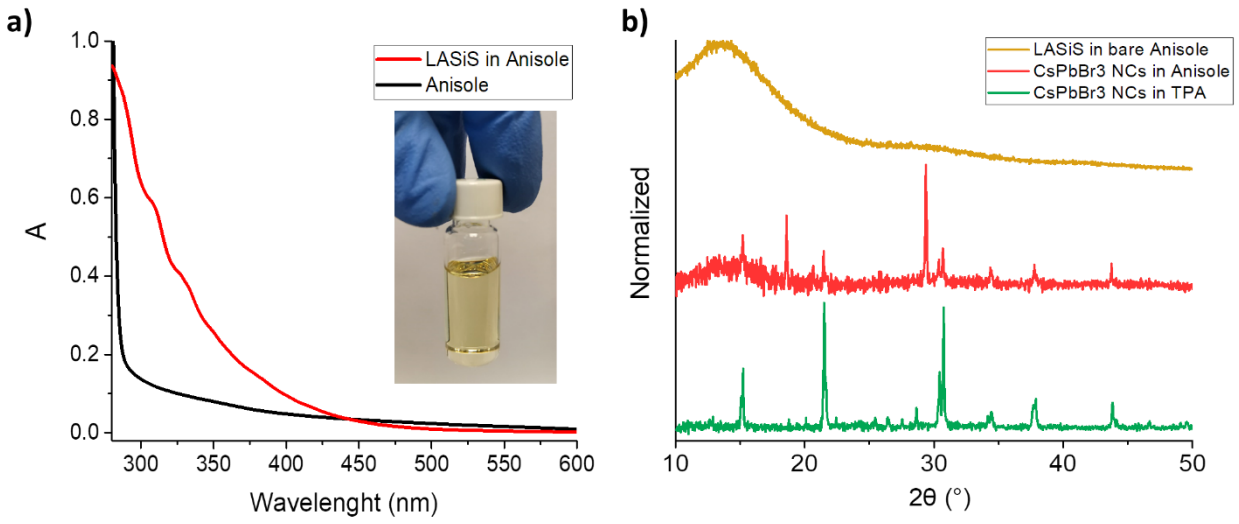

Figure 6.13 a) Comparison between the UV-Vis spectra of anisole before (black line) and after (red line) LASiS. The photograph in the inset shows the yellow colour of the so-obtained solution. b) Comparison between XRD patterns of $CsPbBr_3$ perovskite NCs by LASiS in anisole and the bare ablated solvent. XRD pattern of $CsPbBr_3$ NCs in tert-pentanol was reported for comparison.

A similar emission trend was observed by analyzing the supernatant of the $CsPbBr_3$ NCs colloidal solution by LASiS in anisole (Figure 6.14 b), testifying the CDs formation during LASiS in anisole, regardless the presence of the lead bromide target and/or the perovskite nanocrystals.

Average lifetimes of 4.8 and 4.9 ns, in line with previous studies on CDs emissive properties,[97] were calculated from PL decays of the ablated anisole and the supernatant of $CsPbBr_3$ NCs solution by LASiS in anisole, respectively (Figure 6.14 c). It is easily noticed how these lifetime values are equivalent one to another, indicating the presence of similar emissive species in both the solutions. In addition, they are close to the average PL lifetimes estimated for $CsPbBr_3$ NCs by "2-step" and "in-situ" conversions in anisole (Figure 6.10 c). This similarity in lifetime values, as well as the poor PL intensities registered for the above-mentioned $CsPbBr_3$ samples (Figure 6.10 b), can be explained with a perovskite PL quenching mechanism induced by carbon dots. In fact, CDs can reabsorb the $CsPbBr_3$ fluorescence,[98] provide recombination centers at the interface with perovskite,[79] and/or act as hole/electron acceptor species depleting the photogenerated charges in $CsPbBr_3$ NCs.[99,100]

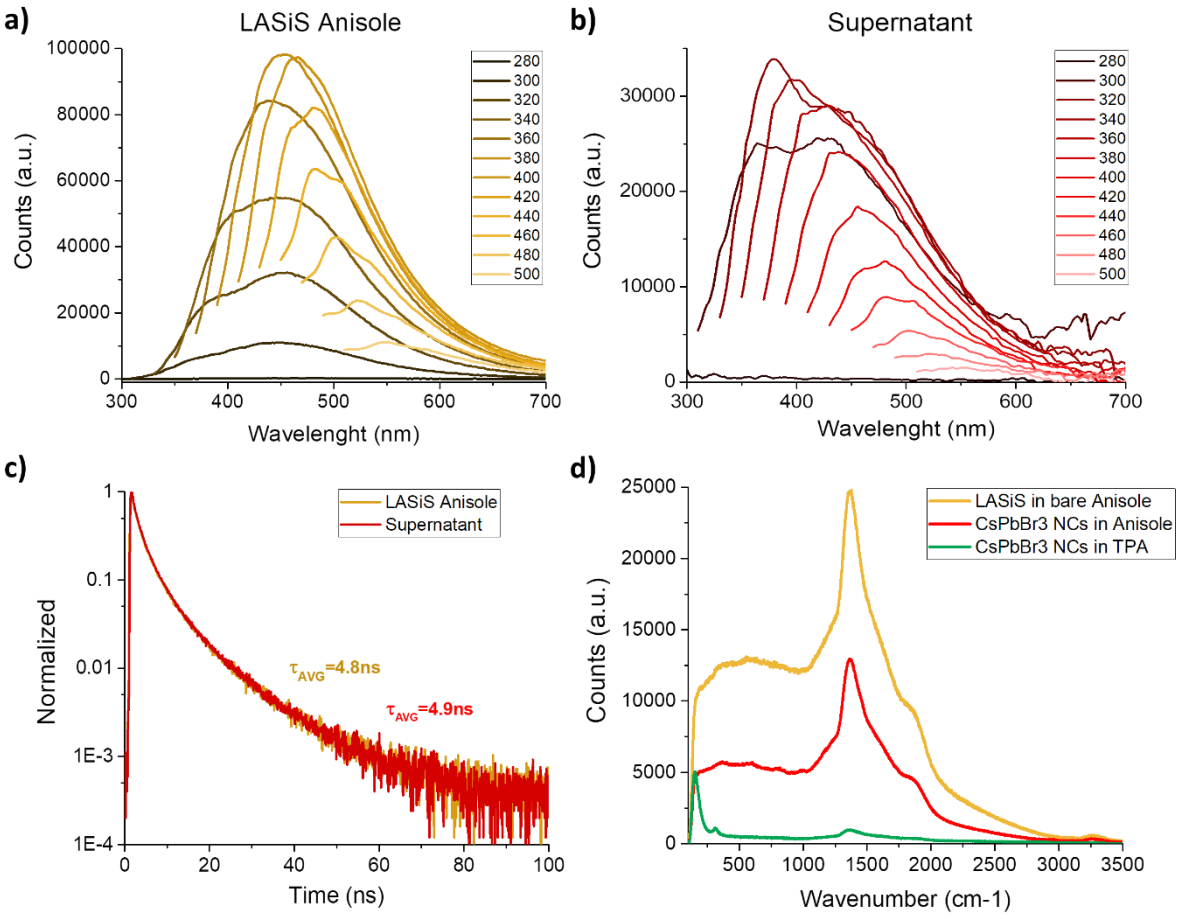

Figure 6.14 Emission spectra of a) the solution obtained by ablating bare anisole, b) the supernatant of $CsPbBr_3$ NCs by LASiS in anisole. An excitation-wavelength dependence can be appreciated in both cases. c) TRPL measurements showing the intensity-averaged lifetimes calculated by three-exponential fit. d) Raman spectra registered for the same samples. Raman spectrum of $CsPbBr_3$ NCs by LASiS in TPA is reported for comparison.

Moreover, C Dots can absorb the incident radiation during SSPL measurements, i.e., causing a lower excitation of the perovskite NCs in solution. However, since a non-optimal perovskite conversion was observed for $CsPbBr_3$ NCs synthesized in anisole (Figure 6.11 a), the worsening of their emissive properties cannot be entirely attributed to the formation of CDs in solution during laser ablation.

Attempts to compare the C content in $CsPbBr_3$ NCs by LASiS in different type of solvents were conducted by Raman spectroscopy and Energy Dispersive X-Ray (EDX) analysis. Figure 6.14 d compares the Raman spectra of $CsPbBr_3$ NCs synthesized in anisole and in tert-pentanol, together with the one obtained by ablating bare anisole. The vibrational peaks around 100 cm^{-1} were attributed to $CsPbBr_3$ perovskite,[47,101,102] only distinguishable in TPA sample. The main contributes to the Raman spectra, around 1350 cm^{-1}, were attributed to the D band associated to disorder/defects in the graphite lattice (i.e., sp^3 carbon atoms). The G (graphitic) band at about 1580 cm^{-1}, related to the vibration of sp^2 carbon networks,[103–105] was convoluted with the D band in the analyzed samples. However, the presumable high ratio, >1, between D and G band intensities indicated a poor carbon crystallinity/order (i.e., conjugated graphitic frameworks).[103,104,106] The big difference in intensity of the D band among the analyzed samples can be related to an analogous difference in carbon content. This pointed out a much lower presence of C materials in the $CsPbBr_3$ NCs synthesized in TPA than in $CsPbBr_3$ NCs by LASiS in anisole and the ablated anisole. The shoulders at the sides of D band were due to the convolution of additional bands at about 1150, 1500 and 1620 cm^{-1}, typical of poorly organized carbon nanomaterials and/or microcrystalline graphite.[96,103] EDX analysis confirmed the C content trend in the same samples analyzed by Raman spectroscopy (Figure 6.15).

Despite no reference standards were used for the measurement and C contaminations due to the material itself, the synthetic method, the samples preparation, and the environment are always present in all samples (in the order of 10-20 atomic %),[107,108] EDX results showed a significant increase in carbon content (more than double C atomic %) in the $CsPbBr_3$ NCs synthesized in anisole than those by LASiS in tert-pentanol. The carbon-lead atomic ratio (C:Pb) is reported in the tables for a better evaluation of the C/$CsPbBr_3$ content in each sample, highlighting a 5-10 times higher value in the case of anisole sample than the one synthesized in alcohol. A further, final confirmation of the presence of C dots in anisole samples was obtained by TEM analysis. CDs of 2-6 nm, grouped in 15-30 nm clusters were observed in both the ablated anisole and the supernatant of $CsPbBr_3$ NCs by LASiS in anisole (Figure 6.16), while no evidence of C nanoparticles were found in $CsPbBr_3$ NCs synthesized in alcohols and acetates.

C Dots

	Spectrum 1	Spectrum 2	Spectrum 2	Spectrum 3	Spectrum 4	Spectrum 5	Spectrum 6	Spectrum 7	Spectrum 8	Spectrum 9	Spectrum 10
C	73.52	76.15	76.16	76.60	73.84	73.38	74.74	76.29	74.34	73.38	72.05
O	25.33	22.64	22.88	22.97	25.52	25.85	24.34	22.41	25.06	25.89	26.74
Na	1.15	1.20	0.97	0.43	0.64	0.78	0.92	1.30	0.60	0.73	1.22

Anisole

	Spectrum 1	Spectrum 2	Spectrum 2	Spectrum 3	Spectrum 4	Spectrum 5	Spectrum 6	Spectrum 7	Spectrum 8	Spectrum 9	Spectrum 10
C	55.45	53.54	52.50	51.26	59.65	59.21	55.09	53.20	56.85	56.91	59.74
O	12.58	11.39	10.45	13.83	12.59	9.40	9.71	8.74	11.07	9.02	9.81
Na	1.76	2.43	1.74	2.32	4.22	2.24	1.96	2.05	2.1	2.09	1.50
Cl	0.34	0.21	0.07	0.23	0.28	0.28	0.41	0.16	0.35	0.26	0.65
Ca	0.25	0.24	0.27	0.38	0.57	0.25	0.34	0.34	0.17	0.29	0.27
Br	17.70	19.33	20.98	19.21	13.74	17.18	19.62	21.46	17.75	18.81	16.28
Pb	5.99	6.45	7.01	6.45	4.56	5.75	6.55	7.12	5.93	6.40	5.44
Cs	5.93	6.41	6.98	6.32	4.39	5.69	6.32	6.93	5.78	6.22	5.31
C:Pb	9.3	8.3	7.5	7.9	13.1	10.3	8.4	7.5	9.6	8.9	11.0

tert-Pentanol

	Spectrum 1	Spectrum 2	Spectrum 2	Spectrum 3	Spectrum 4	Spectrum 5	Spectrum 6	Spectrum 7	Spectrum 8	Spectrum 9	Spectrum 10
C	23.28	18.85	20.85	24.28	16.88	20.53	23.97	18.67	19.15	19.87	17.95
O	13.52	11.41	13.02	11.59	12.74	9.14	9.93	12.71	9.59	10.29	11.55
Na	0.44	1.15	0.68	0.87	0.72	0.68	1.31	1.22	1.03	0.55	0.62
Cl	1.28	1.08	1.21	0.99	1.21	1.05	0.97	1.01	1.24	1.06	1.13
Ca	0.37	0.43	0.39	0.47	0.36	0.41	0.38	0.37	0.37	0.58	0.32
Br	36.74	40.28	38.36	37.08	40.88	40.96	38.29	39.72	41.26	40.69	41.12
Pb	12.23	13.44	12.83	12.40	13.64	13.68	12.62	13.22	13.77	13.58	13.72
Cs	12.14	13.36	12.66	12.32	13.57	13.55	12.53	13.08	13.59	13.38	13.59
C:Pb	1.9	1.4	1.6	2.0	1.2	1.5	1.9	1.4	1.4	1.5	1.3

Figure 6.15 Tables summarizing the results of EDX analysis (% atomic) performed on $CsPbBr_3$ NCs by LASiS in TPA and anisole, as well as on the sample obtained by ablating bare anisole (C Dots). The carbon-lead ratio is reported in each table for a better comparison of C/$CsPbBr_3$ content.

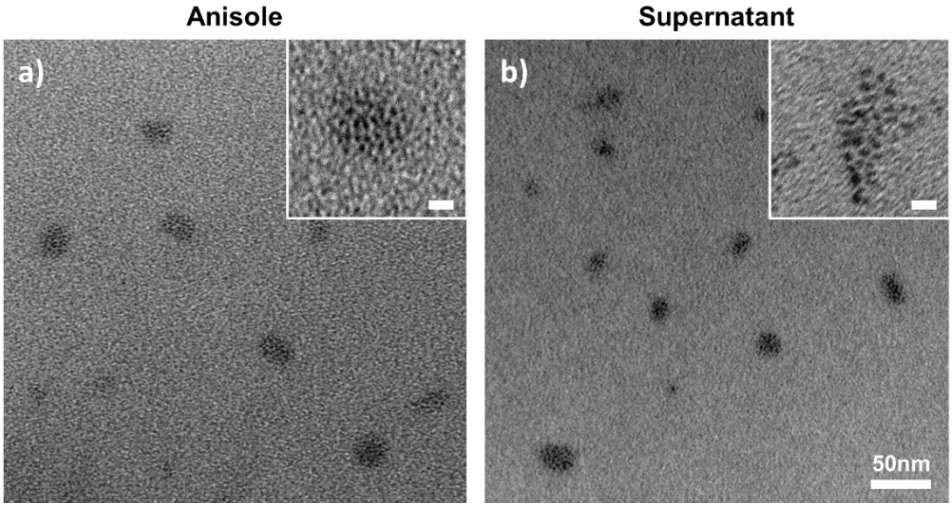

Figure 6.16 TEM images of carbon dots found in the a) solution obtained by ablating bare anisole, and b) supernatant of the $CsPbBr_3$ NCs colloidal solution in anisole. Magnified images are reported in the insets, with 10 nm scale bars.

In conclusion, the presence of laser-generated C dots in anisole solutions was demonstrated by comparing the results of different optical/electron spectroscopies and microscopies. This LASiS side-effect seemed to be heavy in aromatic solvents (i.e., anisole) while negligible in aliphatic ones (i.e., alcohols and acetates), at least in the experimental conditions in which the syntheses were performed.

6.4 Summary

Laser ablation technique was optimized to produce colloidal solutions of $CsPbBr_3$ all-inorganic perovskite nanocrystals in "green" solvents. Environmental, health and safety guidelines were followed for the choice of the solvents to test. By opportunely selecting the polarity and the dielectric constant of different commercially available branched alcohols it was demonstrated that, contrary to what is generally reported for the halide perovskite materials, $CsPbBr_3$ nanocrystals with good optical and morphological properties can be synthesized in this class of eco-sustainable, non-hazardous solvents. The laser beam interaction with the perovskite nanocrystals was found to be important, leading to smaller and more emissive $CsPbBr_3$ nanocrystals when synthesized "in-situ" during laser ablation rather than in a "2-step" process from laser-ablated $PbBr_2$ precursors nanocrystals. Optimized samples showed good crystallinity, high colloidal stability, and high emissivity, with intense and narrow PL emissions (FWHM down to 16nm), long PL lifetimes (up to 17.9 ns), and good PL quantum yields (up to 15.5%) stable over many days under ambient conditions. These values are among the best results obtained in literature for orthorhombic $CsPbBr_3$ nanocrystals produced via top-down approach.

Laser ablation technique was further investigated and applied to the synthesis of $CsPbBr_3$ nanocrystals in other green perovskite antisolvents, namely ethyl acetate, butyl acetate, and anisole. $CsPbBr_3$ nanocrystals with good emissivity were obtained when synthesized "in-situ" in acetates, with PL lifetimes even longer (up to 19.8 ns) than those of samples synthesized in alcohols. However, lower PLQYs (<2%) were measured for these samples, attributed to a lower crystallinity. On the other hand, laser ablation in anisole produced low-quality $CsPbBr_3$ nanocrystals. The XRD analysis highlighted a poor conversion of precursors into perovskite in both "in-situ" and "2-step" samples, ascribed to the negligible solubility of CsBr into anisole. The low emissivity observed for $CsPbBr_3$ nanocrystals synthesized in anisole was correlated to the formation of C-Dots during laser ablation, which presence was demonstrated by comparing the results of different optical and electronic analysis. In the conditions in which the syntheses were performed, this phenomenon

seemed to be heavy in aromatic solvents (i.e., anisole), while negligible in aliphatic ones (i.e., alcohols and acetates).

The results of this study show how, in proper conditions, laser ablation in solution can be an employed as an effective alternative top-down approach to synthesize ligand-free $CsPbBr_3$ nanocrystals colloidal solutions in "green" solvents, facing the urgent call for more sustainable synthesis and/or processing of lead halide perovskite nanomaterials.

6.5 Experimental Section

6.5.1 *Materials*

All reagents were purchased from Sigma-Aldrich and used without further purification, namely lead bromide and cesium bromide (99.999% purity powders), methanol, ethanol, isopropanol, tert-butanol, tert-pentanol, triethyl carbinol, ethyl acetate, butyl acetate, and anisole (>99% purity, anhydrous).

6.5.2 *Perovskite Nanocrystals by Laser Ablation*

2-Step Conversion Method

In the first step, $PbBr_2$ NCs precursor solutions were produced by LASiS in the selected solvents. The third harmonic (355 nm) of a pulsed (20Hz) Nd:YAG laser (Q-smart 450, Quantel) was focused on the surface of a $PbBr_2$ round tablet with a fluence of 3 J/cm^2 (9 ns pulse duration). The target tablet, 1.2 mm thick and with a diameter of 13 mm, was obtained by compressing lead bromide powders with a uniaxial press hydraulic press under 10 tons for 10 minutes. The so-obtained target was placed into a glass vial (14 mm diameter) and immersed in 4.0 ml of solvent (Figure 6.17). To ensure a uniform erosion of the target by the laser beam, the vial was continuously moved by an automated x-y movement system during the whole process at a constant speed of 0.5 mm/s. LASiS were performed for 45 minutes for all samples, obtaining $PbBr_2$ NCs colloidal solutions with a concentration of 0.5–0.7 mM.

The concentration of $PbBr_2$ NCs solutions was estimated by optical extinction in which the lead bromide molar extinction coefficient (ε_{PbBr2}), of about 6300 $M^{-1}cm^{-1}$, was calculated from a calibration line made from $PbBr_2$ standard solutions in DMF (Figure 6.18). After the synthesis, aliquots of $PbBr_2$ NCs solutions were centrifugated for 15 min at 30000 RCF and then their precipitates were digested in DMF.

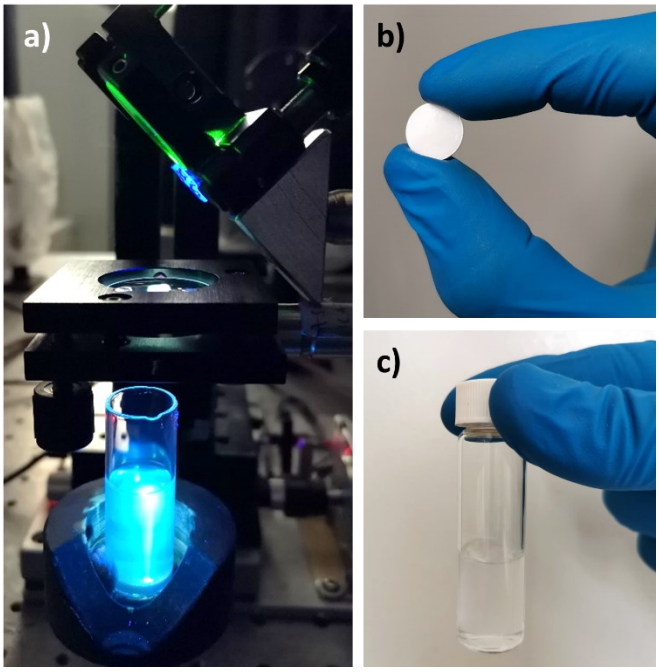

Figure 6.17 Laser ablation synthesis in solution (LASiS) of $PbBr_2$ precursor nanocrystals. a) Picture of LASiS process, b) lead bromide round pellet (13 mm diameter), and c) picture of $PbBr_2$ NCs colloidal solution in alcohol.

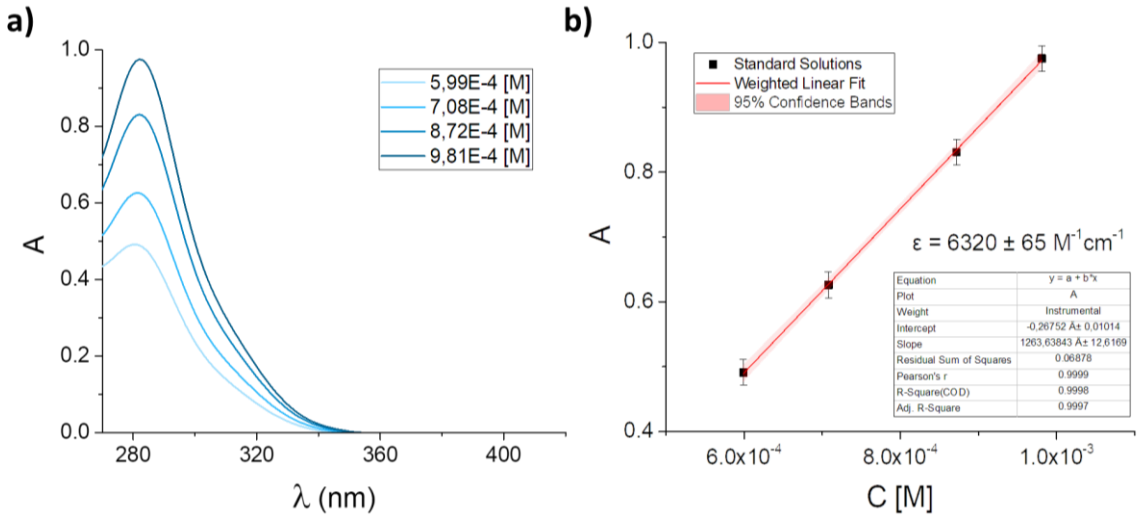

Figure 6.18 Estimation of $PbBr_2$ molar extinction coefficient (ε_{PbBr2}). a) UV-Vis spectra of standard solutions prepared by dissolving $PbBr_2$ powders in DMF. b) Weighted linear fit made by evaluating the Abs peak at 282 nm in function of concentration. By the Lambert-Beer law, ε_{PbBr2} is proportional to the angular coefficient of the calibration line. The concentration of $PbBr_2$ NCs colloidal solutions was determined by centrifugating the solutions, digesting the precipitate in DMF and then evaluating the Abs peak at 282 nm.

The $PbBr_2$ concentrations were then calculated by applying the Lambert-Beer law to the absorption peaks at 282 nm of the so-obtained DMF solutions.[81] In the second step, $CsPbBr_3$ NCs were obtained by mixing 2.0 ml of 0.2 mM $PbBr_2$ NCs diluted solution with 50 µL of 8 mM CsBr ethanol solution for 30 minutes in a sonication bath. Then. solutions were centrifuged for 4 minutes at 5000 RCF and redispersed in the same pure solvent used for LASiS, to get $CsPbBr_3$ NCs colloidal solution without impurities.

In-Situ Conversion Method

With this method, $CsPbBr_3$ NCs colloidal solution were directly produced during LASiS. Before the synthesis, 100µL of 8 mM CsBr solution in ethanol were added to 4.0 ml ablation solvent and then vigorously mixed on a vortex for 5 minutes. The ablation duration, in between 60 and 90 min, was tuned for each sample to get a complete perovskite conversion with no unreacted CsBr in solution. All other experimental conditions/post-treatments were the same as for the "2-step conversion" samples previously described.

6.5.3 *Optical Characterizations*

UV-visible spectra were collected with an Agilent Cary 5000 UV−vis−NIR spectrometer using 0.2 cm quartz cuvettes. Dynamic light scattering and Z-potential measurements were performed with a Malvern Instrument Zetasizer Nano, operating with a 633 nm He−Ne laser. Steady-state and time-resolved PL measurements were performed with an Edinburgh FLS 1000 UV/Vis/NIR photoluminescence spectrometer. SSPL spectra were collected using an excitation wavelength at 400 nm from Xe lamp and a PMT-850 detector. All spectra were acquired by setting 1 nm step and 0.5 s acquisition time. TRPL decays were registered following the time-correlated single photon counting (TCSPC) method using a pulsed laser diode at 402.6nm and high-speed PMT-850 detector. 10^4 peak count and 1024 channels were set for all the measurements. For each sample, the intensity-averaged photoluminescence lifetimes was calculated from the three-exponential fit of its corresponding TRPL decay, using the following formula:[69,109]

$$\tau_{AVG} = \frac{A_1{\tau_1}^2 + A_2{\tau_2}^2 + A_3{\tau_3}^2}{A_1\tau_1 + A_1\tau_1 + A_1\tau_1} \qquad 1.7$$

The A_i pre-exponential factor represents the amplitude associated to the lifetime of the i^{th} component (τ_i). Absolute PL quantum yields were measured using an integrating sphere exciting the samples at 400 nm with a Xe lamp source. All the samples were diluted to get 0.1 Abs at the excitonic peak wavelength. Pristine solvents were used as reference samples, in the same volume as the perovskite NCs solution to analyze. Raman spectroscopy measurements were registered with an inVia Renishaw microRaman instrument, equipped with a laser diode operating at 785 nm. The laser spot diameter was about 5 µm (20x objective). The output laser power was set at 3 mW during all Raman measurements, carried out in laboratory conditions.

6.5.4 *Morphological Characterizations*

TEM images were collected with a FEI TECNAI G2 transmission electron microscope, set at 100kV. The average NCs size were estimated by analyzing the images with ImageJ software, measuring the diameter of 300-500 nanocrystals. X-ray diffraction patterns were recorded in Bragg–Brentano geometry using a BRUKER AXS D8 ADVANCE Plus diffractometer, working with a Cu $K_{\alpha 1}$ anode. All diffraction patterns were recorded at room temperature, with a step size of 0.020° and an acquisition time of 1.0 s. The samples were prepared under extractor wood by drop casting the perovskite NCs colloidal solution onto a zero diffraction plates of (100) Silicon (Sil'tronix Silicon Technologies), kept at 100°C by a hot plate during the depositions. SEM-EDX measurements were performed with a Zeiss Sigma HD microscope, equipped with a Schottky FEG source, one detector for backscattered electrons and two detectors for secondary electrons (InLens and Everhart Thornley). The microscope was coupled to an EDX detector (Oxford Instruments, x-act PentaFET Precision) for X-rays microanalysis, working in energy dispersive mode. All EDX measurements were performed at 20 kV, analyzing 10 different regions (5x5 μm^2) for each sample. AZtec software (Oxford Instruments) was used to collect and process the X-ray spectra.

References

(1) Sansoni, S.; Anoè, F. M.; Meneghetti, M. Synthesis of CsPbBr3 Nanocrystals via Laser Ablation in Alcohol for More Sustainable Perovskite-Based Optoelectronics. *ACS Sustain. Chem. Eng. (to submit)* **2021**.

(2) Yan, F.; Demir, H. V. LEDs Using Halide Perovskite Nanocrystal Emitters. *Nanoscale* **2019**, *11*, 11402. https://doi.org/10.1039/c9nr03533h.

(3) Zou, C.; Zhang, C.; Kim, Y.-H.; Lin, L. Y.; Luther, J. M. The Path to Enlightenment: Progress and Opportunities in High Efficiency Halide Perovskite Light-Emitting Devices. *ACS Photonics* **2021**. https://doi.org/10.1021/acsphotonics.0c01394.

(4) Yuan, J.; Hazarika, A.; Zhao, Q.; Ling, X.; Moot, T.; Ma, W.; Luther, J. M. Metal Halide Perovskites in Quantum Dot Solar Cells: Progress and Prospects. *Joule* **2020**, *4*, 1–26. https://doi.org/10.1016/j.joule.2020.04.006.

(5) Zhihai Wu, Pan Wang, Jun Wu, Jiao Wei, Yanni Sun, Nengping Wang, and Z. Z. Ultra-Stable Phosphor of h-BN White Graphene-Loaded All-Inorganic Perovskite Nanocrystals for White LEDs. *J. Lumin.* **2020**, *219*.

(6) Haiguang Zhao, Yufeng Zhou, Daniele Benetti, Dongling Ma, F. R. Perovskite Quantum Dots Integrated in Large-Area Luminescent Solar Concentrators. *Nano Energy* **2017**, *13*, 214–233.

(7) Zhou, S.; Zhou, G.; Li, Y.; Xu, X.; Hsu, Y.-J.; Xu, J.; Zhao, N.; Lu, X. Understanding Charge Transport in All-Inorganic Halide Perovskite Nanocrystal Thin-Film Field Effect Transistors. *ACS Energy Lett* **2020**, *30*, 47. https://doi.org/10.1021/acsenergylett.0c01295.

(8) Shen, K.; Xu, H.; Li, X.; Guo, J.; Sathasivam, S.; Wang, M.; Ren, A.; Choy, K. L.; Parkin, I. P.; Guo, Z.; et al. Flexible and Self-Powered Photodetector Arrays Based on All-Inorganic CsPbBr3 Quantum Dots. *Adv. Mater.* **2020**, *32* (22). https://doi.org/10.1002/ADMA.202000004.

(9) Li, Z.; Zhou, F.; Yao, H. H.; Ci, Z.; Yang, Z.; Jin, Z. Halide Perovskites for High-Performance X-Ray Detector. *Mater. Today* **2021**, *xxx* (xx). https://doi.org/10.1016/j.mattod.2021.01.028.

(10) Huang, H.; Hao, M.; Song, Y.; Dang, S.; Liu, X.; Dong, Q. Dynamic Passivation in Perovskite Quantum Dots for Specific Ammonia Detection at Room Temperature. *Small* **2020**, *16* (6). https://doi.org/10.1002/SMLL.201904462.

(11) Kagan, C. R.; Bassett, L. C.; Murray, C. B.; Thompson, S. M. Colloidal Quantum Dots as Platforms for Quantum Information Science. *Chem. Rev.* **2021**, *121*, 3186–3233. https://doi.org/10.1021/acs.chemrev.0c00831.

(12) Shamsi, J.; Urban, A. S.; Imran, M.; De Trizio, L.; Manna, L. Metal Halide Perovskite Nanocrystals: Synthesis, Post-Synthesis Modifications, and Their Optical Properties. *Chem. Rev.* **2019**, *119* (5), 3296–3348. https://doi.org/10.1021/acs.chemrev.8b00644.

(13) Akkerman, Q. A.; Valerio D'innocenzo, †; Accornero, S.; Scarpellini, A.; Petrozza, A.; Prato, M.; Manna, L. Tuning the Optical Properties of Cesium Lead Halide Perovskite Nanocrystals by Anion Exchange Reactions. *JACS* **2015**. https://doi.org/10.1021/jacs.5b05602.

(14) Akkerman, Q. A.; Gandini, M.; Di Stasio, F.; Rastogi, P.; Palazon, F.; Bertoni, G.; Ball, J. M.; Prato, M.; Petrozza, A.; Manna, L. Strongly Emissive Perovskite Nanocrystal Inks for High-Voltage Solar Cells. *Nat. Energy* **2017**, *2* (2), 1–7. https://doi.org/10.1038/nenergy.2016.194.

(15) Brown, A. A. M.; Damodaran, B.; Jiang, L.; Tey, J. N.; Pu, S. H.; Mathews, N.; Mhaisalkar, S. G. Lead Halide Perovskite Nanocrystals : Room Temperature Syntheses toward Commercial Viability. *Adv. Energy Mater.* **2020**, *2001349*, 1–19. https://doi.org/10.1002/aenm.202001349.

(16) Brown, A. A. M.; Vashishtha, P.; Hooper, T. J. N.; Ng, Y. F.; Nutan, G. V; Fang, Y.; Giovanni, D.; Tey, J. N.; Jiang, L.; Damodaran, B.; et al. Precise Control of CsPbBr3 Perovskite Nanocrystal Growth at Room Temperature: Size Tunability and Synthetic Insights. *Chem. Mater.* **2021**. https://doi.org/10.1021/acs.chemmater.0c04569.

(17) Song, J.; Li, J.; Xu, L.; Li, J.; Zhang, F.; Han, B.; Shan, Q.; Zeng, H. Room-Temperature Triple-Ligand Surface Engineering Synergistically Boosts Ink Stability, Recombination Dynamics, and Charge Injection toward EQE-11.6% Perovskite QLEDs. *Adv. Mater.* **2018**, *30* (30).

https://doi.org/10.1002/ADMA.201800764.
(18) Zhang, F.; Zhong, H.; Chen, C.; Wu, X. G.; Hu, X.; Huang, H.; Han, J.; Zou, B.; Dong, Y. Brightly Luminescent and Color-Tunable Colloidal CH3NH3PbX3 (X = Br, I, Cl) Quantum Dots: Potential Alternatives for Display Technology. *ACS Nano* **2015**, *9* (4), 4533–4542. https://doi.org/10.1021/acsnano.5b01154.
(19) Gheno, A.; Huang, Y.; Bouclé, J.; Ratier, B.; Rolland, A.; Even, J.; Vedraine, S. Toward Highly Efficient Inkjet-Printed Perovskite Solar Cells Fully Processed Under Ambient Conditions and at Low Temperature. *Sol. RRL* **2018**, *2* (11), 1–8. https://doi.org/10.1002/solr.201800191.
(20) Zhang, M.; Xin, D.; Zheng, X.; Chen, Q.; Zhang, W. H. Toward Greener Solution Processing of Perovskite Solar Cells. *ACS Sustain. Chem. Eng.* **2020**, *8* (35), 13126–13138. https://doi.org/10.1021/acssuschemeng.0c04289.
(21) Vidal, R.; Alberola-Borràs, J. A.; Habisreutinger, S. N.; Gimeno-Molina, J. L.; Moore, D. T.; Schloemer, T. H.; Mora-Seró, I.; Berry, J. J.; Luther, J. M. Assessing Health and Environmental Impacts of Solvents for Producing Perovskite Solar Cells. *Nat. Sustain.* **2021**, *4* (3), 277–285. https://doi.org/10.1038/s41893-020-00645-8.
(22) Doolin, A. J.; Charles, R. G.; De Castro, C. S. P.; Rodriguez, R. G.; Péan, E. V.; Patidar, R.; Dunlop, T.; Charbonneau, C.; Watson, T.; Davies, M. L. Sustainable Solvent Selection for the Manufacture of MAPbI3 Perovskite Solar Cells. *Green Chem.* **2021**. https://doi.org/10.1039/D1GC00079A.
(23) Gardner, K. L.; Tait, J. G.; Merckx, T.; Qiu, W.; Paetzold, U. W.; Kootstra, L.; Jaysankar, M.; Gehlhaar, R.; Cheyns, D.; Heremans, P.; et al. Nonhazardous Solvent Systems for Processing Perovskite Photovoltaics. *Adv. Energy Mater.* **2016**, *6* (14), 1–8. https://doi.org/10.1002/aenm.201600386.
(24) Byrne, F. P.; Jin, S.; Paggiola, G.; Petchey, T. H. M.; Clark, J. H.; Farmer, T. J.; Hunt, A. J.; Robert McElroy, C.; Sherwood, J. Tools and Techniques for Solvent Selection: Green Solvent Selection Guides. *Sustain. Chem. Process.* **2016**, *4* (1), 1–24. https://doi.org/10.1186/s40508-016-0051-z.
(25) Alder, C. M.; Hayler, J. D.; Henderson, R. K.; Redman, A. M.; Shukla, L.; Shuster, L. E.; Sneddon, H. F. Updating and Further Expanding GSK's Solvent Sustainability Guide. *Green Chem.* **2016**, *18* (13), 3879–3890. https://doi.org/10.1039/c6gc00611f.
(26) Clarke, C. J.; Tu, W. C.; Levers, O.; Bröhl, A.; Hallett, J. P. Green and Sustainable Solvents in Chemical Processes. *Chem. Rev.* **2018**, *118* (2), 747–800. https://doi.org/10.1021/acs.chemrev.7b00571.
(27) Prat, D.; Wells, A.; Hayler, J.; Sneddon, H.; McElroy, C. R.; Abou-Shehada, S.; Dunn, P. J. CHEM21 Selection Guide of Classical- and Less Classical-Solvents. *Green Chem.* **2016**, *18* (1), 288–296. https://doi.org/10.1039/c5gc01008j.
(28) Stranks, S. D.; Hoye, R. L. Z.; Di, D.; Friend, R. H.; Deschler, F. The Physics of Light Emission in Halide Perovskite Devices. *Adv. Mater.* **2019**, *31* (1803336). https://doi.org/10.1002/ADMA.201803336.
(29) Xing, G.; Wu, B.; Wu, X.; Li, M.; Du, B.; Wei, Q.; Guo, J.; Yeow, E. K. L.; Sum, T. C.; Huang, W. Transcending the Slow Bimolecular Recombination in Lead-Halide Perovskites for Electroluminescence. *Nat. Publ. Gr.* **2017**. https://doi.org/10.1038/ncomms14558.
(30) Nenon, D. P.; Pressler, K.; Kang, J.; Koscher, B. A.; Olshansky, J. H.; Osowiecki, W. T.; Koc, M. A.; Wang, L.-W.; Alivisatos, A. P. Design Principles for Trap-Free CsPbX3 Nanocrystals: Enumerating and Eliminating Surface Halide Vacancies with Softer Lewis Bases. *J. Am. Chem. Soc.* **2018**, *140* (50), 17760–17772. https://doi.org/10.1021/JACS.8B11035.
(31) Smock, S. R.; Williams, T. J.; Brutchey, R. L. Quantifying the Thermodynamics of Ligand Binding to CsPbBr3 Quantum Dots. *Angew. Chemie - Int. Ed.* **2018**, *57* (36), 11711–11715. https://doi.org/10.1002/ANIE.201806916.
(32) Chen, B.; Rudd, P. N.; Yang, S.; Yuan, Y.; Huang, J. Imperfections and Their Passivation in Halide Perovskite Solar Cells. *Chem. Soc. Rev.* **2019**, *48*, 3842. https://doi.org/10.1039/c8cs00853a.
(33) Dias, J. A.; Santagneli, S. H.; Ribeiro, S. J. L.; Messaddeq, Y. Perovskite Quantum Dot Solar Cells: An Overview of the Current Advances and Future Perspectives. *Sol. RRL* **2021**, *5* (8), 2100205–2100232. https://doi.org/10.1002/SOLR.202100205.
(34) Wang, C.; Song, Z.; Li, C.; Zhao, D.; Yan, Y. Low-Bandgap Mixed Tin-Lead Perovskites and Their Applications in All-Perovskite Tandem Solar Cells. *Adv. Funct. Mater.* **2019**, *29*, 1–30. https://doi.org/10.1002/adfm.201808801.
(35) Yang, Y.; Qin, H.; Jiang, M.; Lin, L.; Fu, T.; Dai, X.; Zhang, Z.; Niu, Y.; Cao, H.; Jin, Y.; et al. Entropic

Ligands for Nanocrystals: From Unexpected Solution Properties to Outstanding Processability. *Nano Lett.* **2016**. https://doi.org/10.1021/acs.nanolett.6b00737.

(36) Wheeler, L. M.; Sanehira, E. M.; Marshall, A. R.; Schulz, P.; Suri, M.; Anderson, N. C.; Christians, A.; Nordlund, D.; Sokaras, D.; Kroll, T.; et al. Targeted Ligand-Exchange Chemistry on Cesium Lead Halide Perovskite Quantum Dots for High-Efficiency Photovoltaics. *JACS* **2018**, *140*, 10504–10513. https://doi.org/10.1021/jacs.8b04984.

(37) Wang, R.; Shang, Y.; Kanjanaboos, P.; Zhou, W.; Ning, Z.; Sargent, E. H. Colloidal Quantum Dot Ligand Engineering for High Performance Solar Cells. *Energy Environ. Sci.* **2016**, *9* (4), 1130–1143. https://doi.org/10.1039/c5ee03887a.

(38) Yuan, J.; Bi, C.; Wang, S.; Guo, R.; Shen, T.; Zhang, L.; Tian, J. Spray-Coated Colloidal Perovskite Quantum Dot Films for Highly Efficient Solar Cells. *Adv. Funct. Mater.* **2019**, *1906615*, 1–7. https://doi.org/10.1002/adfm.201906615.

(39) Hills-kimball, K.; Yang, H.; Cai, T.; Wang, J.; Chen, O. Recent Advances in Ligand Design and Engineering in Lead Halide Perovskite Nanocrystals. *Adv. Sci.* **2021**, No. 2100214, 1–43. https://doi.org/10.1002/advs.202100214.

(40) Moyen, E.; Kanwat, A.; Cho, S.; Jun, H.; Aad, R.; Jang, J. Ligand Removal and Photo-Activation of CsPbBr3 Quantum Dots for Enhanced Optoelectronic Devices. *Nanoscale* **2018**, *10*, 8591–8599. https://doi.org/10.1039/c8nr01396a.

(41) Li, G.; Huang, J.; Zhu, H.; Li, Y.; Tang, J.-X.; Jiang, Y. Surface Ligand Engineering for Near-Unity Quantum Yield Inorganic Halide Perovskite QDs and High-Performance QLEDs. *Chem. Mater.* **2018**, *30*, 6099−6107. https://doi.org/10.1021/acs.chemmater.8b02544.

(42) Cho, S.; Kim, J.; Jeong, S. M.; Ko, M. J.; Lee, J.-S.; Kim, Y. High-Voltage and Green-Emitting Perovskite Quantum Dot Solar Cells via Solvent Miscibility-Induced Solid-State Ligand Exchange. *Chem. Mater.* **2020**, *32*, 8808−8818. https://doi.org/10.1021/acs.chemmater.0c02102.

(43) Amendola, V.; Fortunati, I.; Marega, C.; Abdelhady, A. L.; Saidaminov, M. I.; Bakr, O. M. High-Purity Hybrid Organolead Halide Perovskite Nanoparticles Obtained by Pulsed-Laser Irradiation in Liquid. *ChemPhysChem* **2017**, *18* (9), 1047–1054. https://doi.org/10.1002/cphc.201600863.

(44) Lamberti, F.; Litti, L.; De Bastiani, M.; Sorrentino, R.; Gandini, M.; Meneghetti, M.; Petrozza, A. High-Quality, Ligands-Free, Mixed-Halide Perovskite Nanocrystals Inks for Optoelectronic Applications. *Advanced Energy Materials*. 2017. https://doi.org/10.1002/aenm.201601703.

(45) Rizzo, A.; Lamberti, F.; Buonomo, M.; Wrachien, N.; Torto, L.; Lago, N.; Sansoni, S.; Pilot, R.; Prato, M.; Michieli, N.; et al. Understanding Lead Iodide Perovskite Hysteresis and Degradation Causes by Extensive Electrical Characterization. *Sol. Energy Mater. Sol. Cells* **2019**, *189*, 43–52. https://doi.org/10.1016/j.solmat.2018.09.021.

(46) Sansoni, S.; De Bastiani, M.; Aydin, E.; Ugur, E.; Isikgor, F. H.; Al-Zahrani, A.; Lamberti, F.; Laquai, F.; Meneghetti, M.; De Wolf, S. Eco-Friendly Spray Deposition of Perovskite Films on Macroscale Textured Surfaces. *Adv. Mater. Technol.* **2020**, *5* (2). https://doi.org/10.1002/admt.201901009.

(47) Zhao, A.; Sheng, Y.; Liu, C.; Yuan, S.; Shan, X.; Di, Y.; Gan, Z. Fluorescent Dynamics of CsPbBr3 Nanocrystals in Polar Solvents: A Potential Sensor for Polarity. *Nanotechnology* **2021**, *32* (13). https://doi.org/10.1088/1361-6528/abd2e9.

(48) Rao, L.; Tang, Y.; Song, C.; Xu, K.; Vickers, E. T.; Bonabi Naghadeh, S.; Ding, X.; Li, Z.; Zhang, J. Z. Polar-Solvent-Free Synthesis of Highly Photoluminescent and Stable CsPbBr3 Nanocrystals with Controlled Shape and Size by Ultrasonication. *Chem. Mater.* **2019**, *31* (2), 365–375. https://doi.org/10.1021/acs.chemmater.8b03298.

(49) Lou, S.; Xuan, T.; Wang, J. Stability: A Desiderated Problem for the Lead Halide Perovskites. *Opt. Mater. X* **2019**, *1* (June), 100023. https://doi.org/10.1016/j.omx.2019.100023.

(50) Williams, S. T.; Rajagopal, A.; Chueh, C. C.; Jen, A. K. Y. Current Challenges and Prospective Research for Upscaling Hybrid Perovskite Photovoltaics. *J. Phys. Chem. Lett.* **2016**, *7* (5), 811–819. https://doi.org/10.1021/acs.jpclett.5b02651.

(51) Deng, Y.; van Brackle, C. H.; Dai, X.; Zhao, J.; Chen, B.; Huang, J. Tailoring Solvent Coordination for High-Speed, Room-Temperature Blading of Perovskite Photovoltaic Films. *Sci. Adv.* **2019**, *5* (12), 1–9. https://doi.org/10.1126/sciadv.aax7537.

(52) Burkitt, D.; Patidar, R.; Greenwood, P.; Hooper, K.; Mcgettrick, J.; Dimitrov, S.; Colombo, M.;

Stoichkov, V.; Richards, D.; Beynon, D.; et al. Roll-to-Roll Slot-Die Coated P-I-N Perovskite Solar Cells Using Acetonitrile Based Single Step Perovskite Solvent System. *Sustain. Energy Fuels* **2020**, *4* (7), 3340–3351. https://doi.org/10.1039/d0se00460j.

(53) Reichardt, C.; Welton, T. *Solvents and Solvents Effects in Organic Chemistry (Fourth, Updated and Enlarged Edition)*; Wiley-VCH Verlag GmbH & Co. KGaA, 2011. https://doi.org/10.1016/b978-0-12-416677-6.00029-9.

(54) Speight, J. G. *Lange's Handbook of Chemistry*, 17th Editi.; Mc Graw Hill Education, 2017.

(55) *Strategies and Techniques for Measuring Solvent Vapour Concentrations in the Work Environment - BEST PRACTICE GUIDELINES*; 2018.

(56) Bessonneau, V.; Clément, M.; Thomas, O. Can Intensive Use of Alcohol-Based Hand Rubs Lead to Passive Alcoholization? *Int. J. Environ. Res. Public Health* **2010**, *7* (8), 3038–3050. https://doi.org/10.3390/ijerph7083038.

(57) Cataldo, F. A Revision of the Gutmann Donor Numbers of a Series of Phosphoramides Including TEPA. *Eur. Chem. Bull.* **2015**, *4* (2), 92–97. https://doi.org/10.17628/ECB.2015.4.92.

(58) Gutmann, V. Solvent Effects on the Reactivities of Organometallic Compounds. *Coord. Chem. Rev.* **1976**, *18* (2), 225–255. https://doi.org/10.1016/S0010-8545(00)82045-7.

(59) Bu, T.; Wu, L.; Liu, X.; Yang, X.; Zhou, P.; Yu, X.; Qin, T.; Shi, J.; Wang, S.; Li, S.; et al. Synergic Interface Optimization with Green Solvent Engineering in Mixed Perovskite Solar Cells. *Adv. Energy Mater.* **2017**, *7* (20), 1–10. https://doi.org/10.1002/aenm.201700576.

(60) Wang, H.; Luo, C.; Tian, P.; Li, D.; Jiang, C.; Zhong, C.; Chen, S.; Huang, R.; Lin, H.; Peng, H. Formation and Dispersion of Organometal Halide Perovskite Nanocrystals in Various Solvents. *J. Colloid Interface Sci.* **2018**, *529*, 575–581. https://doi.org/10.1016/j.jcis.2018.06.053.

(61) Li, B.; Binks, D.; Cao, G.; Tian, J. Engineering Halide Perovskite Crystals through Precursor Chemistry. *Small* **2019**, *15* (47), 1–24. https://doi.org/10.1002/smll.201903613.

(62) Strutt, H. J. W. On the Scattering of Light by Small Particles. *Lond. Edinb. Dublin Philos. Mag. J. Sci* **2009**, *41* (275), 447–454. https://doi.org/10.1080/14786447108640507.

(63) Ghosh, S.; Mishra, S.; Singh, T. Antisolvents in Perovskite Solar Cells: Importance, Issues, and Alternatives. *Adv. Mater. Interfaces* **2020**, *7* (18), 2000950–2000973. https://doi.org/10.1002/admi.202000950.

(64) Cui, Y.; Wang, S.; Ding, L.; Hao, F. Green–Solvent–Processable Perovskite Solar Cells. *Adv. Energy Sustain. Res.* **2021**, *2* (2000047). https://doi.org/10.1002/aesr.202000047.

(65) Jung, M.; Ji, S.; Kim, G. Perovskite Precursor Solution Chemistry : From Fundamentals to Photovoltaic Applications. *Chem. Soc. Rev.* **2019**. https://doi.org/10.1039/c8cs00656c.

(66) Li, Y.; Huang, H.; Xiong, Y.; Richter, A. F.; Kershaw, S. V.; Feldmann, J.; Rogach, A. L. Using Polar Alcohols for the Direct Synthesis of Cesium Lead Halide Perovskite Nanorods with Anisotropic Emission. *ACS Nano* **2019**, *13* (7), 8237–8245. https://doi.org/10.1021/acsnano.9b03508.

(67) Hoshi, K.; Chiba, T.; Sato, J.; Hayashi, Y.; Takahashi, Y.; Ebe, H.; Ohisa, S.; Kido, J. Purification of Perovskite Quantum Dots Using Low-Dielectric-Constant Washing Solvent "Diglyme" for Highly Efficient Light-Emitting Devices. *ACS Appl. Mater. Interfaces* **2018**, *10*, 24607−24612. https://doi.org/10.1021/acsami.8b05954.

(68) Liang, Z.; Zhao, S.; Xu, Z.; Qiao, B.; Song, P.; Gao, D.; Xu, X. Shape-Controlled Synthesis of All-Inorganic CsPbBr3 Perovskite Nanocrystals with Bright Blue Emission. *ACS Appl. Mater. Interfaces* **2016**, *8* (42), 28824–28830. https://doi.org/10.1021/acsami.6b08528.

(69) Chen, J.; Zhang, C.; Liu, X.; Peng, L.; Lin, J.; Chen, X. Carrier Dynamic Process in All-Inorganic Halide Perovskites Explored by Photoluminescence Spectra. *Photonics Res.* **2021**, *9* (2), 020151–020170. https://doi.org/10.1364/prj.410290.

(70) Lignos, I.; MacEiczyk, R. M.; Kovalenko, M. V.; Stavrakis, S. Tracking the Fluorescence Lifetimes of Cesium Lead Halide Perovskite Nanocrystals during Their Synthesis Using a Fully Automated Optofluidic Platform. *Chem. Mater.* **2020**, *32* (1), 27–37. https://doi.org/10.1021/acs.chemmater.9b03438.

(71) Rodová, M.; Brooek, J.; Knííek, K.; Nitsch, K. Phase Transitions in Ternary Caesium Lead Bromide. *J. Therm. Anal. Calorim.* **2003**, *71*, 667–673.

(72) Wang, L.; Fu, K.; Sun, R.; Lian, H.; Hu, X.; Zhang, Y. Ultra-Stable CsPbBr3 Perovskite Nanosheets for X-

Ray Imaging Screen. *Nano-Micro Lett.* **2019**, *11* (52). https://doi.org/10.1007/s40820-019-0283-z.
(73) Zhang, D.; Gökce, B.; Barcikowski, S. Laser Synthesis and Processing of Colloids: Fundamentals and Applications. *Chem. Rev.* **2017**, *117* (5), 3990–4103. https://doi.org/10.1021/acs.chemrev.6b00468.
(74) Zeng, H.; Du, X. W.; Singh, S. C.; Kulinich, S. A.; Yang, S.; He, J.; Cai, W. Nanomaterials via Laser Ablation/Irradiation in Liquid: A Review. *Adv. Funct. Mater.* **2012**, *22* (7), 1333–1353. https://doi.org/10.1002/adfm.201102295.
(75) Matthias Kind. Colloidal Aspects of Precipitation Processes. *Chem. Eng. Sci.* **2002**, *57*, 4287–4293.
(76) Hamill, J. C.; Schwartz, J.; Loo, Y. L. Influence of Solvent Coordination on Hybrid Organic-Inorganic Perovskite Formation. *ACS Energy Lett.* **2018**, *3* (1), 92–97. https://doi.org/10.1021/acsenergylett.7b01057.
(77) Feng, J.; Han, X.; Huang, H.; Meng, Q.; Zhu, Z.; Yu, T.; Li, Z.; Zou, Z. Curing the Fundamental Issue of Impurity Phases in Two-Step Solution-Processed CsPbBr3 Perovskite Films. *Sci. Bull.* **2020**, *65* (9), 726–737. https://doi.org/10.1016/j.scib.2020.01.025.
(78) Nasi, L.; Calestani, D.; Mezzadri, F.; Mariano, F.; Listorti, A.; Ferro, P.; Mazzeo, M.; Mosca, R. All-Inorganic CsPbBr3 Perovskite Films Prepared by Single Source Thermal Ablation. *Front. Chem.* **2020**, *8* (April), 1–10. https://doi.org/10.3389/fchem.2020.00313.
(79) Tong, G.; Chen, T.; Li, H.; Song, W.; Chang, Y.; Liu, J.; Yu, L.; Xu, J.; Qi, Y.; Jiang, Y. High Efficient Hole Extraction and Stable All-Bromide Inorganic Perovskite Solar Cells via Derivative-Phase Gradient Bandgap Architecture. *Sol. RRL* **2019**, *3* (5), 1900030–1900038. https://doi.org/10.1002/SOLR.201900030.
(80) Klein, E.; Lesyuk, R.; Klinke, C. Insights into the Formation Mechanism of Two-Dimensional Lead Halide Nanostructures. *Nanoscale* **2018**, *10* (9), 4442–4451. https://doi.org/10.1039/c7nr09564c.
(81) Radicchi, E.; Mosconi, E.; Elisei, F.; Nunzi, F.; De Angelis, F. Understanding the Solution Chemistry of Lead Halide Perovskites Precursors. *ACS Appl. Energy Mater.* **2019**, *2* (5), 3400–3409. https://doi.org/10.1021/acsaem.9b00206.
(82) Brennan, M. C.; Zinna, J.; Kuno, M. Existence of a Size-Dependent Stokes Shift in CsPbBr3 Perovskite Nanocrystals. *ACS Energy Lett.* **2017**, *2*, 1487–1488. https://doi.org/10.1021/acsenergylett.7b00383.
(83) Rosa-Pardo, I.; Rando-Brotons, M.; Pocoví-Martínez, S.; Galian, R. E.; Pérez Prieto, J. Laser Ablation of Hybrid Perovskite Bulks into Nanoparticles: Adamantylammonium Halides as Ligands and Halide Sources. *ChemNanoMat* **2019**, *5* (3), 328–333. https://doi.org/10.1002/cnma.201800621.
(84) Taylor, A. D.; Sun, Q.; Goetz, K. P.; An, Q.; Schramm, T.; Hofstetter, Y.; Litterst, M.; Paulus, F.; Vaynzof, Y. A General Approach to High Efficiency Perovskite Solar Cells by Any Antisolvent. *Nat. Commun.* **2021**, 1–11. https://doi.org/10.1038/s41467-021-22049-8.
(85) Shaikh, A. F.; Tamboli, M. S.; Patil, R. H.; Bhan, A.; Ambekar, J. D.; Kale, B. B. Bioinspired Carbon Quantum Dots: An Antibiofilm Agents. *J. Nanosci. Nanotechnol.* **2018**, *19* (4), 2339–2345. https://doi.org/10.1166/JNN.2019.16537.
(86) Puvvada, N.; Kumar, P.; Konar, S.; Kalita, H.; Mandal, M.; Pathak, A.; Prashanth Kumar, B. N. Synthesis of Biocompatible Multicolor Luminescent Carbon Dots for Bioimaging Applications Synthesis of Biocompatible Multicolor Luminescent Carbon Dots for Bioimaging Applications. *Sci. Technol. Adv. Mater.* **2012**, *13*, 045008–045014. https://doi.org/10.1088/1468-6996/13/4/045008.
(87) De, B.; Karak, N. A Green and Facile Approach for the Synthesis of Water Soluble Fluorescent Carbon Dots from Banana Juice. *RSC Adv.* **2013**, *3*, 8286–8290. https://doi.org/10.1039/c3ra00088e.
(88) Kaczmarek, A.; Hoffman, J.; Morgiel, J.; Mościcki, T.; Stobiński, L.; Szymański, Z.; Małolepszy, A. Luminescent Carbon Dots Synthesized by the Laser Ablation of Graphite in Polyethylenimine and Ethylenediamine. *Materials (Basel).* **2021**, *14* (4), 1–13. https://doi.org/10.3390/ma14040729.
(89) Yu, H.; Li, X.; Zeng, X.; Lu, Y. Preparation of Carbon Dots by Non-Focusing Pulsed Laser Irradiation in Toluene. *Chem. Commun.* **2015**, *52* (4), 819–822. https://doi.org/10.1039/C5CC08384B.
(90) Wang, X.; Feng, Y.; Dong, P.; Huang, J. A Mini Review on Carbon Quantum Dots: Preparation, Properties, and Electrocatalytic Application. *Front. Chem.* **2019**, *0*, 671–678. https://doi.org/10.3389/FCHEM.2019.00671.
(91) Chen, Z.; Zhou, R.; Yan, H.; Li, L. Fabrication of Fluorescent Carbon Dots by Laser Ablation in Alkaline Solution Coupled with Ag Nanoparticles for Enhanced SERS. *MRS Commun.* **2021**. https://doi.org/10.1557/s43579-021-00060-w.

(92) Pal, A.; Palashuddin Sk, M.; Chattopadhyay, A. Recent Advances in Crystalline Carbon Dots for Superior Application Potential. *Matererials Adv.* **2020**, *1*, 553. https://doi.org/10.1039/d0ma00108b.
(93) Yan, F.; Sun, Z.; Zhang, H.; Sun, & X.; Jiang, Y.; Bai, Z. The Fluorescence Mechanism of Carbon Dots, and Methods for Tuning Their Emission Color: A Review. *Microchim. Acta* **2019**, *186*, 583–619. https://doi.org/10.1007/s00604-019-3688-y.
(94) Carbonaro; Corpino; Salis; Mocci; Thakkar; Olla; Ricci. On the Emission Properties of Carbon Dots: Reviewing Data and Discussing Models. *Carbon N. Y.* **2019**, *5* (4), 60–74. https://doi.org/10.3390/c5040060.
(95) Hola, K.; Bourlinos, A. B.; Kozak, O.; Berka, K.; Siskova, K. M.; Havrdova, M.; Tucek, J.; Safarova, K.; Otyepka, M.; Giannelis, E. P.; et al. Photoluminescence Effects of Graphitic Core Size and Surface Functional Groups in Carbon Dots: COO- Induced Red-Shift Emission. *Carbon N. Y.* **2014**, *70*, 279–286. https://doi.org/10.1016/J.CARBON.2014.01.008.
(96) Righetto, M.; Privitera, A.; Fortunati, I.; Mosconi, D.; Zerbetto, M.; Curri, M. L.; Corricelli, M.; Moretto, A.; Agnoli, S.; Franco, L.; et al. Spectroscopic Insights into Carbon Dot Systems. *J. Phys. Chem. Lett.* **2017**, *8* (10), 2236–2242. https://doi.org/10.1021/acs.jpclett.7b00794.
(97) Sharma, A.; Gadly, T.; Gupta, A.; Ballal, A.; Kumar Ghosh, S.; Kumbhakar, M. Origin of Excitation Dependent Fluorescence in Carbon Nanodots. *J. Phys. Chem. Lett.* **2016**, *7*, 3695–3702. https://doi.org/10.1021/acs.jpclett.6b01791.
(98) Rathore, E.; Maji, K.; Rao, D.; Saha, B.; Biswas, K. Charge Transfer in the Heterostructure of CsPbBr3 Nanocrystals with Nitrogen-Doped Carbon Dots. *J. Phys. Chem. Lett* **2020**, *11*, 8002–8007. https://doi.org/10.1021/acs.jpclett.0c02139.
(99) Wang, Y.; Liu, Y.; Xu, Y.; Zhang, C.; Bao, H.; Wang, J.; Guo, Z.; Wan, L.; Eder, D.; Wang, S. (CH3NH3)3Bi2I9 Perovskite Films Fabricated via a Two-Stage Electric-Field-Assisted Reactive Deposition Method for Solar Cells Application. *Electrochim. Acta* **2020**, *329*. https://doi.org/10.1016/j.electacta.2019.135173.
(100) Hassan Algadi, Chandreswar Mahata, Janghoon Woo, Minkyu Lee, M. K. and T. L. Enhanced Photoresponsivity of All-Inorganic (CsPbBr3) Perovskite Nanosheets Photodetector with Carbon Nanodots (CDs). *Electronics* **2019**, *8*, 678–690.
(101) Ibaceta-Jañ, J.; Muydinov, R.; Rosado, P.; Mirhosseini, H.; Chugh, M.; Heinrich, D.; Wagner, M. R.; Kü, T. D.; Szyszka, B.; Kovalenko De, M. V; et al. Vibrational Dynamics in Lead Halide Hybrid Perovskites Investigated by Raman Spectroscopy. *Phys. Chem. Chem. Phys.* **2020**, *5604*, 5604–5614. https://doi.org/10.1039/c9cp06568g.
(102) Hadjiev, V. G.; Wang, C.; Wang, Y.; Su, X.; Calderon, H. A.; Robles Hernandez, F.; Wang, Z. M.; Bao, J. M. Phonon Fingerprints of CsPb2Br5. *J. Phys. Condens. Matter* **2018**, *30*, 405703–405708. https://doi.org/10.1088/1361-648X/aadeb4.
(103) Beyssac, O.; Goffé, B.; Petitet, J. P.; Froigneux, E.; Moreau, M.; Rouzaud, J. N. On the Characterization of Disordered and Heterogeneous Carbonaceous Materials by Raman Spectroscopy. *Spectrochim. Acta - Part A Mol. Biomol. Spectrosc.* **2003**, *59* (10), 2267–2276. https://doi.org/10.1016/S1386-1425(03)00070-2.
(104) Lee, V.; Whittaker, L.; Jaye, C.; Baroudi, K. M.; Fischer, D. A.; Banerjee, S. Large-Area Chemically Modified Graphene Films: Electrophoretic Deposition and Characterization by Soft X-Ray Absorption Spectroscopy. *Chem. Mater* **2009**, *21* (16), 3905–3916. https://doi.org/10.1021/cm901554p.
(105) Hodkiewicz, J. Characterizing Carbon Materials with Raman Spectroscopy. *Thermo Fish. Sci.* **2010**.
(106) Puech; Kandara; Paredes; Moulin; Weiss-Hortala; Kundu; Ratel-Ramond; Plewa; Pellenq; Monthioux. Analyzing the Raman Spectra of Graphenic Carbon Materials from Kerogens to Nanotubes: What Type of Information Can Be Extracted from Defect Bands? *C - J. Carbon Res.* **2019**, *5* (4), 69–88. https://doi.org/10.3390/c5040069.
(107) Postek, M. T. An Approach to the Reduction of Hydrocarbon Contamination in the Scanning Electron Microscope. *Scanning Vol.* **1996**, *18* (4), 269–274. https://doi.org/10.1002/SCA.1996.4950180402.
(108) Farr, N. T. H.; Hughes, G. M.; Rodenburg, C. Materials Monitoring Carbon in Electron and Ion Beam Deposition within FIB-SEM. *Matererials* **2021**, *14*, 3034–3044. https://doi.org/10.3390/ma14113034.
(109) Lakowicz, J. R. *Principles of Fluorescence Spectroscopy - Third Edition (Pages 141-144)*; 2011. https://doi.org/10.1006/abio.2000.4850.

7. Conclusions and Future Outlook

The present doctoral thesis is the result of the efforts devoted to establishing profitably collaborations with different research groups and laboratories, where a series of processes and measurements were performed for a full understanding of perovskite-based device performances.

In the introductive Chapter 1, an overview of the excellent optical and electronic properties of lead halide perovskites is provided to the reader, emphasizing how this class of semiconductor materials has been widely studied and processed for many types of optoelectronic applications in the last decade.

Chapter 2 is devoted to describing the “in liquid” and” in solution” laser ablation processes - the synthetic route selected to produce nanomaterials in solution for the whole thesis project, reporting selected examples aimed at highlighting the main experimental parameters to be controlled for the synthesis of nanomaterials.

Chapter 3 deals with degradation and hysteresis mechanisms of archetypal methylammonium lead iodide hybrid organic-inorganic perovskite material. Thanks to electrical characterizations performed at different scan rates on interdigitated devices, it was possible to recognize the causes behind electrical hysteresis of perovskite, distinguishing between temporary and permanent phenomena generated during current-voltage measurements. A qualitative model describing the bands bending under different conditions was presented to explain the dynamics observed in the devices during the electrical scans. The results indicated no (or negligible) ferroelectric phenomenon in the perovskite material, while ions migration at grain boundaries lead to material degradation. This study, conducted on planar devices but extendable to vertical ones as well, gives provides a wiser view of the ion migration effects proving that it must be suppressed to optimize both functionality and reliability of hybrid organic-inorganic perovskite materials and the devices implementing them.

In Chapter 4, the use of lead iodide nanoparticles as porous precursor-buffer layer for carbon-based perovskite solar cells was presented. The optimization of the laser ablation in solution process to produce highly concentrated nanoparticle colloids and their deposition by spray coating technique have been the major results of this investigation, showing the feasibility of the method. It is speculated that, by this strategy, the scalability of carbon-based perovskite solar cells can be

improved thanks to: (i) a simplification of overall fabrication process by removing the mesoporous oxide spacers, which require thermal sintering at high temperatures; (ii) the avoidance of infiltration step of perovskite precursor solutions through the stack, which usually require toxic solvents and a robotic mesh deposition technique. For these reasons, this investigation constitutes an important step towards more sustainable production of carbon-based perovskite solar cell modules. Future improvements will include different perovskite conversion and/or post–treatment conditions to reduce the roughness and the grain boundaries density in the perovskite layer, identified as the main causes of the high charge recombination observed in the assembled solar cells.

The spray deposition of perovskite thin films on textured surfaces for tandem solar cell devices is the main topic of Chapter 5. The use of laser-produced nanocrystals as perovskite precursors allowed to follow and optimize an eco-friendly procedure. Perovskite thin films with optimal bandgap, controlled thickness, and conformal coverage were obtained by sequential micro-airbrush and ultrasonic spray-coating deposition techniques. The novel fully-automated deposition protocols presented in this study well suits the industrial standards and constitutes a viable way for future large-scale perovskite-silicon tandem solar cells fabrication. Next steps will involve the further optimization of spray coating deposition of perovskite thin films, to achieve flatter covering, as well as the optimization of ultrasonic spray coating of the other layers required to complete the tandem stack.

Finally, Chapter 6 deals with the optimization of laser ablation in solution process to produce ligand-free high-emissive colloidal solutions of all-inorganic cesium lead bromide perovskite nanocrystals for LED applications. By opportunely selecting the dielectric constant and the polarity of the solvents employed for the synthesis, it was demonstrated that alcohols can be employed for the eco-sustainable synthesis of perovskite nanomaterials. “In-situ” synthesis proved to be a more effective synthetic route than “2-step” one, providing colloidal solution of cesium lead bromide perovskite nanocrystals with better optical and morphological features. This investigation showed how, in proper conditions, laser ablation in solution can be an employed as an effective alternative top-down approach to synthesize ligand-free colloids in “green” solvents, facing the urgent call for more sustainable synthesis and processing of lead halide perovskite nanomaterials. The technique has also been extended and optimized to other green solvents, such as acetates and anisole. The results highlighted how aromatic solvents cannot be used for the synthesis due to the formation of carbon dots, acting as quenching species in solution, during laser ablation.

List of Abbreviations

μ	Octahedral Factor
AFM	Atomic Force Microscopy
CD	Carbon Dot
c-Si	Crystalline Silicon
CTM	Charge-Transport Material
DMF	Dimethyl Formamide
DMSO	Dimethyl Sulfoxide
DSSC	Dye-Sensitized Solar Cell
e^-	Electron
EA	Ethyl Acetate
EDX	Energy Dispersive X-Ray
E_F	Quasi-Fermi Level
E_{GAP}	Energy Bandgap
EQE	External Quantum Efficiency
ETM	Electron-Transporting Material
FA^+	Formamidinium
FABr	Formamidinium Bromide
FAI	Formamidinium Iodide
FF	Fill Factor
FTO	Fluorine-doped Tin Oxide
FWHM	Full Width at Half Maximum
h^+	hole
HOIP	Hybrid Organic-Inorganic Perovskite
HOMO	Highest Occupied Molecular Orbital
HTM	Hole-Transporting Material
IPA	Isopropyl Alcohol
IQE	Internal Quantum Efficiency
I_{SC}	Short-Circuit Current
ITO	Indium-Tin Oxide
I-V	Current-Voltage
IZO	Indium-Zinc Oxide
J_M	Maximum Current Density
J-V	Current Density–Voltage
LAL	Laser Ablation under Liquid
LASiS	Laser Ablation Synthesis in Solution
LED	Light-Emitting Diode
LHP	Lead Halide Perovskite
LUMO	Lowes Unoccupied Molecular Orbital
MA^+	Methylammonium
MABr	Methylammonium Bromide
MAI	Methylammonium Iodide
$MAPbI_3$	Methylammonium Lead Triiodide
mC-PSC	Mesoporous Carbon-based Perovskite Solar Cell

NC	Nanocrystal
NIR	Near Infrared
NP	Nanoparticle
OLED	Organic Light-Emitting Diode
PCE	Photo-Conversion Efficiency
PECVD	Plasma Enhanced Chemical Vapor Deposition
P_{IN}	Incident Power
PL	Photoluminescence
P_M	Maximum Power
P_{OUT}	Output Power of Solar Cell
PSC	Perovskite Solar Cell
PV	Photovoltaic
PVD	Physical Vapor Deposition
QD	Quantum Dot
QY	Quantum Yield
R_{SERIES}	Series Resistance
R_{SHEET}	Sheet Resistance
R_{SHUNT}	Shunt Resistance
RT	Room Temperature
SEF	Sequential Eco-Friendly
SEM	Scanning Electron Microscopy
SHE	Safety, Health, and Environmental
SHJ	Silicon Heterojunction
SSPL	Steady-State Photoluminescence
t	Tolerance Factor
TEM	Transmission Electron Microscopy
TRPL	Time-Resolved Photoluminescence
USC	Ultrasonic Spray Coating
UV-Vis	Ultraviolet–Visible
V_M	Maximum Voltage
V_{OC}	Open-Circuit Voltage
W_F	Work Function
XRD	X-Ray Diffraction

Achievements

Publications

1. A. Rizzo et al., “Understanding lead iodide perovskite hysteresis and degradation causes by extensive electrical characterization - *Solar Energy Materials and Solar Cells*, 189 (**2019**) 43–52
2. Sansoni et al., “Eco-Friendly Spray Deposition of Perovskite Films on Macroscale Textured Surfaces” - *Advanced Materials Technologies* **2020**, 1901009-1901014
3. E. Aydin et al., “Scalable Processing of MXene Rear Electrodes for High-Efficiency Industrial-Size Silicon Heterojunction Solar Cells” (submitted to *ACS Nano)*
4. Sansoni et al., “Synthesis of $CsPbBr_3$ Nanocrystals via Laser Ablation in Alcohol for More Sustainable Perovskite-based Optoelectronics” (submitted to *ACS Sustainable Chemistry & Engineering*).

List of Courses

1. Broadband Electric Spectroscopy
2. Bruker Online Training on TOPAS Software for XRD Analysis
3. Brunauer-Emmett-Teller Surface Analysis
4. Dynamic Light Scattering & Z-Potential Analysis
5. Ellipsometry
6. Extended X-ray Absorption Fine Structure & X-ray Absorption Near Edge Structure
7. High resolution particle size analysis using Differential Centrifugal Sedimentation
8. High Resolution X-Ray Diffraction & Reflectivity
9. International School on Hybrid and Organic Photovoltaics (2^{nd}-6^{th} September 2019)
10. Introduction to Transmission Electron Microscopy
11. LabVIEW Core 1 - Online Training Course
12. Nonlinear Optics Z-scan Technique
13. Nuclear Magnetic Resonance & Mass Spectroscopy
14. Online school on Fundamentals of Semiconductive Quantum Dots (11^{th}-13^{th} May 2021)
15. Optical Tweezers
16. Radiation Protection for Personnel Exposed to Laser Radiation
17. Scanning Electron Microscopy & Energy Dispersive X-Ray Analysis
18. Steady-state & Time-Resolved Photoluminescence
19. Temperature-Modulated Differential Scanning Calorimetry
20. UV-Visible-NIR & Raman Spectroscopies
21. X-Ray Photoelectron Spectroscopy

Attended Conferences

1. **Materials For Today's Energy Challenge** – 3rd-4th June 2019, Padova (Italy)
   Oral and Poster Presentations: "Towards a Sustainable Large-Scale Production of Perovskites for Tandem Solar Cells Application"
2. **XLVII National Congress of Physical Chemistry Division**
   1st-4th July 2019, Rome (Italy) – *Oral Presentation*: "Spray Cast Perovskites: Towards Large Scale Production of Perovskite Solar Cells"
3. **EnerCHEM2020: Chemistry for Renewable Energies**
   12th-14th February 2020, Padova (Italy) – *Oral Presentation*: "Eco-Friendly Spray Deposition of Perovskite Thin Films for Textured Tandem Solar Cells"
4. **Virtual Perovskite Conference (ViPerCon)** – 14th April 2020 (Online Conference)
5. **12th International Conference on Hybrid & Organic Photovoltaics (HOPV)** 26th-29th May 2020 (Online Conference) – e*Poster Presentation*: "Eco-Friendly Spray Deposition of Perovskite Films on Macroscale Textured Surfaces"
6. **Perovskite Quantum Dots: Syntheses, Physical Properties and Applications to Optoelectronic Devices** – 12th June 2020 (Online Conference)
7. **nanoGe Fall Meeting** – 20th-23rd October 2020 (Online Conference)
   ePoster Presentation: "Eco-Friendly Spray Deposition of Perovskite Films on Macroscale Textured Surfaces"
8. **Next Generation Solar Energy Conference, 5th edition (NGSE5)**
   7th-9th December 2020 (Online Conference)
9. **International Conference on Advances and Challenges in Perovskite and Organic Solar Cells** – 21st-22nd January 2021 (Online Conference)
10. **Virtual Perovskite Conference (ViPerCon)** – 12th April 2021 (Online Conference)
11. **XXVII National Congress of the Italian Chemistry Society**
    14th-23rd September 2021 (Online Conference) – *Oral Presentation*: "Lead Halide Perovskites by Laser Ablation in Solution for More Sustainable Optoelectronics"

“Don’t give up. Usually, it is the last key
on the ring which opens the door.”

(Paulo Coelho)